MASTER OF SCIENCE

Experimental and theoretical study of encased-plate composite structural walls

Kassem, Wael Abd-Ellah kaoud

Award date:
2010

MASTER OF SCIENCE

Experimental and theoretical study of encased-plate composite structural walls

Wael Abd-Ellah kaoud Kassem

2010

University of Dundee

EXPERIMENTAL AND THEORETICAL STUDY OF ENCASED-PLATE COMPOSITE STRUCTURAL WALLS

by

Wael Abd-Ellah kaoud Kassem
BEng (Hons) MSc

A thesis presented in application for the

fulfilment of the requirements for the degree of

Doctorate of Philosophy,

University of Dundee

December 2010

To my wife, Soha

and my beloved little daughter, Enjy

The best introduction to this work is the first five verses revealed of the Quran:

"Read in the name of thy Lord who created*
Created man out of a clot of congealed blood*
Read and thy Lord is most Generous*
Who taught by the pen*
Taught man what he knew not."

Verses 1-5, Chapter 96

Abstract

Reinforced concrete and steel plate structural walls have been widely used as lateral-load resisting systems in multi-storey buildings. However, they have a number of shortfalls which could be mitigated if a composite construction consisting of steel plates and concrete is used. The encased-plate composite wall studied herein is formed by embedding a steel plate inside a conventionally- reinforced wall.

The behaviour of encased-plate composite walls under pure in-plane shear was studied in an experimental study involving a number of small-scale wall units. In-plane shear tests were carried out on both individual components and on composite walls. The results showed that the behaviour of composite wall was different from its individual components due to the interaction between the encased-plate and the concrete. While the stiffness of the composite wall was higher than that of its individual components, no improvement in ultimate load carrying capacity was associated with composite action.

The test programme further included seven encased-plate composite structural walls tested under in-plane lateral loads. The only test parameter included in the study was the thickness of the encased-plate. The walls were designed to fail in either shear or flexure, and the results demonstrated the effectiveness of the proposed system in resisting shear stresses. A full-field deformation monitoring system based on particle image velocimetry (PIV) and close range photogrammetry was introduced and used to map the deformation and strain distribution of walls during structural testing.

Numerical analysis based on the nonlinear finite element method was carried out within the study. After validation against experimental results, the analysis was applied for a wide range of conventionally-reinforced and encased-plate composite structural walls. Numerical analysis was used to represent the behaviour of encased-plate composite walls within a parametric study that covered a wide variation of parameters that were thought to influence their performance. The finite element model provided better understanding of wall behaviour, and the analysis results showed that walls' aspect ratio, plate thickness, axial loading and central panel's longitudinal reinforcement were the main parameters affecting the behaviour of encased-plate composite walls.

The study also included the development of an analysis method for predicting the shear strength and behaviour of both conventionally-reinforced and encased-plate composite structural walls. The method was based on the softened truss model and utilised a newly proposed cracking angle of diagonal concrete struts. The cracking angle was developed using a regression analysis of the reported shear capacity values of 100 experimental structural walls. The proposed method was then used to predict the shear capacity and deformation behaviour of the new test walls, and the results compared well with the experimental data.

In the light of the experimental observations and numerical modelling, it was concluded that the encased-plate composite structural wall system presented an attractive structural option in lateral load resisting wall applications especially when high shear stresses were expected.

Publications from thesis

1. **Kassem, W.** and Elsheikh, A. (2010), "Estimation of Shear Strength of Structural Shear Walls", Journal of Structural Engineering, ASCE, 136 (10), 1215-1224, DOI:10.1061/(ASCE)ST.1943-541X.0000218.
2. **Kassem, W.** (2008) "Steel/concrete composite shear walls for tall buildings" Young researchers' conference, Abstract No. 19, 19 March, IStructE HQ, London, UK.
3. **Kassem, W.**, Subedi, N. and Elsheikh, A. (2007), Steel/concrete composite shear walls for tall buildings-a new concept", Concrete communication symposium, 9-10 Sept., Sheffield, UK, 36-37.

Acknowledgements

The author would like to express his sincere appreciation to his supervisor Dr Ahmed El-Sheikh, for his guidance and endless support during the course of the study. His patience and friendship will always be valued and sorely missed.

The scholarship provided by The Ministry of Higher Education and the University of El-Minia, Egypt is gratefully acknowledged.

Thanks are also due to all technical staff of the Division of Civil Engineering for providing help and support during the experimental work with gratitude to Mr Christopher Walker, Mr Tim Linford, Mr Gordon Simpson, Mr Michael McKernie, Mr John Anderson, Mr Douglas Robertson, Mr William Hendrson and Mr David Husband. Special thanks to Dr Nutan Subedi, Dr Frazer Smith, Dr Jonathan Knappett and Mr Ernie Kuperus for their valuable advices and suggestions during the experimental investigations.

The author also wishes to thank his friends and colleagues at The University of Dundee for their assistance and dedication, in particular Maher Elabd, Wael Abdu, Farouk Maraqa, Waqas Ahmed, Medhat Osman and Keith Lauder.

The sincere gratitude goes to my wife Soha and my lovely daughter Enjy. Their patience, emotional support and long-term understanding throughout my studies are highly appreciated.

Declaration

I hereby declare that the following thesis and the research work described in it have been composed by me, that all references cited have been consulted, that the work of which it is a record has been carried out by myself, and that it has not been previously accepted for a higher degree.

Wael Kassem

November 2010

Certificate

This is to certify that Wael Kassem has done his research under my supervision, and that he has fulfilled the conditions of Ordinance 14 of the University of Dundee, so that he is qualified to submit the following thesis in application for the Degree of Doctorate of Philosophy in Civil Engineering.

Dr Ahmed El-Sheikh

Senior lecture

Department of Civil Engineering

University of Dundee

November 2010

Table of contents

Chapter 4 Encased-plate composite walls under lateral loading-experimental methodology

Chapter 5 Experimental results and discussion

List of Figures

Chapter 1 Introduction

Chapter 2 Literature review

Chapter 3 Behaviour of encased-plate composite walls under pure in-plane shear

Chapter 4 Encased-plate composite walls under lateral loading-experimental methodology

Chapter 5 Experimental results and discussion

Chapter 6 Numerical modelling of encased-plate composite walls behaviour

Chapter 7 Nonlinear analysis of conventionally-reinforced and encased-plate composite walls

List of Tables

Chapter 3 Behaviour of encased-plate composite walls under pure in-plane shear

Chapter 4 Encased-plate composite walls under lateral loading-experimental methodology

Chapter 5 Experimental results and discussion

Chapter 6 Numerical modelling of encased-plate composite walls behaviour

Chapter 7 Nonlinear analysis of conventionally-reinforced and encased-plate composite walls

Notations

A	Cross-sectional area of a structural wall
d	Principal direction along the axis of concrete struts
d_w	Horizontal length of a structural wall between the centres of boundary elements. In the absence of boundary elements, d_w is taken as 0.8 l_w
E_c	Modulus of elasticity of concrete
E_p	Modulus of elasticity of the encased-plate
E_s	Modulus of elasticity of steel rebars
f'_c	Compressive cylinder strength of concrete
f'_{ct}	Tensile strength of concrete
f_L	Average stress in rebars in L direction
f_{Lp}	Average stress of the encased-plate in L direction
f_s	Average stress of steel rebars
f_t	Average stress in rebars in t direction
f_{tp}	Average normal stress in the encased-plate in t direction
f_y	Yield stress of steel rebars
f_{yp}	Yield stress of the encased-plate
G	Shear modulus
H_w	Wall height
L	The longitudinal direction; usually vertical for a structural wall
l_w	The length of a structural wall
N	Applied axial load on a structural wall
r	Principal direction normal to the axis of concrete struts (d)
t	The transverse direction; usually horizontal for a structural wall
t_p	Thickness of the encased-plate
t_w	Central panel thickness of a structural wall

V	In-plane lateral shear force acting on a typical structural wall
α	Angle of inclination of the *d*-direction with respect to *L*-axis
β	Ratio of plate thickness to central panel thickness = t_p / t_w
γ_{Lt}	Average shear strain in the *L*-*t* coordinate system
Δ	Deflection of a wall top
ε_0	Compression strain at maximum stress in a uniaxial stress-strain curve of concrete cylinder; taken as 0. 002
ε_{ct}	Tensile cracking strain of concrete
ε_d	Average principal strain in *d*-direction
ε_L	Average normal strain in the *L*-direction (positive for tension)
ε_r	Average principal strain in *r*-direction
ε_s	Average strain of steel rebars
ε_t	Average normal strain in *t*-direction
ε_{ut}	Ultimate tensile strain of concrete; taken as 0.002
ε_y	Yield strain of steel rebars
ε_{yp}	Yield strain of encased-plate
ζ	Softening coefficient
ν	Poisson's ratio; taken as 0.3
ρ_L	Average reinforcement ratio in *L*-direction
ρ_t	Average reinforcement ratio in *t*-direction
σ_d	Principal stress in concrete in the principal *d*-direction
σ_L	Normal stress in the reinforced concrete element in *L*-direction
σ_r	Principal stress in concrete in the principal *r*-direction
σ_t	Normal stress in the reinforced concrete element in *t*-direction
τ_{Lt}	Shear stress in reinforced concrete element in *L*-*t* coordinate
τ_{Ltp}	Shear stress in encased-plate

Chapter 1 Introduction

1.1 Overview

Structural walls have been widely used to ensure the lateral stability of both low-rise and high-rise buildings, providing adequate structural performance under service loads at a reasonable cost (Fintel 1991). Documented observations in the period from 1960-1995 on the behaviour of buildings containing structural walls proved their overwhelming success during earthquake excitations (Fintel 1995). Two main types of structural walls are usually used as lateral-load resisting systems in multi-storey buildings all over the world, namely reinforced concrete and steel plate structural walls. While both types have exhibited adequate performance under lateral loadings, they have a number of shortfalls. The main advantages and shortfalls of each wall type are described below.

1.2 Reinforced concrete structural walls

Reinforced concrete structural walls commonly consist of a central panel confined by cross walls or column called boundary elements, Figure 1.1. Boundary elements usually contain concentration of longitudinal reinforcement to provide resistance to flexural stresses, while the central panel contains a uniformly-distributed reinforcement and is designed to resist the shear stresses (Gupta and Rangan 1998).

1.2.1 Advantages

The main advantages of reinforced concrete structural walls are:

- Reinforcement detailing of concrete walls is relatively simple and could be easily implemented on site (Murty 2004).

- Properly designed reinforced concrete walls are a cost effective way for providing adequate resistance to lateral loads so that they are a common choice in earthquake prone countries (Erkmen and Schultz 2007).

1.2.2 Shortfalls

The following is a short list of the shortfalls of reinforced concrete structural walls:

- Concrete tensile cracking and localised compressive crushing are major shortfalls of concrete walls that reduce their load carrying capacity and limit their ductility.
- Relatively high lateral stiffness is customarily provided by concrete structural walls, possibly higher than required to limit drift, therefore high shear forces would be imposed to other structural members which require additional costs to resist these forces (Zhao and Astaneh-Asl 2004).
- Concrete structural walls possess relatively low strength-to-weight ratios when compared with steel plate walls. Thus, concrete walls are not a practical choice in several tall buildings (Zhao and Astaneh-Asl 2007).
- Moreover, concrete as a brittle material should not ordinarily be deemed as suitable means for energy dispersion under shear and compressive stresses (Paulay 1980).

1.3 Steel plate structural walls

Steel plate structural walls are widely accepted as the fundamental lateral force resisting system in high-rise buildings. A steel plate panel, vertical columns and horizontal beams are the main components of a steel plate structural wall system.

1.3.1 Advantages

The main advantages of steel plate structural walls are:

- Architecturally, steel plate structural walls benefit from their smaller thickness compared with concrete walls. A comparative study for the Century Project in the USA suggested that a steel plate wall with average thickness of 45 mm was a substitute to a concrete wall with average thickness of 70 mm, resulting in savings of about 2% in gross area (Seilie and Hooper 2005).
- Steel plate structural walls are commonly associated with significant reductions in building weight. The study by Seilie and Hooper (2005) demonstrated a saving of around 18% in building weight achieved with steel plate structural walls rather than concrete walls, leading to a considerable reduction in foundation loads.
- Steel walls provide an efficient and fast construction system- not only are they fast to construct, but no curing period is required.
- Furthermore, properly designed steel plate walls possess high ductility and exhibit adequate post-buckling capacity without experiencing significant damage up to high drift limits (Zhao and Astaneh-Asl 2002).

1.3.2 Shortfalls

The following is a short list of the shortfalls of steel plate structural walls:

- The major problem facing steel plate walls is buckling under relatively low shear stresses, resulting in not only significant loss of load carrying capacity and stiffness, but also energy dissipation capacity. Thus, transverse stiffeners should be used to limit plate buckling, leading to increased construction costs and time.
- Steel plate structural walls have a significantly lower flexural stiffness compared to concrete walls. Precautions must be taken to provide additional flexural stiffness by means of boundary elements which may increase the overall cost and time of construction (Seilie and Hooper 2005).

- Steel plate walls possess poor resistance against fire, thus fire proofing is essential, which obviously results in increasing building cost.
- Steel plate structural wall system usually suffers from excessive vibration, particularly if it is used as a core enclosing an elevator system (Sabouri-Ghomi 1989).

A better solution for structural walls may be to have a composite construction consisting of both a steel plate and reinforced concrete wall.

1.4 New concept

To render the shortfalls of both steel and concrete structural walls, a novel system is proposed. Encased-plate composite structural wall can alleviate most shortfalls of the two systems while profiting from their attractive features. Composite structural walls consist of a reinforced concrete core with one or more steel plates embedded inside, see Figure 1.1. The presence of vertical and horizontal reinforcement as well as the concrete core around the steel plate would prevent or limit the buckling of the plate. Therefore, no special details may be required to prevent plate buckling.

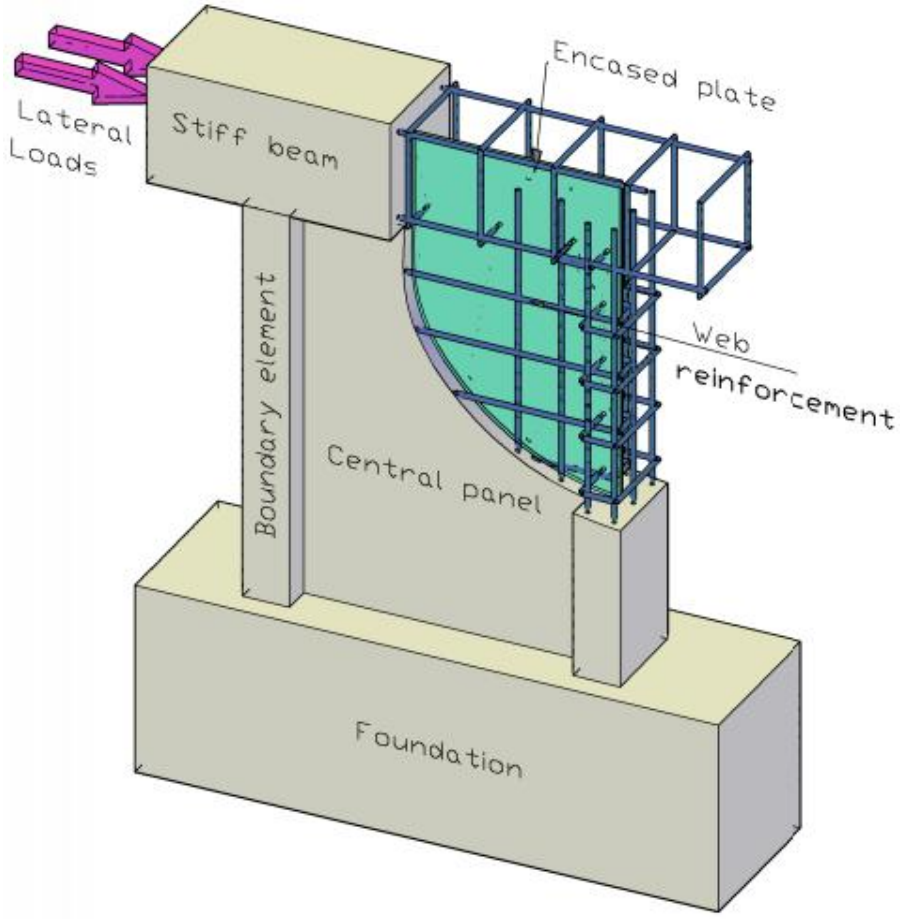

Figure 1.1 Encased-plat**e** composite structural wall system

1.5 Advantages and shortfalls of the proposed system

There are a number of advantages and shortfalls of encased-plate composite structural wall systems over the conventional systems as described below.

1.5.1 Advantages

- For the same shear capacity, encased-plate composite walls possess higher shear stiffness, smaller thickness and less weight compared to conventional concrete walls. The smaller footprint offers a desirable advantage from an architectural point of view, and the reduced weight reduces the forces applied to the columns and foundations, hence reducing the building's total cost.

- Fire proofing, sound and temperature insulation are provided by the concrete encasing the steel plate.
- Composite walls possess relatively high initial stiffness, hence considered effective in controlling the drift.
- In composite walls, the concrete restrains the steel plate and prevents its buckling before yielding.
- The steel plate acts as a concrete reinforcement and reduces dependence on conventional reinforcement leading to considerable savings in construction time and cost.

1.5.2 Shortfalls

- Handling of the large steel plate on site, plate splicing and end fixing are among the main challenges in construction of composite walls.
- Due to the use of plain steel plates, there are concerns about the level of composite action between the plate and concrete core. Some surface roughness or using of shear studs may be necessary although it results in increased cost.
- Potential high cost, due to the manufacturing, transporting and installation of steel plates, in addition to reinforcement preparation and concrete casting.

1.6 Historical background

Historically, encased-plate construction found wide application in simply-supported beams and structural wall coupling beams as a shear reinforcement alternative. In these systems, steel plates are aligned vertically in the beam's cross-section to carry the tensile stresses caused by the applied shear. Encased-plate composite systems in beams attain adequate performance in terms of stiffness, ductility, load carrying capacity and energy dissipation compared to conventionally-reinforced beams (Baglin 1998; Lam *et al.* 2001; 2002; 2003; 2004a; 2004b; 2005). Considering the advantages achieved with

encased-plate construction in beams, the system is now proposed for use in walls and a further understanding of the behaviour in this particular application is therefore required.

1.7 Objectives of the current research

The present research is undertaken to provide a basic understanding of the behaviour of encased-plate structural walls through experimental, numerical and analytical studies. The principal objectives of the research are:

- To study the behaviour of encased-plate composite walls under pure in-plane shear;
- To investigate experimentally the structural behaviour of composite structural walls under combined bending and shear stresses resulted from lateral loading;
- To apply numerical simulation using nonlinear finite element analyses in order to assess the structural behaviour of the composite concrete walls. This has enabled the conduct of a wide parametric study to assess the sensitivity of selected design parameters on strength and ductility of composite system; and
- To develop an analytical model that can predict the strength and behaviour of conventionally-reinforced and encased-plate composite walls.

1.8 Research strategy

The objectives of the current research were accomplished through five consequent phases as described below.

- Phase one commenced by building basic understanding of the behaviour of structural walls and their design strategies as reported in the literature. The literature survey presented in Chapter 2 revealed the shortfalls in the previously proposed systems and highlighted the potential importance of the proposed composite system.

- Phase two: in order to study the behaviour of the composite walls under pure in-plane shear, an experimental study was carried out involving a number of wall units, which represented a typical isolated element of the central panel, see Figure 1.2. The study helped improve understanding of the in-plane shear behaviour of composite walls and provided a detailed investigation at the element level (Chapter 3). The study results pointed to the significant parameters governing the behaviour of composite walls, and helped to design the next experimental programme to study the behaviour of composite walls under lateral loads. A full-field deformation monitoring system based on particle image velocimetry (PIV) and close range photogrammetry was introduced and used to map the deformation and strain distribution of walls during structural testing.

- Phase three involves an experimental study on the behaviour of encased-plate composite walls under motonically increased lateral loads. Seven structural walls were prepared and tested. The specimens had either flanged or rectangular cross-section and were designed such that their failure mode was associated with shear and flexure. The details of the test programme, including details of specimens, material properties, manufacturing process, test setup, instrumentation and test procedures, are presented in Chapter 4. The test results and discussion are presented in Chapter 5.

- Phase four focused on the development of a 3D nonlinear finite element model that simulates the behaviour of encased-plate composite walls. The numerical model was validated against the experimental results available in the literature and the current study. Following successful validation, the model was used to conduct a parametric study to assess the effect of variables which were thought to have a considerable

influence on the behaviour of the encased-plate composite structural walls (Chapter 6).

- Phase five presented an analysis method for predicting the shear strength and behaviour of conventionally-reinforced walls under both monotonic and cyclic loading. The proposed analysis method was based on the softened truss model and utilised a newly proposed cracking angle of the concrete strut. The cracking angle was developed using a regression analysis of the reported shear capacity values of 100 experimental structural walls. The analysis paid particular attention to parameters expected to influence the walls' shear capacity including the geometric properties, reinforcement ratios, internal stresses and concrete strength. The proposed method was used to predict the shear capacity of the tested walls and their deformation behaviour both pre- and post-cracking, and the results compared well with the experimental data. The proposed analysis method was adapted to consider the effect of the encased-plates in composite walls. Experimental and mathematical results were compared and conclusions were drawn on the validity of the proposed model, (Chapter 7).

- The research summary and the main conclusions are finally presented in Chapter 8. The outline of the thesis is briefly described in the flow chart presented in Figure 1.3.

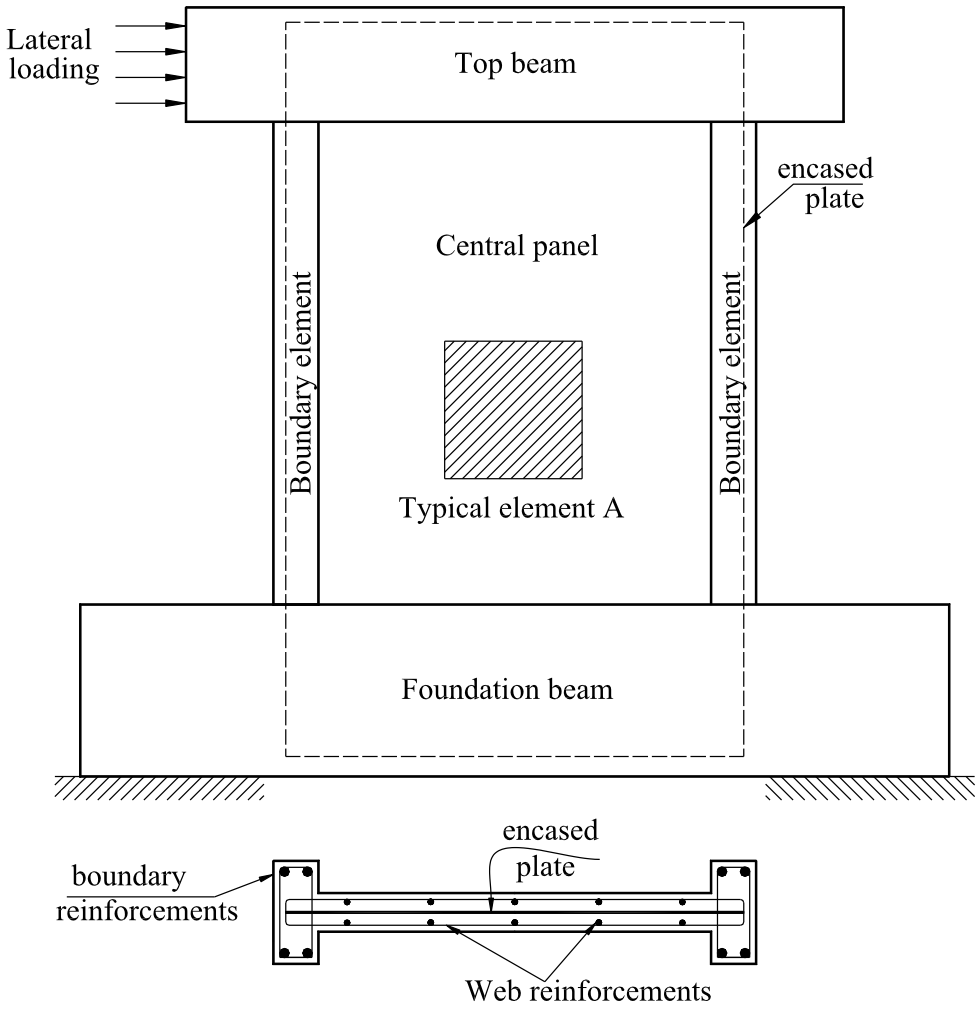

Figure 1.2 View of a typical encased-plate composite structural wall system with an isolated element

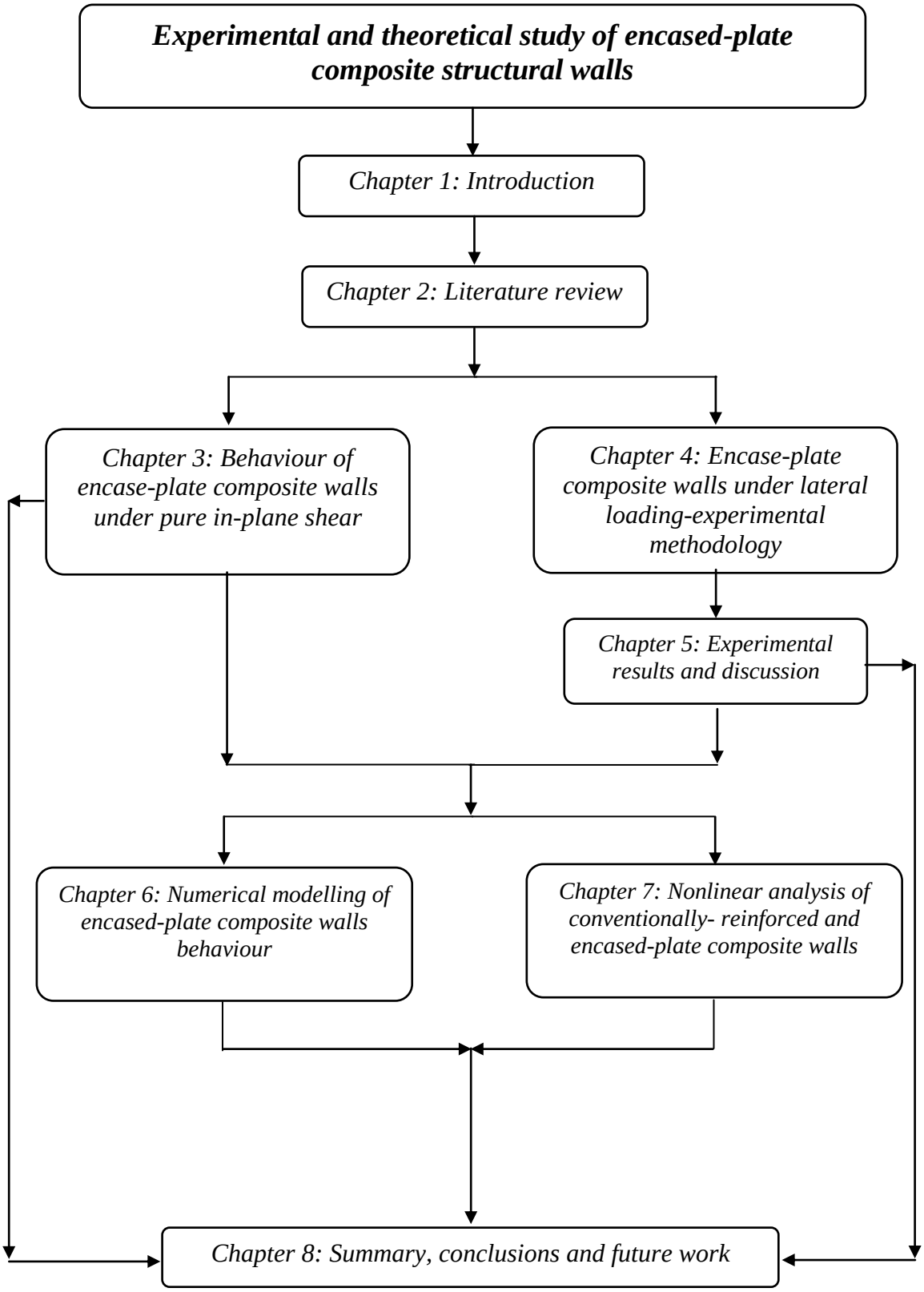

Figure 1.3 Thesis outline

Chapter 2 Literature review

2.1 Introduction

In the last decades, significant attention was devoted to study the behaviour of structural walls due to their key role in protecting buildings against lateral loading either from wind loads or earthquake attacks. Satisfactory performance was exhibited by structural walls under severe earthquakes (Fintel 1995). The main functions of structural walls are to limit excessive deformations and avoid structural damage under earthquake excitations (Paulay and Priestley 1992). The components of buildings might be protected by structural wall systems due to their innate large stiffness. Several types of structural walls have been proposed as lateral-load resisting systems in multi-storey buildings. These wall types will be discussed briefly in Section 2.2, both advantages and disadvantages of each system will be investigated briefly. The literature revealed the potential improvements in performance that can be achieved with encased-plate composite structural walls, as discussed in Section 2.3. The chapter further contains a review of the development stages of encased-plate construction in Section 2.4.

The behaviour of isolated structural walls is generally governed by their relative dimensions, and can be classified as short, squat or cantilever according to their height-to-width ratio (Figure 2.1) and may have planar, flanged or core shape (Figure 2.2). Cantilever walls behave in a primarily flexural style, while short walls act more like deep beams in which shear is the predominate behaviour (Irwin 1984). Walls are usually pierced by a regular pattern of opening to accommodate windows, doors and service ducts forming what is known as coupled walls. Openings can take the form of a single row, two rows or staggered (Figure 2.3).

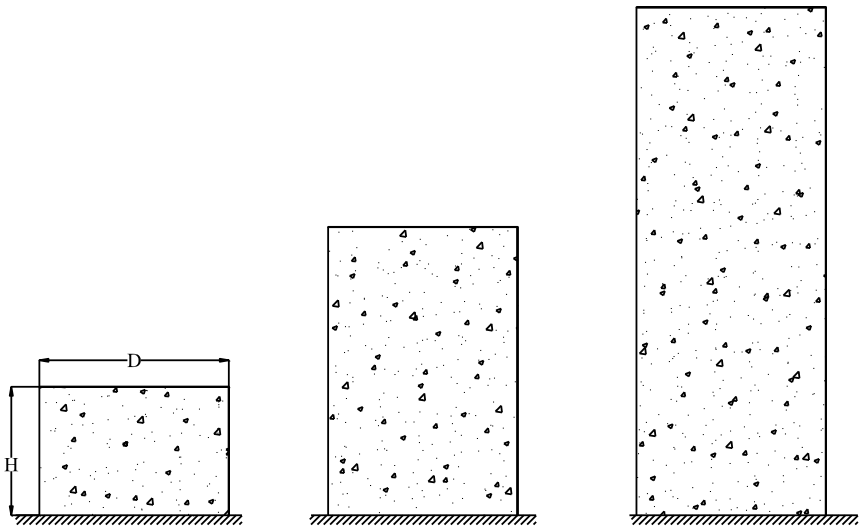

Figure 2.1 Basic types of isolated structural walls (Irwin 1984)

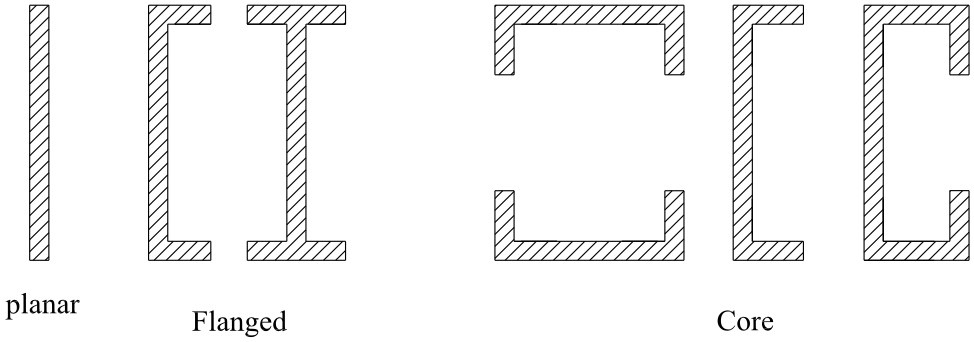

Figure 2.2 Shapes of walls

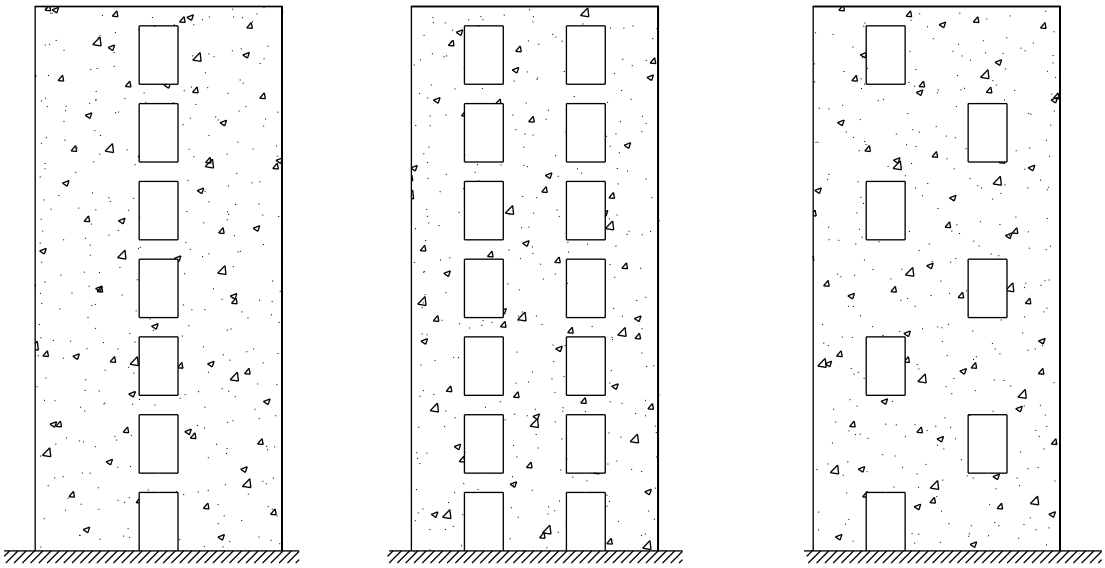

Figure 2.3 Forms of coupled walls

2.2 Alternative designs of structural wall systems

Research on the different types of structural wall systems has been carried out by several investigators in the past six decades. The following discussion concentrates on the types that have been proposed and tried. Some were accepted in the construction industry namely; conventionally-reinforced concrete walls, diagonally reinforced concrete walls, steel plate walls, steel plate composite walls and steel-concrete-steel composite walls, while others were not implemented in applications including double skin-profiled composite walls and perforated steel plate composite walls.

2.2.1 Conventionally reinforced concrete walls

Generally, walls should be designed to behave fully elastically under wind loads and inelastic deformations are allowed to take place under large earthquake attacks. Concrete walls should be designed to be ductile and brittle or even limited ductility failures must be avoided. Ductile behaviour can be achieved by developing a desirable failure mechanism and selecting a suitable detailing of the plastic regions. Due to its brittle nature, concrete should not be deemed a considerable source of energy dissipation either in compression or shear (Paulay 1980). The yielding of the main flexural reinforcements in the plastic zones (usually at wall base) is an example of a desirable failure mechanism (Figure 2.4), while shear failure must be avoided. To ensure the required ductility, the main part of the internal forces in the plastic zone of a structural wall should therefore be assigned to the reinforcement (Paulay and Priestley (1992).

Paulay *et al.* (1982) highlighted that the modes of failure for squat and short walls are highly affected by their relative dimensions, boundary conditions and the way shear forces are introduced to walls. Accordingly, these walls have three main shear failure modes.

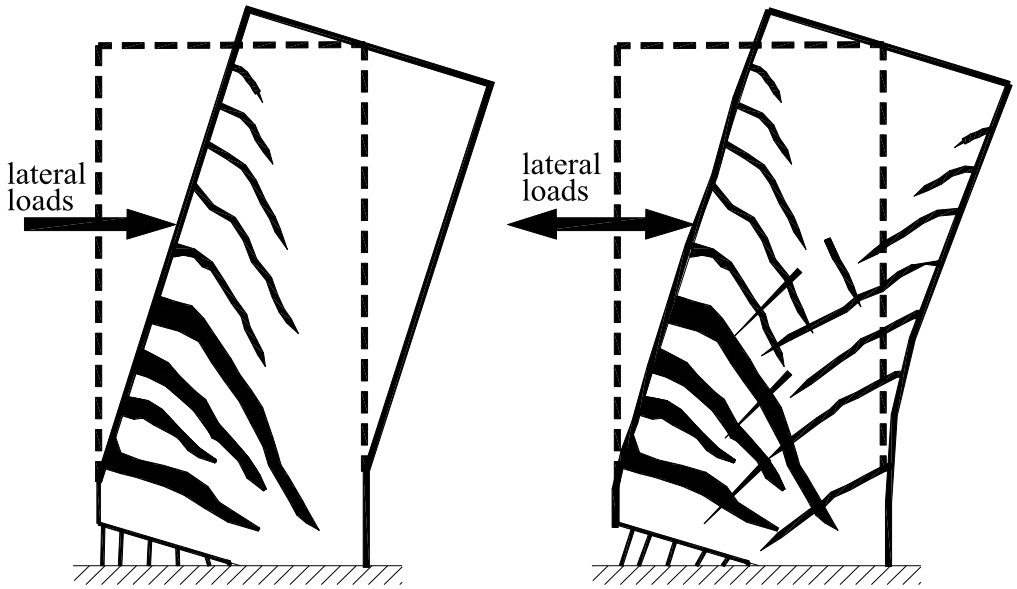

(a) Monotonic loading (b) Cyclic loading

Figure 2.4 Desirable mode of failure according to Paulay and Priestley (1992)

Shear failure by diagonal tension takes place when a corner-to-corner failure plane may develop in walls with insufficient transverse reinforcements, Figure 2.5a. Shear failure by diagonal compression occurs in walls that have adequate transverse shear reinforcements and comes under high shear stresses. The failure is characterised by concrete crushing in the most stressed zone in the compression side near the wall base, Figure 2.5b. Walls failed by shear in diagonal compression suffer from abrupt drop in strength. Thus, this mode of failure must not be allowed when ductile behaviour is required. The third mode of failure is sliding shear in which a continuous horizontal crack, originated from flexural action, develops along the base of the wall, Figure 2.5c. This mode of failure is highly undesirable since it causes significant deterioration of stiffness and energy dissipation capacity, particularly at low shear stresses.

Shear failure by diagonal tension and diagonal compression can be avoided by providing sufficient transverse shear reinforcement and limiting nominal shear stress. The pernicious effects of sliding shear can be controlled by providing some diagonal reinforcement crossing the sliding plane (Paulay *et al.* 1982).

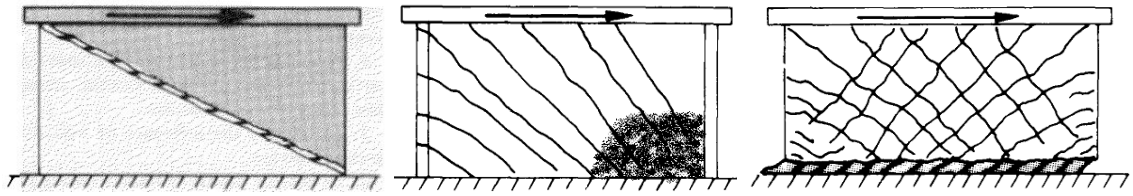

(a) diagonal tension failure (b) diagonal compression (c) sliding shear

Figure 2.5 Shear modes of failure according to Paulay *et al.* (1982)

2.2.2 Diagonally reinforced concrete walls

Diagonal web reinforcement was proposed to be installed in concrete walls to improve their performance and to reduce excessive sliding shear displacements at the wall base. The advantages obtained from using web diagonal reinforcement were first observed by Iliya and Bertero (1980) . The authors tested a number of wall specimens with conventional and diagonal reinforcement. The test results showed that diagonal reinforcement had considerable improvements in energy dissipation and stiffness.

Paulay *et al.* (1982) observed that walls with low height-to-width ratios may suffer from the undesirable sliding shear and their behaviour may improve when a considerable part of the shear stresses was resisted by diagonal reinforcements. Cyclic tests were carried out on four wall specimens with height-to-width ratio of 0.5 (Figure 2.6). Two specimens were reinforced with a uniform grid of conventional reinforcement in their webs, while in the other two some of the conventional reinforcement was replaced by diagonal bars intersecting at mid-height of the specimens (Figure 2.7). Test results showed that the diagonal reinforcement was inadequate to prevent slip; however, a significant improvement in energy dissipation was achieved.

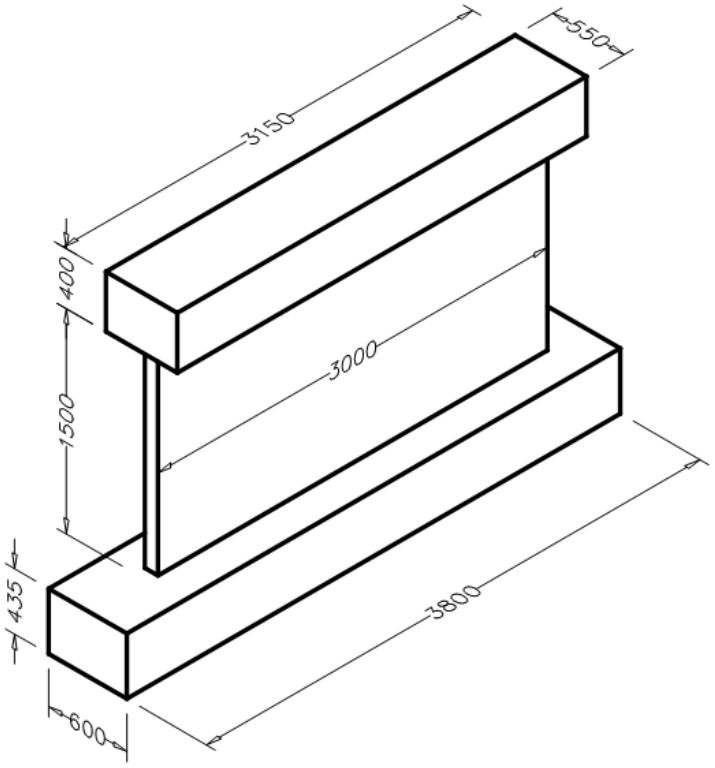

Figure 2.6 Dimensions of specimens tested by Paulay *et al.* (1982)

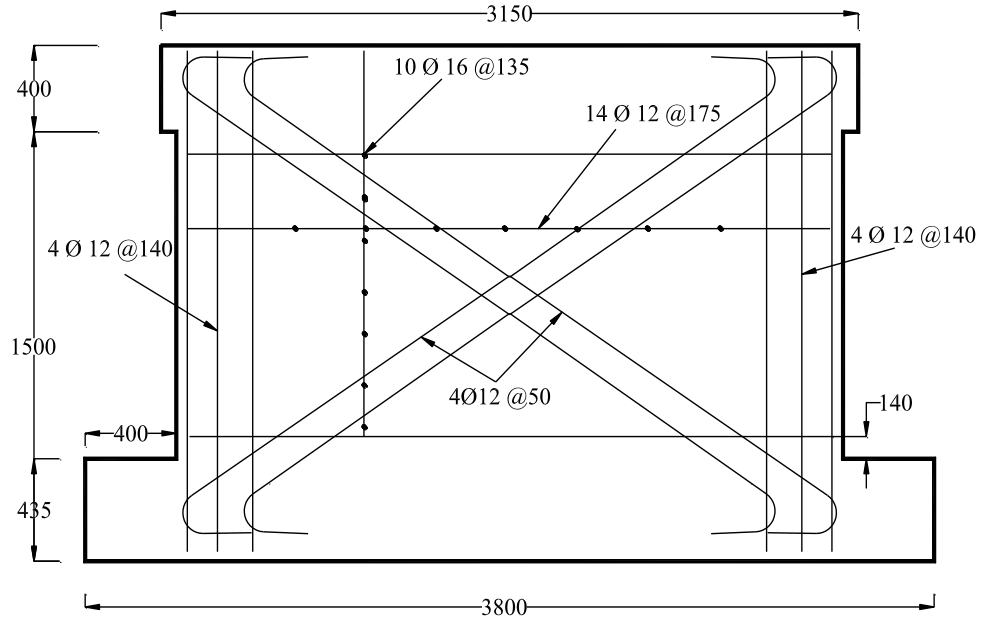

Figure 2.7 Reinforcement details in specimens tested by Paulay *et al.* (1982)

Specimens reinforced with diagonal reinforcement failed due to buckling of the diagonal compression bars after concrete spalling. Buckling of diagonal bars reduced the efficiency of these bars in limiting the sliding shear, and reduced the rate of energy

dissipation. The study concluded that links were required to control the buckling of diagonal bars.

In order to further investigate the behaviour of concrete walls reinforced with diagonal reinforcement, Salonikios *et al.* (1999; 2000) conducted tests on 11 wall specimens. The walls had aspect ratios of 1 and 2, and were reinforced with two curtains of longitudinal and transverse reinforcement in their webs. For comparison purposes, four specimens were designed with diagonal reinforcement intersecting close to the base or at a distance equal to half the wall width (Figure 2.8). The wall specimens were tested under different combinations of axial and cyclic loads. Overall, diagonal reinforcement had a considerable effect in limiting sliding shear and offered a substitute to current practice from an economic point of view. Since diagonal bars intersected the inclined shear cracks almost at right angles, they acted mainly in direct tension and were efficient in controlling the propagation of web inclined shear cracks resulting in a better performance. It was also observed that diagonal reinforcements intersecting close to wall base were more efficient in controlling slide displacements than diagonal bars intersecting above the base, and this was particularly evident in walls with aspect ratio of one. However, walls reinforced with diagonal bars intersecting at a distance equal to half of the wall width resulted in higher strength and energy dissipation capacity.

Recently, Shaingchin *et al.* (2007) carried out cyclic tests on five wall specimens designed with diagonal web reinforcement, see Figure 2.9. The specimens had a flanged cross-section with aspect ratio of 1.5. The test results showed that using diagonal reinforcement could result in changing the failure mode from brittle failure to a more ductile one with considerable reduction in the shear and sliding displacement components. Also, the energy dissipation capacity of walls designed with diagonal web reinforcement was superior to walls with conventional web reinforcement.

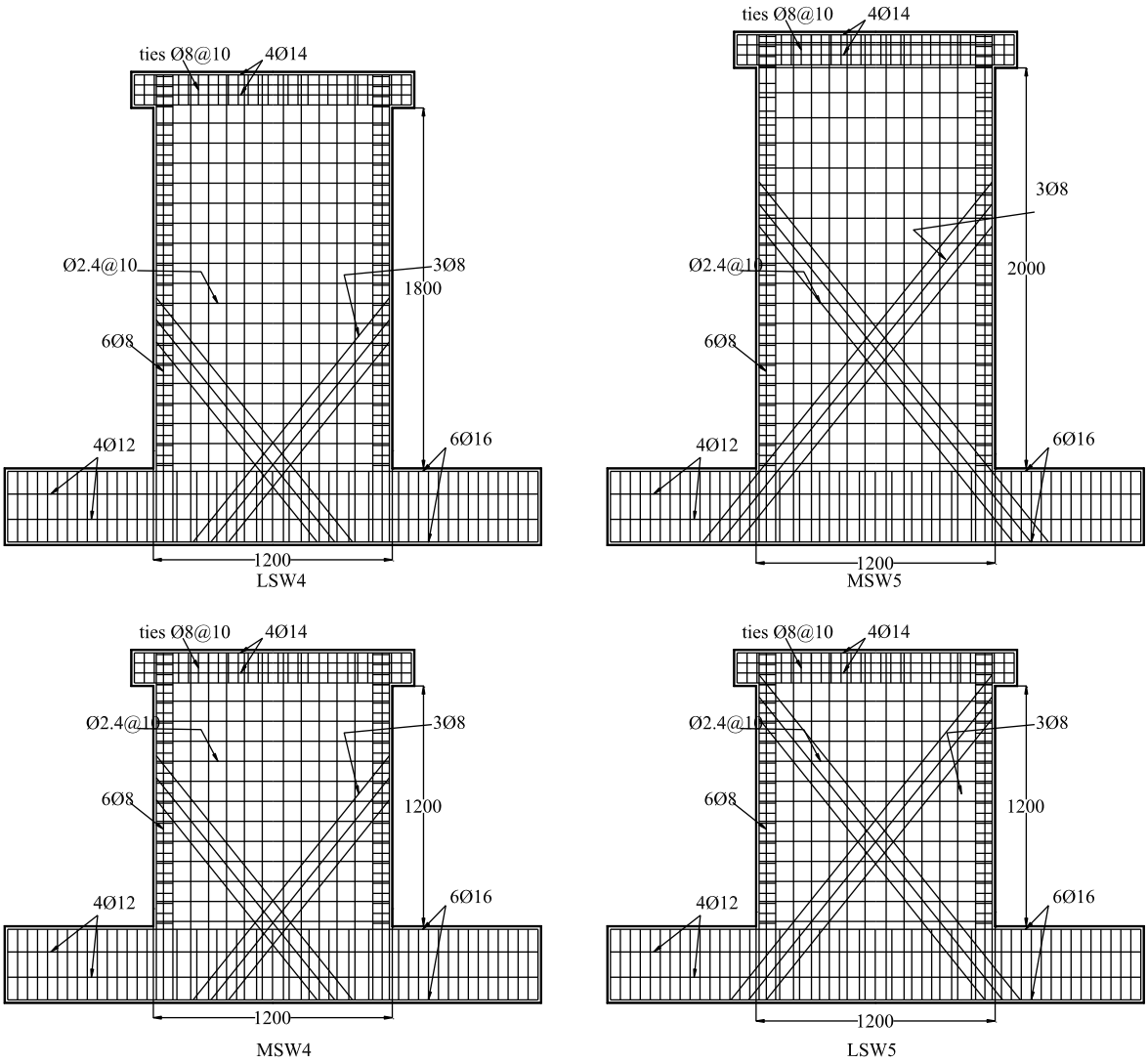

Figure 2.8 Diagonal reinforcements in wall specimens tested by Salonikios *et al.* (1999; 2000)

Although structural walls designed with diagonal reinforcement possess significant improvements in structural performance and offer more resistance to sliding shear, the use of this form of reinforcement encounters practical difficulties related to preparation and placing of diagonal bars during construction. The use of steel plates was therefore proposed for use within the following wall forms; steel plate walls, composite steel plate walls and composite concrete walls. These systems are discussed briefly in the next section.

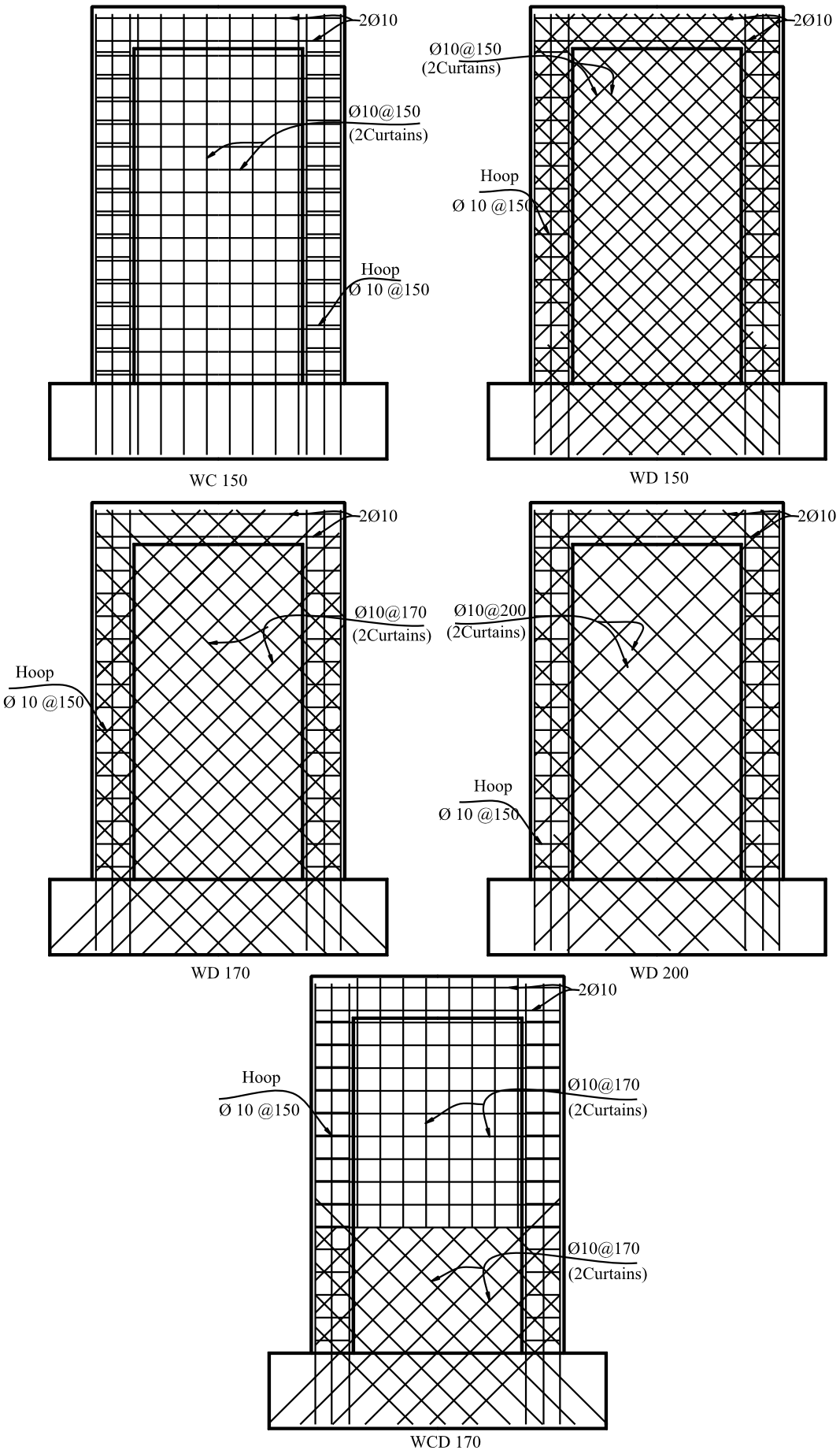

Figure 2.9 Details of specimens tested by Shaingchin *et al.* (2007)

2.2.3 Steel plate structural walls

Steel plate structural walls are currently used in high-rise buildings in several countries including the USA and Japan to resist lateral loading either from earthquakes or wind. Generally, the system is suitable for steel buildings, in which the steel plate is welded to the columns and floor beams forming vertical plate girder-like structures. Altogether, the boundary columns act as the flanges and the steel plate acts as a web, while the horizontal floor beams act as transverse stiffeners for the steel plate. The advantages and shortfalls of this system were discussed in detail in Chapter 1. Steel plate structural walls were the subject of much research over the last five decades and their behaviour is well understood (Seilie and Hooper 2005). This section focuses on the experimental studies conducted on steel plate walls to gain a better understanding of their behaviour under lateral loading. A selection of the experimental investigations available in the literature is discussed briefly.

The first design approach was to prevent plate buckling either by using thick plates or stiffened thin plates, Figure 2.10. Plate buckling, by formation of diagonal tension fields under shear loading, was first documented by Wagner (1931), who observed the formation of a series of inclined waves or buckles in unstiffened thin aluminium aircraft panels tested under shear. The buckles acted as stabilisers to the thin panel and provided substantial post-buckling strength. Wagner (1931) developed the "pure" tension field theory, in which the diagonal tension field developed in thin plate was the primary mechanism for shear resistance. Kuhn *et al.* (1952) developed the "incomplete" diagonal tension theory, which assumed that plate under shear was in a state of stress intermediate between true shear and pure diagonal tension. The two theories were implemented to estimate the ultimate capacity of steel plate girders (Basler 1961).

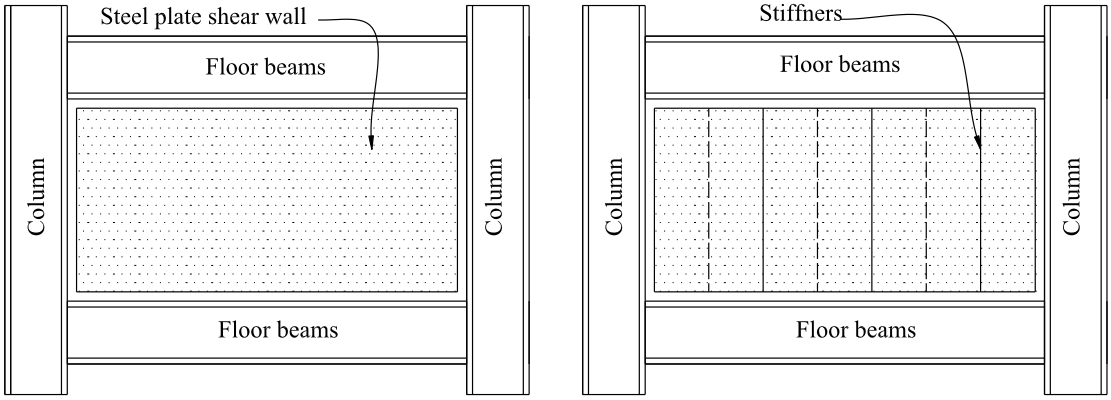

(a) Unstiffened steel plate wall system (b) Stiffened steel plate wall system

Figure 2.10 Steel plate structural walls (Astaneh-Asl 2001)

Probably the first comprehensive experimental research programme to investigate the behaviour of steel plate walls under alternating lateral loads was conducted by Takahashi *et al.* (1973). The experimental work comprised twelve 2100 mm × 900 mm steel plate panels, with different plate thicknesses and stiffener sizes and arrangement. The test results showed the adequate ductility and superior buckling stability obtained by stiffening, which obviously in turn increased the overall cost. Mimura and Akiyama (1977) proposed a numerical model to predict the hysteretic load deflection behaviour of these walls. The numerical results compared well with the experimental results and showed the effectiveness of the model in predicting the hysteretic load deflection behaviour of steel plate walls.

In 1983, Thorburn *et al.* (1983) developed a mathematical model termed the strip model to characterise the tension field behaviour. The model simulated the tensile zone of the unstiffened plate as a series of inclined truss members, inclined at the same orientation as the diagonal tension fields, Figure 2.11. The model was used to study the distribution of stresses developed in the plate and a good agreement was found with experimental results.

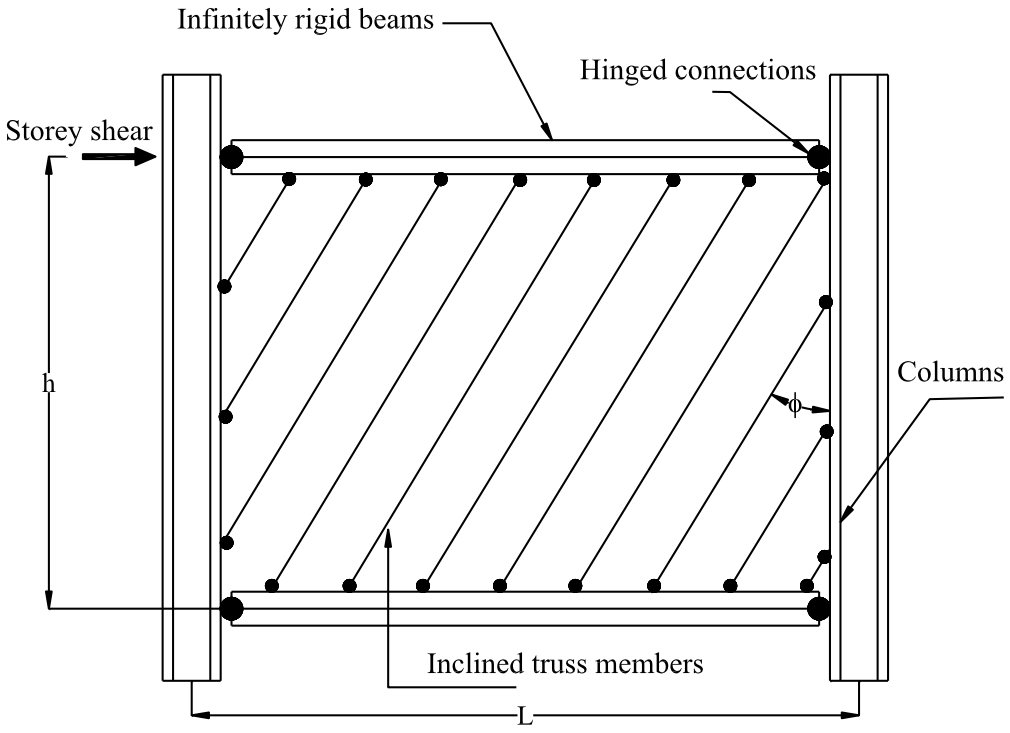

Figure 2.11 Strip model (Thorburn *et al.* 1983)

Timler and Kulak (1983) conducted an experimental study to validate the strip model. The experimental programme comprised a full-scale, two single-storey, one-bay steel plate wall tested under strain-control cyclic loading, see Figure 2.12. The experimental results showed that the strip model could be used successfully to represent the behaviour of steel plate structural walls under lateral loading.

Tromposch and Kulak (1987) tested a steel plate wall that was similar to that tested by Timler and Kulak (1983) to further validate the strip model and to assess the hysteretic behaviour of steel plate walls. The wall demonstrated a ductile behaviour that was attributed to the buckling of infill plate and flexibility of the boundary frame. It was also concluded that the strip model yielded conservative estimates of the initial stiffness and ultimate strength of steel plate walls.

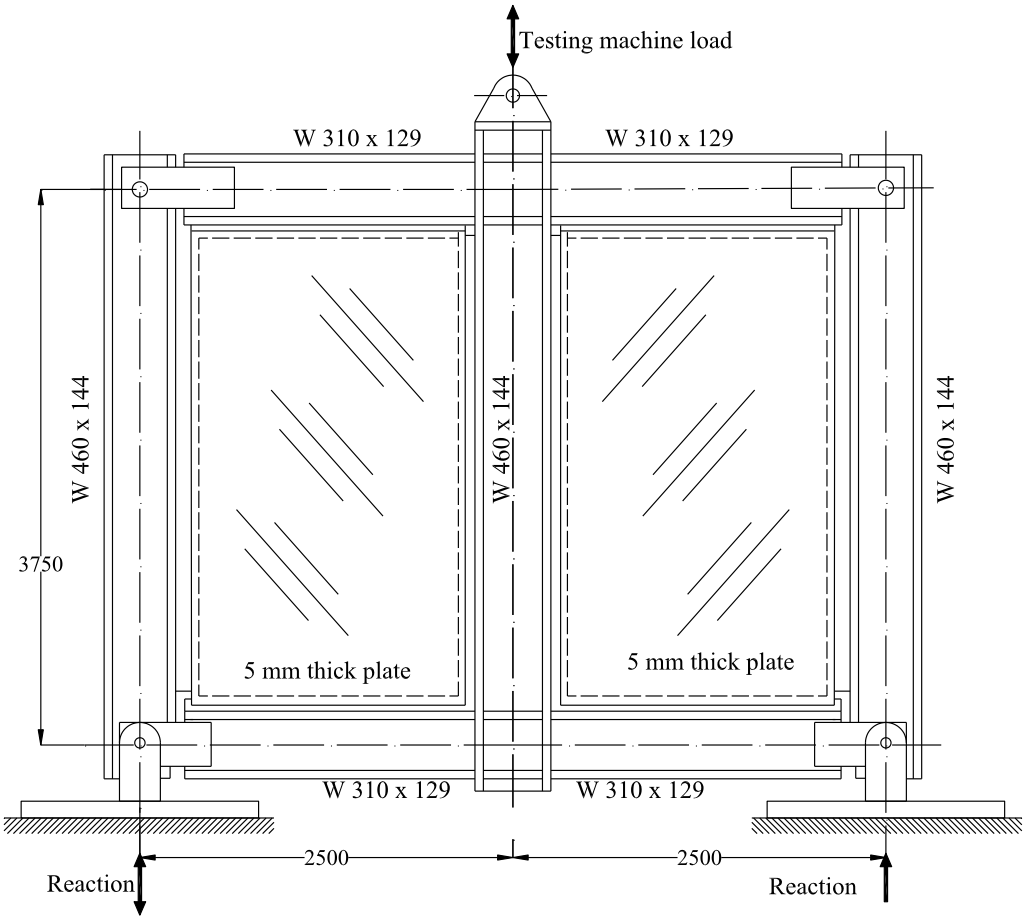

Figure 2.12 Specimen tested by Timler and Kulak (1983)

Caccese *et al.* (1993) conducted cyclic tests on six, one-quarter scale test specimens. Specimens were designed with varying plate thickness and beam-to-column connections, Figure 2.13. The specimens were tested in a strain-control mode in the test rig shown in Figure 2.14. The test results highlighted the importance of using stiffeners in controlling plate buckling. Specimens incorporating stiffened plates had higher stiffness, ultimate strength and better energy dissipation when compared to unstiffened specimens. Moreover, significant differences in failure modes were associated with plate thickness; while specimens with thinner plates showed an inelastic behaviour that was controlled by yielding of the thin plate, specimens with thicker plates exhibited an inelastic behaviour that was primarily governed by the columns, and the capacity of the specimens was controlled by column instability.

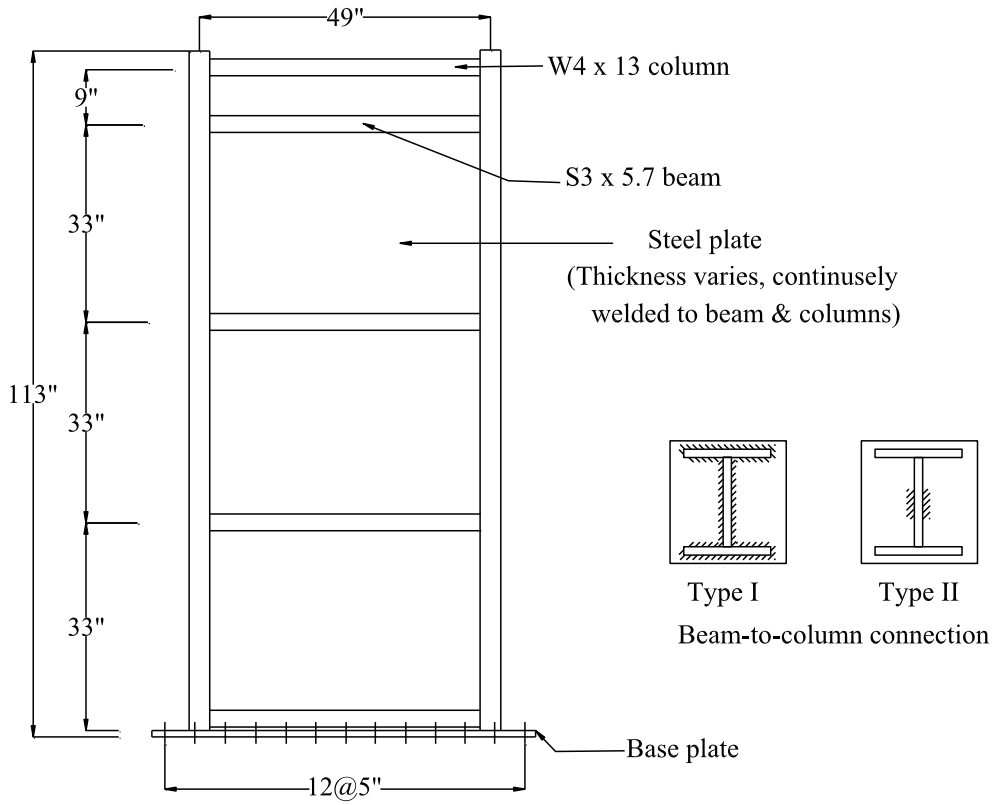

Figure 2.13 Details of specimens tested by Caccese *et al.* (1993)

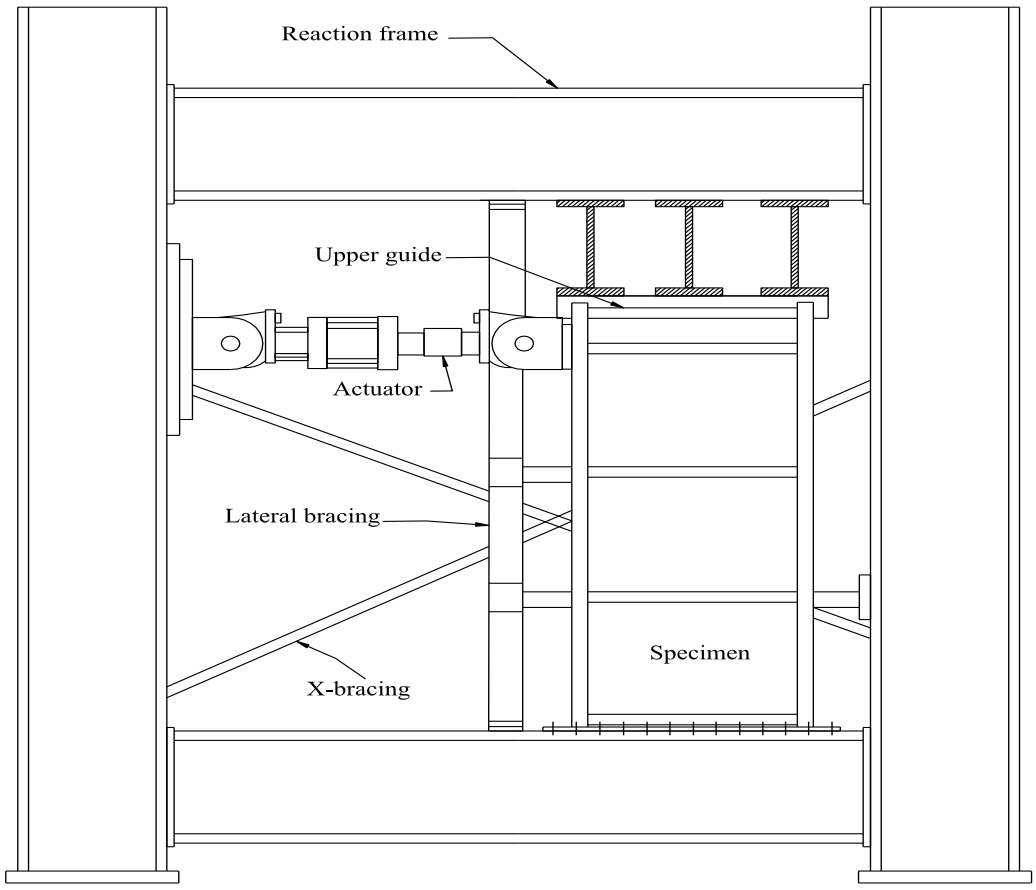

Figure 2.14 Test setup (Caccese *et al.* 1993)

Further tests were carried out by Driver *et al.* (1998) on a large-scale, four-story, single-bay steel plate wall with unstiffened panels, Figure 2.15. The main objective of the research was to investigate the behaviour under severe earthquake excitation. The wall showed adequate ductility with stable post-ultimate behaviour and demonstrated the superior performance of a properly designed and detailed steel plate wall system.

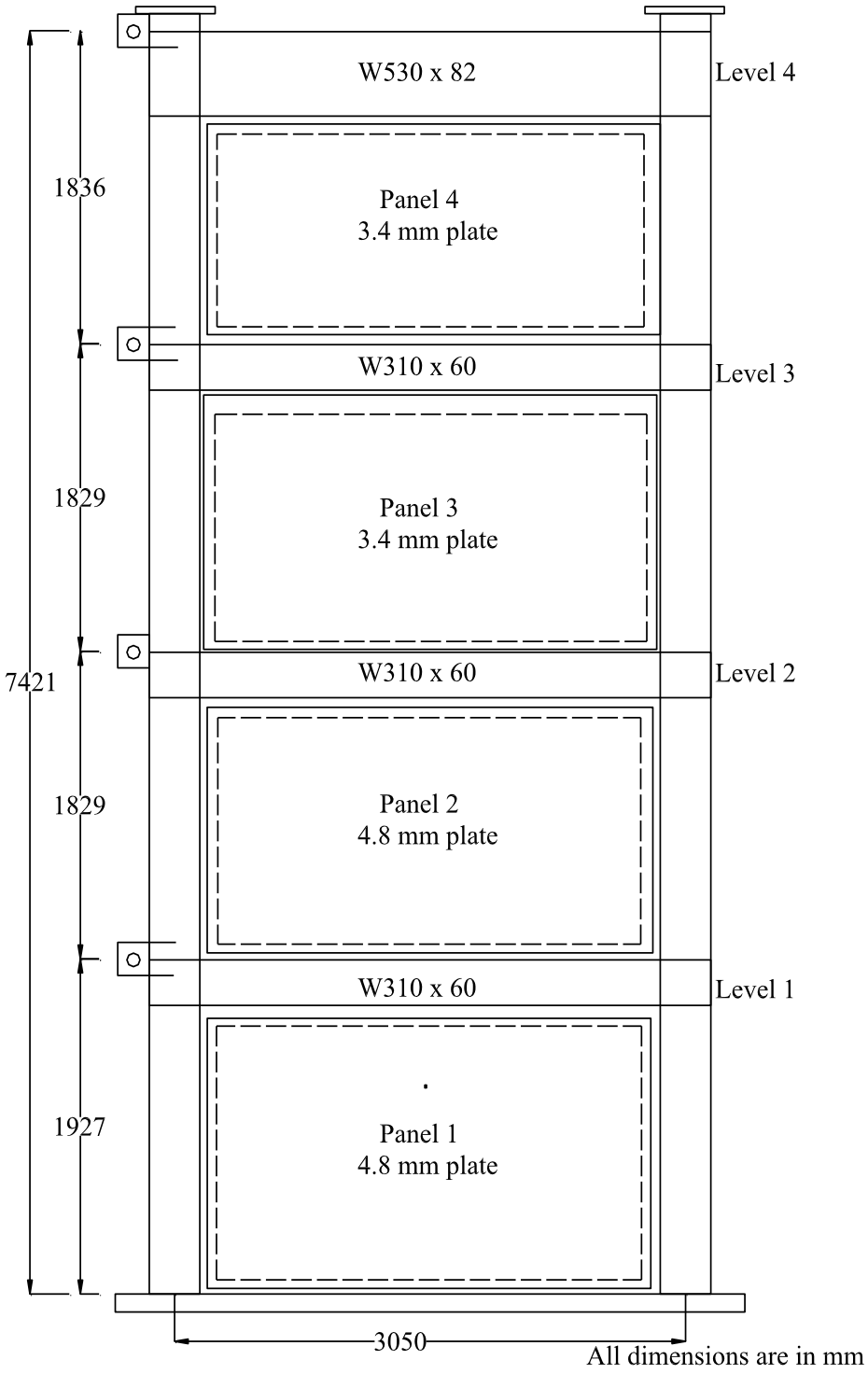

Figure 2.15 Details of steel plate wall specimen tested by Driver *et al.*(1998)

2.2.4 Composite steel plate walls

In order to reduce the effects of buckling in steel plate walls, Zhao and Astaneh-Asl (2002) proposed two composite wall systems. The composite systems consisted mainly of a steel plate panel, boundary columns, horizontal beams and a precast reinforced concrete wall. In both wall systems, the system was fabricated by welding the steel plate to the end columns and beams, and a precast reinforced concrete wall was fastened to the steel plate wall by means of bolts to create the composite action. In the first system, the precast wall was in direct contact with the steel columns, while in the second a gap was left in between, Figure 2.16. Like steel plate walls, the proposed systems are also suitable for steel buildings. The first system was used to ensure the lateral stability of 18-storey hospital building in San Francisco in 1977, see Figure 2.17.

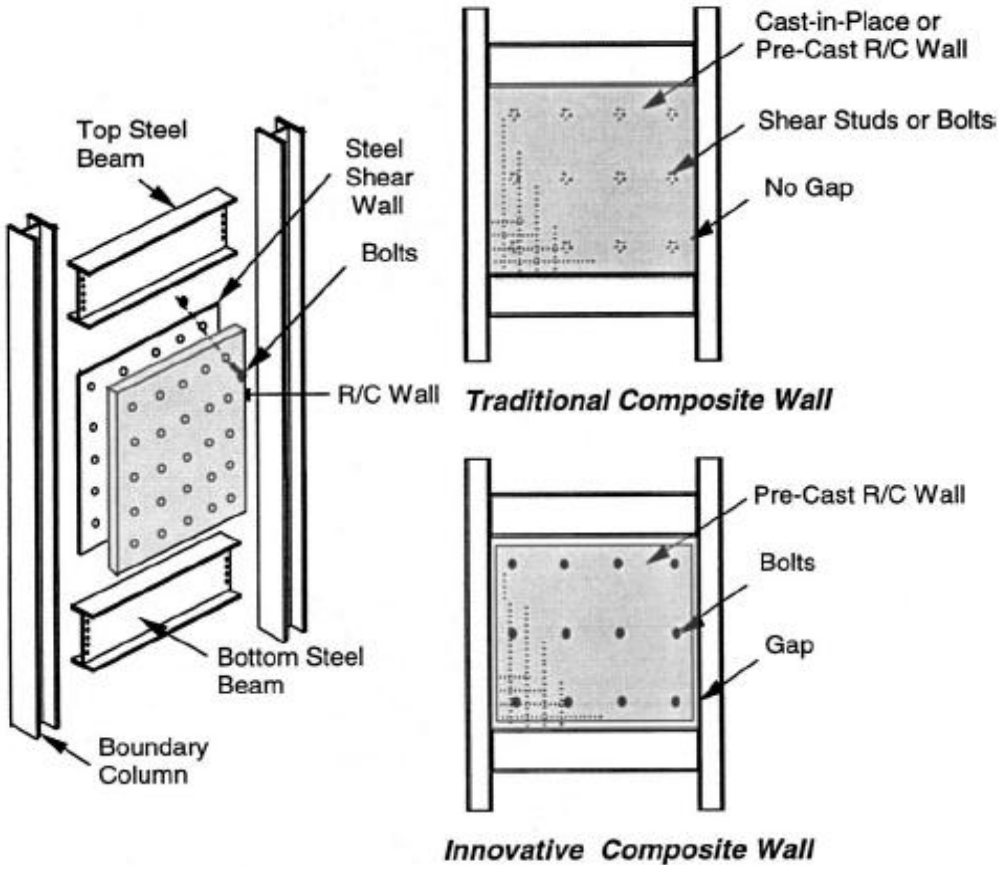

Figure 2.16: Components of composite structural walls studied by Zhao and Astaneh-Asl (2002)

Cyclic tests were carried out on two specimens designed with and without a gap between the steel plate and the steel columns (Zhao and Astaneh-Asl 2004). The experimental results revealed that both systems showed a favourable ductile response and stable cyclic post-yielding behaviour. The anchorage system between the precast concrete wall and the steel plate was able to develop composite action which supported the plate and prevented its buckling up to relatively high drift. At high lateral loads, the concrete wall was severely damaged and inelastic local buckling of the steel plate observed in the areas between the bolts with the composite action almost lost. The benefits of the gap were clear in a more ductile behaviour and less damage in the precast concrete wall. Although this system showed high energy dissipation, it was quite complicated and expensive.

(Photos: Courtesy of Degenkolb Engineers, San Francisco)

Figure 2.17 General view of the hospital and a concrete wall

2.2.5 Composite concrete walls

Three forms of composite concrete walls were considered, namely steel-concrete-steel composite walls, double skin-profiled composite walls and perforated steel plate composite walls. This section discusses briefly the main features of the systems.

A. Steel-concrete-steel composite walls

This composite system could be considered as an efficient and powerful system to replace the traditional reinforced concrete structural walls (Tsuda *et al.* 2001). Generally, steel-concrete-steel composite walls are formed by connecting two steel plates, presenting outer skins, by using shear studs and filling the space between the plates by concrete, Figure 2.18. The composite system found applications in sea-walls, underwater tunnels, blast walls, air-craft hangars, wave-energy generating systems and bridges (Subedi and Coyle 2002). Full bond between the plates and concrete core must be ensured at all stages of loading to get the best benefits of the system through providing either full-length studs, crossbars or overlapping studs at certain spacing. Crossbars and overlapping studs were proposed due to the difficulties associated with the fabrication of full-length studs.

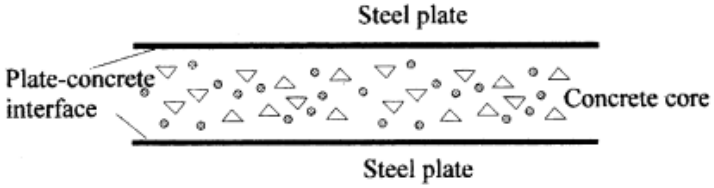

(a) Steel-concrete-steel double-skin element: general form

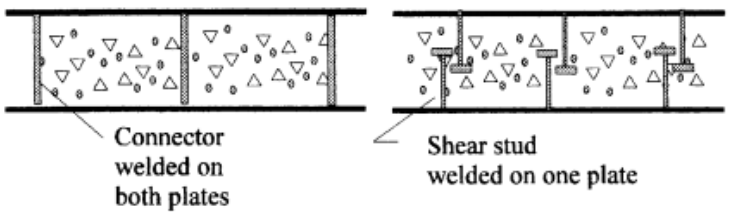

(b) S-C-S composite beam: Cross bar connectors and overlapping shear studs

Figure 2.18 Steel-concrete-steel double skin construction (Subedi and Coyle 2002)

Tsuda *et al.* (2001) tested four steel-concrete-steel structural walls as bearing elements in nuclear power plants, see Figure 2.19. Test results showed that the main failure cause was the slippage of the wall from the concrete base which was accompanied with shear yielding of the steel plates in the web and flanges. The ultimate capacity of the walls was estimated based on this failure mode. The application of this system in construction requires a special joint system between the composite wall and the base to prevent wall slippage, Figure 2.20.

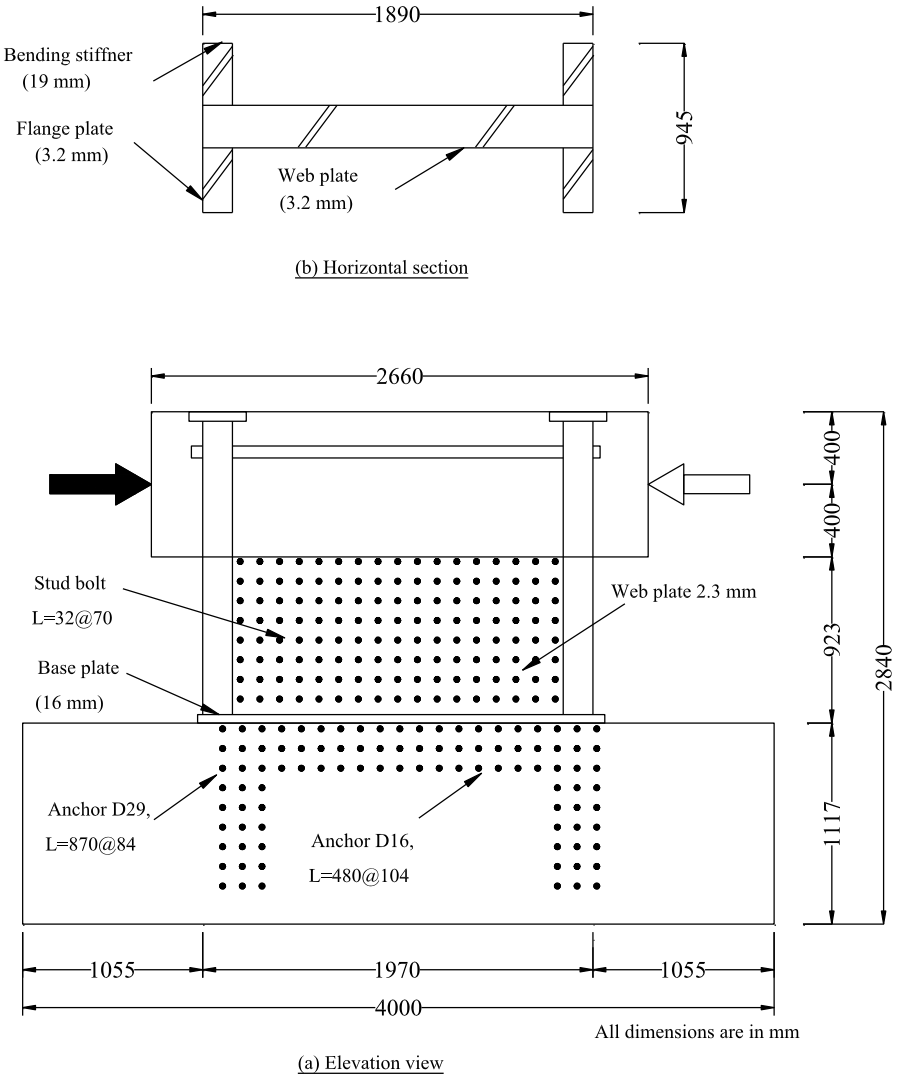

Figure 2.19 Steel-concrete-steel structural walls tested by Tsuda *et al.* (2001)

The test specimens showed high energy dissipation, ductility and high blast resistance. However, wall slippage at the base was the most critical problem for this system and

material costs were higher than in conventional reinforced concrete alternatives. This system usually relies upon speed of construction to provide it with a cost advantage over alternative systems.

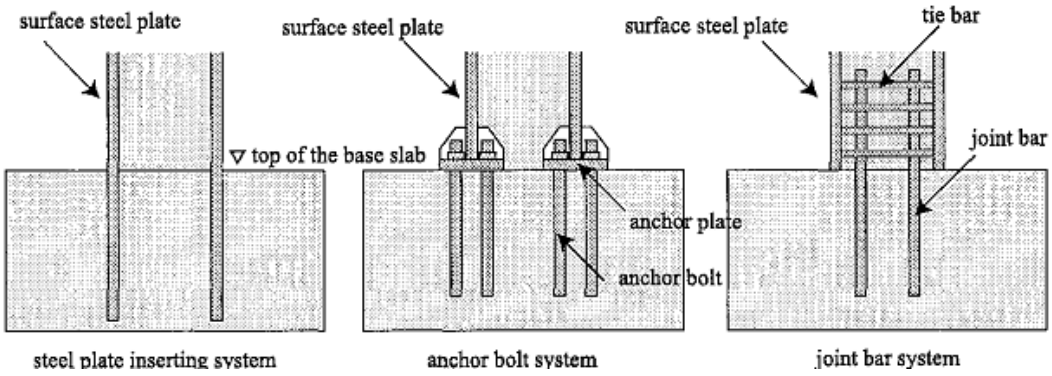

Figure 2.20 Joint system types used in steel-concrete-steel composite walls (Tsuda *et al.* 2001)

B. Double skin-profiled composite structural walls

To reduce costs and construction time, the shear studs, used in the steel-concrete-steel composite walls, were removed and skin plates were profiled forming what is known as double skin-profiled composite system. This composite walling system consists of two profiled steel sheeting and an infill of concrete as shown in Figure 2.21 (Wright *et al.* 1992; Gallocher 1993; Wright *et al.* 1994; Hossain and Wright 2004a). The composite system has a number of benefits when used in junction with composite flooring and may be used as shear or core walls in steel framed buildings. During the construction stage, the profiled steel sheeting is considered as a formwork for the infill concrete and provides a bracing system against wind, while in the service stage it may act as main reinforcement (Hossain and Wright 1995; Hossain and Wright 2004b).

In-plane shear tests were carried out on small-scale models of one-sixth scale to study the individual behaviour of profiled steel sheeting, concrete core and composite walls (Figure 2.22). The results showed that higher stiffness and strength were attained by composite walls compared to the sum of the individual contributions from the sheeting and concrete core. However, serious concerns about system behaviour under axial

loading arose. The concerns originated from load transfer between the profiled sheeting and concrete core, buckling of steel sheeting and loss of chemical bond between concrete and sheeting leading to a brittle failure.

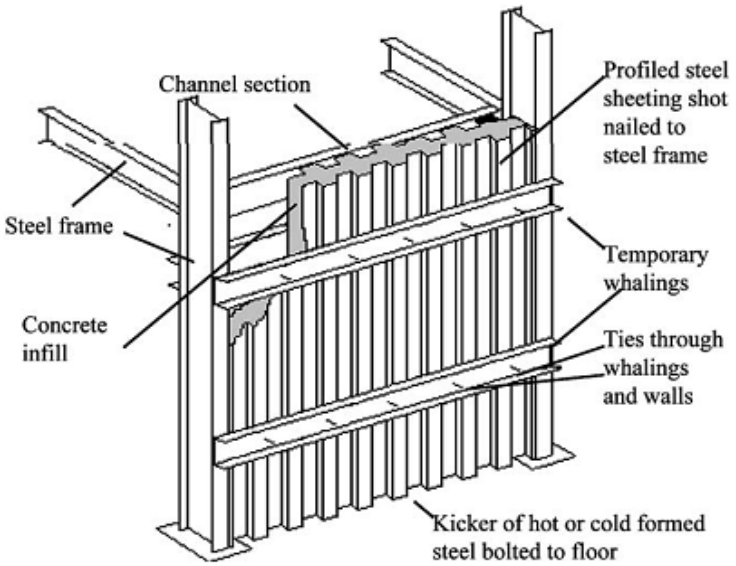

Figure 2.21 Schematic diagram of a composite walling system, (Hossain and Wright 2004a)

It was concluded that the induced strains in a composite walling system were a function of the initial debonding of the sheet–concrete interface, crack propagation and buckling of the sheeting (Hossain and Wright 2004b). Composite specimens failed mainly due to loss of chemical bond leading to debonding

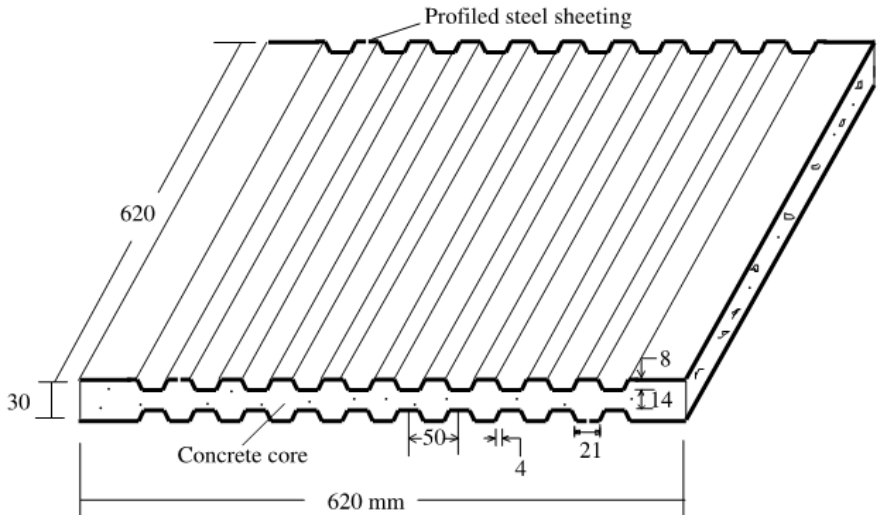

Figure 2.22 Detail of composite wall, profiled steel sheeting and concrete core tested by Hossain and Wright (2004b)

C. Perforated steel plate composite concrete walls

In the past, perforated plates were used as stirrups in columns, main reinforcement in beams and reinforcement mesh in slabs (Khaloo 2002; Khaloo and Shokoufi 2002). Khaloo and Shokoufi (2002) suggested a new system of wall reinforcement in which perforated steel plates were used as the wall's main reinforcement. The behaviour of three structural walls that were reinforced with steel perforated plates instead of conventional steel rebars were investigated under cyclic loading. The dimensions of the specimens and the plate profile are given in Figure 2.23. In order to prevent plate buckling, a special detail comprising additional plates, steel screws and pipes was implemented. Experimental results revealed considerable improvements in ductility, flexural strength and energy absorption capacity for walls designed with this form of reinforcement. The main disadvantages of this system were the buckling and subsequent separation of the perforated plates from the concrete core and the cost of plate fabrication. To the best knowledge of the author, this wall design did not find any applications in construction.

2.3 Current research

Since structural wall systems play a vital role in protecting buildings from lateral loading either from wind or earthquakes, considerable research was therefore carried out on various designs of structural walls to evaluate their performance, feasibility and cost effectiveness. Section 2.2 compares basic advantages and shortfalls of different systems and explains the situations under which each design is more appropriate.

Overall, composite alternatives appear to provide robust systems with desirable high strength, ductility and energy dissipation. However, concerns remain related to plate buckling at relatively low shear stresses, overall cost and feasibility. Based on the comparison between various alternative designs, a design of an encased-plate composite

structural wall system is introduced. The proposed system consists of a reinforced concrete wall with a steel plate embedded inside it, see Figure 1.1. The reinforcement bars were glued to the steel plate; a feature which provides stiffeners to the plate against buckling and improves the composite action with the concrete core. The next section provides basic information related to the development stages of encased-plate construction system.

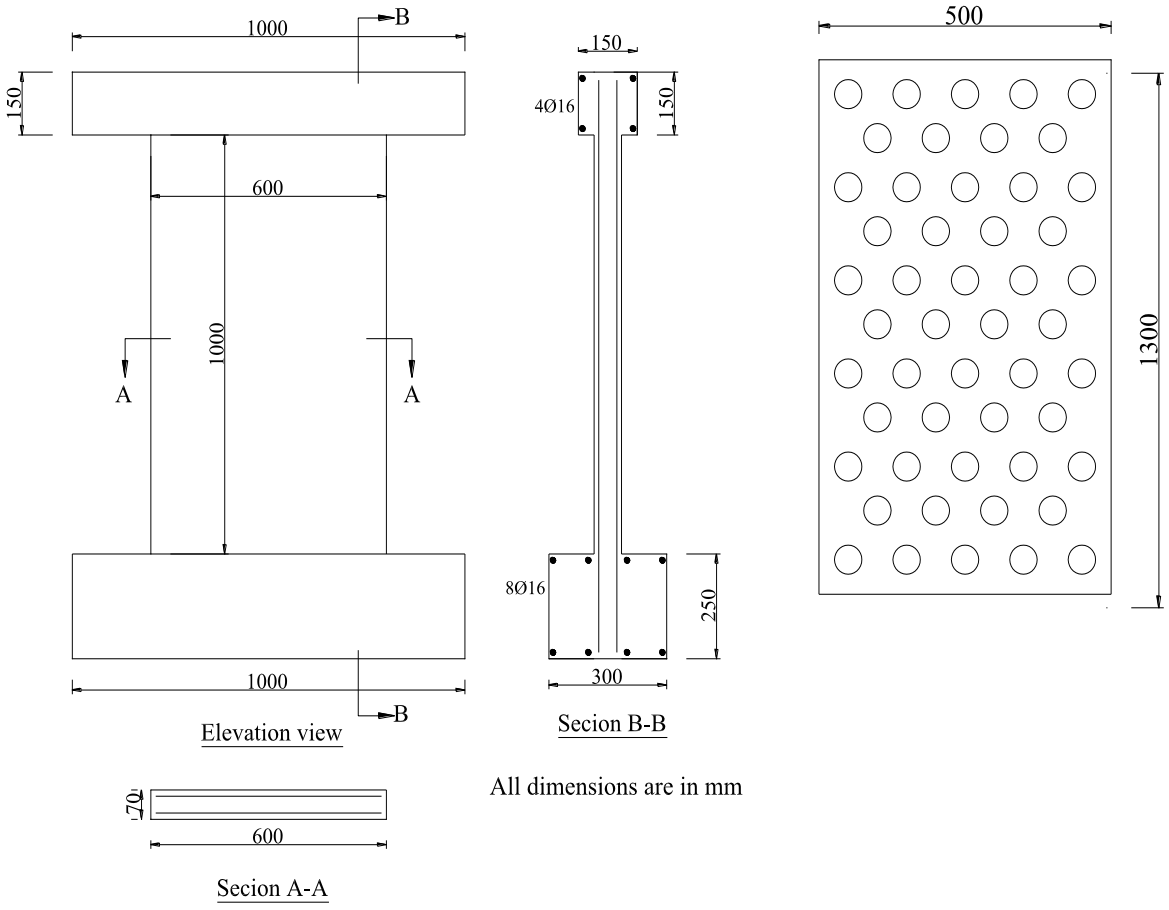

(a) wall specimens (b) profile of perforated plate

Figure 2.23 Steel perforated structural walls tested by Khaloo and Shokoufi (2002)

2.4 Encased-plate construction System

The concept of encased-plate construction was initiated about 25 years ago as an alternative for shear reinforcement whenever high shear forces were involved. Encased-plate construction found applications mainly in coupling beams and simply-supported

beams. The primary target of the technique was to produce a substitute detailing for coupling beams in coupled wall systems.

2.4.1 Background

Encased-plate construction in beams comprises vertically aligned steel plates that resist the tensile component of shear stresses and conventional reinforcing bars to resist flexural stresses. The steel plates are usually continuous over the whole beam span to provide a medium for shear transfer, Figure 2.24. Plate stability is produced by the surrounding concrete which provides lateral support for the encased-plate (Baglin 1998).

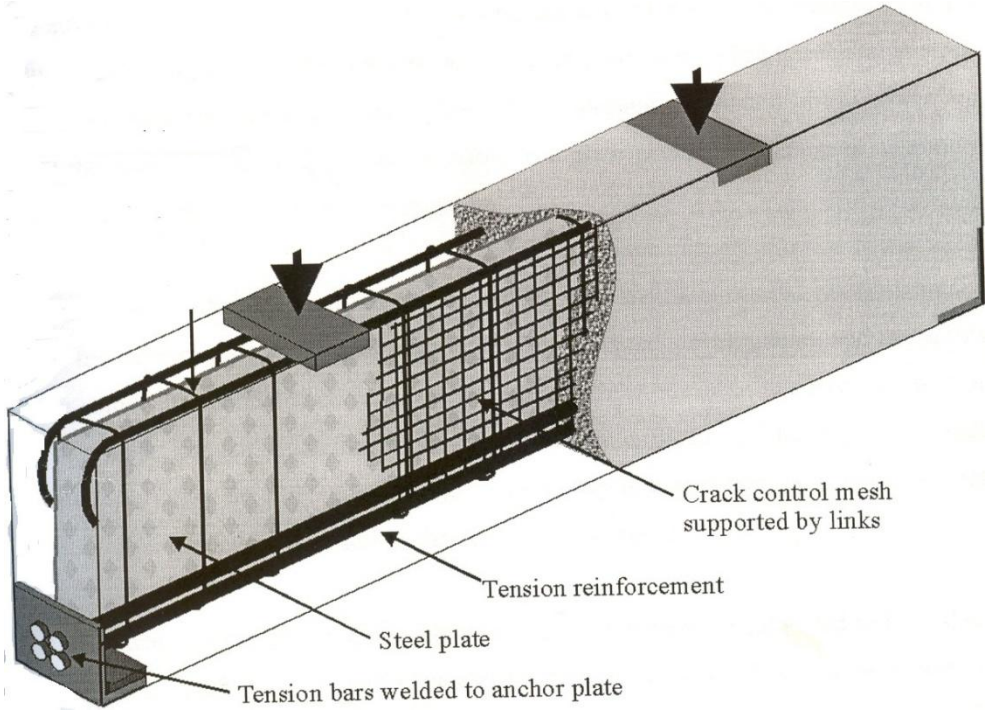

Figure 2.24: Typical encased-plate construction in beams (Baglin 1998)

Encased-plate construction provides a number of benefits from a practical point of view including reductions of cross-section size, more flexible design and cost savings. The replacement of stirrups offers simpler construction with direct saving in assembly time and cost. Higher shear strength was obtained for simply-supported encased-plate beams

with shear capacity up to 20 N/mm^2. Plate geometry assures high resistance to shear cracking in terms of crack formation and propagation (Baglin 1998).

For coupling beams, which are subjected to high shear stresses, vertical stirrups are commonly used to resist shear stresses resulting in severe congestion and difficulties in concrete placement. To solve this problem, two possible solutions are adopted; either increase the beam size or develop an alternative beam design. Diagonally reinforced coupling beams (Paulay and Binney 1974), steel coupling beams (Harries *et al.* 1993), and rectangular steel tube coupling beams with concrete infill (Teng *et al.* 1999) present alternative designs for coupling beams. Experimental results proved the better performance for these design alternatives compared to the conventional reinforcement system (Lam *et al.* 2004).

The application of encased-plate construction in coupling beams would alter the failure mechanism from brittle shear failure to a ductile flexural failure. Accordingly, the rate of energy absorption is markedly increased with reductions in stiffness degradation. Vertical alignment of steel plate in beams enables concrete to be cast and compacted easily, avoiding the honeycomb type of defects (Lam *et al.* 2002).

In practice, this technique in conjunction with conventional shear reinforcement has been employed to resist high shear stresses in the coupling beams in the construction of the National Westminster Tower as shown in Figure 2.25 (Sainsbury and Shipp 1983), and in a private residential building in Hong Kong (Figure 2.26) (Lam *et al.* 2005). The previous studies related to the development of encased-plate construction in simply-supported and coupled beams are discussed briefly in the next section.

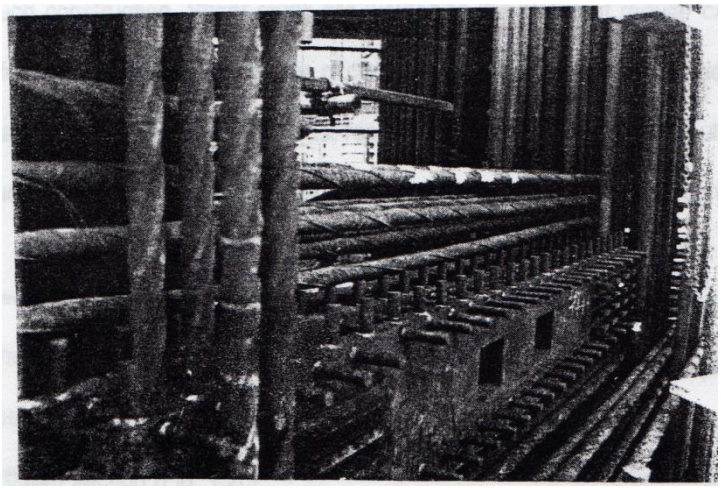

Figure 2.25: Coupling beam reinforcement including steel plates (Sainsbury and Shipp 1983)

Figure 2.26: On-site photo of reinforcement cage (Lam *et al.* 2005)

2.4.2 Encased-plate coupling beams

The first documented study of encased-plate construction was initiated in 1984 at the University of Dundee to investigate the behaviour of encased-plate coupling beams. The study involved a comprehensive programme to investigate the effectiveness of shallow depth and full depth encased-plates on the behaviour of beams, Figure 2.27. The test results demonstrated that plate reinforcement was a feasible proposal for use in construction (Subedi 1989). Moreover, experimental results proved the similarity in behaviour between encased-plate beams and conventionally-reinforced concrete coupling beams.

Different techniques were offered to improve the bond between the steel plate and the surrounding concrete either by using shear studs (Lam *et al.* 2001, 2002, 2003, 2004, 2005) or plate surface roughening (Baglin 1998).

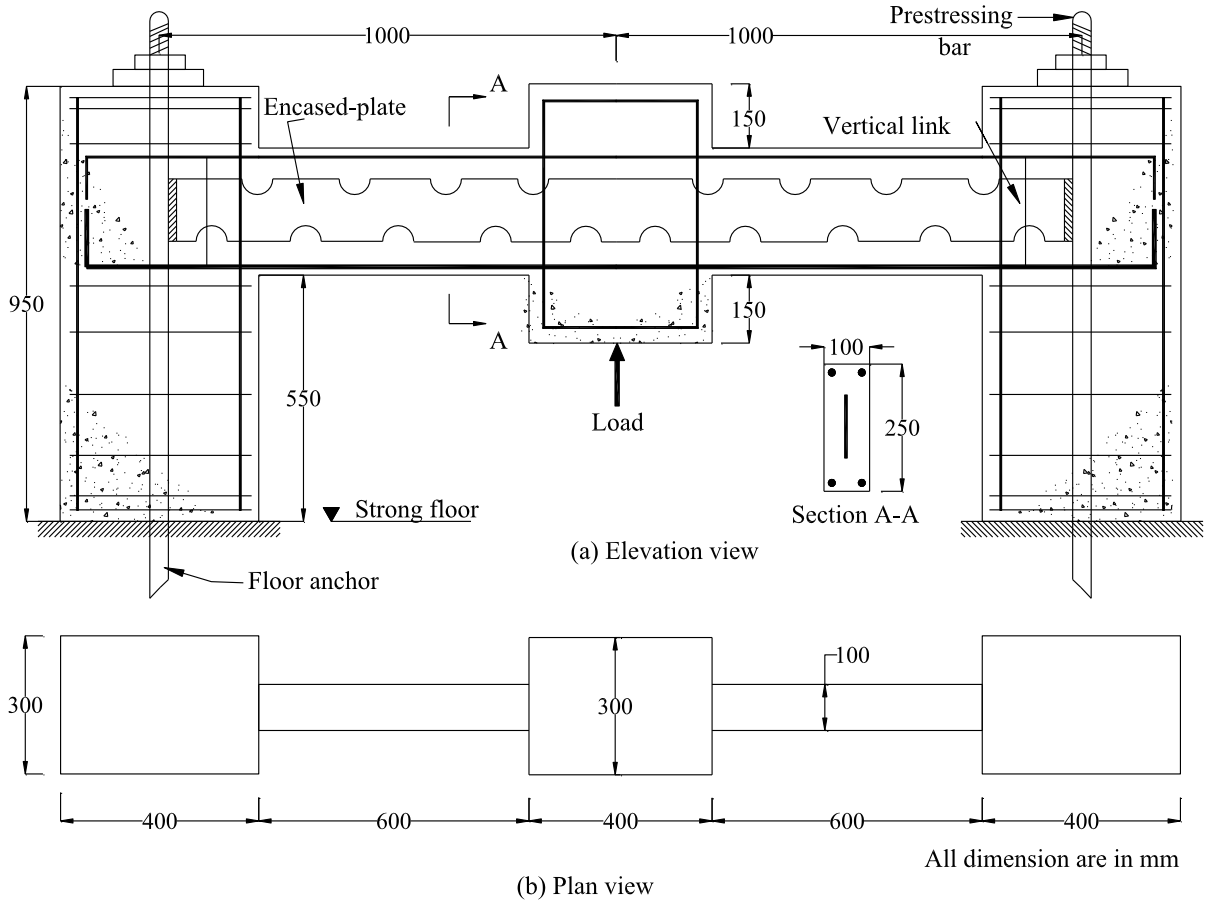

Figure 2.27: Details of coupled beams tested by Subedi (1989)

Eighteen encased-plate coupling beams with shear studs to improve the composite action between the steel plate and the concrete were tested by Lam *et al.* (2001, 2002, 2003, 2004, 2005), Figure 2.28. The results showed that encased-plates were effective in both resisting high shear stresses and restraining inelastic deformations. It was also found that encased-plates could enhance the strength and the stiffness of coupling beams, while shear studs were necessary to improve the composite action between the steel plate and the surrounding concrete. It was hoped that this technique could be

widely employed by the construction industry to get better performance in terms of strength and ductility (Lam *et al.* 2005).

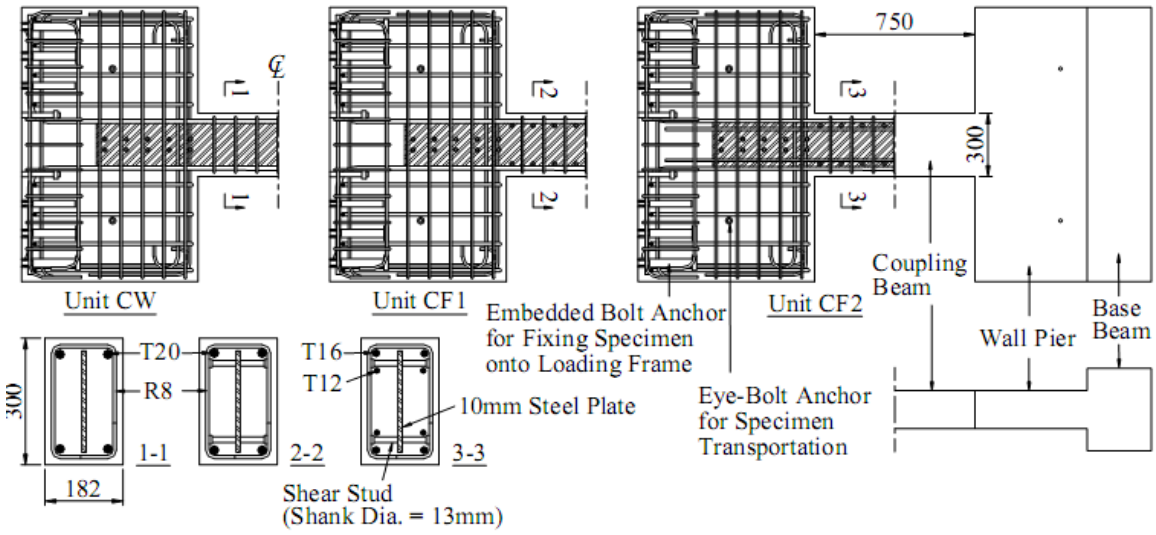

Figure 2.28 Encased-plate composite coupling beam specimens tested by Lam *et al.* (2001, 2002, 2003, 2004, 2005)

2.4.3 Encased-plate simply-supported beams

Simply-supported concrete beams reinforced with full depth plates were firstly tested by Choo (1990). A number of encased-plate simply-supported beams were tested, in which the encased plates were provided with surface roughness or cut-outs to increase plate anchorage. The test result showed that the proposed anchorage technique was not sufficient to develop the full strength of the beams.

Afterwards, a comprehensive series of tests were carried out by Abdullah (1993) on plate reinforced simply-supported beams. In some of the tested beams, the surface of the plates was sand blasted and provided with semi circular cut-outs to act as shear connectors to prevent horizontal slip possibly caused by insufficient bond between the plate and the concrete. Single-plated beams performed well, while double-plated beams suffered premature failure with signs of plate instability. The premature failure was attributed to the insufficient concrete cover to prevent plate buckling. All beams

suffered from shrinkage cracking of the concrete cover due to plate restraint during early curing.

Baglin (1998) extended the work of Abdullah (1993) through a more extensive experimental programme for encased-plate construction involving 20 encased-plate simply-supported beams, Figure 2.29. The beams were designed to cover a wide range of parameters in addition to two types of plate anchorage. The study suggested that the encased-plate construction enabled reduced cross-section sizes for shear dominated simple beams, leading to greater flexability in design.

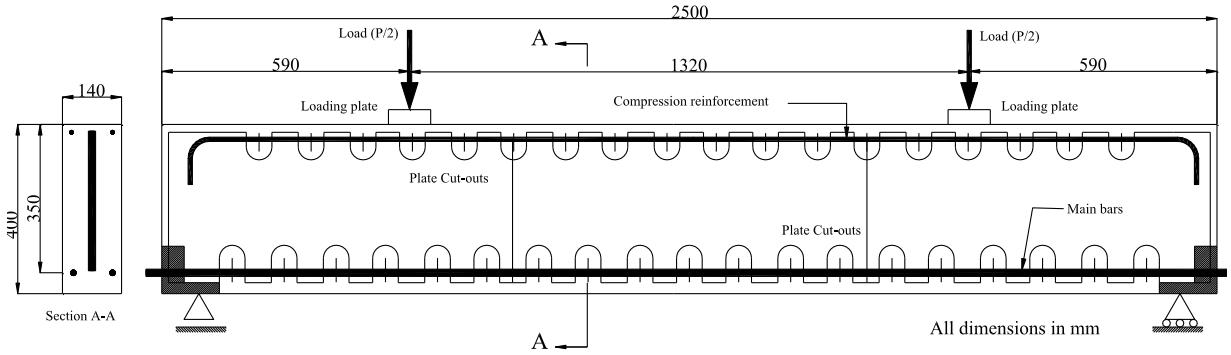

Figure 2.29 Encased-plate simply-supported beams tested by Baglin (1998)

2.5 Summary

The behaviour of conventionally-reinforced concrete structural walls was reviewed briefly. Because of the inadequacy of these walls in earthquake load design, various alternative designs were proposed in the past. Some were accepted in the construction industry namely; diagonally reinforced concrete walls, steel plate walls, steel plate composite walls and steel-concrete-steel composite walls, while others were not implemented in applications including double skin-profiled composite walls and perforated steel plate composite concrete walls. All designs were shown to improve the performance of structural walls but suffered from various limitations. Overall, composite alternatives appeared to provide robust systems with high strength, extended

ductility and adequate energy dissipation. However, concerns remained related to plate buckling at relatively low shear stresses and overall high cost. Based on the comparison between various alternatives, a design of an encased-plate composite structural wall system was introduced. The proposed system consisted of a reinforced concrete wall with a steel plate embedded inside it. Encased-plate construction found wide application in simply-supported beams and structural wall coupling beams as a shear reinforcement alternative. Encased-plate composite systems in beams attain adequate performance in terms of stiffness, ductility, load carrying capacity and energy dissipation compared to conventionally-reinforced beams. Considering the advantages achieved with encased-plate construction in beams, the system is now proposed for use in walls and a further understanding of the behaviour in this particular application is therefore required.

Chapter 3 Behaviour of encased-plate composite walls under pure in-plane shear

3.1 Overview

The understanding of encased-plate composite walls behaviour under lateral loading can be achieved by considering the pure in-plane shear behaviour which represent the typical behaviour of walls' central panel and the behaviour under combined shear and bending stresses. In the current chapter, the behaviour of encased-plate composite walls under pure in-plane shear was studied in an experimental study involving a number of small-scale wall units. The dimensions, reinforcement layout, materials, instrumentation, testing environment and test results and discussion are described in detail in this chapter. A full-field deformation measurement system based on particle image velocimetry (PIV) and close-range photogrammetry was adopted to determine the distribution of deformation and strain over the whole specimen's surface area at all test stages.

The composite unit is formed by embedding a steel plate in a conventional reinforced concrete wall. In this investigation, the behaviour of the individual components was first investigated before discussing the behaviour of composite walls. The study concentrated on the effect of plate thickness, concrete strength, reinforcement content and wall thickness on the behaviour of composite walls subjected to pure in-plane shear.

3.2 Small-scale model

Structural walls commonly consist of a central panel confined by cross walls or columns called boundary elements, Figure 3.1a. It is widely believed that axial and bending stresses are resisted by the boundary elements while shear stresses are primarily resisted by the central panel (Gupta and Rangan 1998). Accordingly, the central panel may be assumed to be subjected to pure in-plane shear stresses. The behaviour of the central panel under these conditions is the main interest of the current chapter.

The full-scale prototype wall selected in this study has square dimensions of 3050 × 3050 mm and bounded with two columns, Figure 3.1a. The selected model represents 1:10 scale model of the prototype as shown in Figure 3.1b.

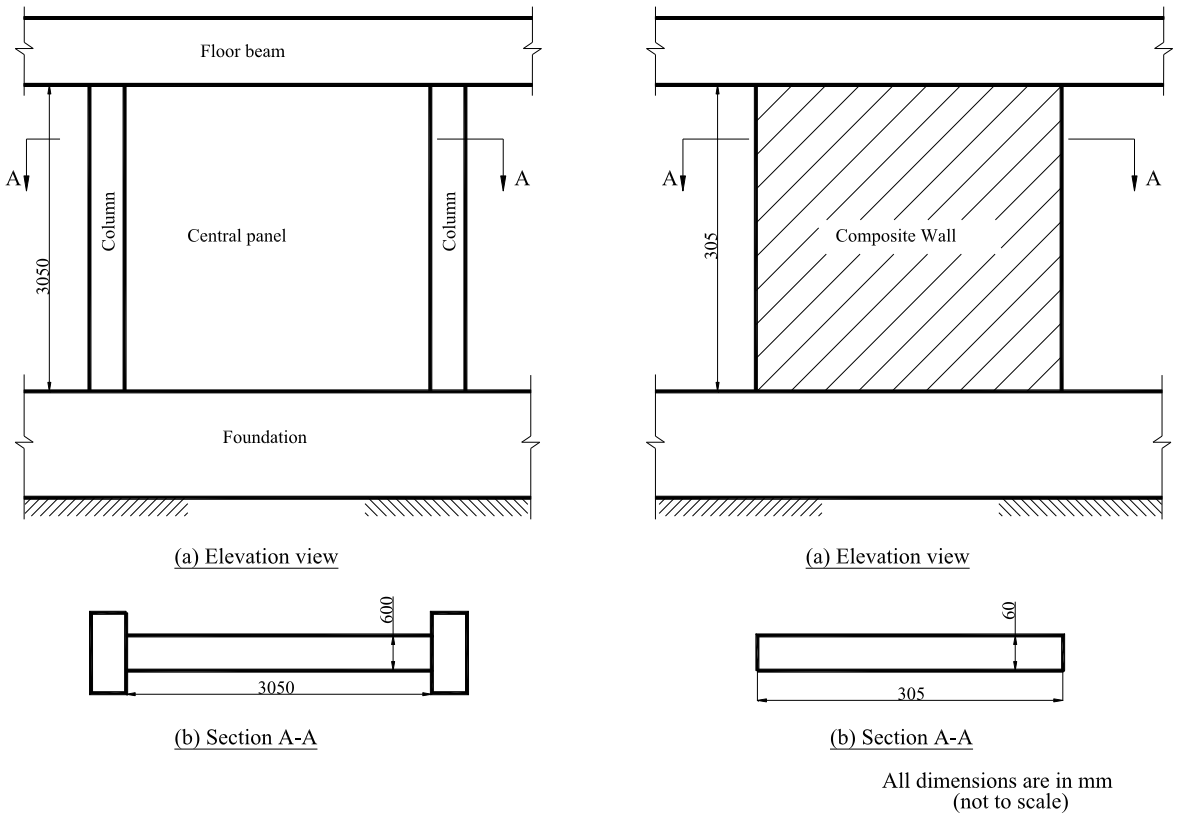

(a) Full-scale prototype wall (b) Small-scale model wall

Figure 3.1 Dimensions of prototype and model walls

3.3 Test setup

3.3.1 Introduction

Testing of reinforced concrete under pure in-plane shear is a challenge due to technical difficulties associated with biaxial testing of large panels (Hsu 1993). Review of shear tests in the literature showed that different techniques were implemented to test concrete panels under in-plane shear. In 1981, Vecchio and Collins proposed a shear rig facility which enabled the application of in-plane shear stresses to square and rectangular concrete panels.

The steel frame, rigid links and 37 double-acting hydraulic jacks are the main components of the rig as shown Figure 3.2. The shear stresses were applied by compressing and tensioning the test unit with equal magnitude in the vertical and horizontal directions, respectively. The assembly was too expensive to be used in the current research.

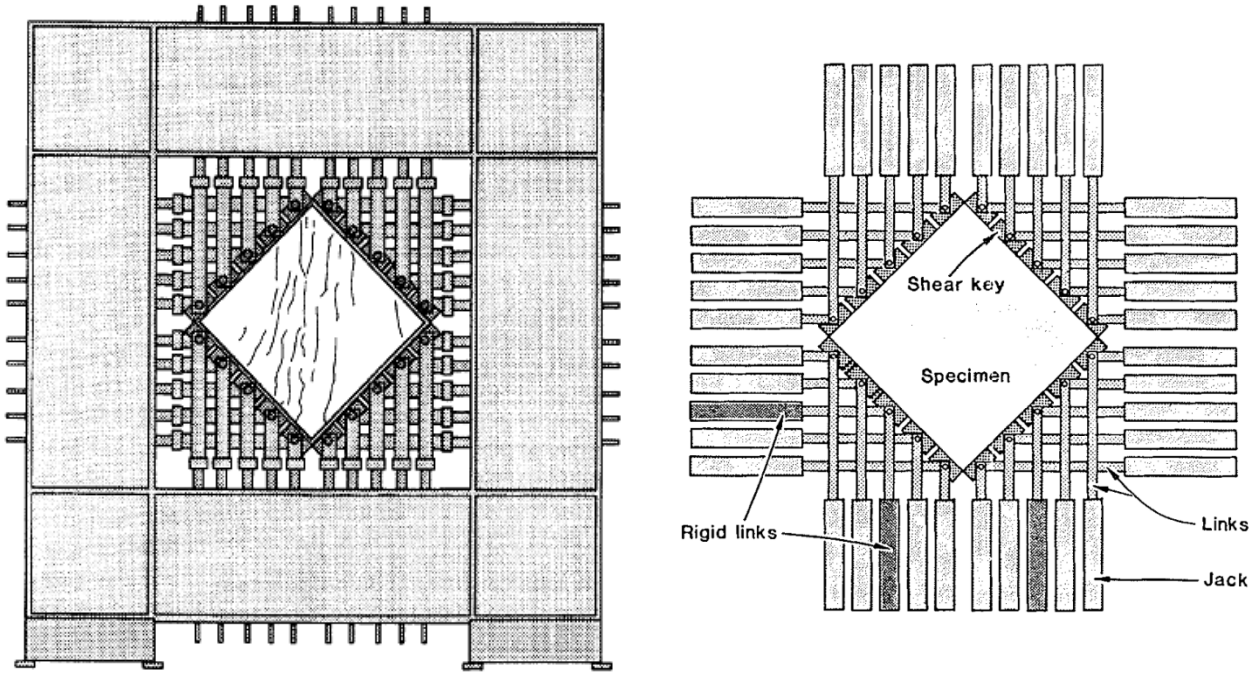

(a) General view of shear rig (b) Jacks and links assembly

Figure 3.2 Test rig proposed by Vecchio and Collins (1981)

Sabouri-Ghomi (1989) proposed a simpler technique to investigate the in-plane shear behaviour of unstiffened steel plate walls under monotonic and cyclic loads, Figure 3.3, and the same technique was used to study the in-plane shear behaviour of profiled composite walling (Hossain and Wright 2004a; 2004b), Figure 3.4. Following the success of this rig in earlier studies, it was used in the current research.

Figure 3.3 Shear rig proposed by Sabouri-Ghomi (1989)

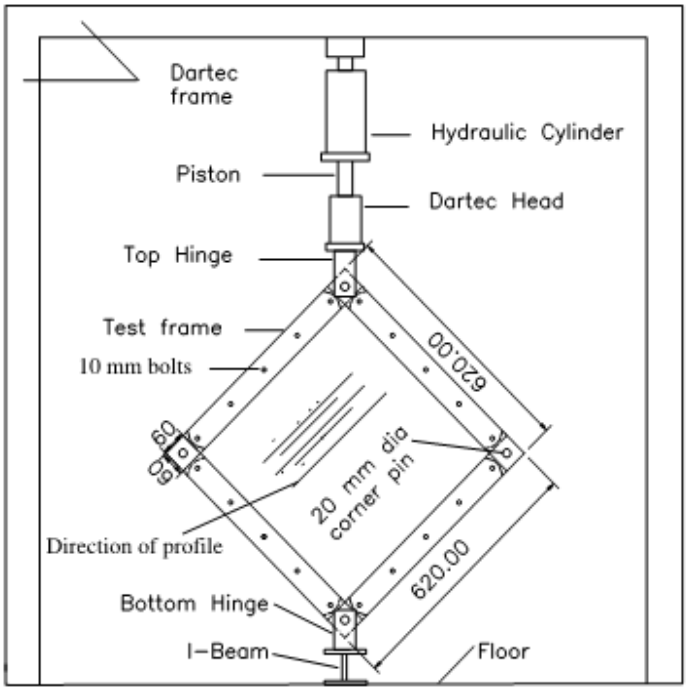

Figure 3.4 Details of shear rig used by Hossain and Wright (2004a; 2004b)

3.3.2 Test idealisation

The proposed test rig is capable of applying vertical tensile or compressive force across a diagonal of a test unit. In order to simplify calculations, the following assumptions were made:

- Frame members provided rigid boundary conditions to the test unit, but did not contribute to its load carrying capacity;
- Frame members exhibited the same rotation at the hinges at all stages of loading;
- Out of plane movement of the system was negligible;
- Although the shear stress was applied to the test unit through the connecting bolts, the assumption of uniform shear stress along the edges of the test unit can be accepted; and

- Slip at the connecting bolts was insignificant and had no effect on the applied shear stresses.

Figure 3.5 presents the undeformed and deformed shapes for a square unit. The isolated element, ABCD, shown in Figure 3.5a, reinforced with a rebar grid and encased-plate becomes under two equal shear forces, F_1, which make up the applied vertical force, F. The shear forces, F_1, produce a shear stress in the test unit according to the following formula:

$$\tau = F_1 / (h\ t_w) \qquad (3.1)$$

where

τ is the applied shear stresses,

h and t_w are the length and thickness of the test unit, respectively

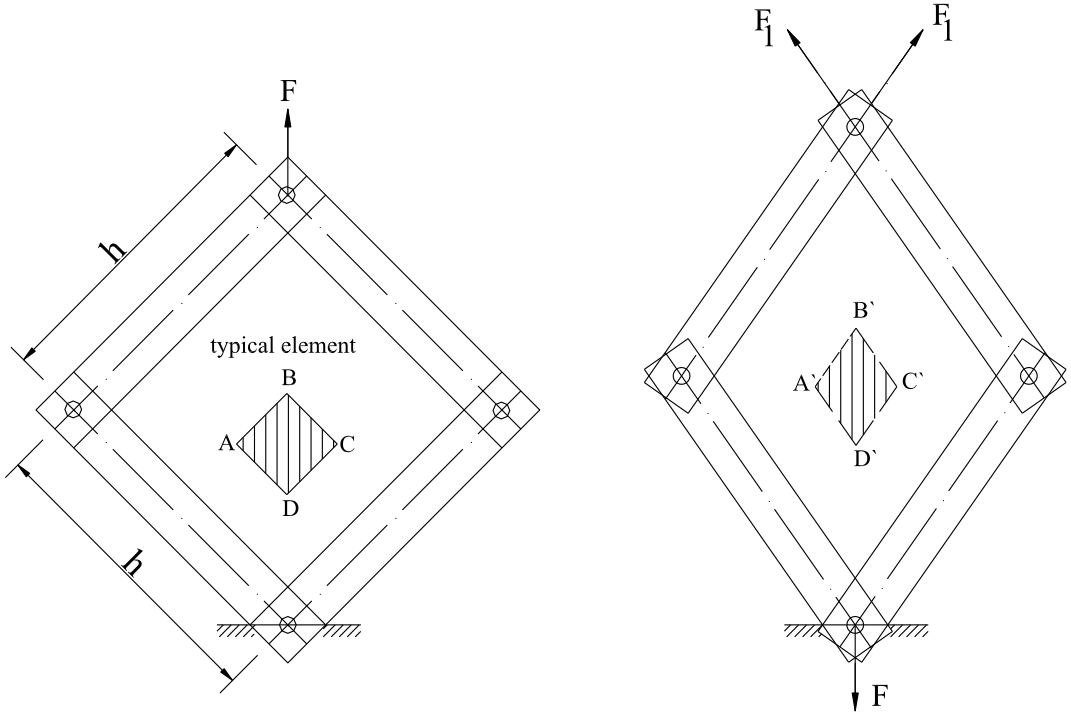

(a) Undeformed shape (b) Deformed shape

Figure 3.5 Loading mechanism

The element ABCD in Figure 3.6a is in equilibrium under a shear stress system, τ ,which distorts the element into the shape A`B`C`D` as shown in Figure 3.6b. By rotating both the

undeformed and deformed elements such that edges CD and C`D` coincide with the horizontal axis, the shear strain, γ, resulting from shear stress, τ, can be calculated as (Megson 1996) :

$$\gamma = \emptyset \text{ (radians)} = B`B/BC \qquad (3.2)$$

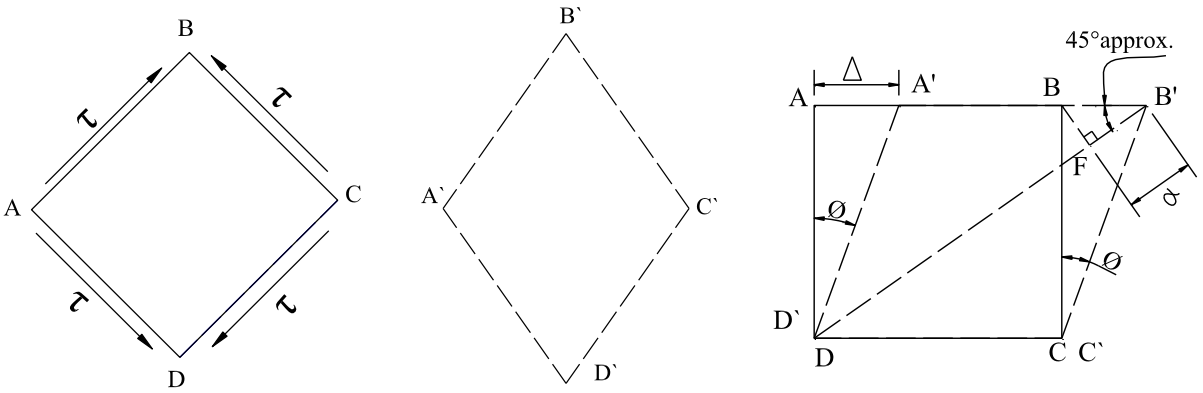

(a) (b) (c)

Figure 3.6 element deformations after load application

Since angle $\emptyset$ has a small value, the increase in length of the diagonal DB to DB` is approximately equal to FB` where BF is perpendicular to DB`, see Figure 3.6c. Thus the shear deformation can be calculated according to the following formula:

$$\Delta = \alpha / \cos 45° \qquad (3.3)$$

Where Δ is the shear deformation and α is the diagonal deformation of the test unit.

3.4 Experimental methodology

3.4.1 Design of test rig

A special rig was designed and fabricated to apply pure shear stresses to the wall units. The shear rig consisted of three parts; a test frame and top and bottom hinges. The test frame

comprised four pairs of steel frame members and four additional plates used as packing for the frame members. The test unit was clamped between pairs of frame members firmly by means of 16 bolts. The frame members were pinned at their ends with four 30 mm diameter high-strength pins, Figure 3.7. The frame members were connected to the testing machine through the top and bottom hinges as shown in Figure 3.8.

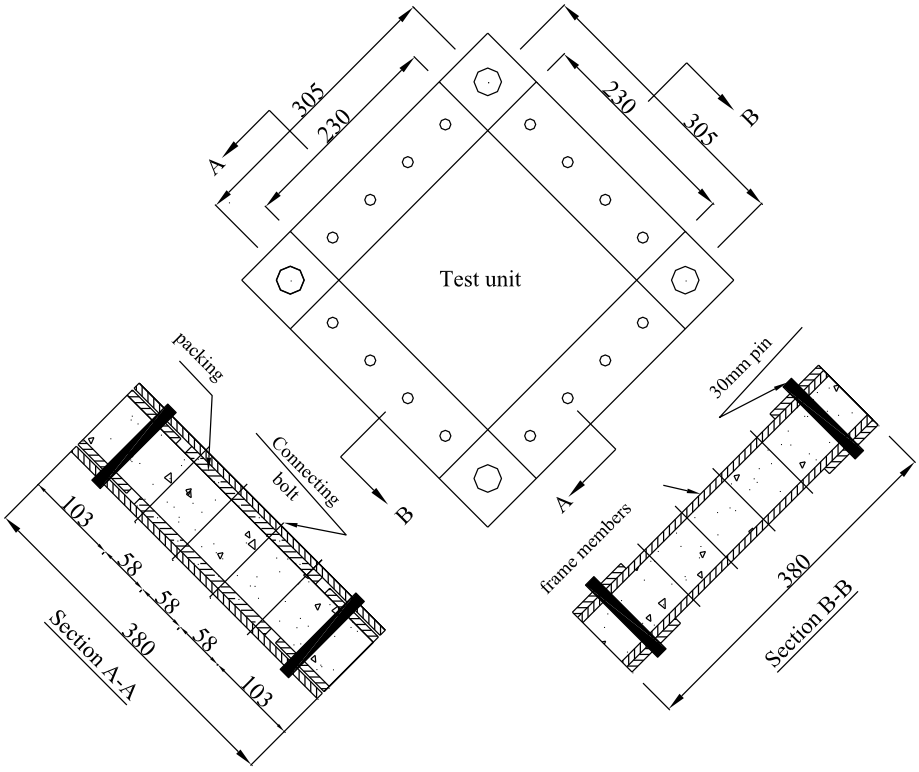

Figure 3.7 Dimensions of tests units and shear rig

The frame members were designed according to British standards (BS EN 1993-1-1:2005). Precautions were taken to ensure the elastic behaviour of frame members and that members' yield was not reached under the applied loads. The members were made from 8 mm thick and 75 mm wide high-tensile steel (grade S460). The external dimensions of the test frame were 380 mm × 380 mm, which provided internal and effective dimensions of 230 mm × 230 mm and 305 mm × 305 mm, respectively for the test units, Figure 3.7. One row of 12 mm diameter high-strength bolts (grade 8.8) was used to firmly clamp the test

unit between pairs of frame members. The bolts were designed to safely transfer the forces from the test frame to the test unit by friction with no slip. To avoid any slack, bolts were a tight fit in the holes of the frame members. The corner pins were carefully designed to transfer the forces to the frame members, while maintaining the hinging action. The ends of the packing plates were machined precisely to allow the corners to work as a pinned connection.

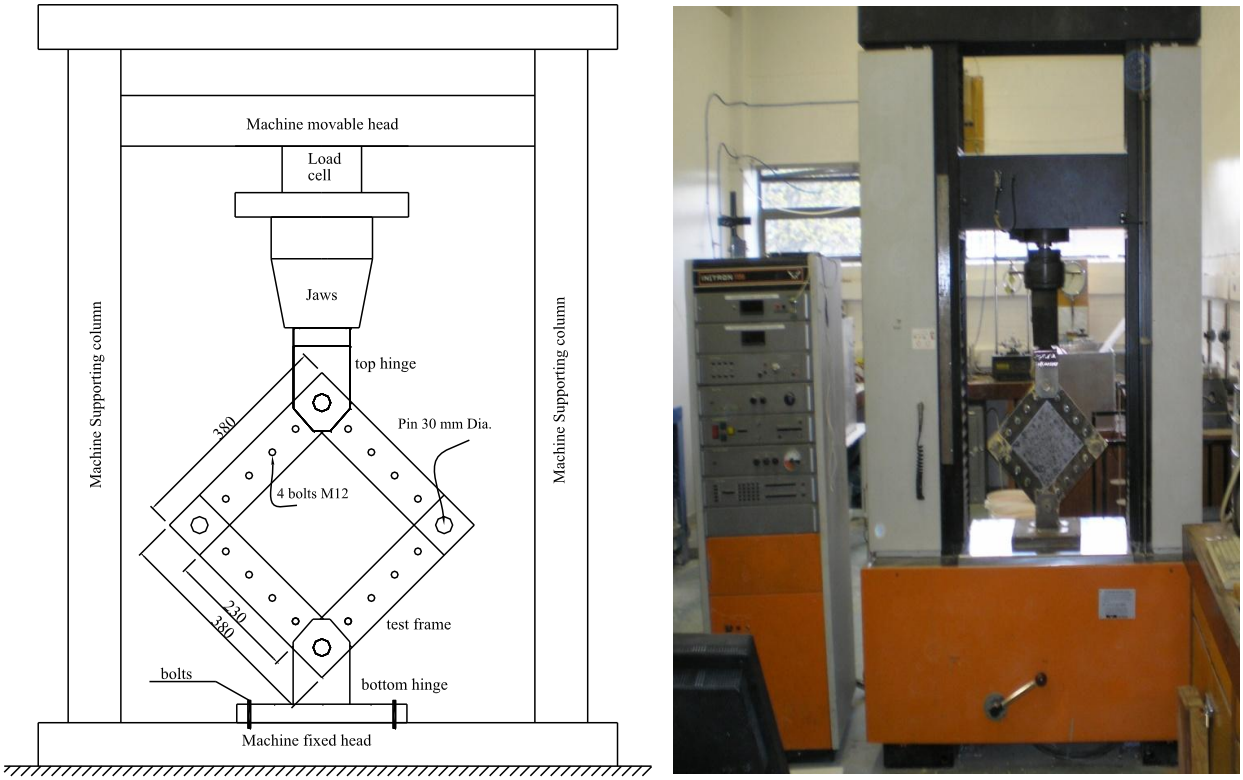

Figure 3.8 Shear rig and testing machine

An Instron 1196 loading machine was used to apply the required forces to the test units. The test frame was connected to the testing machine through top and bottom hinges as shown in Figure 3.8. Since the machine jaws were designed to sustain tension load, only tensile force was applied to the test units. The bottom hinge consisted of a clamp welded to 32 mm thick steel plate which was connected to the machine through four high-strength bolts, while the top hinge comprised a clamp welded to a vertical plate which was clamped

between the top machine jaws. Holes were drilled on both clamp sides to host the pins, see Figure 3.9.

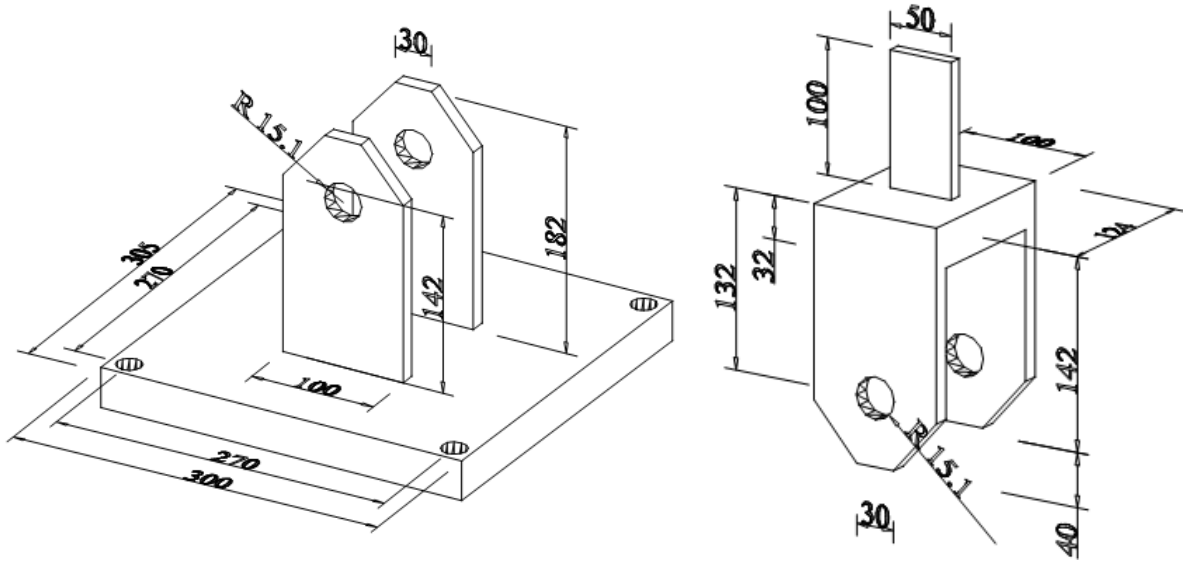

(b) Bottom hinge (a) Top hinge

Figure 3.9 Details of top and bottom hinges

Since the behaviour of the test rig is of great importance, more attention was paid to examine its performance. The test rig was connected solely to the loading machine to check that the frame members acted as a mechanism and did not contribute to the load carrying capacity, see Figure 3.10. The results showed that the frame members acted as desired and a negligible load equal to the rig weight was registered, although the value of diagonal deformation reached 85 mm.

3.4.2 Test units

Tests were carried out first on the individual components of the composite wall unit before considering the composite wall. Ten small-scale units were designed and tested, two of which, S1 and S2, were unstiffened steel plates, unit P1 was conventionally-reinforced and seven units, P2-P8, were encased-plate composite. Tests on units P2-P8 were mainly intended to cover the behaviour up to failure, taking into consideration the following

parameters: (1) plate thickness, (2) concrete strength, (3) reinforcement content and (4) wall thickness.

Figure 3.10 Assessment of test rig behaviour

The test units were designed such that their failure would take place under a diagonal load below 250 kN, the maximum capacity of the Instron machine. Due to this experimental constraint, the maximum unit thickness and plate thickness were selected to be 60 and 1.5 mm, respectively.

All the test units had a square shape with external dimensions of 380 × 380 × 60 mm and effective dimension 305 × 305 × 60 mm except unit P8 which had a smaller thickness of 40 mm. The test units were divided into four series, each designed to study the effect of one parameter as shown in Table 3.1. In the first group, three units were designed to study the effect of increasing the plate thickness from 0.0 to 1.5 mm on the shear behaviour of encased-plate composite concrete units. The second group contained two units to study the impact of increasing concrete strength from 25 to 70 N/mm^2. To evaluate the effect of increasing the reinforcement content from 0.46 to 0.62%, two units were cast and tested in the third series. Series four contained only one additional unit which had the same dimensions as the units in the other series, but with a thickness of 40 mm to study the effect

of wall thickness. Two unstiffened plates of 0.8 and 1.5 mm thick were further included in the fifth series. The details of the test units are given in Figures 3.11 and 3.12.

Table 3.1 Details of test units

Series			(1)			(2)		(3)		(4)	(5)	
Test unit			P1	P2	P3	P4	P5	P6	P7	P8	S1	S2
External dimensions	Length (mm)		380	380	380	380	380	380	380	380	380	380
	Width (mm)		380	380	380	380	380	380	380	380	380	380
	Thickness (mm)		60	60	60	60	60	60	60	40	0.8	1.5
Reinforcement	Plate	thickness (mm)	0	0.8	1.5	0.8	0.8	0.8	0.8	0.8	----	-----
		ratio (%)	0	1.33	2.5	0.8	0.8	1.33	1.33	1.33	----	-----
	Rebars in both directions	Rebars	2Ø6	2Ø6	2Ø6	2Ø6	2Ø6	3Ø6	4Ø6	2Ø6	----	-----
		Ratio (%)	0.31	0.31	0.31	0.31	0.31	0.46	0.62	0.31	----	-----
Main parameter			Plate thickness			Concrete strength		Reinforcement content		Wall thickness	Unstiffened plates	

To ease casting and manufacturing of the units, the corners of the test units were cut in a quarter round shape as shown in Figures 3.11 and 3.12. This technique was proposed to avoid concrete cracking at the corners and prevent any contact with the pins which might hinder the desired hinge action.

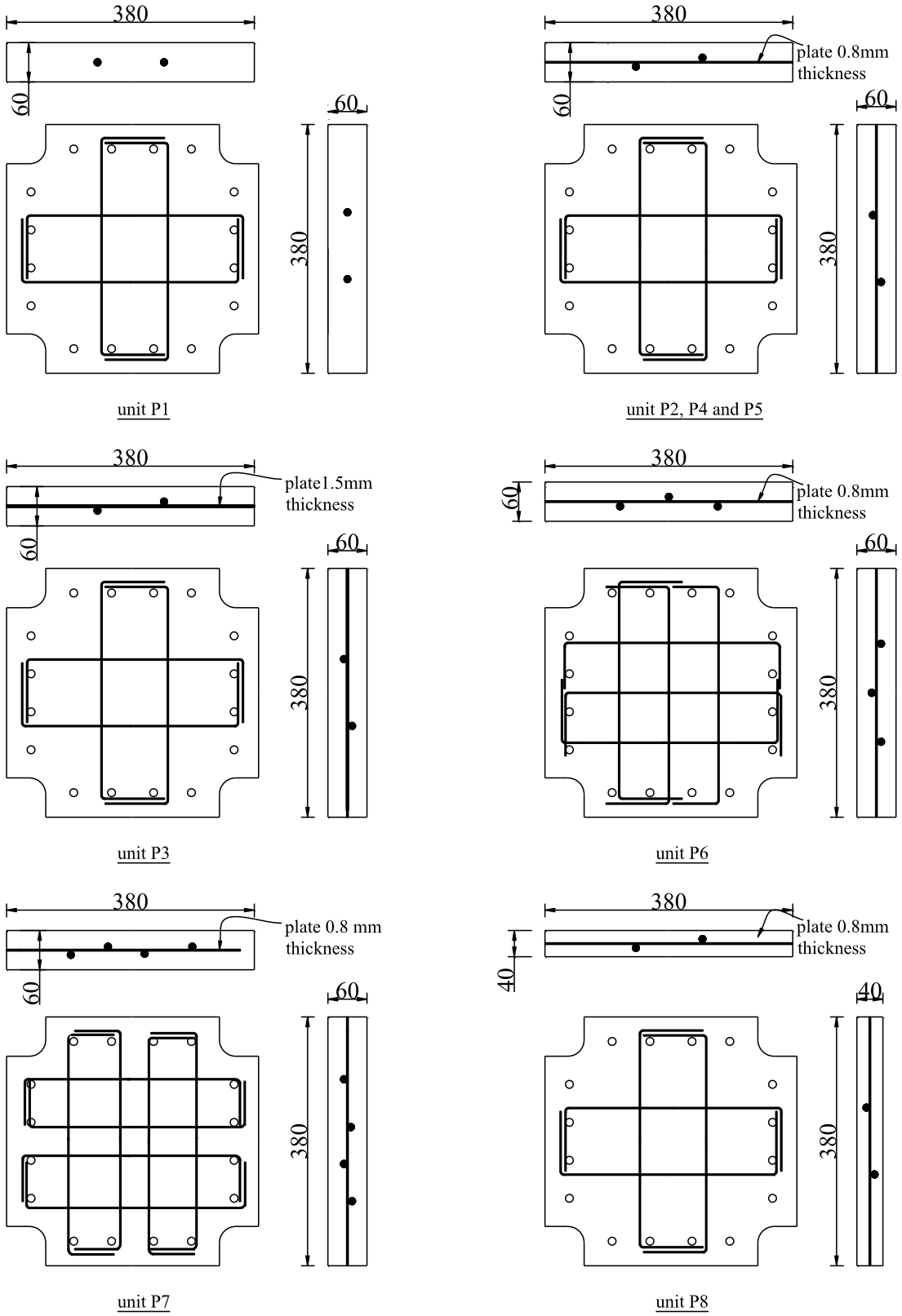

All bars are 6 mm diameter
All dimensions are in mm

Figure 3.11Dimensions and reinforcement details of test units

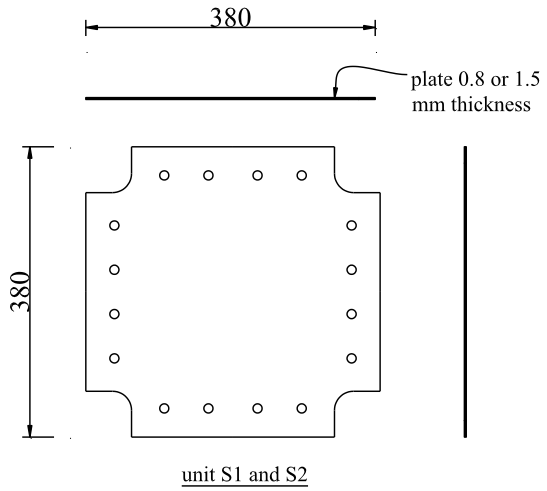

Figure 3.12 Dimensions of unstiffened plates

3.4.3 Material Properties

A. Concrete

The concrete materials used were crushed graded aggregates with a nominal size of 6 mm, natural river sand and ordinary portland cement. Three concrete mixes, giving target strength values of 25, 40 and 70 N/mm^2 at 28 days with 100 to 120 mm slump, were designed according to the Building Research Establishment (BRE) guide (Teychenné *et al.* 1998) and used in the test units. The mix proportions are given in Table 3.2. The workability of the concrete mix was improved using a super-plasticizer. The super-plasticizer used in this investigation was Glenium 51 from Master Builders. Glenium 51 is based on a modified polycarboxylate ether type of polymer and the dry content is approximately 35%.The exact amount of super-plasticizer was varied depending on the weather conditions, which affected the moisture content of the aggregates.

From each concrete mix, six 100 mm cubes were cast and tested to determine the compressive strengths at 7 days and on the test day. Three 100 × 300 mm and 150 × 300 mm cylinders were also cast and tested to determine the splitting tensile strength and elastic

modulus of the concrete, respectively on the test day. The concrete was mixed, cast, cured and tested according to Part 125 of BS 1881:1986 and the compressive strength and modulus of elasticity were determined in accordance with Part 3 of BS EN 12390-3:2002. The results of cube and cylinder tests are given in Table 3.3.

Table 3.2 Concrete mixes proportions

Ingredients	Coarse aggregate	Fine aggregate	Cement	water	Super-plasticizer
Mix with target strength value of 25 N/mm^2					
Ratio	1.90	1.90	1	0.57	150-200/100 kg of cement
Weight, Kg/m^3	830	830	439	250	1000-1250 ml
Mix with target strength value of 40 N/mm^2					
Ratio	1.67	1.54	1	0.5	200-250/100 kg of cement
Weight, Kg/m^3	832	768	500	250	1000-1250 ml
Mix with target strength value of 70 N/mm^2					
Ratio	0.81	0.72	1	0.3	230-270/100 kg of cement
Weight, Kg/m^3	671	596	833	250	1915-2250 ml

Table 3.3 Concrete properties as determined from cubes and cylinder tests

unit		Cube compressive strength (N/mm^2)	Cylinder splitting strength (N/mm^2)	Modulus of Elasticity (kN/mm^2)	Unit weight (kN/m^3)
P1	7 days	29.10±3.20	2.97	28.10	22.12
	Day of test (28 days)	38.61±5.70			
P2	7 days	29.19±3.20	3.22	27.41	20.40
	Day of test (30 days)	38.10±3.20			
P3	7 days	29.70±5.20	3.13	29.13	19.87
	Day of test (28 days)	39.16±9.20			
P4	7 days	20.50±2.98	2.93	22.52	23.20
	Day of test (29 days)	24.91±3.94			
P5	7 days	54.28±8.56	4.34	34.43	25.60
	Day of test (28 days)	71.36±13.1			
P6	7 days	31.43±1.56	3.32	24.65	21.34
	Day of test (30 days)	38.20±0.65			
P7	7 days	30.12.±2.10	2.98	29.87	23.65
	Day of test (29 days)	37.97±6.18			
P8	7 days	28.16±5.87	3.12	28.37	21.98
	Day of test (29 days)	34.39±6.77			

B. Rebars

The rebars used in all test units were 6 mm diameter plain mild steel. The mechanical properties of rebars were determined from the tensile testing of three representative samples according to ASTM A370-06 (Standard Test Methods and Definitions for Mechanical Testing of Steel Products) and the results are presented in Figure 3.13. The yield strength was determined at 0.2% offset strain by finding the intersection of the stress-strain curve with a line parallel to the initial slope of the curve and which intercepts the abscissa at 0.2%.The average yield and ultimate stress of the rebar specimens are given in Table 3.4.

Table 3.4 Mechanical properties of the reinforcing steel

Rebars diameter (mm)	Yield stress (N/mm^2)	Ultimate stress (N/mm^2)	Young's modulus (kN/mm^2)
6	455	586	183

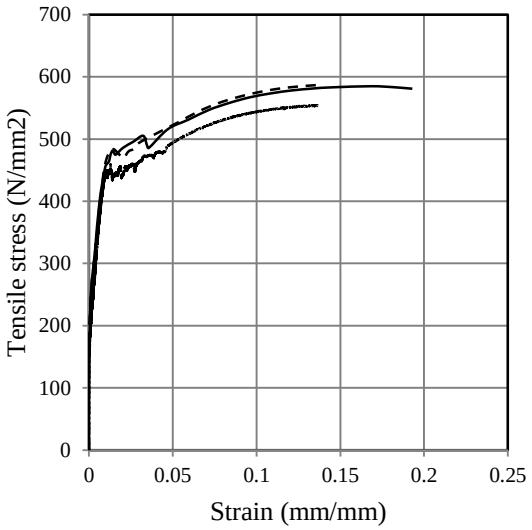

Figure 3.13 Stress-strain behaviour of 6 mm diameter rebars

C. Steel plates

The plates used in test units were plain mild steel. The mechanical properties of plates were determined from subjecting coupon specimens to uniaxial tensile tests. Three coupons were

prepared for each plate thickness and tested according to ASTM A370-06. The average results are summarised in Table 3.5 and presented in Figure 3.14.

Table 3.5 Mechanical properties of steel plates

Test unit	Plate thickness (mm)	Yield stress (N/mm^2)	Ultimate strength (N/mm^2)	Young's modulus (kN/mm^2)
P2	0.8	239	341	197
P4-P7	0.8	210	317	210
P8	0.8	168	301	196
S1	0.8	249	357	198
P3, S2	1.5	181	304	208

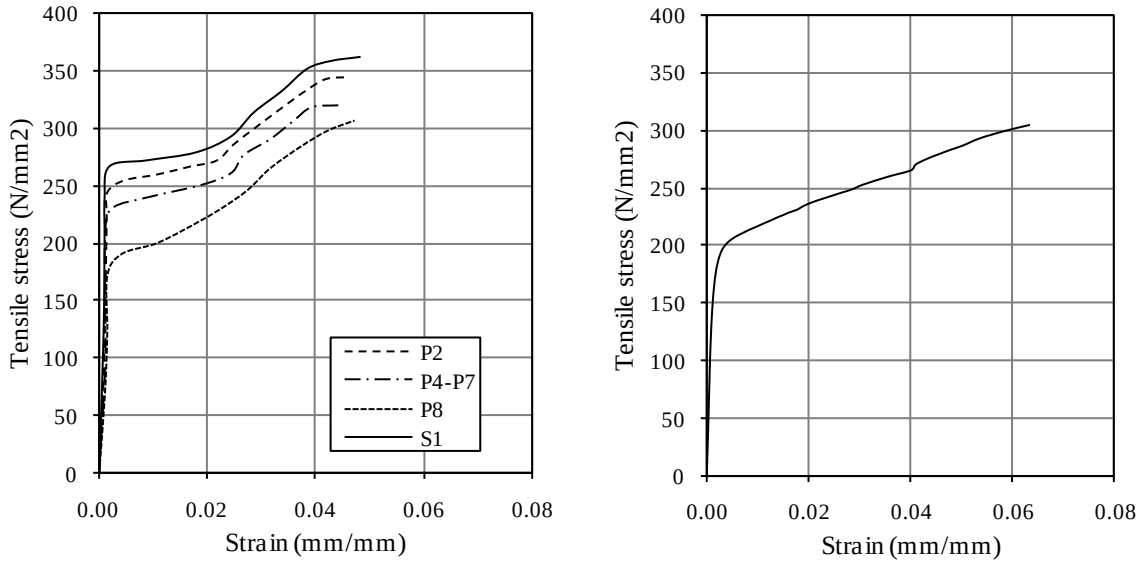

(a) Tests with 0.8 mm thick plates (b) Tests with 1.5 mm thick plates

Figure 3.14 Stress-strain behaviour of steel plates

3.4.4 Fabrication of test units

A. Formwork assembly

Test units were cast in a custom-built timber formwork shown in Figures 3.15 and 3.16. The formwork was made of 18 mm thick plywood panels and constructed with ± 0.5 mm tolerance, Figure 3.15. The plywood panels were bolted together using 8 mm diameter threaded bars, and the inner sides of the formwork were sealed with silicon and covered with a thin layer of oil to prevent attachment of concrete. Holes were drilled in the plates for the intermediate bolts according to their exact positions in the frame members before assembly. Then, the frame members of the rig were clamped to the formwork using the 16 bolts to support the formwork and secure the encased-plate in its exact position, see Figure 3.15.

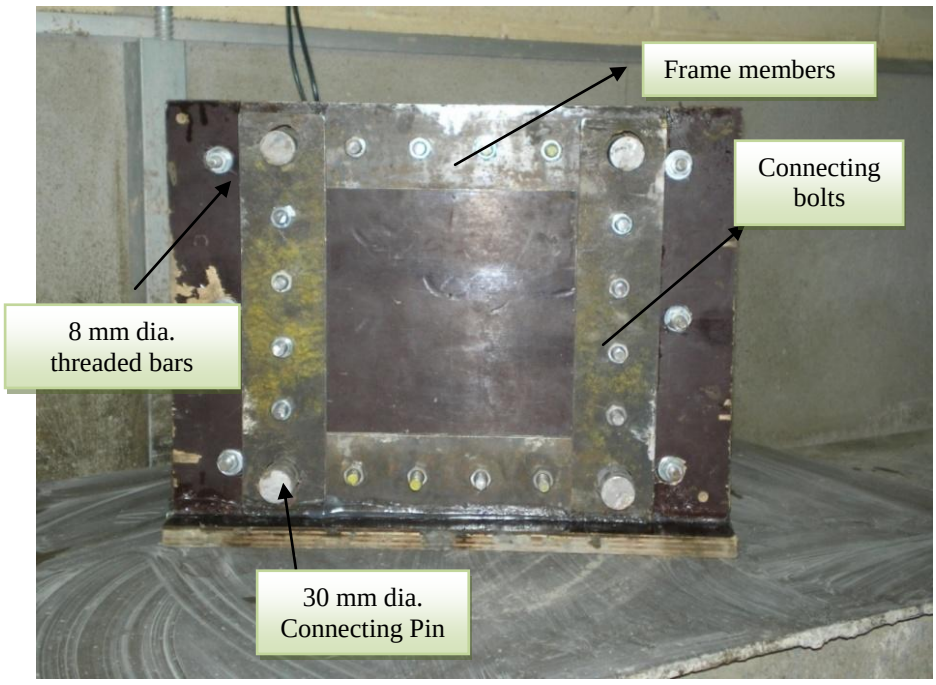

Figure 3.15 A close up of formwork assembly on vibrating table

B. Reinforcement formation and assembly

The rebars were cut to length and bent according to the required dimensions. In order to provide the required anchorage for the rebars, they were bent around and welded to the

connecting bolts. The plates were cut to the required dimensions at the local supplier and cleaned using Acetone. To improve the bond between the plate and the concrete mix, rebars were glued to the plate using a suitable epoxy adhesive. The reinforcement and plate were instrumented with strain gauges at the desired locations as given in Section 3.4.5, and placed centrally in the formwork.

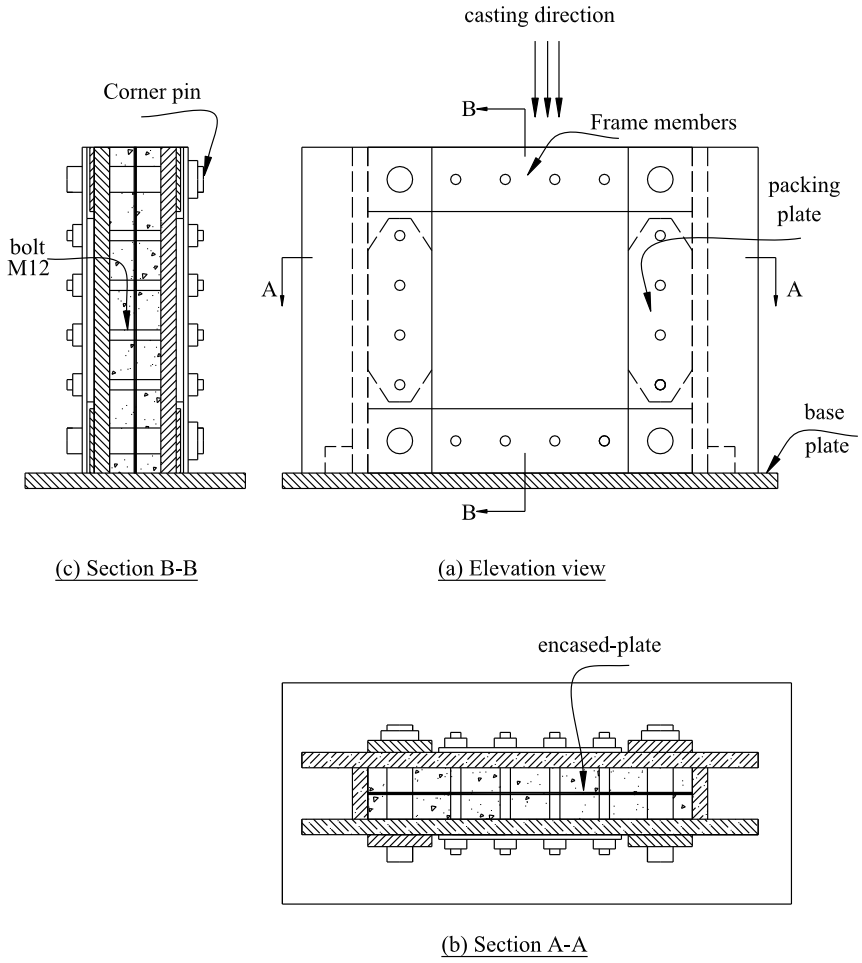

Figure 3.16 Details of formwork assembly

C. Concrete casting

The concrete was mixed mechanically in a horizontal pan type mixer of 0.1 m^3 capacity. Dry materials were prepared by weight according to the proportions detailed in Table 3.2. The constituents were mixed in a dry state for a few minutes to ensure mix uniformity.

Super-plasticizer and water were then added gradually and the contents were mixed until a homogeneous mix was obtained. The formwork was placed on a vibrating table and the concrete was placed in the formwork with hand shovels. The test unit was cast in four layers. After pouring of each layer, the vibrating table was turned on for a few seconds until good compaction had been achieved. Control cubes and cylinders were simultaneously cast with the test unit. The test unit, control cubes and cylinders were covered immediately after casting using damp hessian and polythene sheets. The units were stripped three days after casting while the cubes and cylinders were demoulded on the day after casting, and covered with damp hessian sheet. Curing of concrete continued for four weeks keeping the hessian damp at all times.

3.4.5 Instrumentation

The displacement of the vertical diagonal of the test unit was monitored using one LVDT as shown in Figure 3.17. A Canon PowerShot G9 digital camera with a resolution of 3264 × 2448 pixel was used to capture digital images of the units during the test. The images were later analysed using close-range photogrammetry and particle image velocimetry (PIV) to determine the distribution of deformation and strain over the whole specimen's surface area at all test stages as explained in Section 3.5.

Four strain gauges were additionally attached to the rebars and plate at key locations to measure the induced strains in one unit, P2. The strain gauges were used to provide additional information on the load levels at which rebars and plate yielding were achieved. Unit P2 was selected to represent a typical strain development in composite units. The positions of the strain gauges are depicted in Figure 3.18.

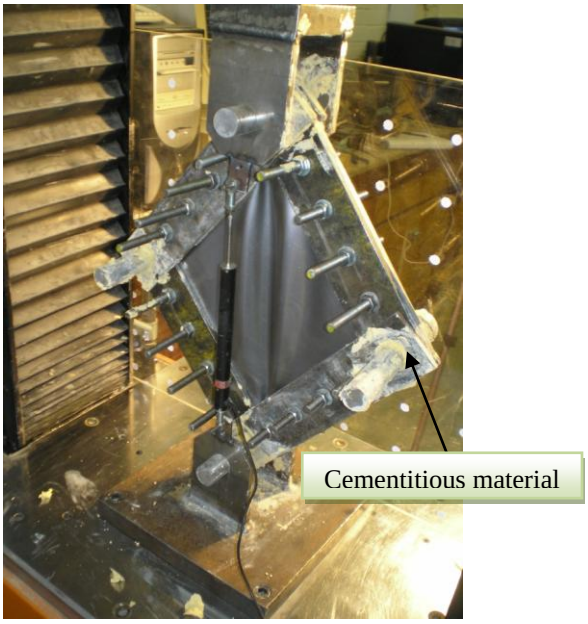

Figure 3.17 Position of the LVDT

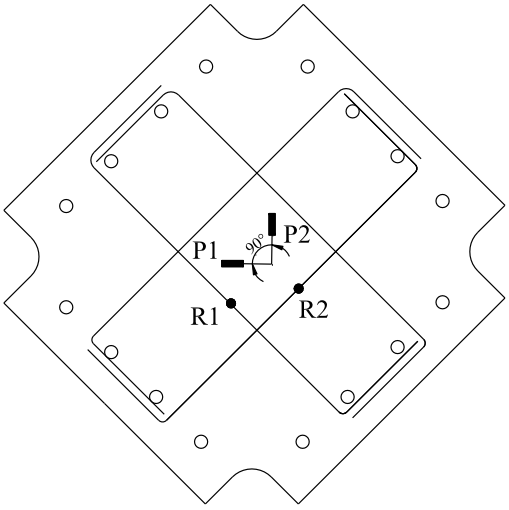

Figure 3.18 Locations of strain gauges in unit P2

3.4.6 Testing

All wall units were tested at about 28 days from casting day. The test unit was fitted to the test frame using the 16 intermediate connecting bolts, and the test frame assembly was placed in such way that a diagonal was aligned vertically and then connected to the testing machine using the hinges and corner pins, see Figure 3.17. In order to reduce the slack at

the connecting pins, a high-strength cementitious material was used to fill the gaps around the pins as shown in Figure 3.17. The load was applied by the Instron 1196 machine in a strain control mode.

The load was applied incrementally to a diagonal of the test unit while monitoring its displacement. At the beginning of the test, few cycles of loading and unloading up to 5kN were applied to the test unit to minimise the possible effects of slack in the intermediate bolts and connecting pins. The diagonal load increased gradually until failure occurred.

3.4.7 Data recording

Data obtained from the LVDT, the strain gauges and the load obtained from the testing machine were collected by a Spectra data logger connected to a personal computer. The analysis software offered immediate monitoring of all used channels and chart presentation for two selected channels. These features enabled close monitoring of test unit behaviour during the testing process. Moreover, digital photographs were taken of the units during all test stages.

3.4.8 Crack monitoring

Crack propagation was monitored after each load increment until failure occurred. At each load increment, cracks were highlighted and marked with their corresponding load value. The load that produced the first crack and the load that produced the unit failure were recorded and noted as cracking and failure load. Finally, the pattern of cracks for each unit was neatly sketched and photographed.

3.5 Full field deformation measurement system for structural testing

3.5.1 Overview

Experimental testing has been used to assess the strength and deformations of reinforced concrete structures in serviceability and ultimate limit state as well as to validate finite element codes. Experimental testing often requires an enormous amount of manpower in addition to being expensive to set up and run. Therefore, it is important to obtain as much information as possible from the test, especially in destructive testing. This section presents a full-field deformation measuring system for use in structural testing. The disadvantages of conventional measuring instruments and the potential for the proposed system are presented in detail. The analysis technique is discussed briefly followed by evaluation of the proposed system against experimental results obtained from testing the units.

3.5.2 Conventional measuring instruments

Conventional methods for measuring displacement and strain during testing of concrete structures comprise of using dial gauges or linear variable deflection transducers (LVDTs) to measure one-dimensional displacements, demountable mechanical strain gauges (DEMEC) to estimate the strain on a concrete surface, and electrical strain gauges for measuring strains either in reinforcement or on a concrete surface.

A. Dial gauges and transducers

Dial gauges and transducers are commonly used to measure the deformation during structural testing. Dial gauges present an inexpensive instrument to measure the deformation especially when the data is not required to be registered electronically, see Figure 3.19.

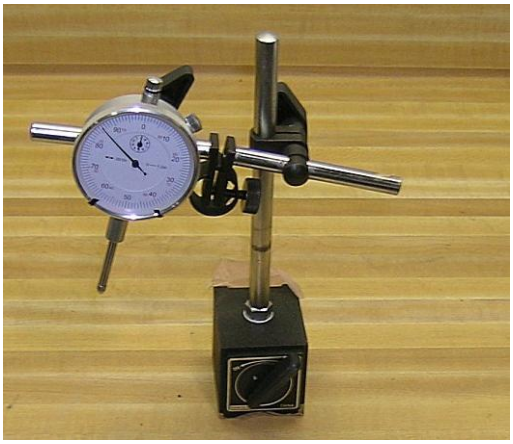

Figure 3.19 A view of a dial gauge

Although LVDTs are suitable for laboratory use and provide accurate results, their performance can be affected by the presence of any magnetic fields available nearby (Whiteman *et al.* 2002). Another problem arising from using LVDT is the limited measuring range (travel) which bounds the magnitude of measured deformation and the accuracy is markedly reduced outside the linear travel range. Moreover, a practical consideration should be taken into account, especially in destructive testing, damage to instrumentation that requires its removal, thus preventing deflection measurement at failure. In addition, armatures (Figure 3.20) of the dial gauge and LVDT have to be fixed to a stable stand near the structure and the device must be pressed against the structure. Consequently, a considerable amount of preparation work is needed for the test setup including fixing of instrumentation and calibration of individual components resulting in an extensive cabling amount with complex and laborious wiring (Woodhouse *et al.* 1999; Whiteman *et al.* 2002).

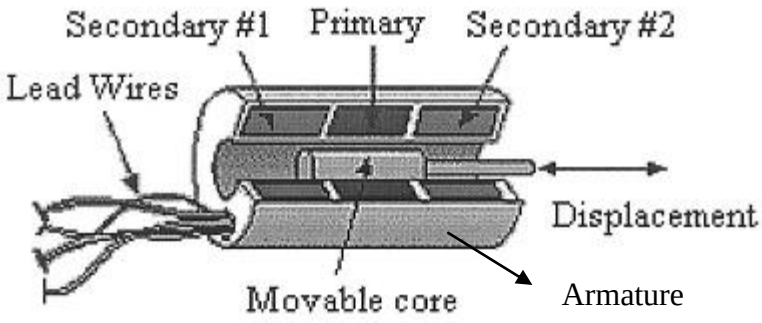

Figure 3.20 Internal components of a LVDT (Woodhouse *et al.* 1999)

B. Electrical strain gauges

Electrical strain gauges are regularly used to measure uniaxial strains and can be embedded in concrete to measure steel strains or attached to a concrete surface. Whilst accurate and the only way to measure strains in embedded bars in concrete, strain gauges encounter problems during cage fixing, placing and concrete casting. Moreover, attachment of strain gauges to concrete surface is not convenient. Once a crack passed under an electrical strain gauge, the gauge could be failed and the reading could not be considered reasonable.

C. Demountable mechanical strain gauges (DEMEC)

The Cement and Concrete Association developed the demountable mechanical strain gauge system to measure the distance between two targets attached to a structure surface. The system involves a standard dial gauge fixed to an invar bar with two conical locating points, one fixed and the other is movable, Figure 3.21. Two pre-drilled stainless steel discs, termed as targets or demecs, are fixed to the structure's surface using adhesive. Readings are taken from the dial gauge by inserting the conical points of the gauge into the holes in the discs. Use of DEMEC gauges requires direct access to the targets which make it unsuitable at all positions on concrete surface. Also, to measure the strain over a wide

surface, an extensive arrangement of target grids must be attached to the surface which needs more time and effort. Moreover, DEMEC gauges normally give average strain values rather than local strain values. Therefore, a more convenient measuring system is needed to measure the deformation and strain during testing of structures (Woodhouse *et al.* 1999). The method of close-range photogrammetry was therefore proposed to offer this possibility.

Figure 3.21 A demountable mechanical strain gauge system

3.5.3 Background

Close-range photogrammetry was used in applications in geomechanics, biomechanics, chemistry, architecture and automotive and aerospace industries. Although close-range photogrammetry has not been well known in measuring deformation and strain during structural testing as in other fields, the examination of current methods has established the potential of using this approach (Dallas 1996; Fraser 2000; Pappa *et al.* 2001; Jiang *et al.* 2008).

Two image-based approaches found practical application in measuring geometry deformations and structural test monitoring. The approaches included laser-interferometry (Hegger *et al.* 2004) and close-range photogrammetry. Photogrammetry is used to determine the three-dimensional shape of bodies by measuring and analysing their two-dimensional images.

The application of laser-interferometry, which is based on the interference of reflected waves of a laser light with the object, is still restricted due to the limitations of cost, safety and other experimental constraints. On the other hand, the close-range photogrammetry method was used to measure planar deformations of a bridge deck and supporting beams by using video cameras, retro-reflective monitoring targets and digital computerized analytical tools (Bales 1985; Bales and Hilton 1985; Kim 1989; Cooper and Robson 1990; Forno *et al.* 1991; Abdel-Sayed *et al.* 1994; Johnson 2001; Jauregui *et al.* 2003). This technique depends on tracking the movement of retro-reflective targets during load application.

The confidence in using retro-reflective monitoring targets has a number of shortfalls. A dense grid of targets needs considerable time and effort in fixing and adjusting them, while a widely spaced grid of targets may result in sparse data (White *et al.* 2003). This system possesses a serious problem due to the use of video cameras which produce lower quality images compared to digital still cameras. The analogue transfer of video signals causes image degradation, and saving on tape creates line jitter (White *et al.* 2003). However, digital still images experience analogue–digital transformation inside the camera, avoiding additional noise during transfer and storage phases (White *et al.* 2003).

3.5.4 Particle image velocimetry (PIV)

The term “particle image velocimetry (PIV)” was first introduced in 1984 to measure velocities and related properties in seeded fluids in the field of experimental fluid mechanics (Adrian 1991; 2005). The technique was adapted for use in measuring soil planner deformation and strain. In this approach, the sand’s own texture was used for image processing instead of fluid seeding. The analysis technique comprises two subsequent stages. In the first stage, the image-space displacements are estimated using the GeoPIV

software (White and Take 2002), while in the second, the image-space displacements are converted to object-space measurements using the centroiding method.

To calculate image-space displacement vectors between two images, the first test image is divided into a uniform grid of patches. The patch movement during the interval between the images is obtained by detecting the crest of the auto-correlation function of each patch. The auto-correlation function is used to determine the offset between two subsequent images which gives the displacement vector of the patch. Figure 3.22 demonstrates the image manipulation during PIV analysis, in which the image was split into a grid of patches, $I_{test}(U)$, of L × L pixel size. The patch movement between each image pair can be estimated through a search patch $I_{search}(U+S)$ in the second image. The accuracy of the PIV measurements is strongly affected by software algorithm and image quality. Validation experiments proved the accuracy of the technique with an accuracy of $1/100^{th}$ of a pixel (White *et al.* 2003). For full details about the mathematical approach used in the PIV analysis technique, a reference can be made to White *et al.* (2003).

Since the data obtained from PIV is in image-space coordinates, i.e. units of pixels, a transformation technique should be implemented to get the data in object-space units (mm). A series of reference targets, with known object-space coordinates in image plane, is used for this transformation centroiding method. Also, this technique enables the detection and correction of any image space displacement of the control markers due to camera movement.

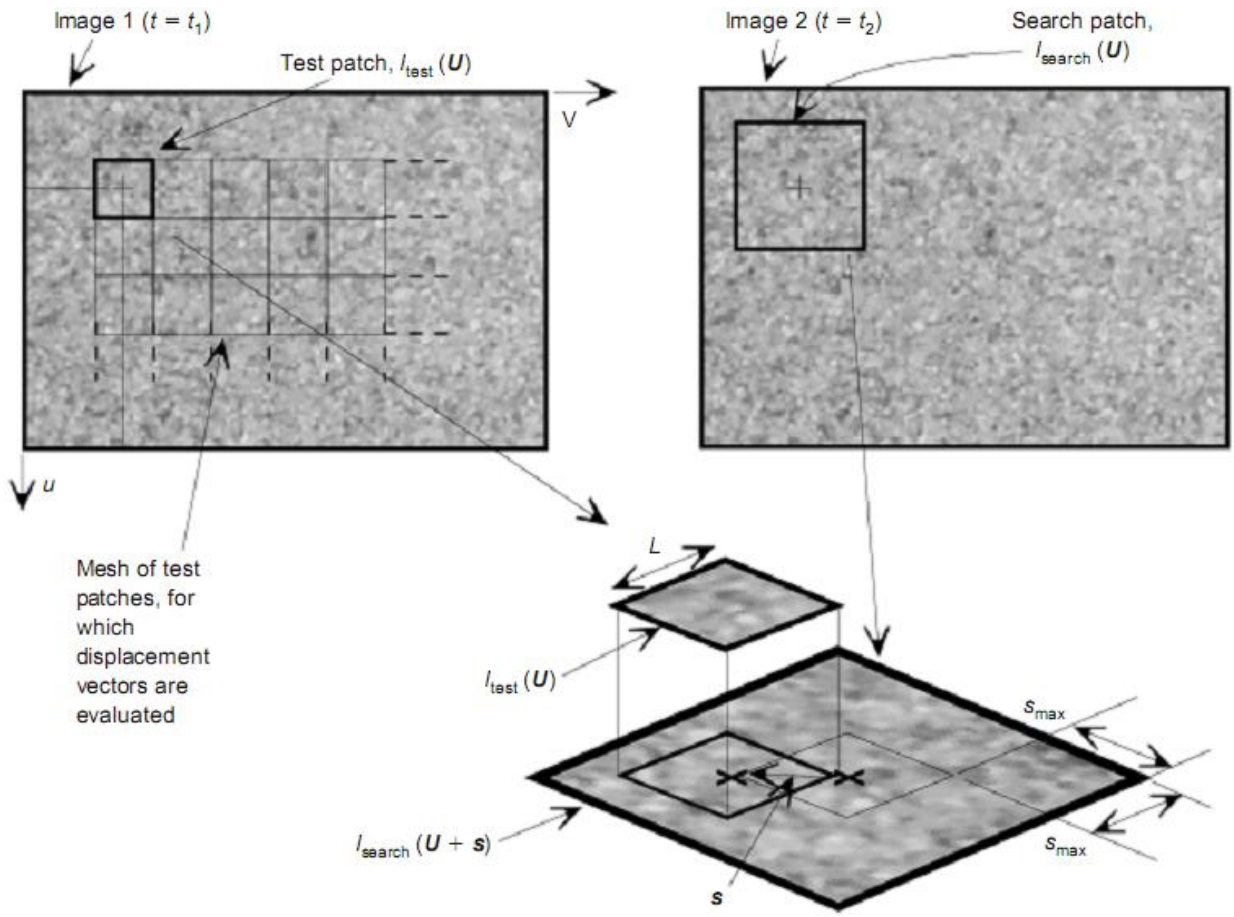

Figure 3.22 PIV processing technique (White *et al.* 2003)

3.5.5 Application of PIV technique to unit tests

The PIV technique was used to measure the displacements and strains induced during the testing of concrete units under pure in-plane shear loading. PIV requires that the surface has a pattern of dark and light contrasting features to track its movement. The surface of the concrete unit was painted with a thin coat of white emulsion paint and then a black paint was sprayed in dots over the surface to provide the spatial variation in brightness required by PIV to track the movements of the concrete surface, see Figure 3.23a. A series of control markers, with known object-space coordinates, was drawn on a perspex sheet and placed in the front of the test unit. Control markers are small black circles drawn on a white background to give an extreme contrast that can be located in image-space (Figure 3.23a).

A Canon PowerShot G9 digital camera with a resolution of 3264 × 2448 pixel was used for image capturing. The camera was carefully located to reduce image distortion and was controlled remotely through a USB link from a personal computer, and images were saved and checked during test progress. A halogen lamp was used to provide a stable and uniform lighting on the surface of the test unit. The lighting was positioned carefully to reduce reflections from the control markers placed on the perspex sheet, see Figure 3.23b.

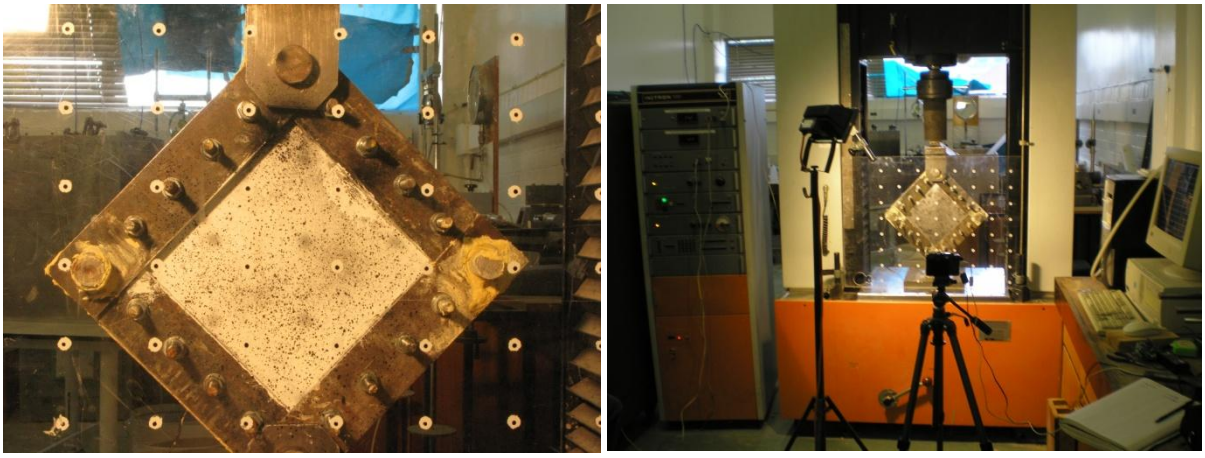

(a) Produced surface texure (b) Camera and light

Figure 3.23 Setup of PIV system

3.5.6 Evaluation of PIV performance

The PIV technique was extensively used in the field of geotechnical modelling and used to calculate soil deformation and strain during centrifuge modelling (White *et al.* 2005, Ahmed and Bransby 2009). The technique was also used to quantify the development of strain over the surface of fibre reinforced polymer (FRP) confined concrete cylinders (Bisby *et al.* 2007).

Since the displacement measurement points are the PIV patches defined in image-space, the movement of any point on a concrete surface can be monitored. Consequently, deformation fields and strain contours can be plotted for further investigation of results obtained during the test.

In order to check the performance of PIV deformation measurements, the technique was used to monitor the displacement of the vertical diagonal occurring during the destructive testing of all units under in-plane shear and compared to the data obtained using LVDT. One patch was placed on the top hinge to track its movement during the application of the diagonal load, Figure 3.24. The grid of control markers, placed in front of the units, allowed the conversion from image-scale to object real scale, Figure 3.24. The load was applied in a displacement control mode with a rate of 1 mm/min. In order to ensure compatibility between the PIV and LVDT results, the data obtained from the testing machine, the transducer and the images were collected every 20 seconds allowing a vertical displacement of about 0.33 mm between images.

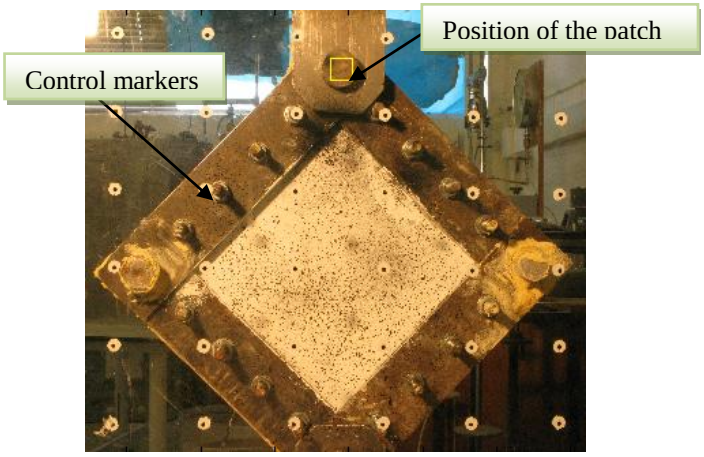

Figure 3.24 Typical test unit showing selected patch position

For comparison purposes, Figure 3.25 presents the load-displacement behaviour obtained from the LVDT and the PIV systems for six units. The figure clearly indicates that the PIV measurement technique was successful in measuring the displacement of concrete structures under destructive testing. Consequently, it can be used to plot full-field surface strains during the test. GeoPIV software (White and Take 2002) offers the capability to calculate wide range of strain components including principal, shear and volumetric strains.

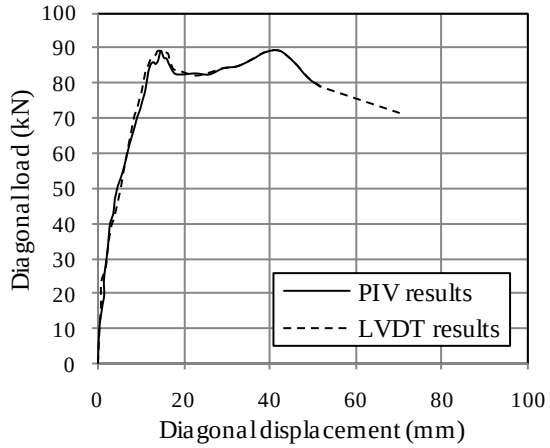

(a) Unit P1

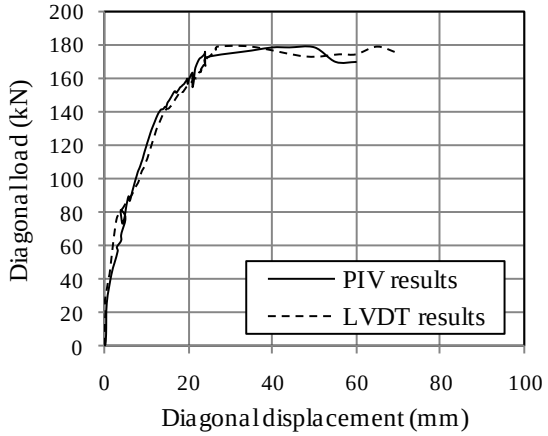

(b) Unit P3

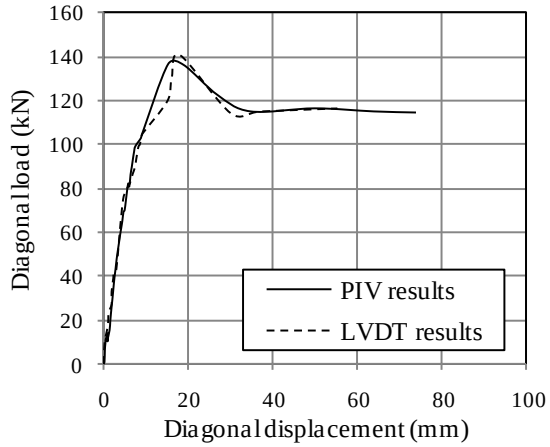

(c) Unit P4

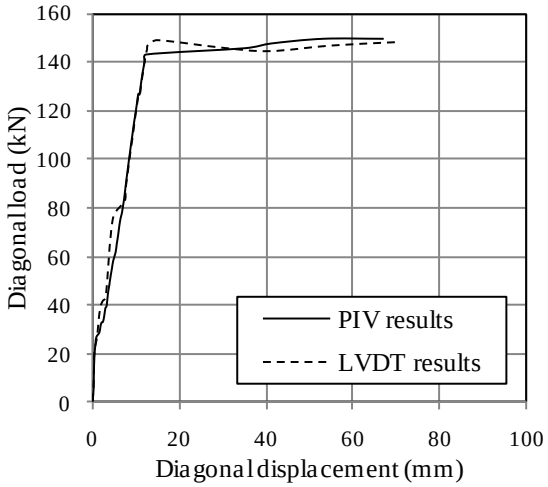

(d) Unit P5

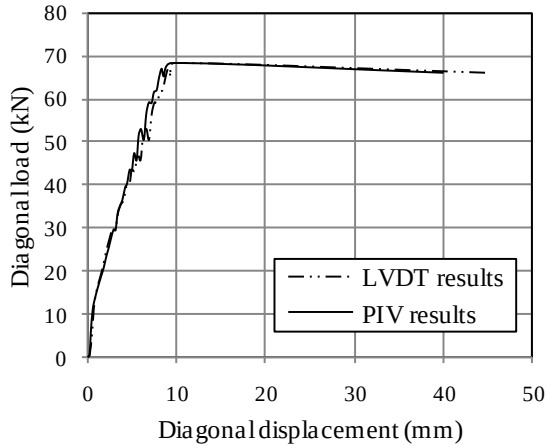

(e) Unit P8

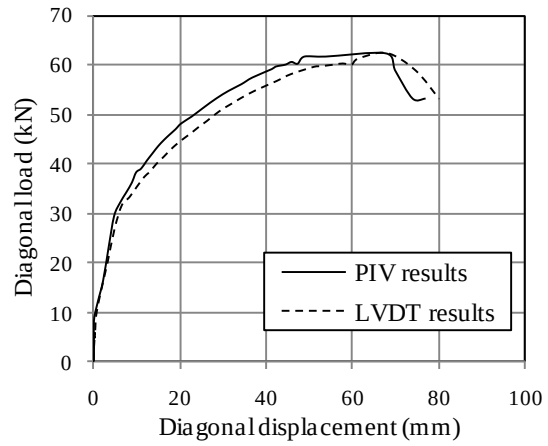

(f) Unit S1

Figure 3.25 Diagonal load-displacement behaviour as obtained from LVDT measurement and PIV analysis

3.6 Test results and observations

The results obtained from testing the 10 units are discussed in detail in this section. The behaviour of individual components is first discussed followed by the behaviour of composite walls.

3.6.1 Unstiffened plates

Two unstiffened plates with 0.8 and 1.5 mm thickness were tested in the test rig under pure in-plane shear. The behaviour of the two plates was almost identical with an initial elastic stage followed by final buckling. The shear load, F1, at buckling was 22.16 and 39.45 kN for the 0.8 and 1.5 mm thick plates, respectively. The development of plate buckling was accompanied with the formation of tension field which progressed with further load increments. The inclination of the a tension field in the plates was approximately 45° to the edges (almost vertical), see Figure 3.26. The shear load-displacement behaviour of the two plates is given in Figure 3.27.

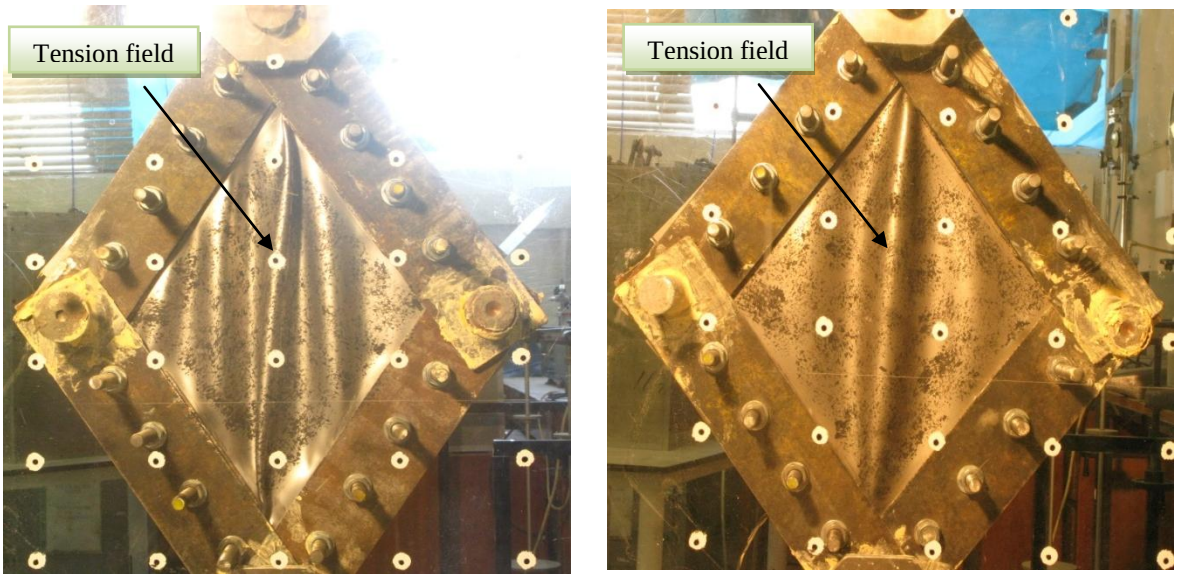

(a) Unit S1 (b) Unit S2

Figure 3.26 Development of tension field in unstiffened plates

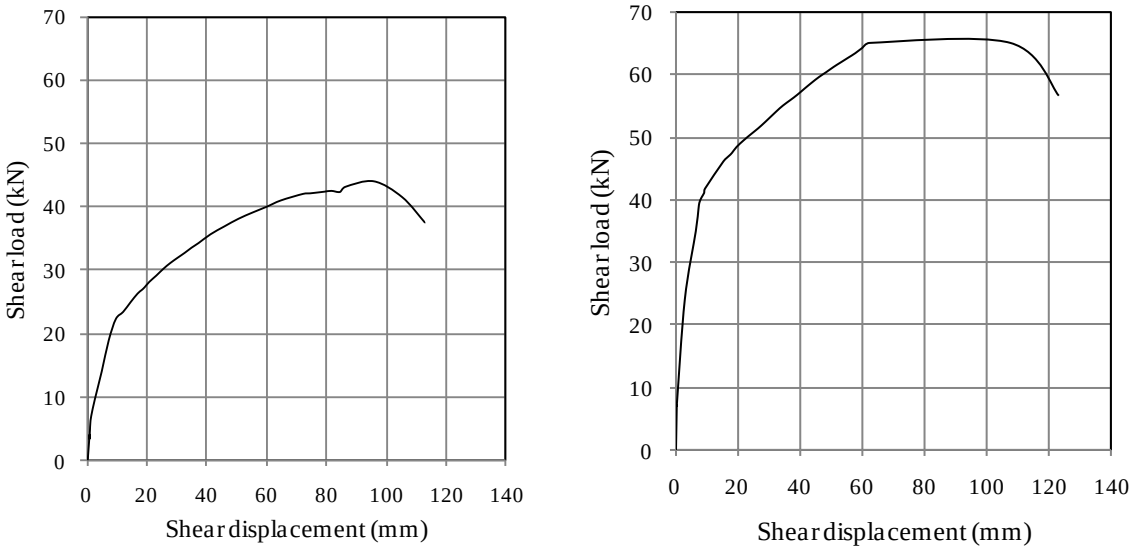

(a) 0.8 mm thick plate (b) 1.5 mm thick plate

Figure 3.27 Shear load-displacement behaviour of unstiffened plates

The points of buckling initiation are clearly observed in the load-displacement behaviour. Also, the figure indicates that the plates exhibited strain hardening behaviour after buckling, and showed considerable post-buckling strength before failure was observed at a shear load, F1, of 44.07 and 64.07 kN for the 0.8 and 1.5 mm thick plates, respectively. At the end of the test, the frame members were removed and signs of yielding and tearing in the plates around the connecting bolts were clearly observed, see Figure 3.28.

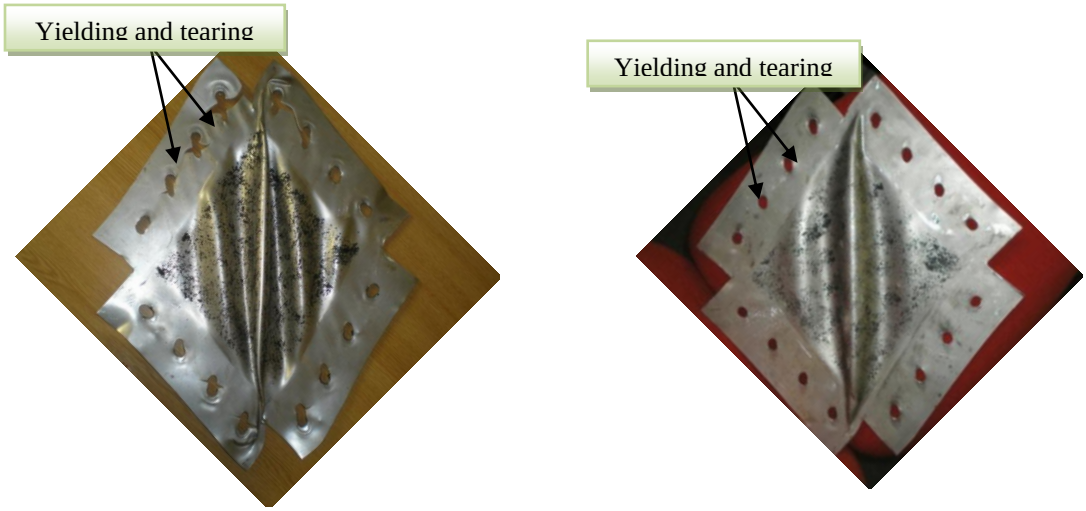

(a) Unit S1 (b) Unit S2

Figure 3.28 Failure of unstiffened steel plates

No electric strain gauges were attached to the plates; however, the PIV system was used to estimate the full-field displacement vector fields during the test. The full-field displacement vectors were obtained by placing a mesh comprising 475 patches distributed across the image, see Figure 3.29. The relative displacements of the patches were used to calculate the maximum principal strains using the GeoPIV software. Figure 3.30 depicts the distribution of cumulative maximum principal strains at failure (115 mm diagonal displacement) for unit S1, which confirmed the formation and spread of the tension field across the plate. It worth noting that Figure 3.30 ignores the out of plane displacement occurred due to plate buckling since only one camera was used and the strain plot presented here could be used as a guide on strain trends rather than values.

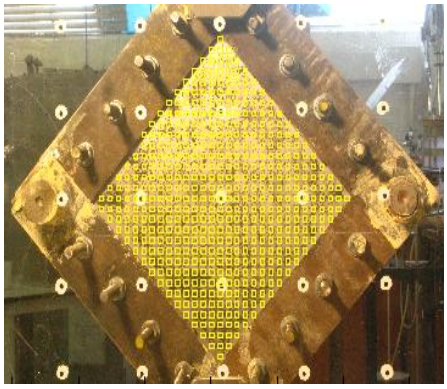

Figure 3.29 Positions of patch mesh

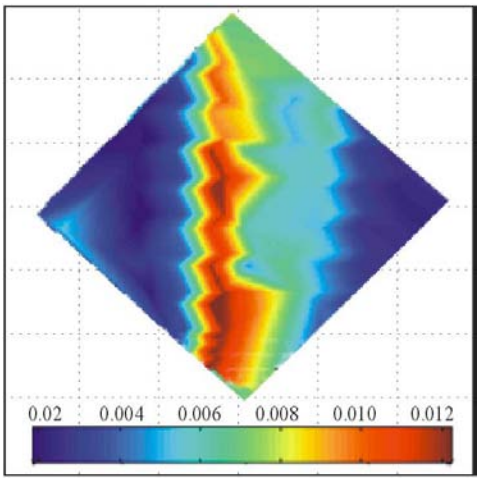

Figure 3.30 Distribution of cumulative maximum principal strains-unit S1 at failure (115 mm diagonal displacement)

In order to estimate the strains at selected positions, the term “virtual strain gauge” was introduced. A virtual strain gauge comprises a pair of patches placed at desired positions, see Figure 3.31. The relative displacement of patches was calculated using the PIV technique, and the strain was determined by dividing the relative displacement by the initial distance between the patches. In order to investigate the strain propagation along the loaded

diagonal (vertical diagonal) and off-diagonal (horizontal diagonal), a series of virtual strain gauges were placed at key positions as shown in Figure 3.31.

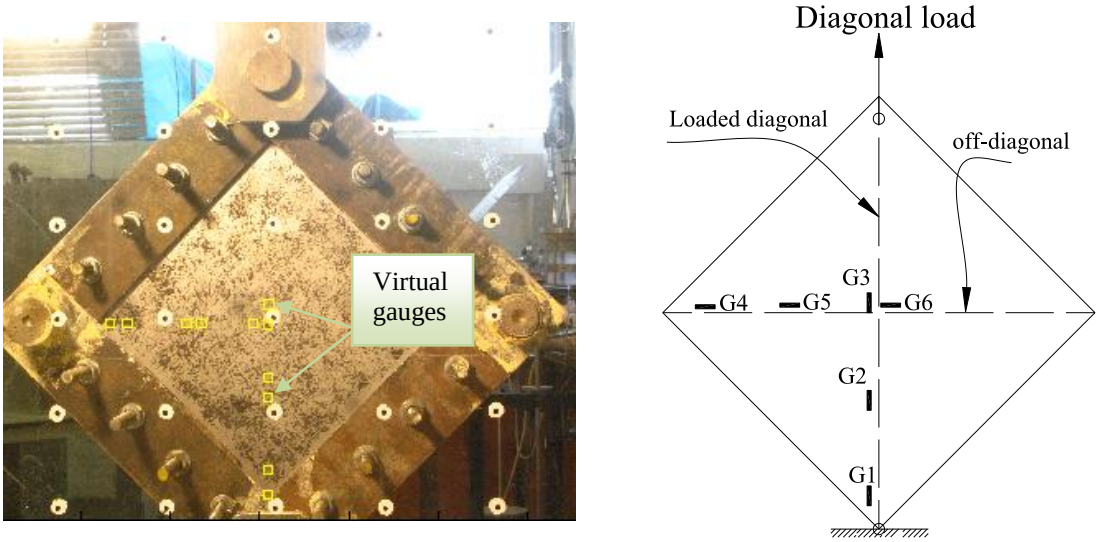

Figure 3.31 positions of virtual strain gauges

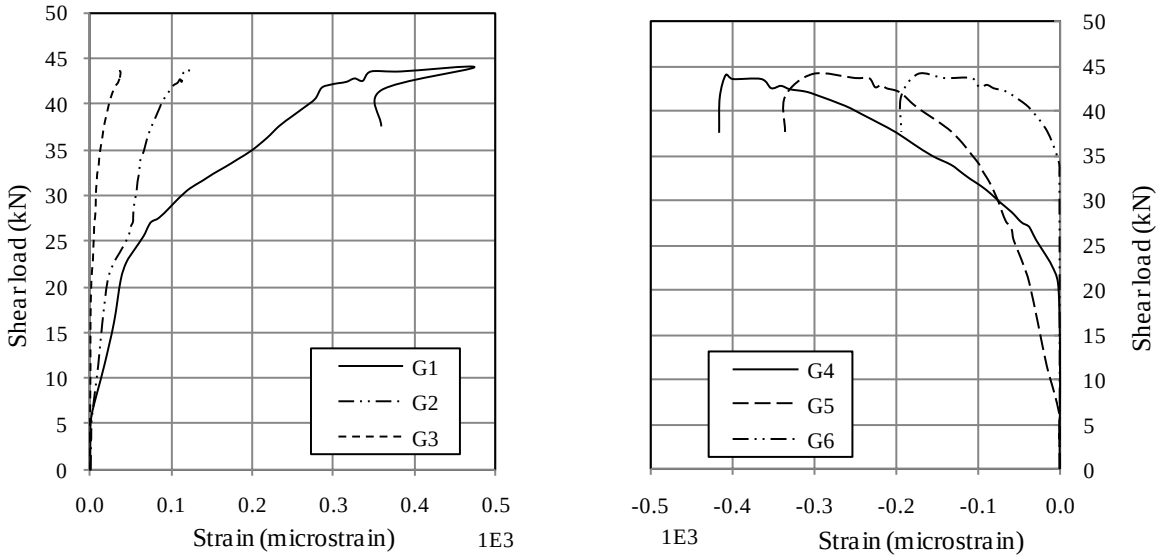

(a) along loaded diagonal (b) along off-diagonal

Figure 3.32 Propagation of strains along the loaded diagonal and off-diagonal with shear load in unit S1

Figure 3.32 illustrates strain propagation along the loaded diagonal and off-diagonal with shear load in unit S1. Basically, all the gauges along the loaded diagonal were under

tension, with linear response until the initiation of buckling. The strain at the bottom hinge (G1) was much higher than that far from the bottom corner (G2 and G3), which implies that strains reduced gradually from the position close to the bottom hinge towards unit centre, and yielding began at the bottom pin and gradually proceeded until reached the top corner of the plate, see Figure 3.32a. On the other hand, all strain gauges along off-diagonal were under compression during all loading stages. Strain analysis showed that higher strains developed at the corner pin (G4) and less strain at the unit centre (G6), Figure 3.32b.

3.6.2 Conventionally-reinforced unit

Unit P1 was conventionally-reinforced with a grid of two 6 mm diameter bars in each direction as shown in Figure 3.11. The unit's first crack developed in the top third of the unit horizontally at a shear load of 28.28 kN. Further increases in the diagonal load resulted in developing more horizontal cracks and widening of existing ones. The major horizontal crack appeared at 36.06 kN shear load with a crack width significantly higher than the others. After the application of 43.84 kN load, no more new horizontal cracks were observed until failure of the unit at 63.07 kN shear load. After failure, the unit was split into a series of concrete pieces and full failure was observed around the connecting bolts, see Figure 3.33. Reinforcement buckling was also noticed after removing the frame members and damaged concrete at the end of the test.

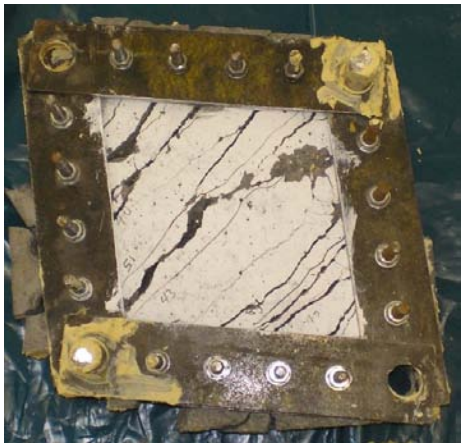

Figure 3.33 Unit P1 form after failure

The formation of horizontal cracks (Figure 3.34) and distribution of maximum principal strains on concrete surface (Figure 3.35) showed that the designed shear rig could properly handle small-scale concrete units and apply pure shear loading. The crack pattern is depicted in Figure 3.36, while Figure 3.37 presents the shear load-displacement behaviour of the unit, which suggested that the unit exhibited ductile behaviour due to the yielding of reinforcement.

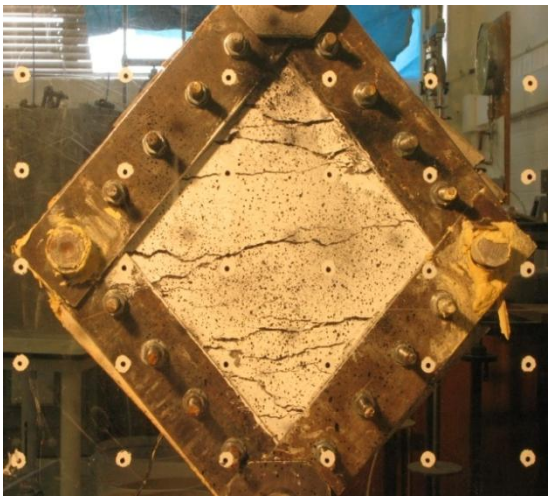

Figure 3.34 Unit P1 form at failure

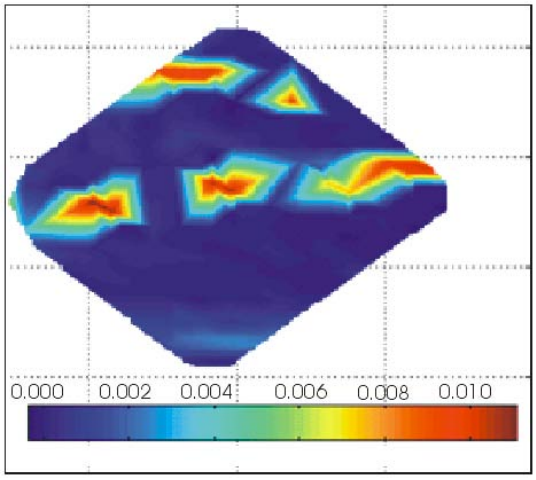

Figure 3.35 Cumulative maximum principal strains at failure on concrete surface-unit P1

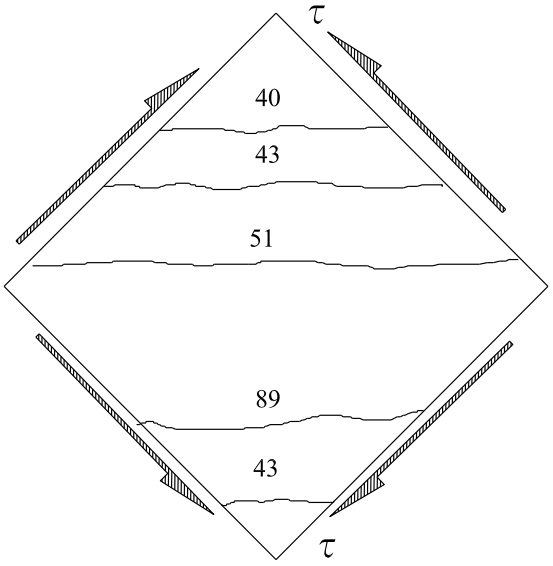

Figure 3.36 Crack pattern for unit P1 at failure

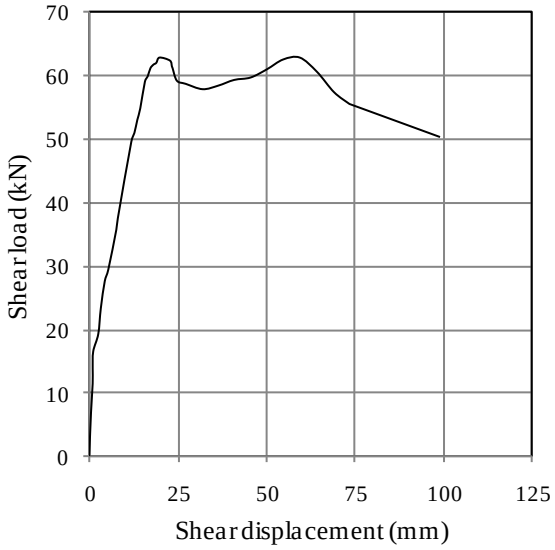

Figure 3.37 Shear load-displacement behaviour of unit P1

A series of virtual strain gauges were placed at key positions to investigate the propagation of strain along the loaded diagonal and off-diagonal as given in Figure 3.31. All the gauges along the loaded diagonal were under tension with higher strains at the centre of the unit due the concrete cracking as shown in Figure 3.38a. Conversely, the off-diagonal was under compression during all stages of loading with higher strains at the corner pins and reduced gradually towards the centre of the unit, which was predominantly under diagonal tension due to the applied diagonal load, see Figure 3.38b.

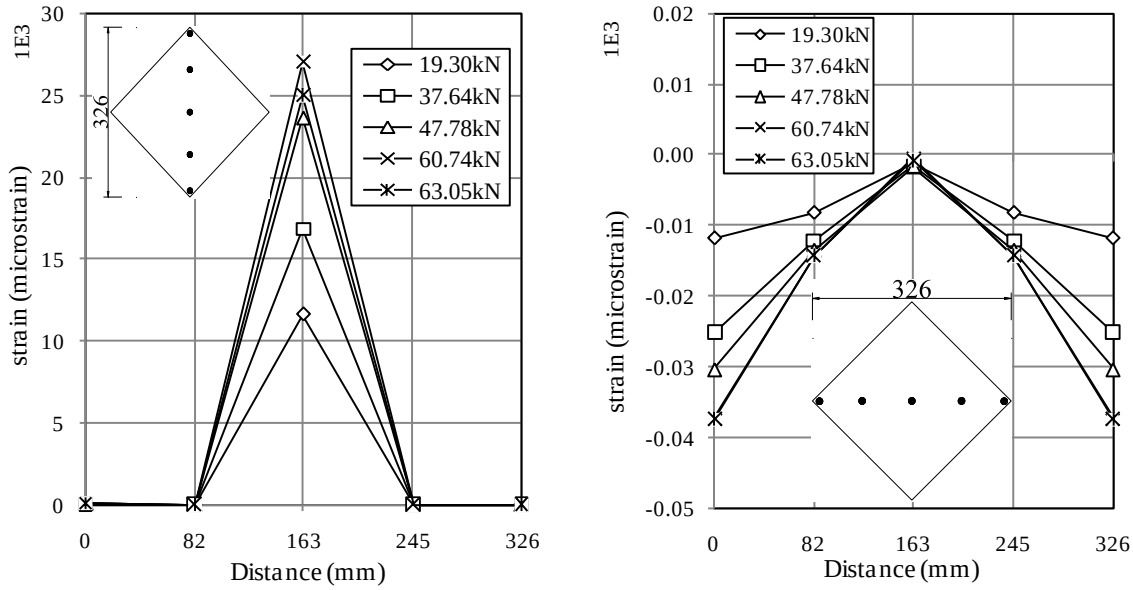

(a) loaded diagonal (b) off-diagonal

Figure 3.38 Strain distribution along the loaded diagonal and off-diagonal of unit P1

3.6.3 Encased-plate composite units

A. Introduction

The test programme included seven encased-plate composite units, P2-P8. Testing of composite units started with the application of a few cycles of loading and unloading up to 5kN to minimise effects of slack at the intermediate bolts and connecting pins, then the diagonal load increased gradually until units' failure. All composite units were reinforced

with a plate of 0.8 or 1.5 mm thickness and a grid of rebars uniformly-distributed in both directions, see Table 3.1 and Figure 3.11. All composite units had almost the same behaviour under the applied load except unit P8 which had a smaller thickness. Therefore, only the behaviour of a typical unit P2 and unit P8 will be discussed in detail in the next section. The test units form at failure are pictured in Figure 3.39, while the crack patterns of all composite units are depicted in Figure 3.40. Further, the shear load-displacement behaviour patterns of the units are plotted in Figure 3.41. The principal results obtained from the tests are summarised in Table 3.6.

B. Structural behaviour

i. Unit P2

Similar to unit P1, unit P2 developed the first crack parallel to the off-diagonal in the middle third of the unit at 28.28 kN shear load, F1. Further loading resulted in the gradual development of additional horizontal cracks and widening of existing ones, Figure 3.40a. Although plate buckling could not to be monitored during the test, no signs of debonding between the encased-plate and the surrounding concrete, prior to the point when maximum load was achieved, were observed. Beyond the ultimate load, the concrete cover spalling off was observed in the areas around the loaded diagonal in the unit (see Figure 3.39a), which was thought to be associated with plate buckling and the formation of diagonal tension field in the encased-plate. The unit failed when the shear load reached 102.05 kN. The unit failed due to extensive concrete damage and plate yielding. The formation of the diagonal tension field, the tearing and yielding of the plate around the connecting bolts and rebars buckling were clearly observed after removing the frame members and the damaged concrete at the end of the test, see Figure 3.42.

(a) unit P2

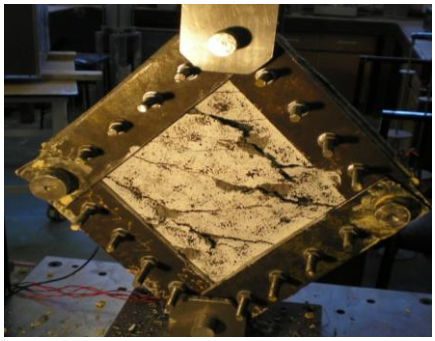

(b) unit P3

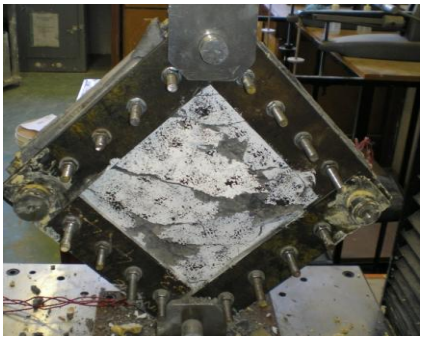

(c) unit P4

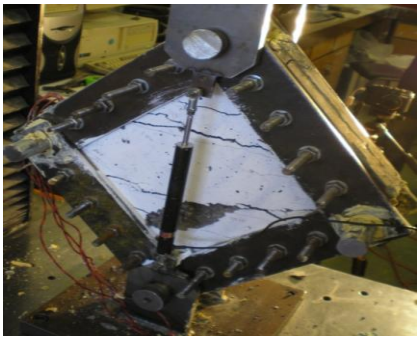

(d) unit P5

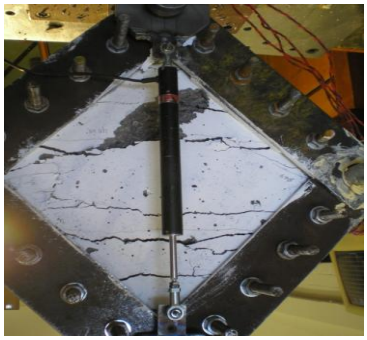

(e) unit P6

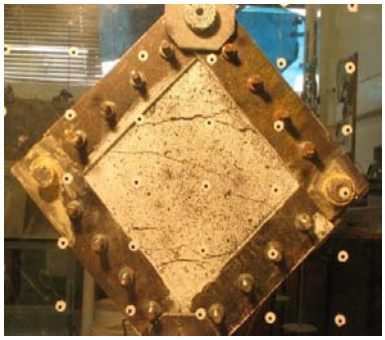

(f) unit P7

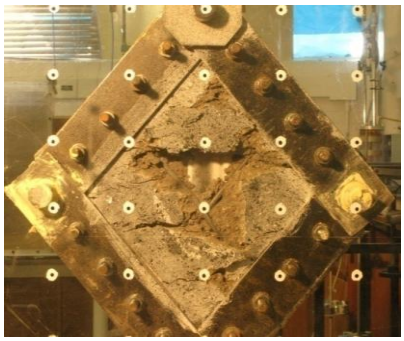

(g) unit P8

Figure 3.39 Encased-plate composite units form at failure

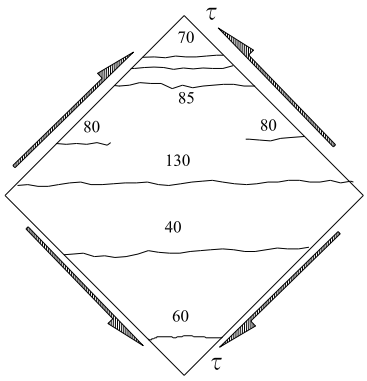

(a) unit P2

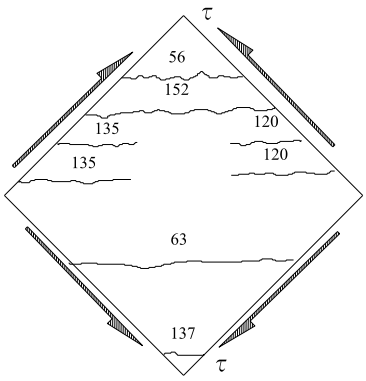

(b) unit P3

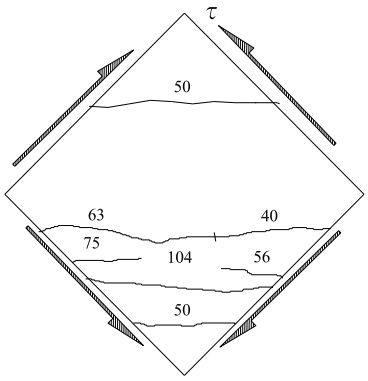

(c) unit P4

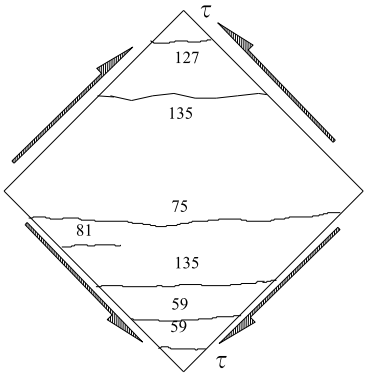

(d) unit P5

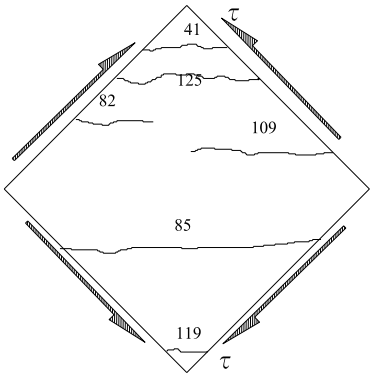

(e) unit P6

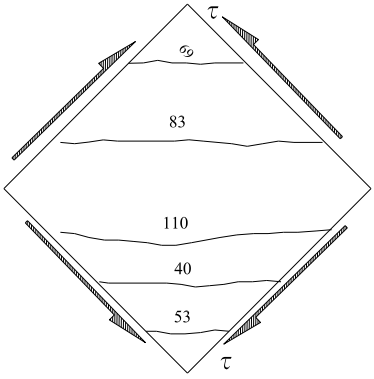

(f) unit P7

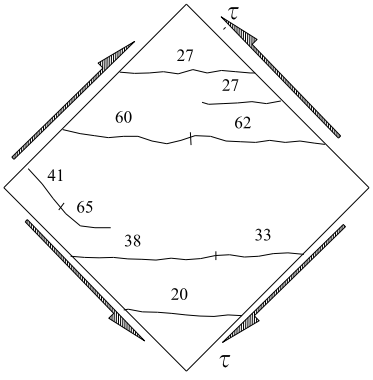

(g) unit P8

Figure 3.40 Crack pattern for encased-plate composite units

(load values represent diagonal load)

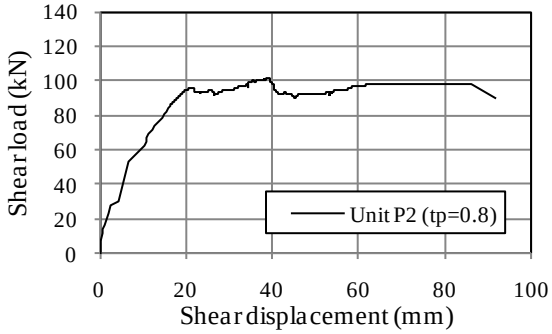

(a) unit P2

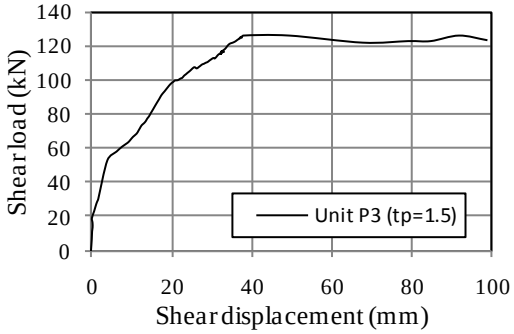

(b) unit P3

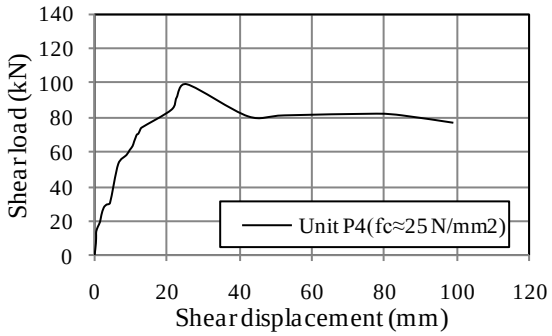

(c) unit P4

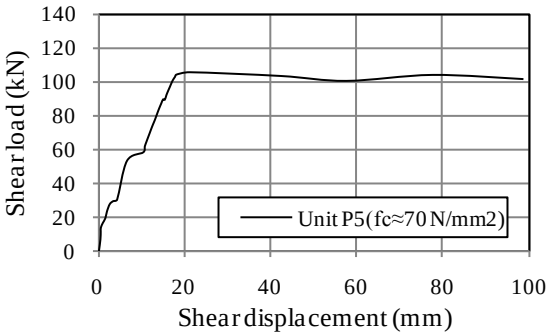

(d) unit P5

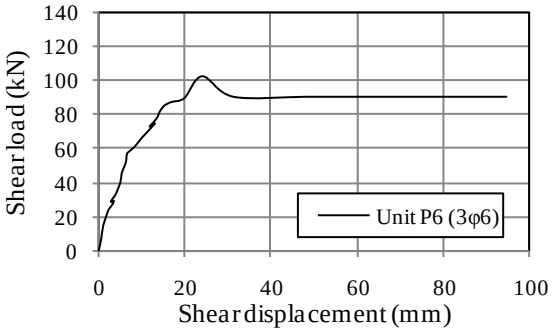

(e) unit P6

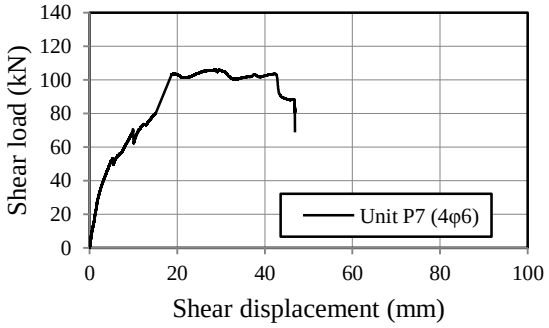

(f) unit P7

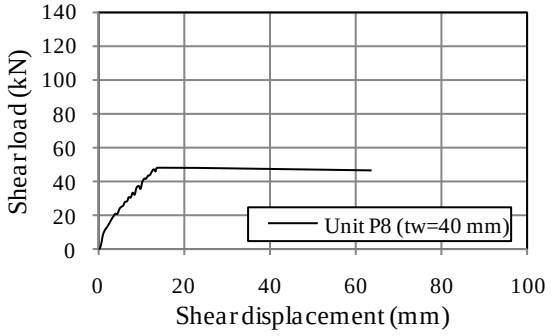

(g) unit P8

where:
t_p is the plate thickness
f_c is the concrete compressive strength
t_w is the unit thickness

Figure 3.41 Shear load-displacement behaviour of composite units

Table 3.6 Principal results obtained from composite test units

Test unit	Shear load at first cracking (kN)	Shear load at ultimate (kN)	Shear stress at first cracking (N/mm^2)	Shear stress at ultimate (N/mm^2)
P1	28.29	63.05	1.55	3.45
P2	28.29	102.05	1.55	5.58
P3	39.59	126.36	2.16	6.90
P4	28.29	99.71	1.55	5.45
P5	41.72	105.59	2.28	5.77
P6	28.99	102.53	1.58	5.60
P7	28.29	106.04	1.55	5.79
P8	14.14	48.29	1.16	3.96
S1	------	44.07	------	180.61
S2	------	64.07	------	140.04

Figure 3.42 Formation of diagonal tension field in composite units P2

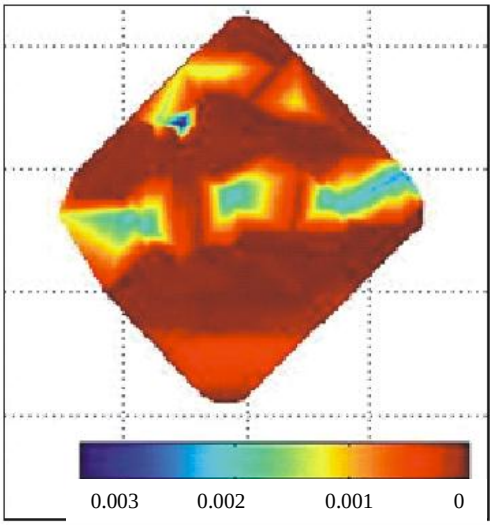

Figure 3.43 Typical distribution of cumulative maximum principal strains on concrete surface at failure (95 mm diagonal displacement) for composite units

Considerable ductility was demonstrated by the test unit before failure as depicted in Figure 3.41a, which illustrates the shear load-displacement behaviour of the unit. The demonstrated ductility is attributed to the yielding of rebars and the formation of diagonal tension field in the encased-plate.

The loss of concrete cover and the formation of diagonal tension field were also observed in the other composite units (P3-P7), with similar load-displacement behaviour; however, the cracking patterns were slightly different from that of unit P2 (see Figure 3.40).

The distribution of maximum principal strains on concrete surface and strain progression along the loaded diagonal and off-diagonal for composite unit P2 were almost the same as discussed for unit P1, see Figures 3.43 to 3.45.

Four internal strain gauges were attached to the rebars and encased-plate of unit P2 at the key positions as illustrated in Figure 3.17. Only three strain gauges (P1, P2 and R1) operated properly during the test. The variation of strain along and normal to the loaded diagonal in the encased-plate is illustrated in Figure 3.46a, while the strain development in a rebar is illustrated in Figure 3.46b. The figures suggest that tensile and compressive plate yielding was achieved at a shear load , F1, of 66.6 kN and that tensile rebar yielded at almost the same load value. The figures also showed a sudden change in strain in load range 21.21-35.35 kN, which coincided with the concrete's first visible cracking at 28.28 kN.

ii. Unit P8

Unit P8 had the same size as unit P2 except that concrete thickness was reduced to 40 mm from 60 mm for unit P2, providing an effective concrete cover to the plate of 19.6 mm. Unit P8 developed the first crack horizontally at a shear load of 14.14 kN, which was 50% lower than that of unit P2. The reduction in the first cracking load was mainly due to the decrease in concrete cross-section. As the diagonal load increased further, a series of horizontal cracks appeared parallel to the off-diagonal and cover spalling progressed gradually, see Figures 3.39g. The unit failed at 48.29 kN shear load due to significant concrete damage, allowing plate buckling and the formation of diagonal tension field in the plate. The unit's

ultimate load presented only 47% that of unit P2. Tearing and yielding around the connecting bolts, formation of diagonal tension field in the plate and buckling of rebars were also observed, as was observed in unit P2, Figure 3.42.

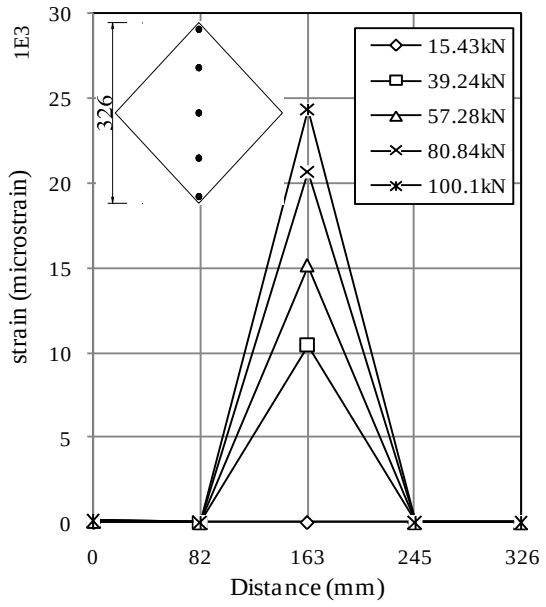

Figure 3.44 Typical average strain distribution along loaded diagonal-unit P2

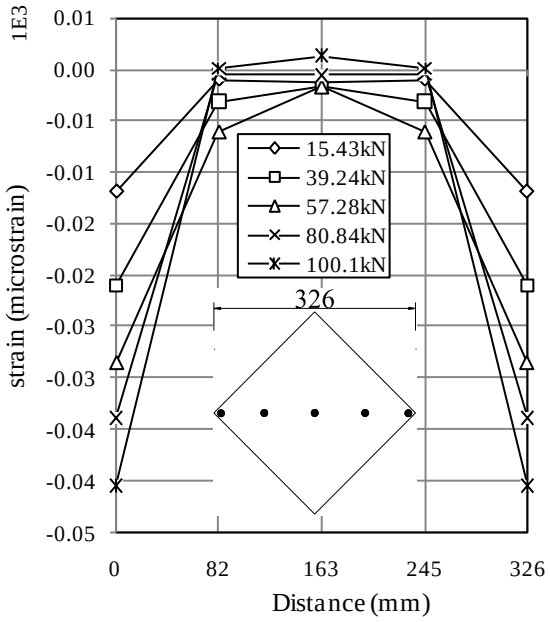

Figure 3.45 Typical average strain distribution along off-diagonal-unit P2

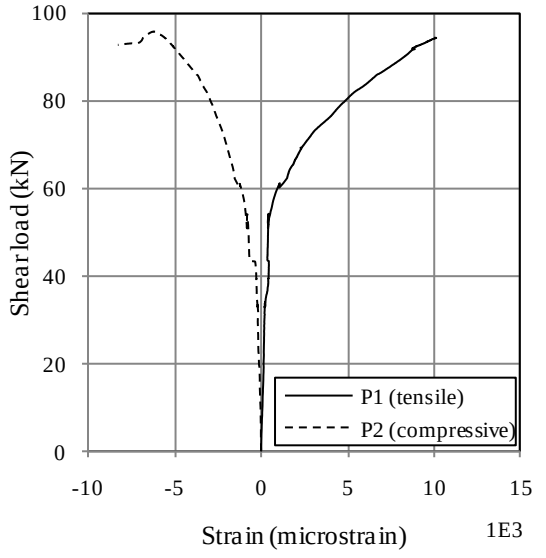

(a) Encased-plate

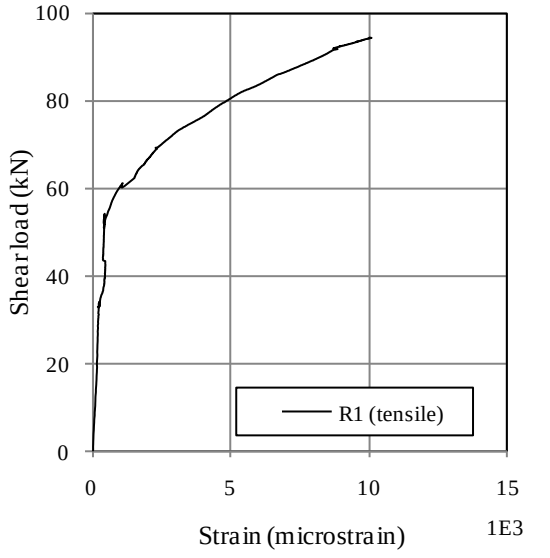

(b) Rebars

Figure 3.46 Variation of strains in the reinforcement of unit P2

3.7 Analysis and discussion of experimental results

3.7.1 Comparison between response of individual components and composite wall

Due to the interaction between the encased-plate and the surrounding concrete, the behaviour of composite wall was found different from the behaviour of its individual components. The shear load-displacement behaviour of composite units P2 and P3 is compared to the behaviour of their individual components in Figure 3.47. The initial stiffness and ultimate load of the composite units and their individual components are presented in Table 3.7 and Figures 3.48 and 3.49.

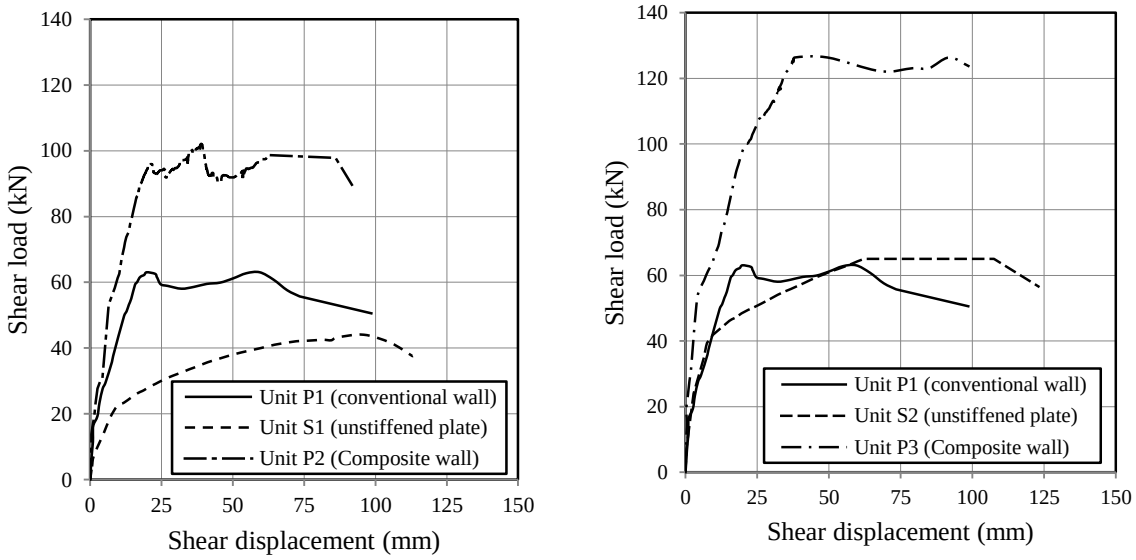

(a) Unit P2 (b) Unit P2

Figure 3.47 Comparative study of shear load-displacement behaviour

In both composite units, the initial stiffness was higher than the sum of their individual components. The composite units achieved 23.3 and 49.1% increase in the initial stiffness compared to the sum of the initial stiffness of their individual components for units P2 and P3, respectively as shown Figure 3.48 and Table 3.7. However, no improvement was achieved in the load carrying capacity (Figure 3.49 and Table 3.7).

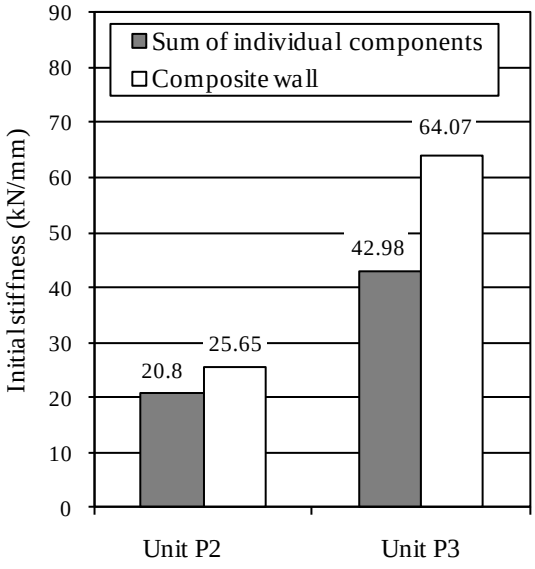

Figure 3.48 Comparison of initial stiffness

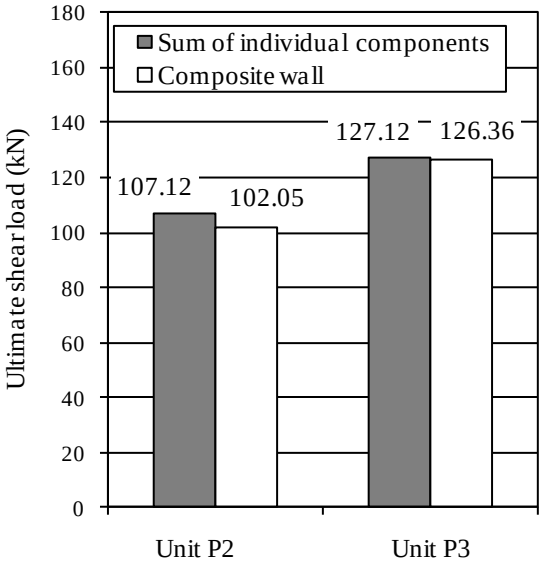

Figure 3.49 Comparison of ultimate load

Table 3.7 Initial stiffness and ultimate load of composite units and their individual components

(a) Unit P2

	Initial stiffness (kN/mm)	Ultimate shear load (kN)
Conventionally-reinforced unit (unit P1)	14.56	63.05
Unstiffened plate (unit S1)	6.24	44.07
Sum of individual components	20.80	107.12
Composite unit (unit P2)	25.65	102.05
Enhancement (%)	23.31	-4.74

(b) Unit P3

	Initial stiffness (kN/mm)	Ultimate shear load (kN)
Conventionally-reinforced unit (unit P1)	14.56	63.05
Unstiffened plate (unit S2)	28.42	64.07
Sum of individual components	42.98	127.12
Composite unit (unit P3)	64.07	126.36
Enhancement (%)	49.06	-0.50

The ultimate load of unit P3 was almost equal to the sum of the ultimate load of its individual components, while the ultimate load of unit P2 was 4.7% less than the sum of the ultimate load of its individual components, see Figure 3.49 and Table 3.7. One possible reason for this reduction is the difference in the yield stress of the encased-plates used in composite unit and unstiffened plate. The yield stress of the encased-plate in unit P2 was 239 N/mm^2, which was 4.2% lower than the yield stress of the unstiffened plate of unit S1 (249 N/mm^2). The difference in yield stress had only an impact on the ultimate load, but not the stiffness since they have almost the same value of modulus of elasticity.

3.7.2 Failure mechanisms

A. Unstiffened plates

To investigate the failure mechanism of an unstiffened plate tested under pure in-plane shear, consider the unstiffened plate depicted in Figure 3.50. The diagonal force, F, is resolved into two equal forces, F_1, which produces a shear stress, τ, on any element of the plate. Since the plate is subjected to pure shear, the principal tensile stress, $\sigma_{t,}$ and the principal compressive stress, σ_c, are equal to the shear stress, τ, and coincide with the vertical and horizontal directions, respectively. As the diagonal load increases, the shear stress, τ, increases correspondingly until the critical buckling stress of the plate is reached, leading to plate buckling. Plate buckling is characterised by out-of-plane displacement and formation of a diagonal tension field in the plate. Beyond plate buckling, the compressive principal stress, σ_c, would not increase any further, while the plate could sustain more load until the tensile principal stress, σ_t, reached the material yield stress. At this point, no more load could be sustained by the plate and failure would take place.

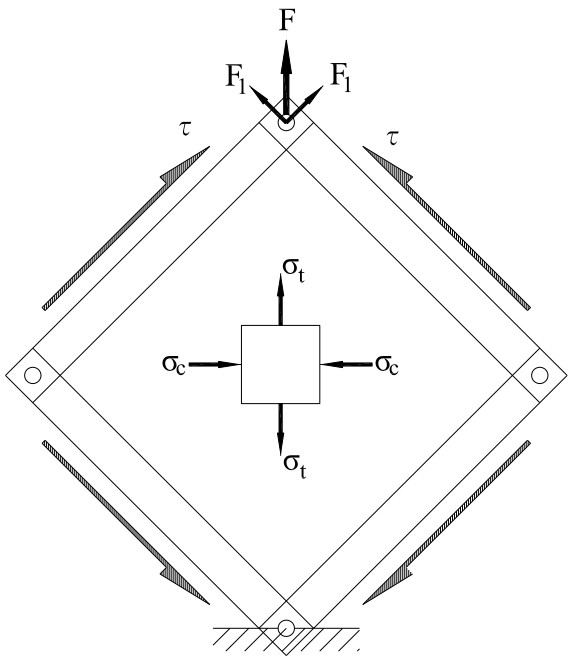

Figure 3.50 Failure mechanism for unstiffened plates

B. Encased-plate composite walls

The behaviour of encased-plate composite walls under pure in-plane shear may be explained as follows:

- Consider the composite wall shown in Figure 3.51a. The wall is reinforced with a plate and a uniformly-distributed rebar grid in both directions as shown in Figure 3.51b, and is subjected to shear force, F_1, which produces a shear stress, τ, on the unit edges.
- The shear force, F_1, acting on section A-A is resisted by the encased-plate and the reinforced concrete depending on their relative stiffness. The shear force, F_1, is equal to the sum of the forces resisted by the plate, P_s, and the reinforced concrete, P_c (Figure 3.51c).
- At an early stage of loading and while concrete is still uncracked, the rebars and concrete provide lateral support to the plate and prevent its buckling, Figure 3.51c. At this stage, both the reinforced concrete and the plate fully contribute to the load

carrying capacity and the stiffness of the composite wall, thus the initial stiffness is significantly higher than the sum of its components, see Table 3.7.

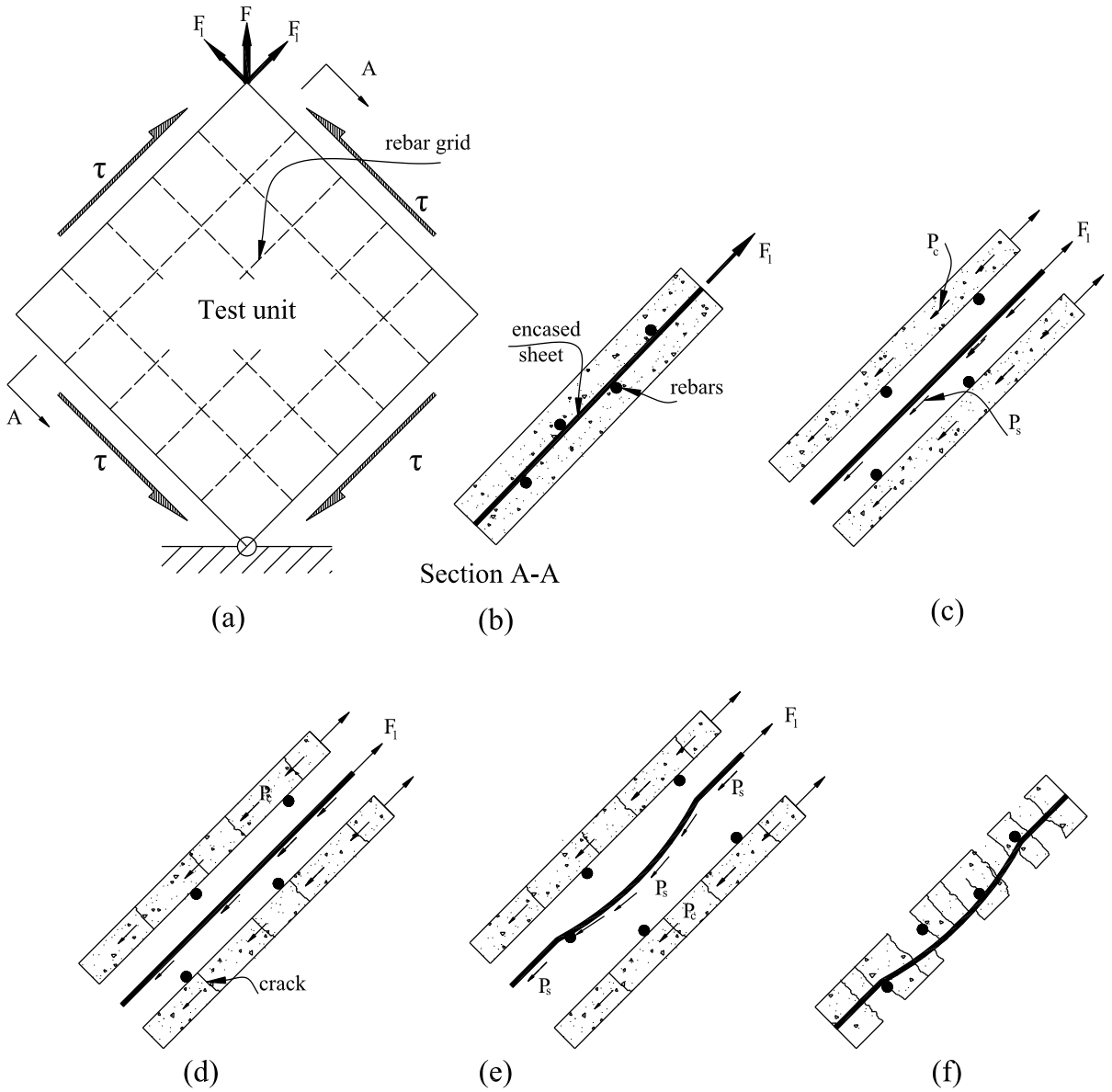

Figure 3.51 Failure mechanism for encased-plate composite walls under pure in-plane shear

- As the load is increased, the concrete starts cracking leading to sudden reduction in stiffness. Additional loading results in development of more cracks, widening of existing cracks and yielding of rebars. At this stage, the plate tensile principal stress, σ_t,

reaches the material yield, Figure 3.51d. However, concrete was still strong enough to prevent plate buckling, and the composite unit was able to undergo large plastic deformations under the maximum load level.

- After the achievement of maximum load, extensive cracking weakens the concrete and makes it unable to prevent the buckling of the thin plate, Figure 3.51e. Plate buckling is usually associated with out-of-plane movement. This movement alters the path of load carried by the plate, P_s, see Figure 3.51e. Beyond plate buckling, the plate compressive principal stress, σ_c, could not increase any further. This out-of-plane movement leads to cover damage, peeling and development of tension field in the plate as shown in Figure 3.51f.
- Failure of the composite unit is associated with extensive concrete damage, yielding of rebars and formation of a diagonal tension field in the encased-plate. The suggested failure mechanism highlights the potential importance of the interaction between the encased-plate and the surrounding concrete, and the lateral support provided by the concrete and rebars to the plate.
- The failure mechanism also suggests that if the concrete cover to the plate is insufficient, it would not be able to prevent plate buckling, leading to cover peeling and a premature failure. Also, the mechanism suggests that there is strain compatibility between the plate and concrete during loading prior to failure, and the assumption of full bond can be considered reasonable.

3.7.3 Comparative study to determine effects of experimental parameters

Comparison between the experimental results obtained from testing eight wall units under pure in-plane shear is given in Table 3.8. The table also provides a comparison of the initial stiffness and ultimate load values for each unit relative to the control unit. The results were

divided into four series, in the first series unit P1 (conventionally-reinforced) acted as the control unit, while composite unit P2 acted as the control unit in the remaining series.

Table 3.8 Principal results obtained from test units

Series	(1)			(2)		(3)		(4)
Test unit	P1	P2	P3	P4	P5	P6	P7	P8
Initial stiffness (kN/mm)	14.56	25.65	64.07	24.21	24.63	24.53	26.76	8.22
Initial stiffness as percentage of control (%)	100	176.17	440.05	94.39	96.02	96.11	103.89	32.04
First cracking load (kN)	28.29	28.29	39.59	28.29	41.72	28.99	28.29	14.14
First cracking load as percentage of control (%)	100.00	100.00	139.94	100.00	147.47	102.47	100.00	49.98
Ultimate load (kN)	63.05	102.05	126.36	99.71	105.59	102.53	106.04	48.28
Ultimate load as percentage of control (%)	100	161.86	200.41	97.71	103.47	100.47	103.91	47.31
Shear stress at first cracking (N/mm^2)	1.55	1.55	2.16	1.55	2.28	1.55	1.55	0.77
shear stress at ultimate(N/mm^2)	3.44	5.58	6.91	4.64	5.77	5.60	5.79	2.64

A. Plate thickness

The plate thickness was varied on a limited range from 0 to1.5 mm, due to the limited load capacity of the test machine (250 kN). The shear load-displacement behaviour of units with different plate thickness values is depicted in Figure 3.52, while the variation of initial stiffness and ultimate load values are clearly described in Figures 3.53 and 3.54. The figures suggest that the plate provided a substantial contribution to the section stiffness. Moreover, the general trend of increasing the initial stiffness and ultimate load capacity as the plate thickness increased is clearly shown. The initial stiffness attained improvement in the order of 76.2 and 340.1% in composite units with 0.8 and 1.5 mm thick plates, respectively, compared to the conventionally-reinforced unit P1, see Table 3.8. Similarly, higher shear carrying capacity was achieved by composite units as expected. In particular,

the ultimate load increased by 61.9 and 100.4% for composite units with 0.8 and 1.5 mm thick plates, respectively, compared to unit P1. In the same way, the shear strength considerably improved from 3.4 N/mm^2 in conventionally-reinforced unit, P1, to 5.6 and 6.9 N/mm^2 for units P2 and P3 reinforced with 0.8 and 1.5 mm thick plates, respectively, see Table 3.8. These results highlight the benefits gained from using steel plates as reinforcement in shear-dominated structures and agree well with the results obtained for encased-plate construction in beams (Subedi and Baglin 1999; Su *et al.* 2009).

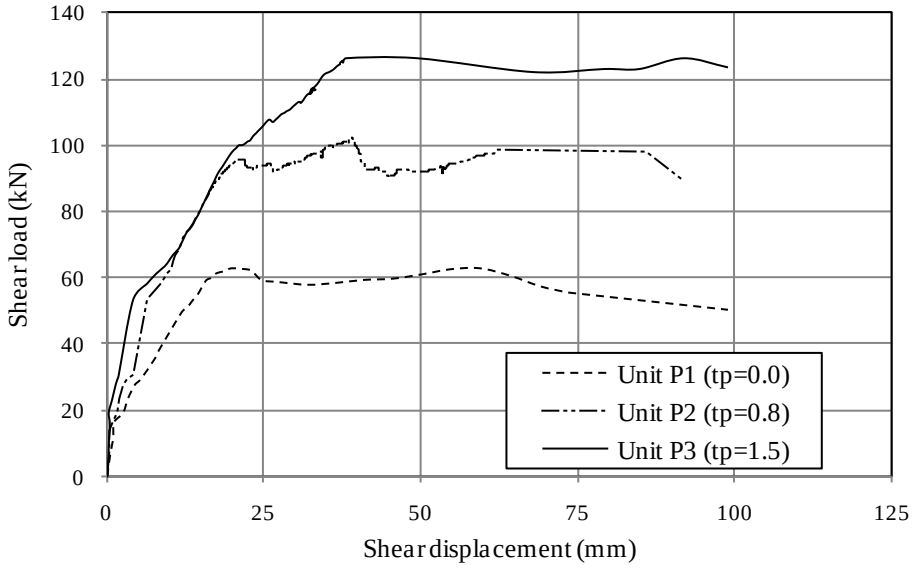

Figure 3.52 Shear load – displacement behaviour of units with different plate thickness

B. Concrete strength

To study the effect of concrete strength on the behaviour of encased-plate composite walls under pure shear, three units, P4, P2 and P5, were considered. The units were manufactured from three concrete mixes producing characteristic strength value of 25, 40 and 70 N/mm^2 at 28 days, respectively. The behaviour of the units was similar during the whole course of the loading. The shear load-displacement behaviour of the three units is depicted in Figure 3.55. Comparisons of initial stiffness and ultimate load values of the units are depicted in Figures 3.56 and 3.57, respectively. The figures show that concrete strength had no

significant effect on either the initial stiffness or the ultimate load carrying capacity. Concrete strength had only an impact on the initiation of first cracking. For example, increasing the concrete strength from 25 to 70 N/mm^2 increased the first crack load by 47.5% (from 28.3 kN for unit P4 to 41.7 kN for unit P5), see Table 3.8.

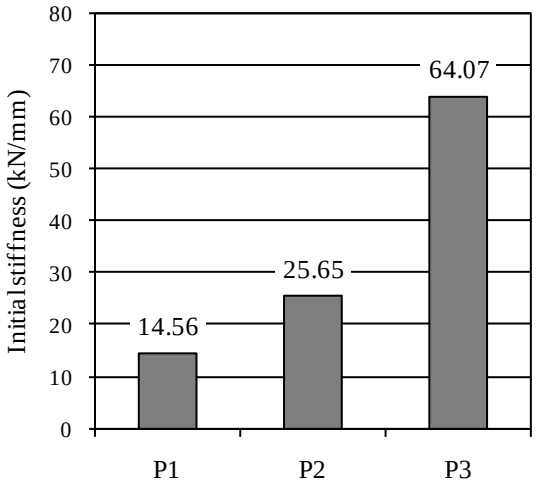

Figure 3.53 Variation of initial stiffness for walls with varying plate thickness values

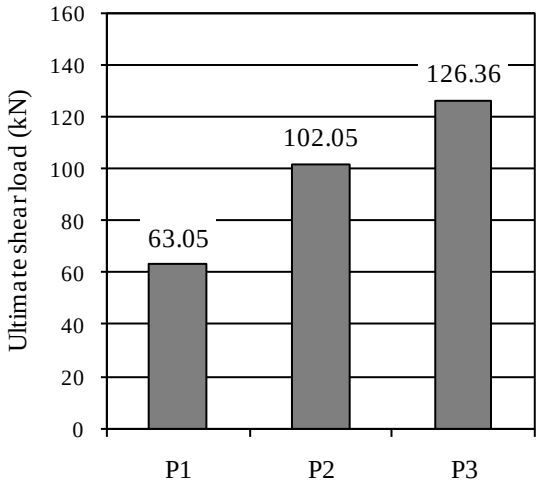

Figure 3.54 Variation of ultimate shear load for walls with varying plate thickness values

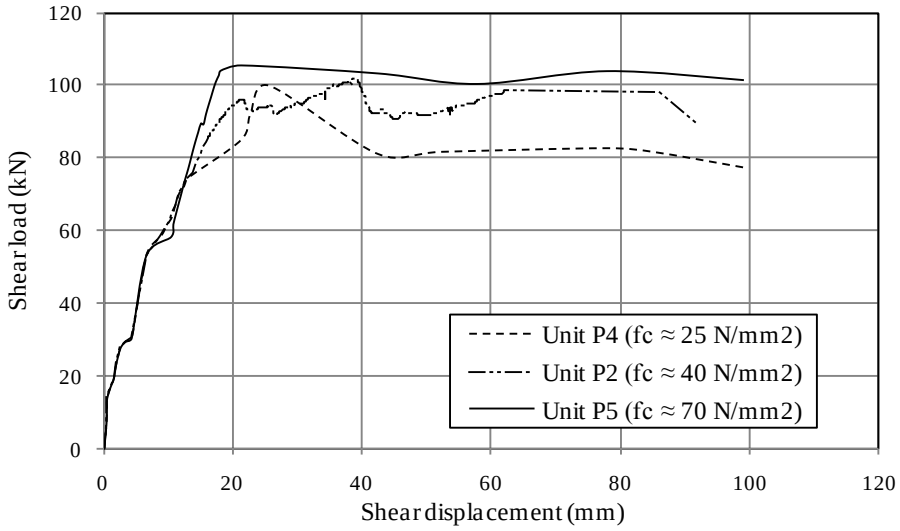

Figure 3.55 Shear load – displacement behaviour with varying concrete strength

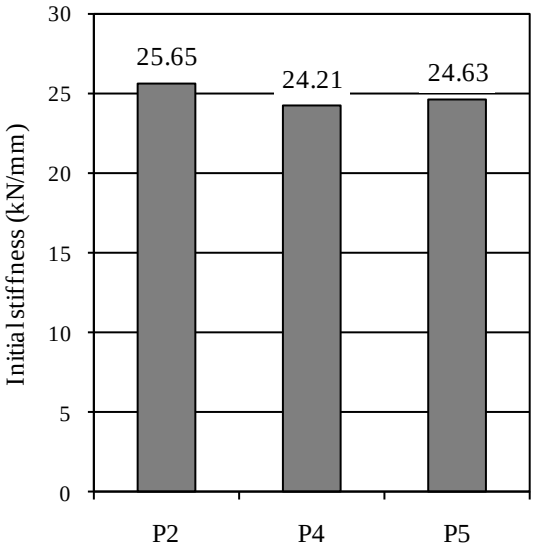

Figure 3.56 Variation of initial stiffness for walls with varying concrete strength values

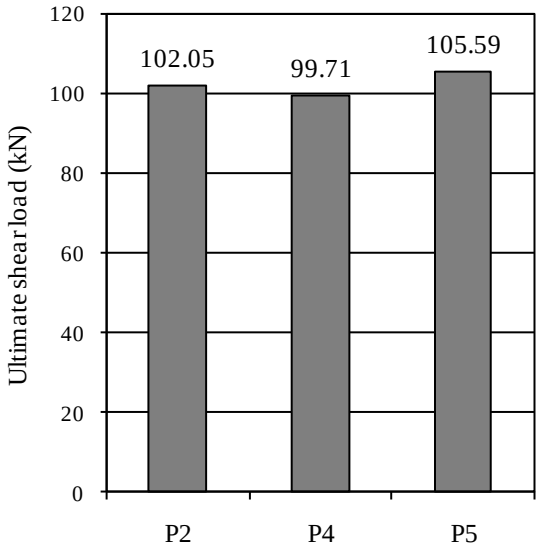

Figure 3.57 Variation of ultimate shear load for walls with varying concrete strength values

C. Reinforcement content

The composite units P2, P6 and P7 were reinforced with a uniformly-distributed grid of 2Ø6, 3Ø6 and 4Ø6, respectively in both directions, and were considered to study the effect of reinforcement content on the behaviour of encased-plate composite walls under pure in-plane shear. All the units exhibited almost the same response under the applied diagonal load. The shear load-displacement behaviour of the three units is depicted in Figure 3.58, and comparisons of initial stiffness and ultimate load values of the units are depicted in Figures 3.59 and 3.60. Despite the increase in the reinforcement content from 0.31 to 0.62%, the initial stiffness and the load carrying capacity were only slightly increased by 3.9 and 6.0% for unit P7, respectively, see Figures 3.59 and 3.60. These results show that increasing the reinforcement content appeared to have little effect on the behaviour of encased-plate composite walls tested under in-plane pure shear and the behaviour was dominated by the encased-plate.

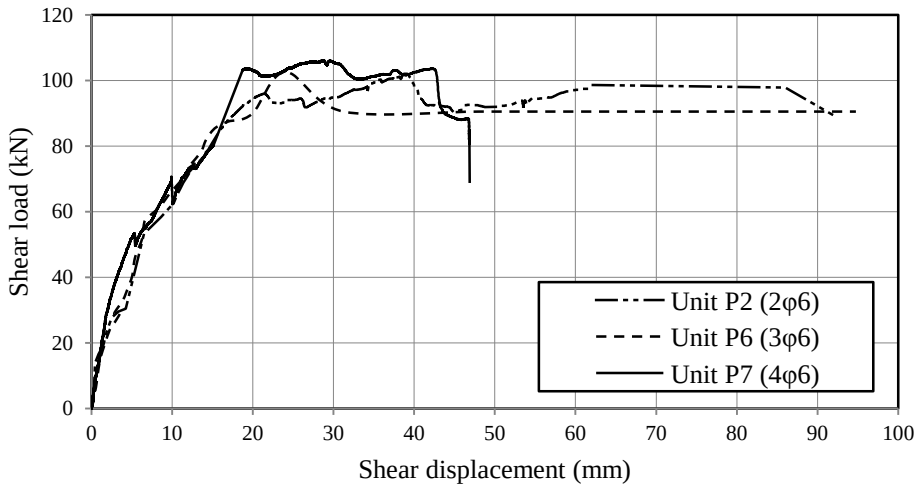

Figure 3.58 Shear load – displacement behaviour with varying reinforcement content

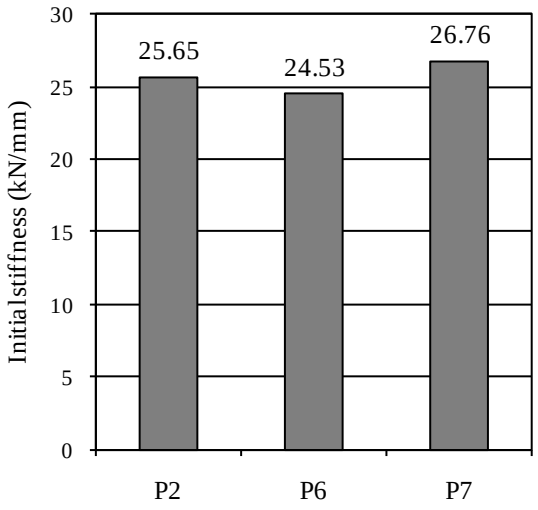

Figure 3.59 Variation of initial stiffness for walls with varying reinforcement content

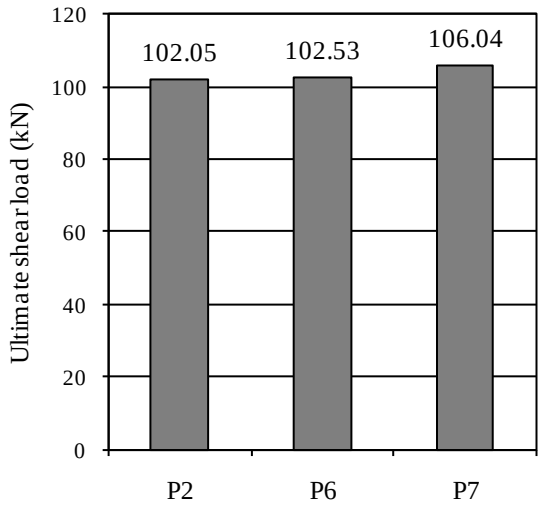

Figure 3.60 Variation of ultimate shear load for walls with varying reinforcement content

D. Wall thickness

Contrary to the satisfactory performance of unit P2, unit P8, which had a smaller concrete thickness, could only develop 47.3% of the shear capacity of unit P2 and could sustain relatively low deformations. Concrete cover to the plate appears to play a vital role governing the behaviour of encased-plate walls. Sufficient cover to the plate is required to

prevent the buckling of thin plate, and hence maintain both the plate and the concrete without significant damage under high load levels. Unit P8, which had smaller wall thickness, failed prematurely due to extensive damage of concrete cover, early plate buckling and formation of diagonal tension field.

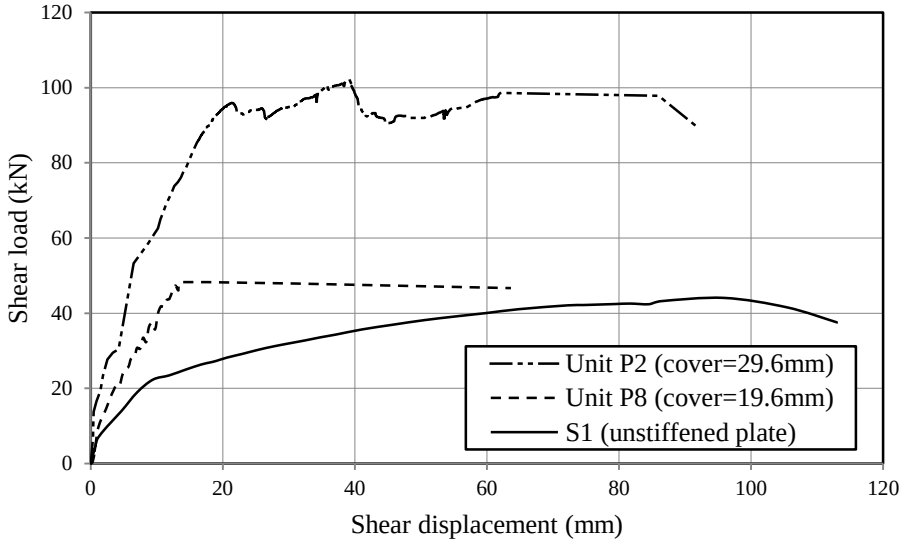

Figure 3.61 Comparative shear load –displacement behaviour with respect to concrete cover

The shear load-displacement behaviour of composite units P2, P8 and unstiffened plate unit S1 are superimposed in Figure 3.61. The initial stiffness of unit P8 was 31.7% higher than that of the unstiffened plate S1, and 68% lower than that of the 60 mm thick unit, P2, see Figure 3.62 and Table 3.8. This result implies that the initial stiffness of the unit was mainly provided by the unstiffened plate and the reinforced concrete only provided about one-third of the initial stiffness. Similarly, the unstiffened plate provided 90% of the unit's ultimate load with concrete contributing only the remaining 10%. Moreover, the ultimate load of unit P8 was 53% lower than that of unit P2, see Figure 3.63. This shows that in encased-plate composite walls, improper selection of concrete cover to the plate not only

adversely affects the stiffness and ductility, but also prevents the development of full load-carrying capacity of the wall. Therefore, precautions must be taken in the design of encased-plate composite walls in respect of concrete cover to the plate to prevent the undesirable premature failure and to allow the full utilisation of the cross-section.

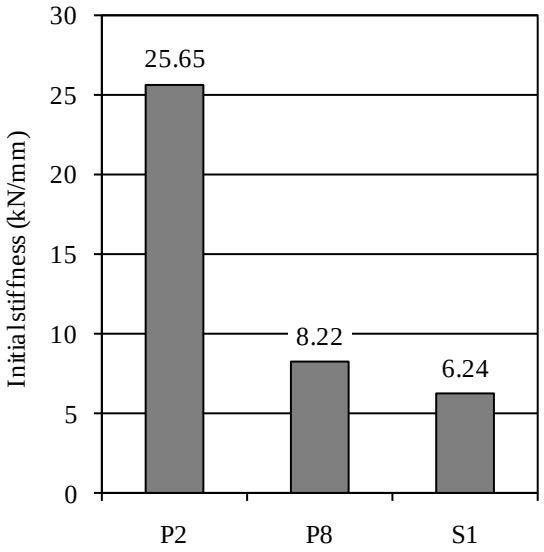

Figure 3.62 Comparative comparison of initial stiffness

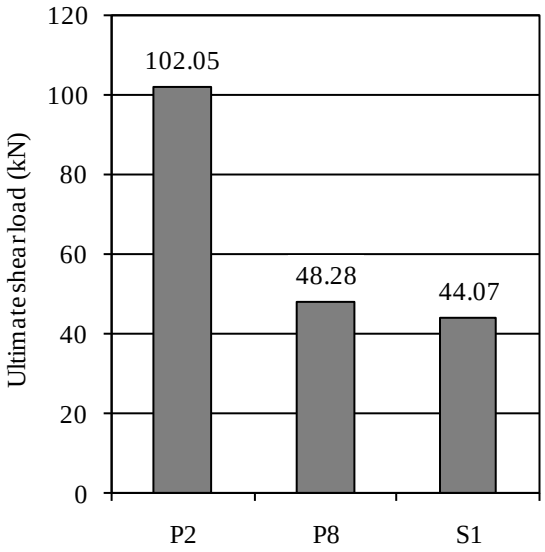

Figure 3.63 Comparative comparison of ultimate shear load values

3.8 Summary and conclusions

This chapter discussed the in-plane shear behaviour of encased-plate composite structural walls. A special test rig was designed and fabricated to test unstiffened plates, conventionally-reinforced and encased-plate composite wall units. The rig proved its suitability to apply pure shear loading on small-scale models.

The behaviour of composite walls was different from its individual components due to the interaction between the encased-plate and the concrete. While the initial stiffness of the composite wall was significantly higher than that of its individual components, no improvement was achieved in the ultimate load carrying capacity with composite action.

Common failure mechanisms for unstiffened plates and composite walls under in-plane shear were suggested and discussed in detail.

Four parameters were included in the experimental study including the plate thickness, the concrete strength, the reinforcement content and the wall thickness. Only the concrete cover to the plate and the plate thickness had a considerable effect on the behaviour of composite walls under pure in-plane shear. Based on the above results, plate thickness was selected as a parametric study on the behaviour of encased-plate composite structural walls under lateral loading in the next two chapters.

The test programme used a full-field deformation measurement system based on digital photogrammetry and particle image velocimetry (PIV). The performance of the technique was assessed against the experimental results obtained from the testing of units, and showed its success in monitoring concrete displacement.

Chapter 4 Encased-plate composite walls under lateral loading-experimental methodology

4.1 Overview

In the framework of the preliminary investigations to study the behaviour of encased-plate composite walls under lateral loading, tests were carried out on seven specimens. This Chapter presents the details of the test programme, including details of specimens, material properties, manufacturing process, test setup, instrumentation and test procedure. The specimens represented the critical storey element of a structural wall system with a scale of approximately 1:5 of a prototype structural wall in a multi-storey building.

4.2 Specimen nomenclature

Each specimen was noted by four characters; the first two characters (***EW***) indicating Encased Wall, the third representing the group number and the last indicating the specimen number. For example, EW22 represents an encased-plate wall in the second group with a specimen number 2.

4.3 Test specimens

In this research, steel plates of different thickness values were embedded in conventionally-reinforced concrete wall specimens. The specimens were designed to fail in either a shear or flexural mode. Depending on the results obtained from investigating the behaviour of encased-plate composite walls under pure in-plane shear described in Chapter 3, the main parameter included in this study was the plate thickness. Seven specimens were tested under monotonically increased static lateral loading and identified as EW11, EW12, EW13, EW21, EW22, EW23 and EW31. Two types of walls were tested in the experimental programme; Type 1 (flanged walls) and Type 2 (rectangular walls). The specimens were divided into three groups including,

three flanged specimens in the first group (EW11, EW12 and EW13), three rectangular specimens in the second group (EW21, EW22 and EW23); all six specimens were designed to fail in shear. In the last group, only one rectangular specimen (EW31) was designed to fail in flexure. Conventionally reinforced concrete walls were designed according to the ACI (2008) method on the shear design of walls.

4.4 Specimens dimensions

Generally, the specimens consist of a central panel bounded by two boundary elements. The boundary elements are usually in two forms, either apparent or concealed columns. The boundary elements usually have concentration of longitudinal reinforcement to provide resistance against flexure.

The specimens in the first and second groups represented squat walls that had height-to-width ratio of 1, and were designed to fail in shear. The geometric dimensions of wall specimens in the first group were identical; 750 mm long × 750 mm wide, and the walls were monolithically connected to a stiff beam and a base block as shown in Figure 4.1. Two boundary elements (750 mm long × 160 mm wide × 70 mm thick) were constructed at the ends of each wall simulating columns or cross-walls that may exist at the ends of a wall in a real structure. The clear dimensions of the central panel were 750 mm in length, 610 mm in width and 60 mm in thickness. The walls were connected to a stiff beam (750 mm long × 200 mm deep × 200 mm thick), which acted as the element through which lateral loads were applied to the walls. Due to lab constraints, the walls were tested in a horizontal position and cantilevered from a heavily reinforced base block (1400 mm long × 1200 mm deep × 400 mm thick) which was utilised to clamp down the specimen to the laboratory strong floor, simulating a rigid foundation. Specimen EW11 was conventionally-reinforced and acted as control specimen, while

specimens EW12 and EW13 were reinforced with a grid of longitudinal and transverse rebars and steel plates with thickness of 0.8 and 1.5 mm, respectively.

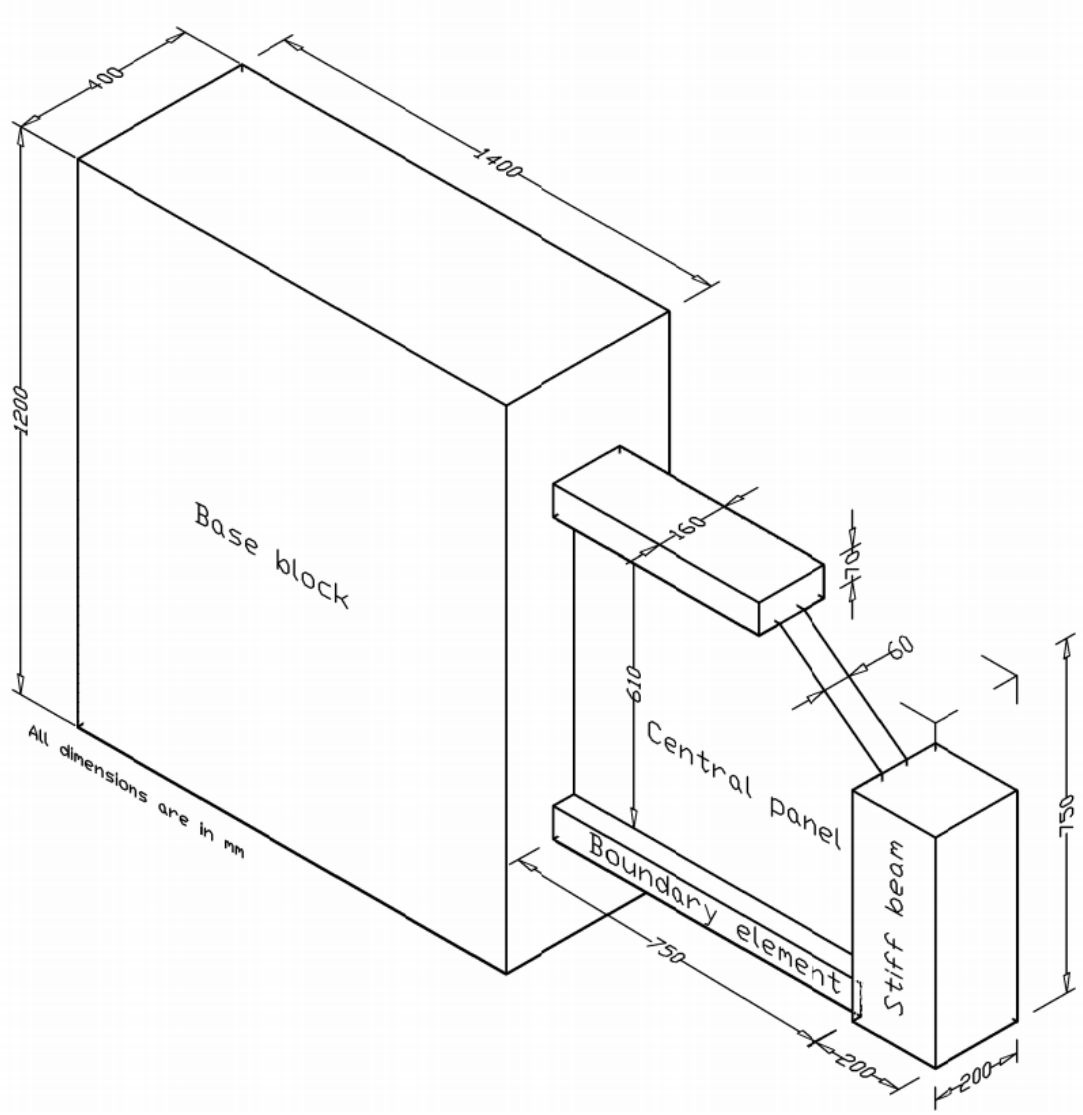

Figure 4.1 Typical details of all specimens in first group

In the second group, three identical rectangular walls with dimensions of 750 mm long × 750 mm wide × 70 mm thick were constructed. In order to reduce the quantity of cast concrete, reinforcement preparation, time and labour, the base block in the first group was replaced with a footing with smaller dimensions in the second and third groups, see Figures 4.2 and 4.3. The footing had a square cross-section with dimensions of 300 mm long x 1200 mm deep x 300 mm thick. This change required a change in the test setup for these specimens as described in Section 4.9.2. All the specimens in this group were designed to fail in shear. Specimens EW22, EW23 were reinforced with steel plates of

0.8 and 1.5 mm thick, respectively, as well as a reinforcement grid, while specimen EW21 was conventionally-reinforced and acted as control specimen.

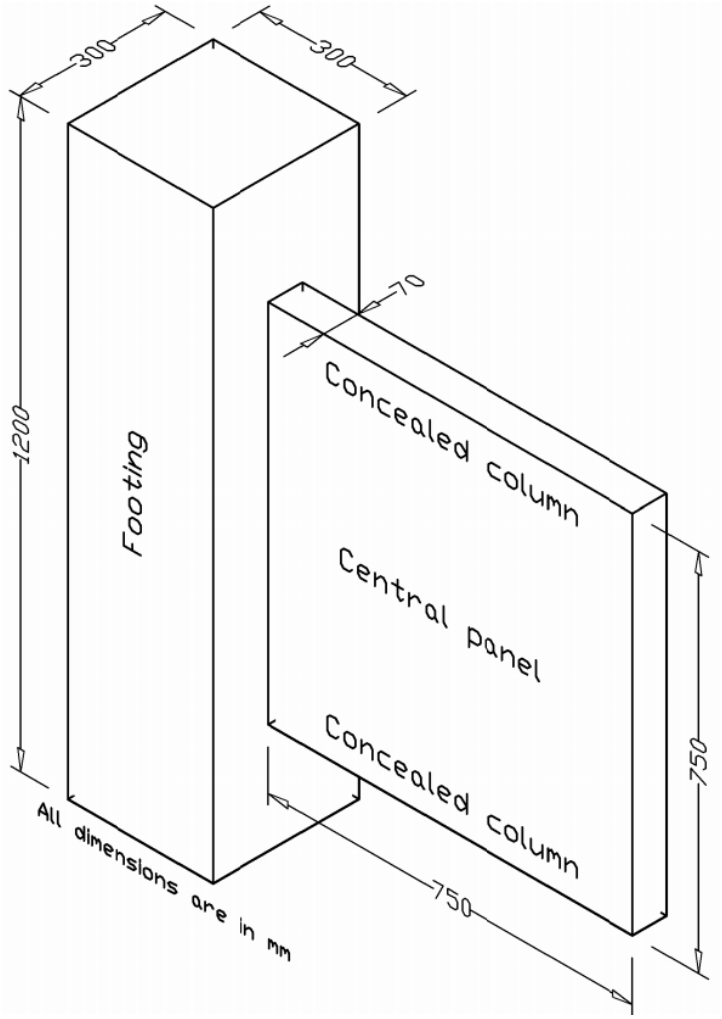

Figure 4.2 Typical details of all specimens in second group

One rectangular wall specimen with height to width ratio of 1.67 (1000 mm long × 600 mm wide × 45 mm thick) was constructed in the third group, Figure 4.3. The wall was designed to fail in flexure and was reinforced with 1 mm thick steel plate. The dimensions of all test specimens are summarised in Table 4.1.

4.5 Reinforcement plan

4.5.1 Rebars

The reinforcement of the central panel consisted of 6 mm diameter plain rebars uniformly distributed longitudinally and transversely. For the first and second group, 12

mm diameter rebars were used as longitudinal reinforcement in the boundary elements and confined with additional 6 mm diameter hoops. In the third group, 6 mm diameter plain rebars were used as main reinforcement and no additional hoops were provided. Reinforcement details were kept the same for all specimens within each group. Main reinforcing rebars were provided with 90-degree hooks at their ends to prevent slippage before reaching their full tensile strength. Anchorage lengths were calculated according to Eurocode 2 (2008). Figures 4.4 to 4.6 present the reinforcement configuration for all seven specimens.

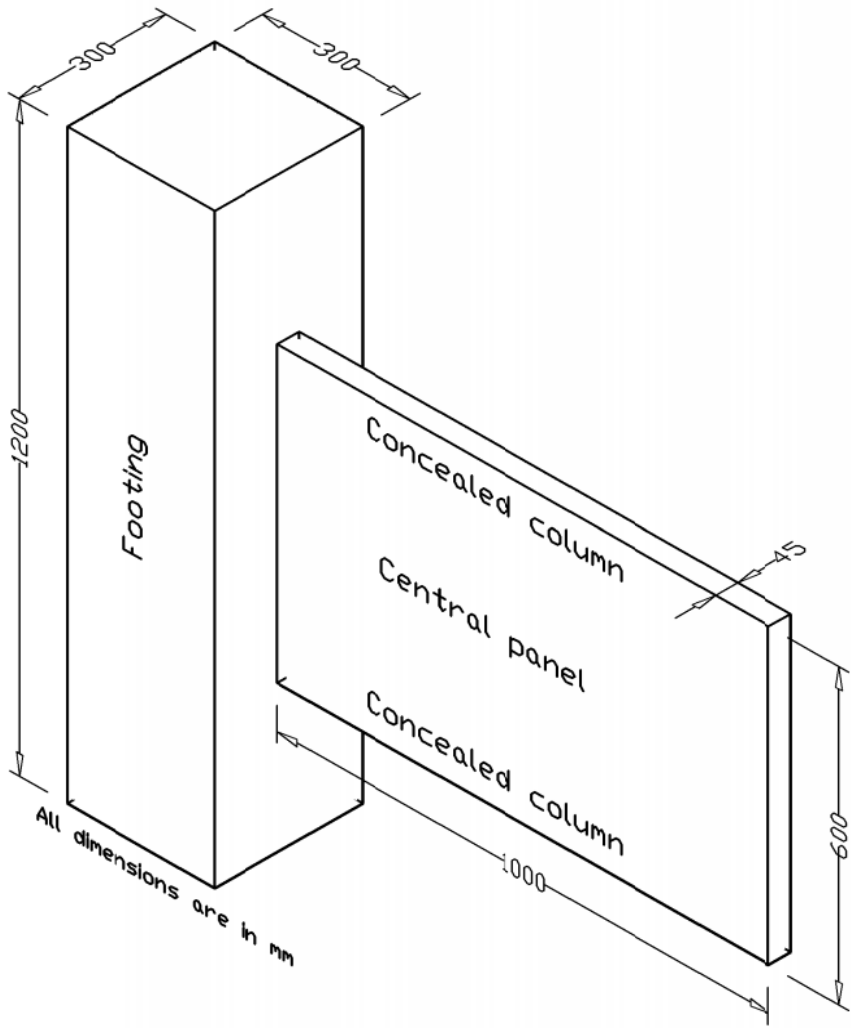

Figure 4.3 Details of specimen EW31

Table 4.1 Details of experimental programme

Details				Specimen						
				EW11	EW12	EW13	EW21	EW22	EW23	EW31
Geometric dimensions	Boundary elements	Length (mm)		750	750	750	----	----	----	----
		Width (mm)		160	160	160	----	----	----	----
		Thickness (mm)		70	70	70	----	----	----	----
	Central panel	Length (mm)		750	750	750	750	750	750	1000
		Width (mm)		610	610	610	750	750	750	600
		Thickness (mm)		60	60	60	70	70	70	45
Reinforcement layout	Boundary elements	Longitudinal	Rebars	4Ø12	4Ø12	4Ø12	6Ø12	6Ø12	6Ø12	2Ø6
			ρ_{flex} (%)	4.04	4.04	4.04	6.46	6.46	6.46	1.97
		transverse	rebars	7Ø6	7Ø6	7Ø6	22Ø6	22Ø6	22Ø6	----
			ρ_c (%)	1.97	1.97	1.97	5.24	5.24	5.24	----
	Central panel	Longitudinal	Rebars	4Ø6	4Ø6	4Ø6	7Ø6	7Ø6	7Ø6	5Ø6
			$\rho_{long,}$ (%)	0.31	0.31	0.31	0.63	0.63	0.63	0.67
		transverse	Rebars	3Ø6	3Ø6	3Ø6	11Ø6	11Ø6	11Ø6	10Ø6
			$\rho_{trans,}$ (%)	0.38	0.38	0.38	1.18	1.18	1.18	1.26
	Plate	thickness (mm)		0	0.8	1.5	0	0.8	1.5	1
		$\rho_{s,}$ (%)		0	1.23	2.3	0	1.06	2	2.11

Note:
ρ_{flex} = ratio of main flexural reinforcement to gross concrete area of boundary element;
ρ_c = ratio of effective volume of confinement reinforcement to the volume of the core;
ρ_{long}= ratio of longitudinal web reinforcement to gross concrete area of cross-section of wall panel;
ρ_{tran} = ratio of transverse reinforcement to gross concrete area of wall panel;
ρ_s = ratio of plate area to gross concrete area of wall section.

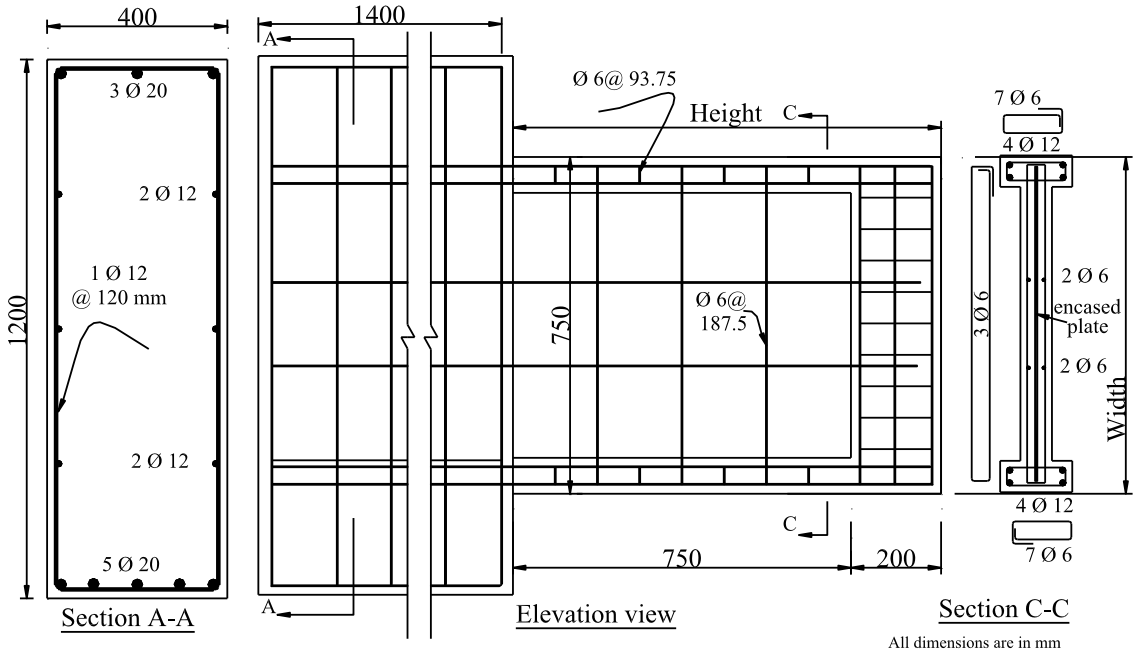

Figure 4.4 Reinforcement details of first specimen group

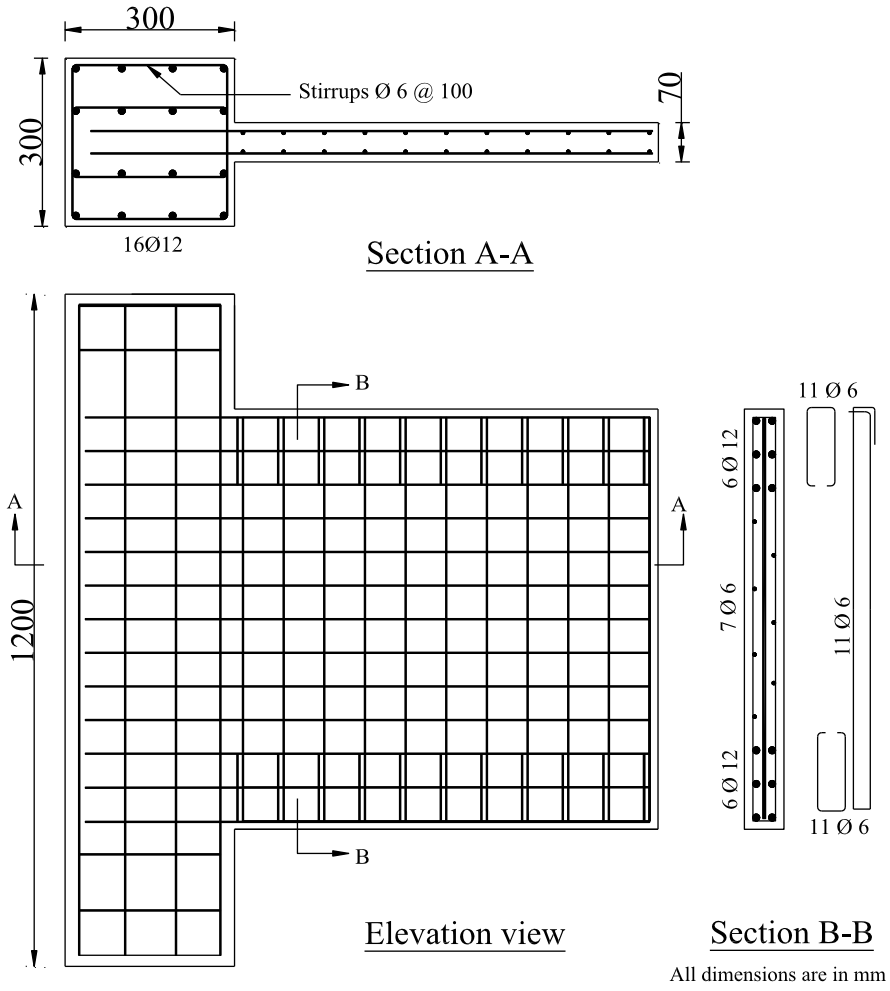

Figure 4.5 Reinforcement details of second specimen group

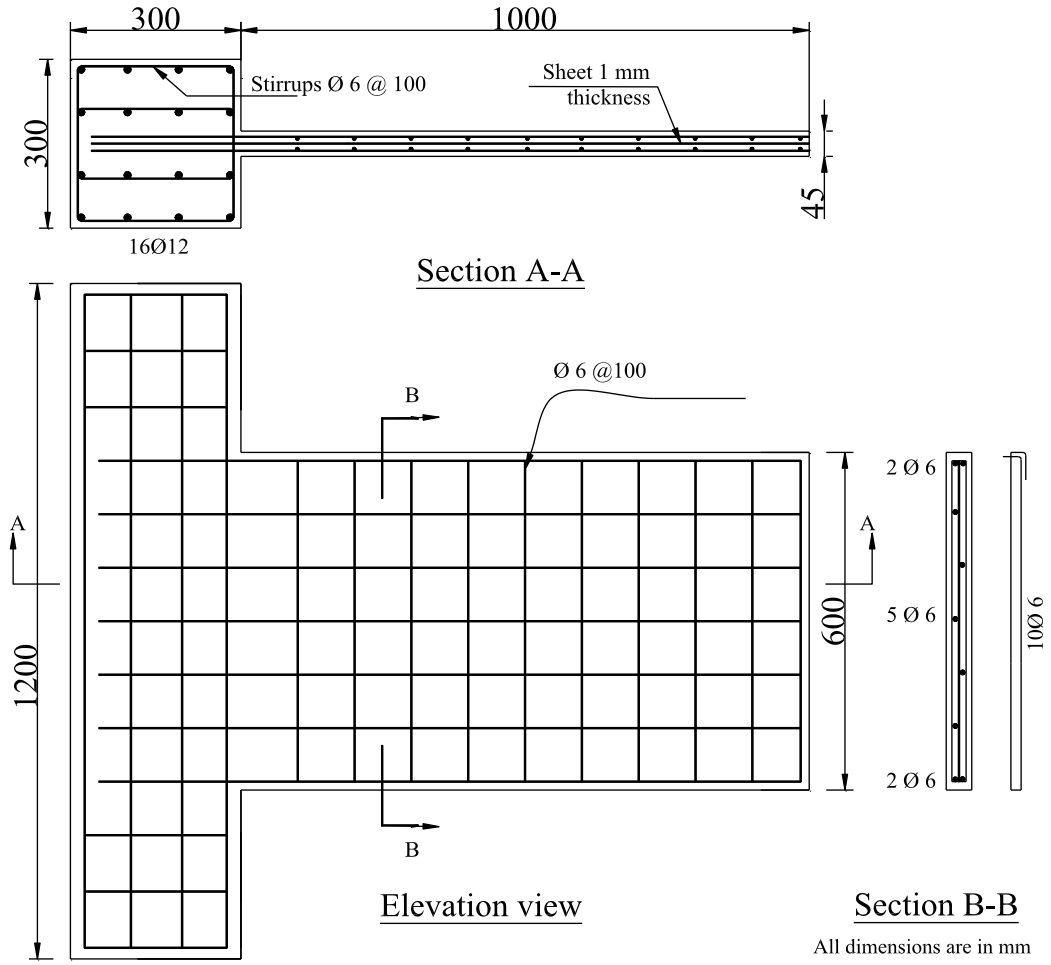

Figure 4.6 Reinforcement details for specimen EW31

4.5.2 Plate reinforcement

The composite specimens were manufactured with mild steel plates with varying thickness. In order to prevent plate slippage, three U-shape anchor bars with 16mm diameter were placed in the base block/footing. Holes were drilled first in the plate and then anchor bars were placed in their predetermined positions before concrete casting. The positions and dimensions of the anchor bars are given in Figure 4.7.

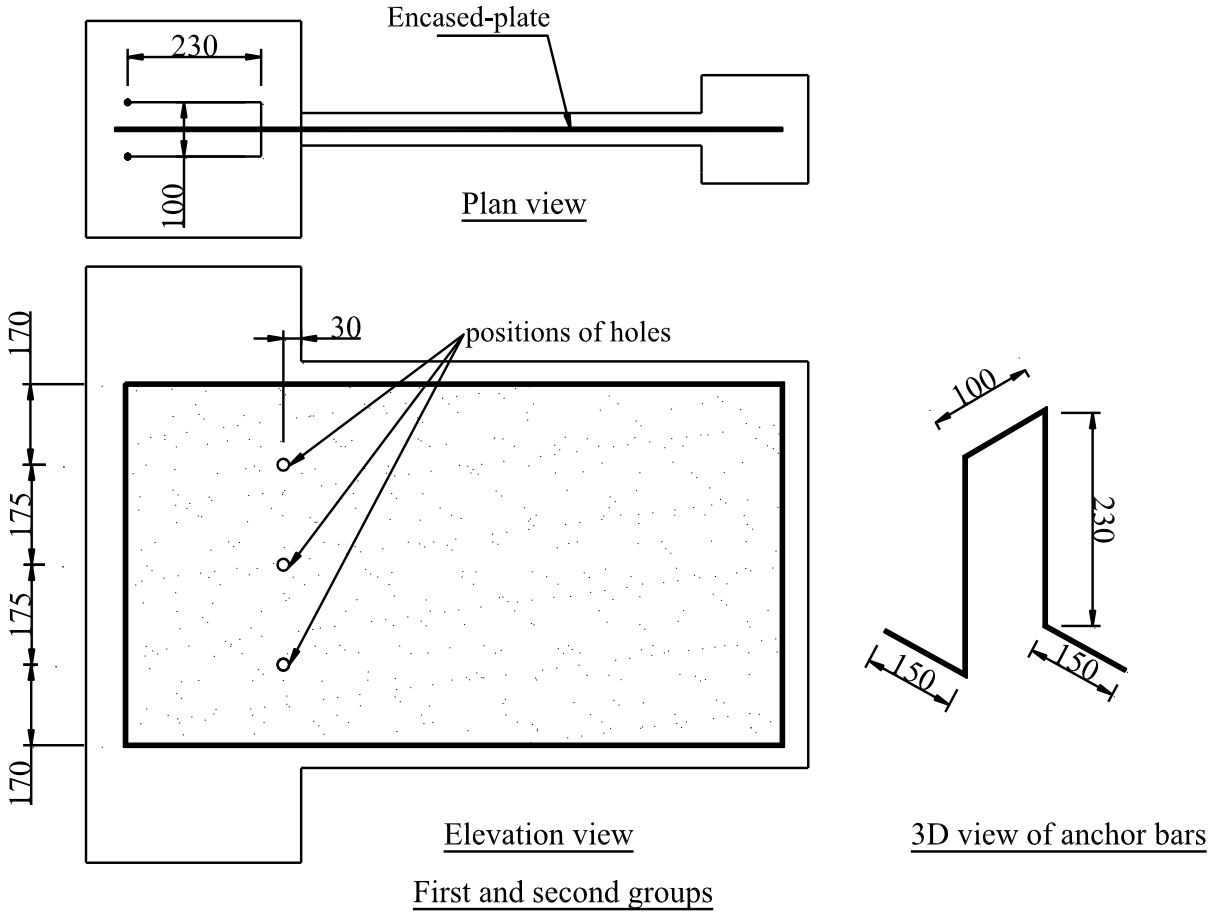

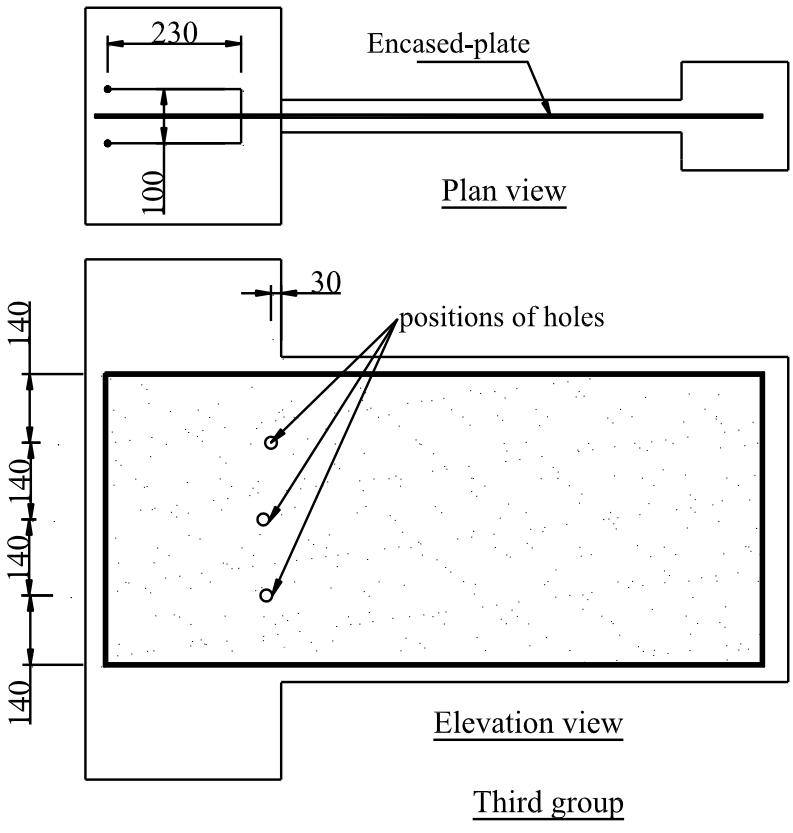

Figure 4.7 Details of plate anchorage

4.6 Material Properties

4.6.1 Concrete

The concrete materials used were crushed graded aggregates with a nominal size of 6 mm, natural river sand and ordinary portland cement. A concrete mix, giving target strength value of 40 N/mm^2 at 28 days with 100 to 120 mm slump, was designed according to the Building Research Establishment (BRE) guide (Teychenné *et al.* 1998) and used in the walls. The mix proportions are given in Table 4.2. The workability of the concrete mix was improved using a super-plasticizer. The super-plasticizer used in this investigation was Glenium 51 from Master Builders. Glenium 51 is based on a modified polycarboxylate ether type of polymer and the dry content is approximately 35%.The exact amount of super-plasticizer was varied depending on the weather conditions, which affected the moisture content of the aggregates.

From each concrete mix, nine 100 mm cubes were cast and tested to determine the compressive strengths at 7 and 28 days, and on the test day. Three 100 x 300 mm and 150 x 300 mm cylinders were also cast and tested on the specimen test day to determine the splitting tensile strength and elastic modulus of the concrete, respectively. The concrete was mixed, cast, cured and tested according to Part 125 of BS 1881:1986 and the compressive strength and modulus of elasticity were determined in accordance with Part 3 of BS EN 12390-3:2002. The results of cube and cylinder tests are given in Table 4.3.

Table 4.2 Concrete mix proportions

	Coarse aggregate	Fine aggregate	Cement	water	Plasticizer
Ratio	1.67	1.54	1	0.5	200-250/100 kg of cement
Weight, Kg/m^3	832	768	500	250	1000-1250 ml

Table 4.3 Concrete properties as determined from cubes and cylinder tests

Specimen		Cube compressive stress (N/mm^2)	Cylinder splitting strength (N/mm^2)	Modulus of Elasticity (kN/mm^2)
EW11	7 days	25.36±0.75	1.63	25.1
	28 days	42.33±2.47		
	Day of test (29 days)	42.67±3.49		
EW12	7 days	30.13±4.88	2.46	24.2
	28 days	46.20±2.15		
	Day of test (35 days)	48.56±1.68		
EW13	7 days	26.10±2.46	1.48	23.5
	28 days	39.94±3.67		
	Day of test (35 days)	43.21±0.61		
EW21	7 days	31.20±1.42	2.03	24.4
	28 days	45.13±4.15		
	Day of test (36 days)	49.00±2.24		
EW22	7 days	31.20±1.42	2.13	24.4
	28 days	45.13±4.15		
	Day of test (40 days)	50.38±2.27		
EW23	7 days	31.20±1.42	2.74	24.4
	28 days	45.13±4.15		
	Day of test (89 days)	59.63±3.39		
EW31	7 days	35.80±1.37	1.63	23.73
	28 days	45.90±3.58		
	Day of test (33 days)	47.60±3.30		

4.6.2 Rebars

The mechanical properties of rebars were determined from the tensile testing of three representative samples according to ASTM A370-06 (Standard Test Methods and Definitions for Mechanical Testing of Steel Products) and the average results are presented in Figure 4.8. The yield and ultimate stress of the rebar specimens tested are given in Table 4.4.

Table 4.4 Mechanical properties of the reinforcing steel

Rebar diameter (mm)	Yield stress (N/mm^2)	Ultimate strength (N/mm^2)	Young's modulus (kN/mm^2)
6	428	543	225
12	512	592	170

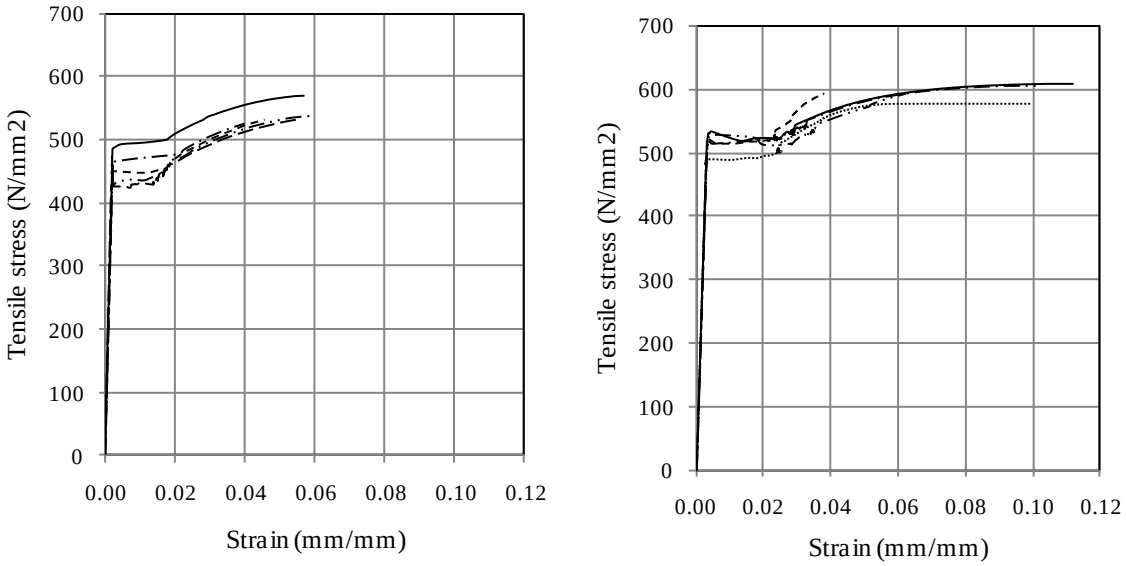

(a) Tests with 6 mm diameter rebars (b) Tests with 12 mm diameter rebars

Figure 4.8 Stress-strain behaviour of rebars

4.6.3 Steel plates

The mechanical properties of plates were determined from subjecting coupon specimens to uniaxial tensile tests. Three coupons were prepared for each plate thickness and tested according to ASTM A370-06. The average results are summarised in Table 4.5 and presented in Figure 4.10.

Table 4.5 Mechanical properties of steel plates

Plate thickness (mm)	Yield stress (N/mm^2)	Ultimate stress (N/mm^2)	Young's modulus (kN/mm^2)
0.8	265	346	225
1.0	252	324	217
1.5	270	350	192

4.7 Manufacture of specimens

The process of manufacturing the specimens consists of three main steps namely, formwork assembly, plate and reinforcement formation and assembly and concrete casting. These steps are presented in detail below.

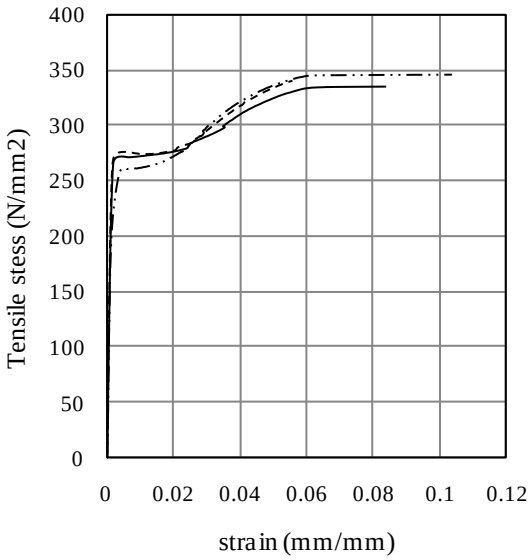

(a) Tests with 0.8 mm thick plate

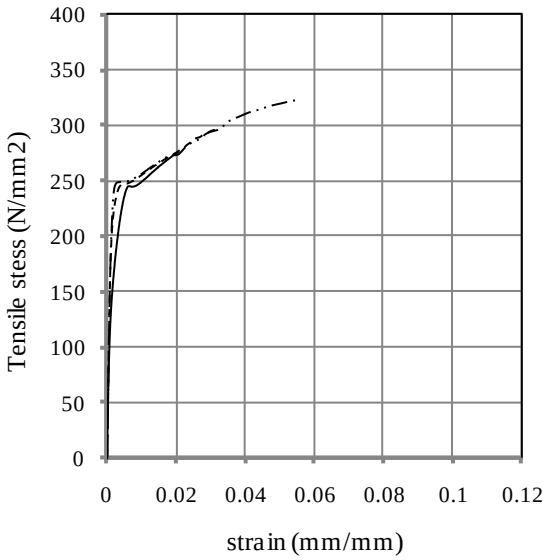

(b) Tests with 1.0 mm thick plate

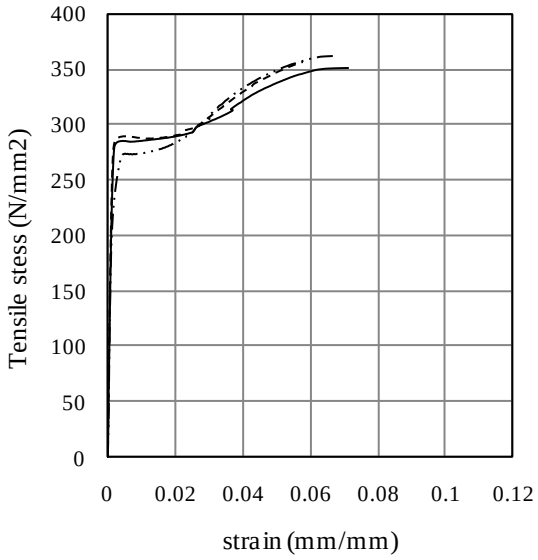

(c) Tests with 1.5 mm thick plate

Figure 4.9 Stress-strain behaviour of plates

4.7.1 Formwork assembly

Test specimens were cast in three different custom-built timber formworks, see Figure 4.10. The formwork was made of 18 mm thick plywood panels constructed with ± 0.5 mm tolerance. The plywood panels were bolted together using 10 mm diameter threaded bars, and the sides of the formwork were sealed with silicon and covered with a thin layer of oil to prevent the attachment of concrete. In order to provide a sufficient room for the hydraulic jack and the load cell, a custom-built concrete pedestal was also

constructed. Figures 4.10a and b show the details of the formwork assembly on the vibrating table before concrete casting, while Figure 4.10c presents the formwork assembly of the pedestal. Figures 4.11 and 4.12 present full details of the formwork used for specimens casting.

(a) First group

(b) Second group

(c) Pedestal

Figure 4.10 Assembled formwork before concrete casting

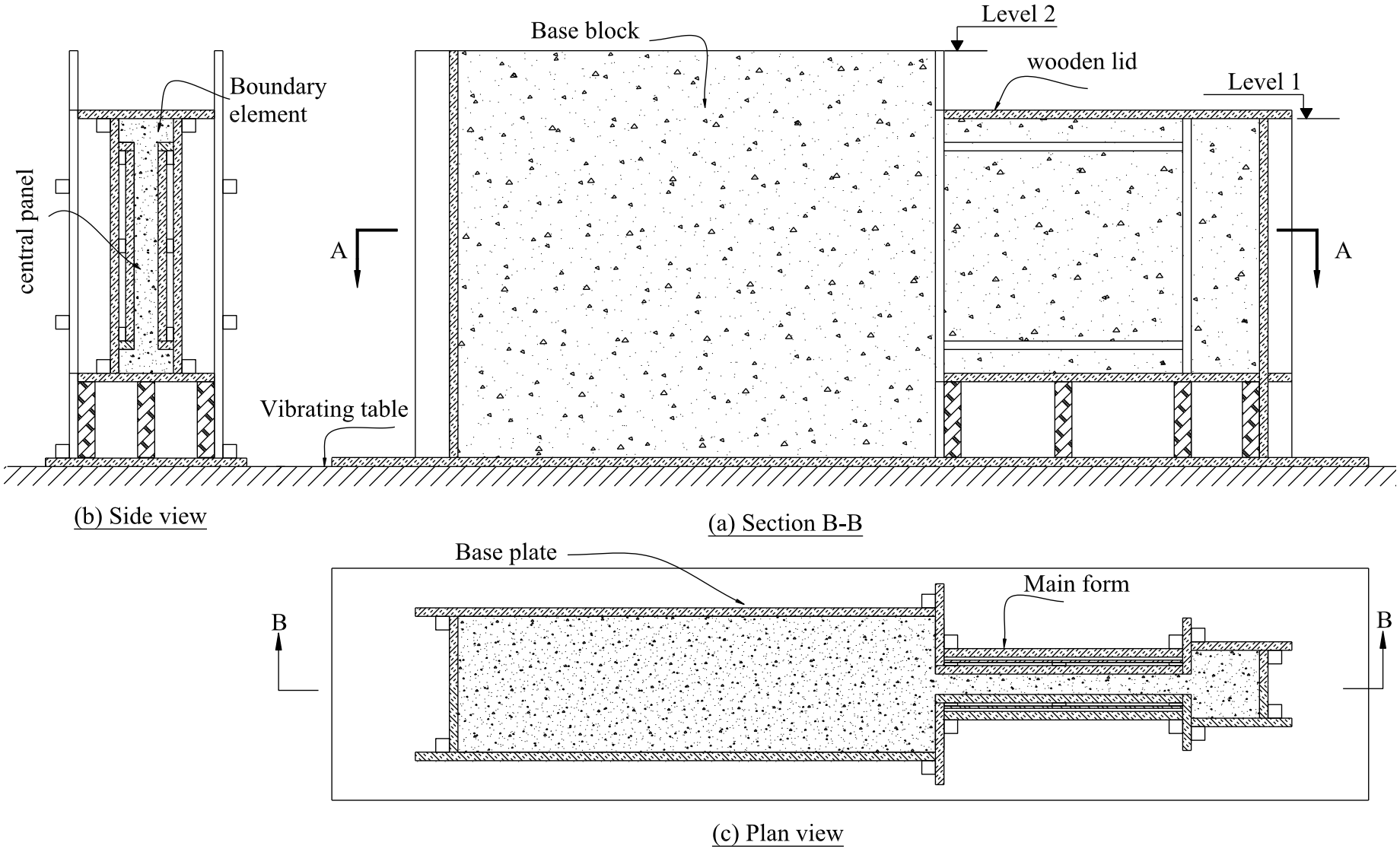

Figure 4.11 formwork of test specimens in the first group

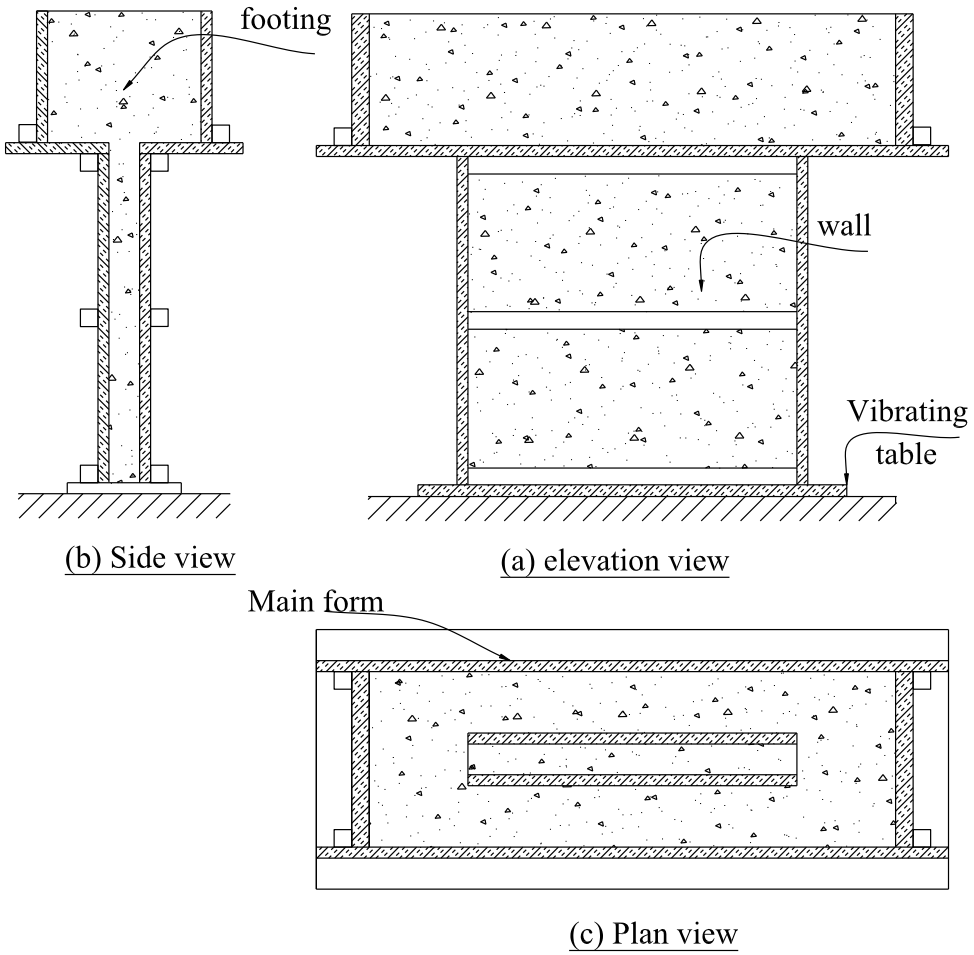

Figure 4.12 formwork of test specimens in the second and third groups

4.7.2 Reinforcement formation and assembly

The rebars were cut to length using a steel saw and bent according to the required dimensions. Since the specimens were heavily reinforced, the reinforcement cage was assembled using conventional steel wires and tack welding to hold the cage during concrete casting. Non-load bearing welds of rebars are common in the concrete construction industry and used to secure reinforcement without providing additional strength for the structure. The plates were also cut to the required dimensions at the local supplier and cleaned using Acetone. Holes were drilled in the plates for anchor bars at the predetermined positions, see Figures 4.7 and 4.13. Since the bond between the plate and the surrounding concrete is important to have a composite action, longitudinal rebars in the central panel were cleaned and surface smoothed using glass-paper and glued to the plate using a suitable epoxy adhesive, see Figure 4.13.

Eventually, the reinforcement cage and plate were instrumented with strain gauges at the desired locations as explained in Section 4.8.3, and placed carefully in the formwork.

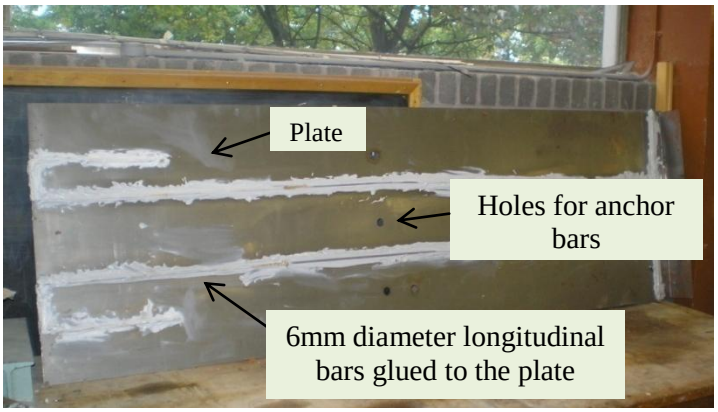

(a) Plate with the reinforcement (b) Anchor bar

Figure 4.13 Plate arrangement

4.7.3 Concrete casting

The concrete was mixed mechanically in a horizontal pan type mixer of 0.15 m^3 capacity. Dry materials for each batch were prepared by weight according to the proportions detailed in Table 4.2. The constituents were mixed in a dry state for a few minutes to ensure the mix uniformity. Super-plasticizer and water were then added gradually and the contents were mixed until a homogeneous mix was obtained. The concrete was placed in the formwork with hand shovels. After pouring of each batch, the vibrating table was turned on for a few seconds until good compaction had been achieved. Two lifting eyes were attached to the base block and footing reinforcement to facilitate lifting and handling of the specimen after casting. Care was taken to keep the strain gauges safe during casting.

Specimens in the first group were cast in a two-step process to avoid the creation of a construction joint. First, the base block and the wall were cast until the concrete reached level 1 (Figure 4.11), and then a wooden lid was placed and fixed to the formwork over

the wall part. Second and while the concrete was still wet, casting continued into the base block up to level 2. Specimens in the second and third groups were cast in a one-step process. Figure 4.14 presents the completed specimens after casting and before curing. Control cubes and cylinders were simultaneously cast with the specimen from each batch. The specimens, control cubes and cylinders were covered immediately after casting using damp hessian and polythene sheets. The specimens were stripped four days after casting, while cubes and cylinders were demoulded on the day after casting, and covered with damp hessian sheets, see Figure 4.15. Curing of concrete continued for four weeks keeping the hessian damp at all times.

Figure 4.14 Completed test specimens

Figure 4.15 Curing of test specimen

4.8 Instrumentation

4.8.1 Overview

Both external and internal instruments were used to measure the specimen's response to applied loading. Externally, linear variable deflection transducers (LVDTs) were used to monitor the wall displacements and the support movements. Internally, a number of strain gauges were used to monitor strain propagation in rebars and encased-plates. A Canon PowerShot G9 digital camera with a resolution of 3264 x 2448 pixel was also used to capture images of the specimens during all test stages, and the images were later analyzed to estimate specimen deformations using the PIV technique as described in Section 3.5. The PIV technique was available for use for specimens EW11, EW13 and EW23 only.

4.8.2 Linear variable deflection transducers (LVDTs)

Sixteen LVDTs were used to monitor the displacements of the test specimens at the following locations, see Figures 4.16 to 4.18:

- Transducers 1 to 4 monitored the vertical displacements along wall edge;
- Transducers 5 and 6 monitored the extension and the contraction of the boundary elements, respectively;
- Transducer 7 monitored the uplift movement of the base block/footing;
- Transducers 8 to 10 monitored the out-of-plane movement of walls;
- Transducers 11 and 12 monitored the out-of-plane movement of base block/footing;
- Transducers 13 and 14 measured the relative diagonal displacement of wall's opposite corners in the first and second groups only; and
- Transducers 15 and 16 monitored the rotation of base block/footing.

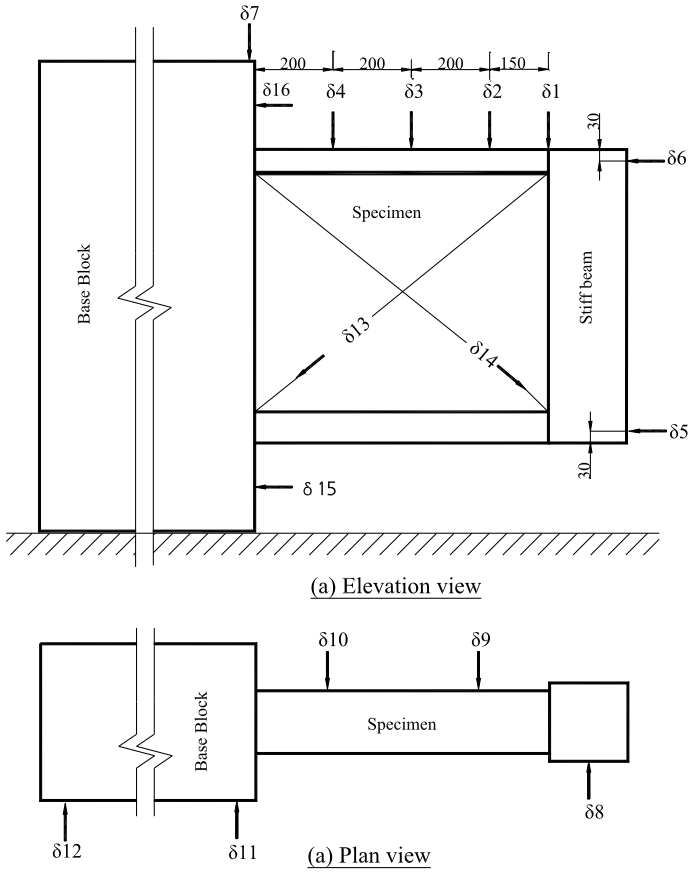

Figure 4.16 Locations of LVDTs in first group specimens

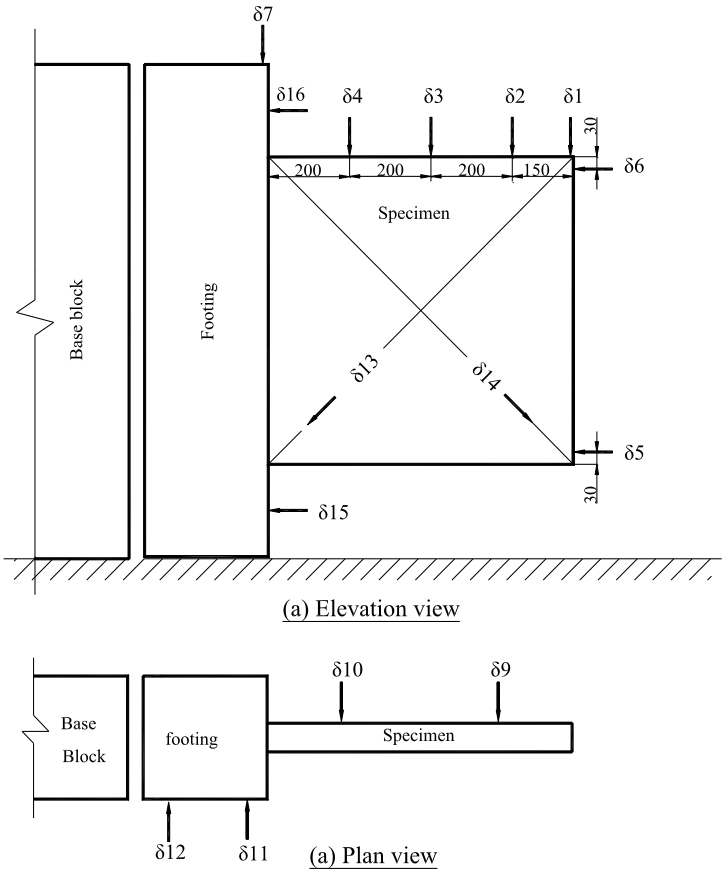

Figure 4.17 Locations of LVDTs in second group specimens

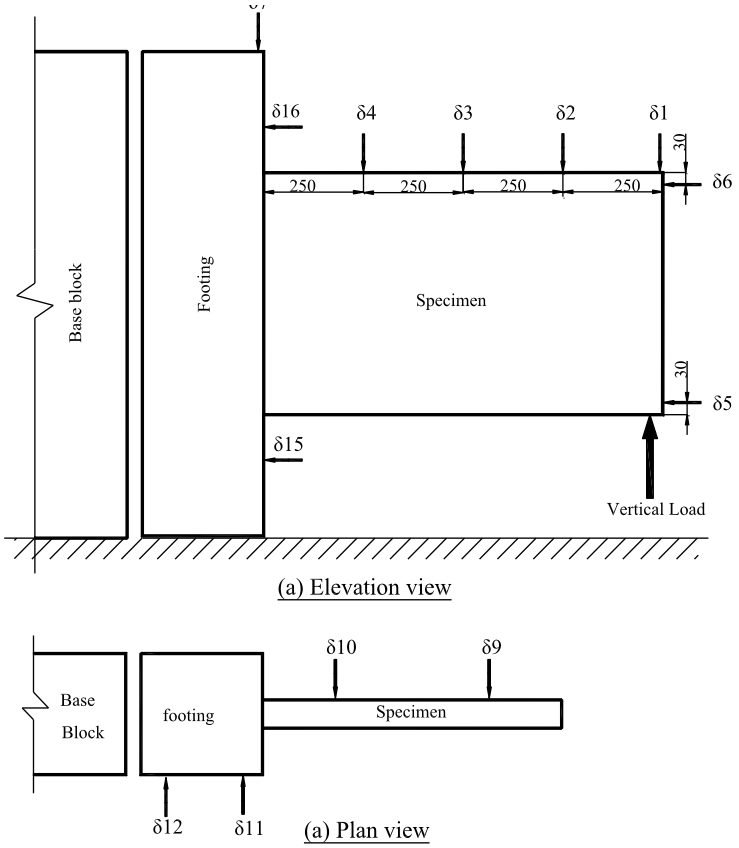

Figure 4.18 Locations of LVDTs in specimen EW31

All transducers had a travel range of ± 100 mm with accuracy of 0.0075 mm. The data obtained from LVDT 13 and 14 were used to measure the average shear distortion of the specimen. The vertical displacement of the wall end, δ1, was divided into two components; flexural and shear. The shear displacement component was evaluated using the readings obtained from the diagonal transducers, δ13 and δ14, according to the method presented in Figure 4.19. The flexural displacement component was estimated by subtracting the shear displacement from the total vertical displacement.

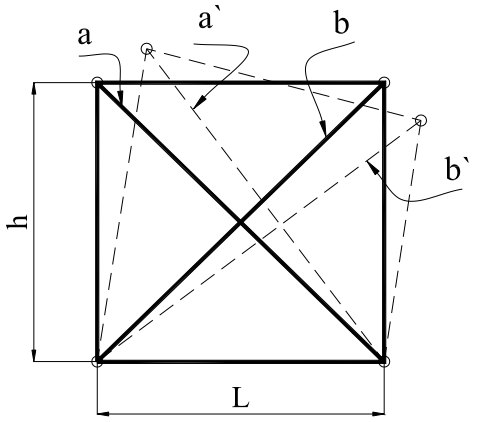

$$\text{Average shear distortion} = \frac{(b`-b)-(a`-a)}{2lh}$$

$$\text{Average shear displacement} = \frac{(b`-b)-(a`-a)}{2l}$$

where,
a and b = Original lengths of diagonal lines
$a`$ and $b`$ = deformed lengths of diagonal lines

Figure 4.19 Estimation of shear displacement (Raongjant 2007, Shaingchin *et al.* 2007)

4.8.3 Strain gauges

An extensive arrangement of electrical strain gauges was used at key locations to measure the induced strains in the encased-plates and rebars. Most strain gauges were located near the wall base where maximum strains were expected, Figure 4.20. Plate and rebar strain gauges were placed at almost the same level to assess the efficiency of composite action between the plate and the rebars. Depending on the reinforcement details for each specimen, the locations of strain gauges were varied slightly, as shown in the Figure 4.20. Figure 4.21 shows the strain gauges used in specimen EW31.

4.9 Test protocol

4.9.1 Pre-test Preparations

In preparation for testing, specimens' surfaces were painted with a thin coat of white emulsion paint. On one face, a grid was drawn to enable the detection and marking of crack propagation under load. On the other face, a black spray paint was sprayed in dots to provide the spatial variation in brightness required by PIV to track the movements of concrete surface, see Figure 4.22.

For first group specimens, the load was applied to the specimen through a 30 mm thick steel plate to avoid stress concentration at the loading point. For second group specimens, a 16 mm thick steel box was manufactured and attached to the loading point to prevent local failure, see Figure 4.22. The top surface of the base block/footing was levelled with a thin mortar layer to ensure a uniform contact between the base block/footing and the upper reaction beams, see Figure 4.23. The specimens were then carefully placed on the concrete pedestal and positioned in the test rig. LVDTs were calibrated before each use and attached to their supporting framework, and their needles were accurately positioned.

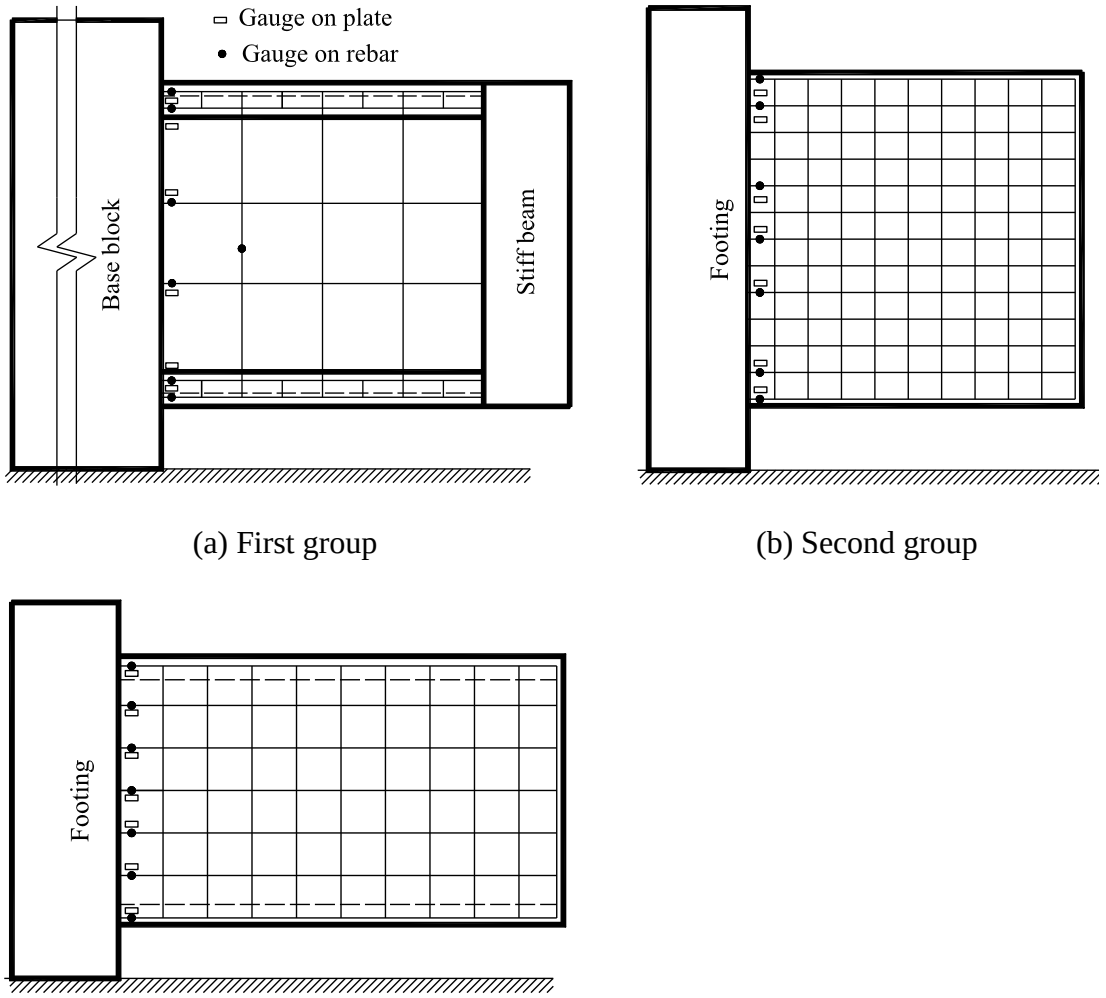

(a) First group

(b) Second group

(c) Third group

Figure 4.20 Locations of strain gauges

The camera was carefully located to reduce image distortion and was controlled remotely through a USB link from a personal computer, and images were saved and checked during test progress. A series of control markers, with known object-space coordinates, was drawn on a perspex sheet and placed in front of the specimen, Figure 4.22. A halogen lamp was used to provide a stable and uniform lighting on the specimen surface. The lighting was positioned carefully to reduce reflections from the control markers placed on the perspex sheet. Finally, all strain gauge wires and LVDT cables were linked to a data logger.

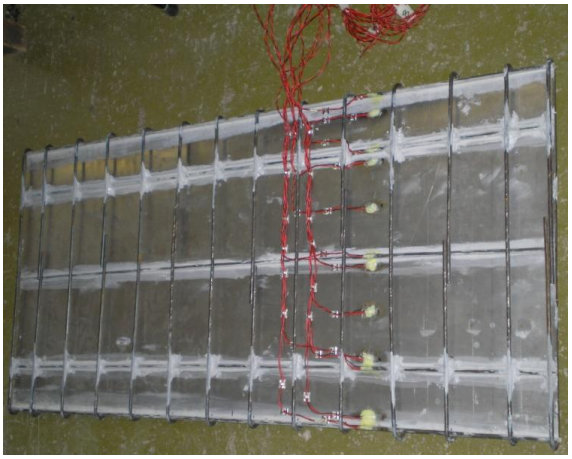

Figure 4.21 Strain gauges used in specimen EW31

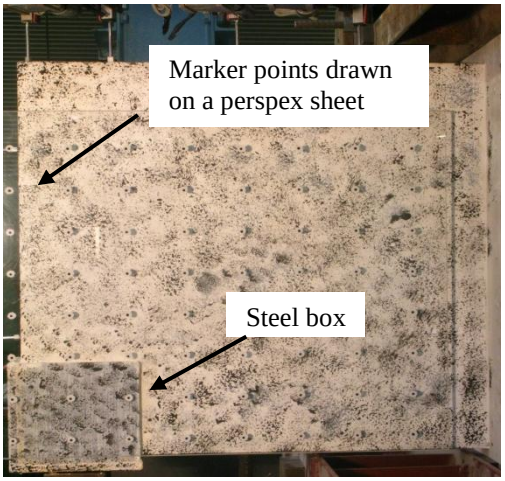

Figure 4.22 Setup of PIV system

4.9.2 Test setup

The specimens were tested in a purpose-built test rig in the Structures Laboratory of the University of Dundee. A 500 kN hydraulic Jack, hand operated with a separate pumping unit, was used to apply the load in an upward direction to the specimen, see Figures 4.23 and 4.24.

The jack was bolted to a 30 mm thick steel plate and placed on a previously marked position on the lab floor. In order to measure the applied load, a 500 kN load cell was incorporated with the hydraulic jack and placed under the specimen.

For first group of specimens, the test setup consisted of two main components termed as upper reaction beams and bottom supporting girders, see Figures 4.23 and 4.24. The process of building the test setup essentially involved three steps. Initially, the bottom supporting girders were positioned carefully and prestressed to the lab strong floor, through floor holes that were 1060 mm apart, with the aid of eight 30 mm diameter Dywidag prestressing threaded bars. The specimen was placed on the pedestal at the required position. The base block was then tied down firmly to the bottom supporting girders by means of two reaction beams placed over its ends to prevent uplift of the specimen. The upper reaction beams were anchored to the bottom supporting girders through four hand tight Dywidag prestressing threaded rebars. The upper reaction

beams and bottom supporting girders formed a reaction frame to support the load from the hydraulic jack, see Figures 4.23 and 4.24.

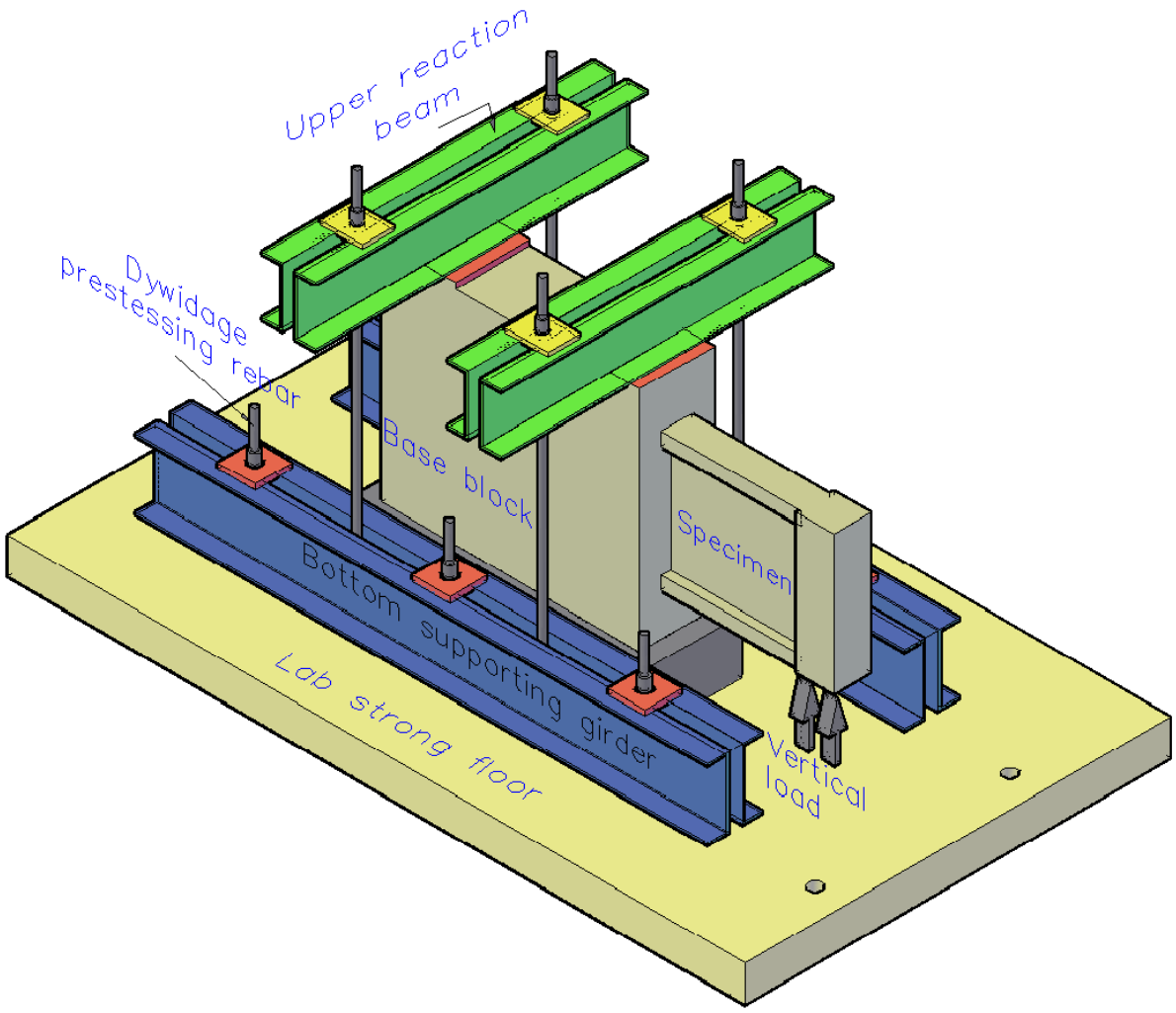

Figure 4.23 An isometric view of test setup for first group specimens

The change in base block size in the second and third groups required some alteration in the test setup. Test specimen EW11 was rotated through 180° and was connected to the test setup as described above. To test a specimen of the second and third groups, the specimen was placed on the pedestal in such way that it was in back-to-back with specimen EW11, see Figure 4.25. Two addition beams were placed horizontally over and under the specimen to connect the base block and the footing together through four Dywidag prestressing threaded rebars. Moreover, another beam was placed over the

footing of the specimen and connected to the bottom supporting girders through two Dywidag prestressing threaded rebars, see Figure 4.26.

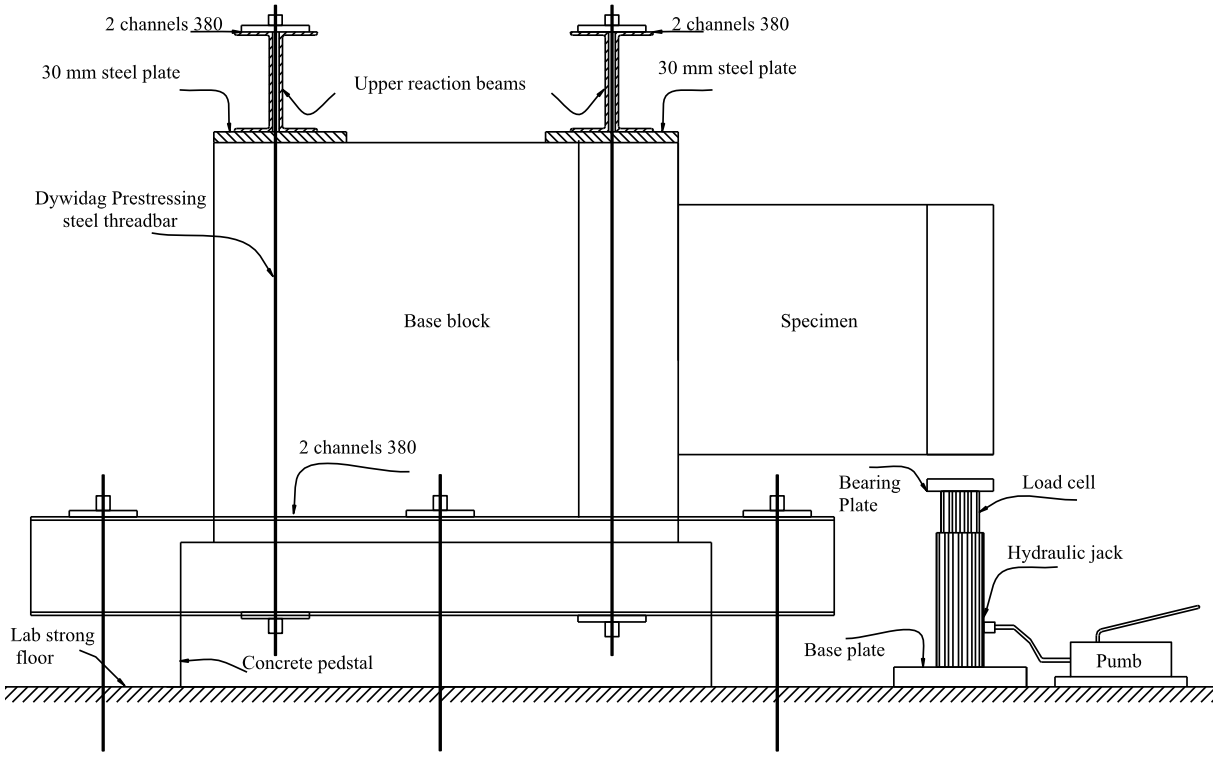

(a) Elevation view

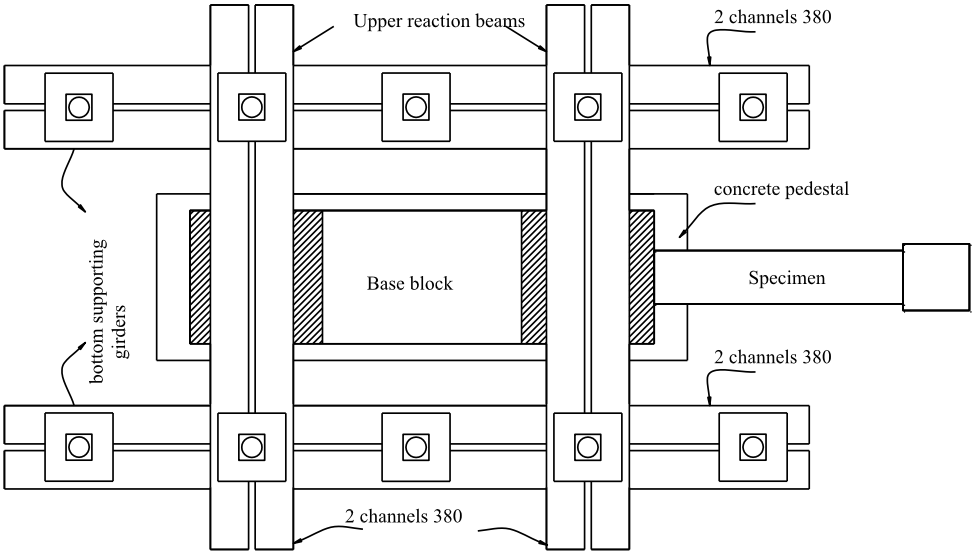

(b) Plan view

Figure 4.24 Details of test setup for first group specimens

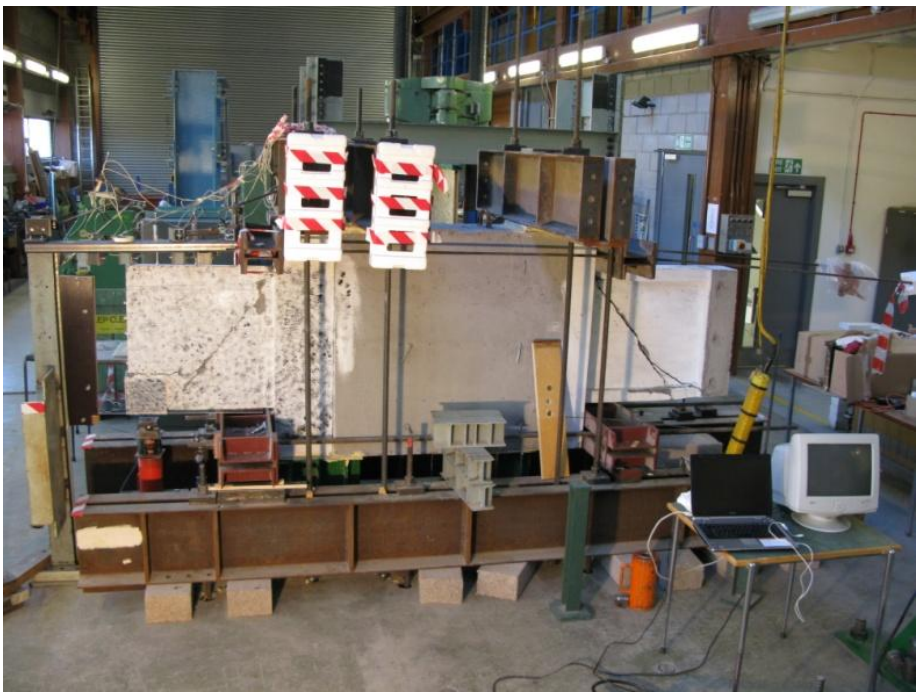

Figure 4.25 Test setup for second and third group specimens

4.9.3 Loading process

In each test, a specimen was loaded in three cycles, the first two involving load up to 15 and 40% of the expected ultimate load, and the third cycle continuing to overall specimen failure. The first and second cycles were expected to demonstrate elastic and elastic-plastic behaviour, respectively. The two cycles were conducted to allow an initial assessment of specimen behaviour prior to overall failure in the third and final loading stage.

4.9.4 Data Recording

Data from the load cell, the LVDTs and the strain gauges at each load increment were collected by a Spectra data logger connected to a personal computer. The analysis software offered immediate monitoring of all channels and chart presentation for two selected channels. These features enabled close examination of wall behaviour during the loading process. Moreover, photographs were taken of the test specimens during and after testing.

4.9.5 Crack monitoring

Crack propagation was monitored after each load increment until failure occurred. At each load increment, cracks were highlighted and marked with their corresponding load value. The load that produced the first crack and specimen failure were registered and noted as cracking and failure load. Finally, the pattern of cracks for each specimen was neatly sketched and photographed.

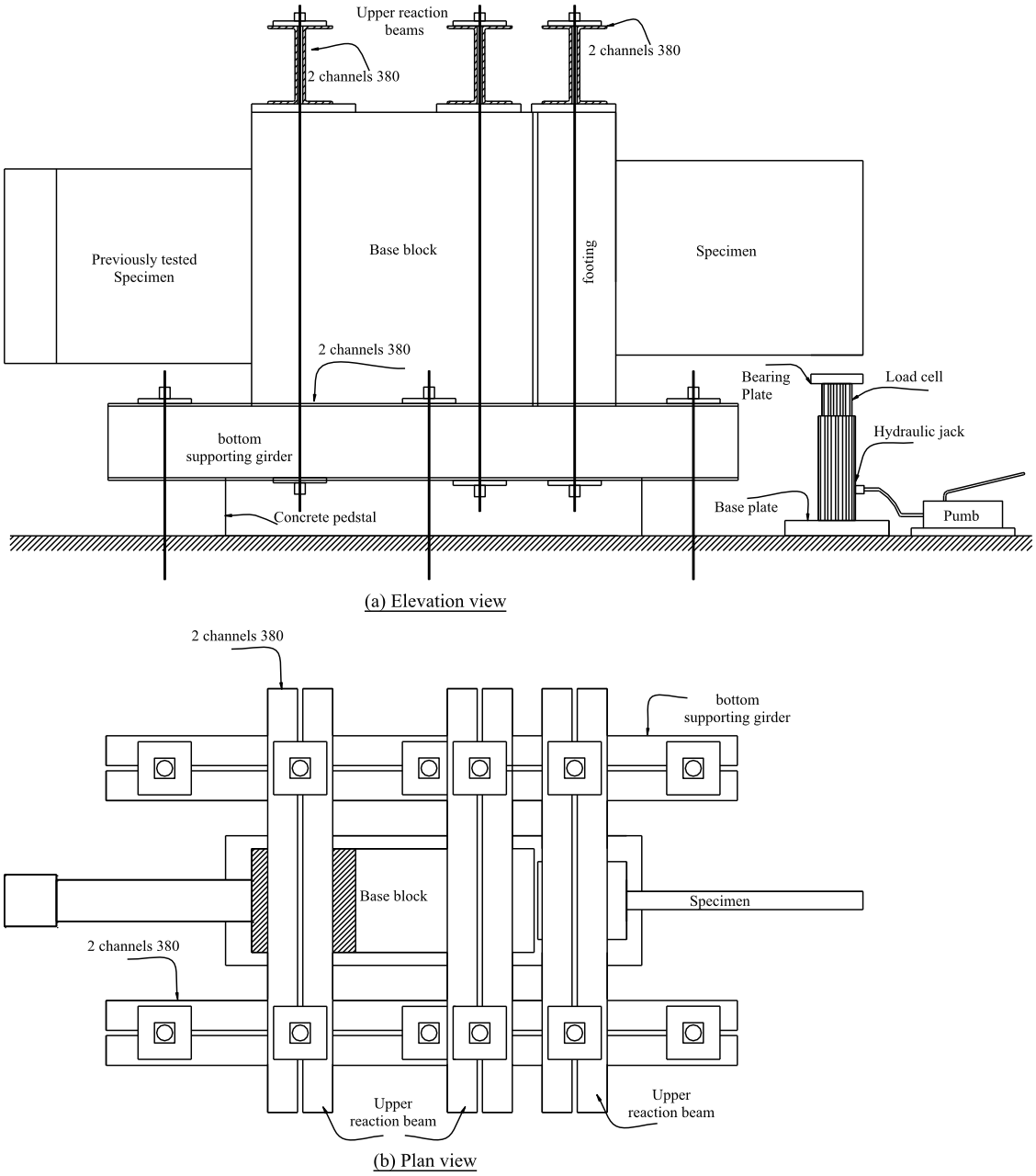

Figure 4.26 Details of test setup for second and third group specimens

4.10 Summary

This chapter presents the details of seven structural wall specimens tested under lateral loading, including specimens' dimensions, material properties, manufacturing process, test setup, instrumentation and test procedure. Three flanged specimens, EW11, EW12 and EW13, were designed to fail in shear by diagonal tension, while three rectangular specimens, EW21, EW22 and EW33, were designed to fail in shear by diagonal compression. In addition to specimen EW31 which was designed to fail in flexure. The specimens represented the critical storey element of a structural wall system with a scale of approximately 1:5 of a prototype structural wall in a multi-storey building.

Chapter 5 Experimental results and discussion

5.1 Overview

This chapter presents a qualitative description of the results of testing the seven structural wall specimens described in Chapter 4. The results include the overall wall displacements, the strains in rebars and encased-plates, the crack patterns and the behaviour under applied load to failure. The final discussion covers the overall behaviour and the modes of failure, and is based on the detailed presentation of results in Section 5.2.

5.2 Test results and observations

5.2.1 Introduction

The displacement response at each load increment was monitored using several transducers positioned such that their measurements could provide important insight on the walls' performance under load. The positions of the transducers were changed slightly for each group as shown in Figure 5.1. For each specimen, three figures are given to present information related to:

(1) the vertical displacements at different positions along the wall top edge (δ1-δ4);

(2) the horizontal displacements of wall boundaries, δ5-δ6, which referred to the elongation and shortening of the tensile and compressive boundary elements, respectively; and

(3) contributions of flexural and shear deformation components to the vertical displacement. The vertical displacement of the wall end, δ1, was divided into two components; flexural and shear. Shear deformation was evaluated using the readings obtained from the diagonal transducers, δ13-δ14, as discussed in Section 4.8.2, while the flexural component, which is related to rotation of the wall section, was calculated by subtracting the shear component from the total displacement.

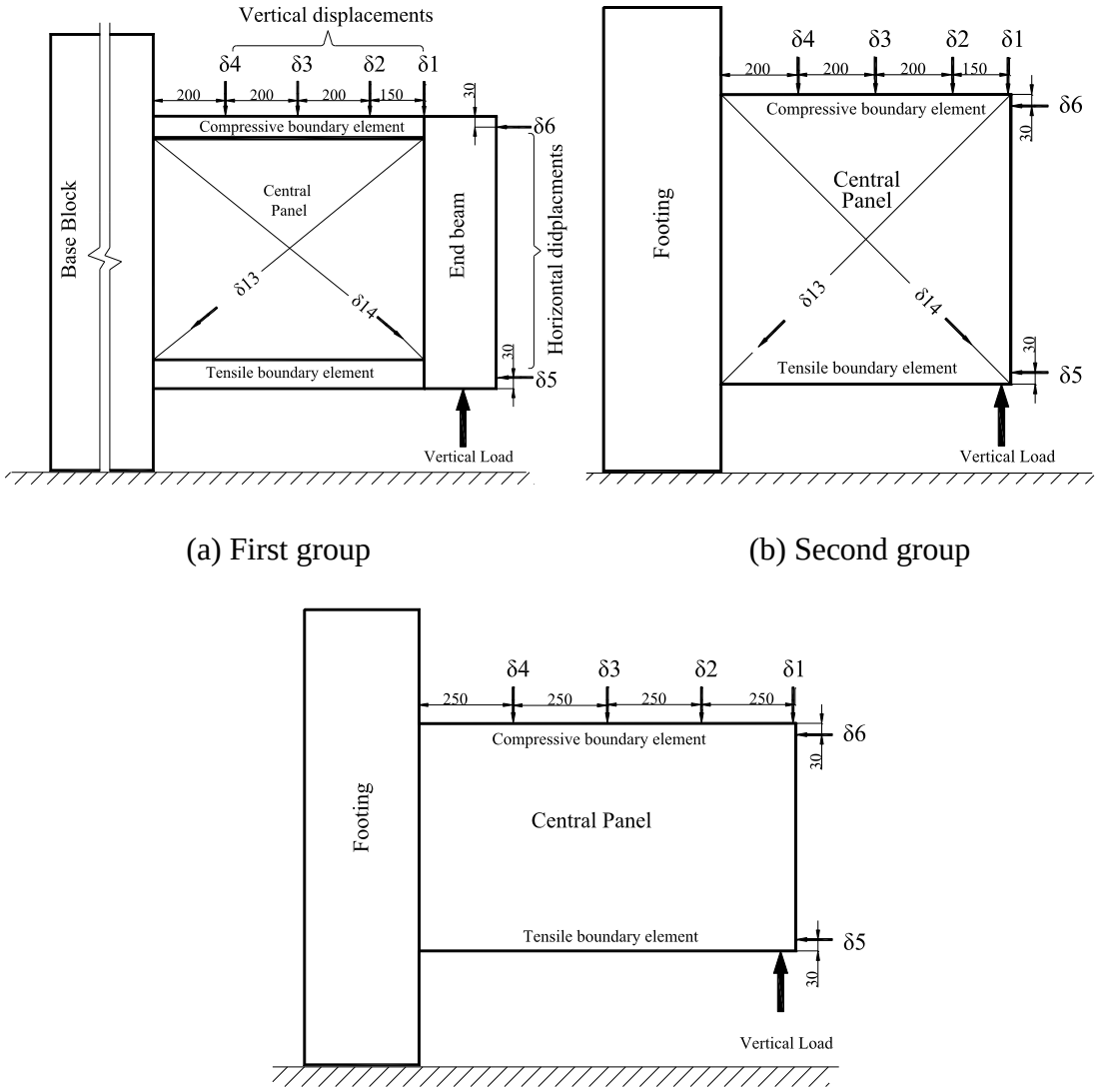

(a) First group

(b) Second group

(c) Third group

Figure 5.1 Positions of deflection transducers

An extensive arrangement of electrical strain gauges was used at selected locations to measure the strains in the encased-plates and the rebars. Depending on the reinforcement details for each specimen, the locations of strain gauges varied slightly as shown in Figure 5.2. The yield strain of 6 and 12 mm diameter bars were 0.00166 and 0.00164, respectively, which were used to determine the load level at which the first yield of reinforcement was reached.

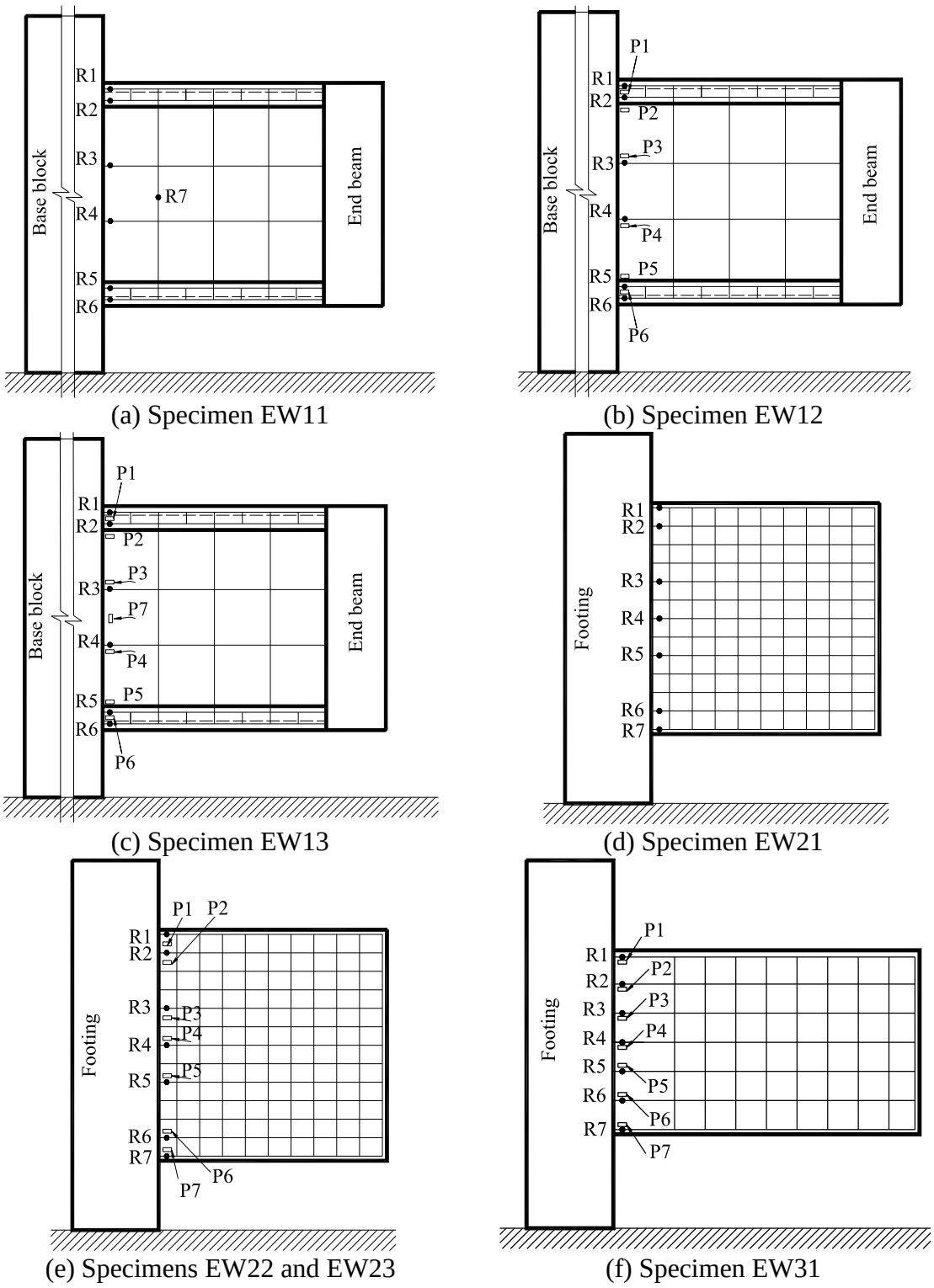

Figure 5.2 Positions of strain gauges used in test specimens

5.2.2 Structural behaviour

This section contains a detailed description of the overall structural behaviour, the strain development in rebars and steel plates and the crack patterns as observed for all specimens.

All the specimens were able to undergo large plastic deformations under the maximum load level except specimen EW22, which failed prematurely as will be discussed later. In this experimental investigation, the tests were stopped when excessive deformations were recorded and no further load increments were registered. This trend of test termination limits displacement values at specimens' overall failure and should be avoided if an accurate estimation of walls' ductility is required.

A. Specimen EW11

Specimen EW11 had a flanged cross-section and was conventionally-reinforced. This specimen acted as a control specimen for the first group. The load-displacement behaviour patterns of the specimen are depicted in Figure 5.3. The load-vertical displacement behaviour patterns (Figure 5.3a) were initially linear indicating elastic behaviour, and becoming nonlinear upon crack initiation. The stiffness reduction observed in behaviour was associated with the formation and progression of flexural cracks and became more pronounced after the first yield of rebars.

Flexural cracks initially appeared vertically in the tensile boundary element (point A in Figure 5.4) under 40 kN load. Increasing the applied load resulted in gradual propagation and widening of flexural cracks in the tensile boundary element. The first diagonal crack appeared at 50 kN load, when the flexural cracks penetrated the central panel at point B. Further increases in load led to the development of additional diagonal cracks in the central panel. The major diagonal crack appeared at 90 kN load, and extended close to the point of load application towards the opposite corner as shown in Figure 5.4. Beyond a load level of 130 kN, The main diagonal crack penetrated both the tensile boundary element close to the point of load application (point C), and the wall's compressive side. The specimen failed at 180 kN when the main diagonal crack widened and formed a diagonal tension failure plane.

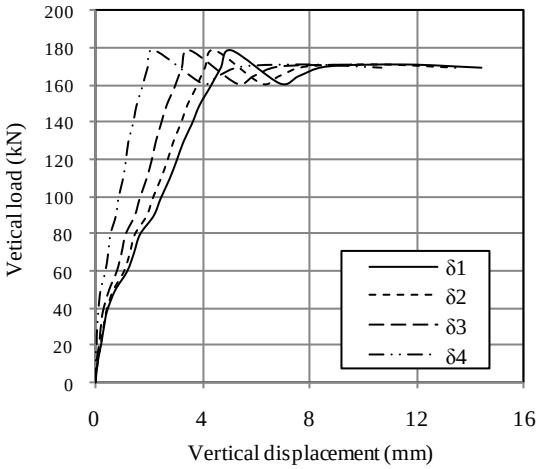

(a) Vertical displacements

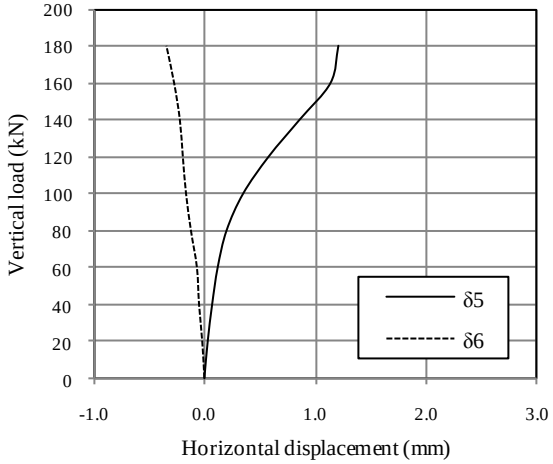

(b) horizontal displacements

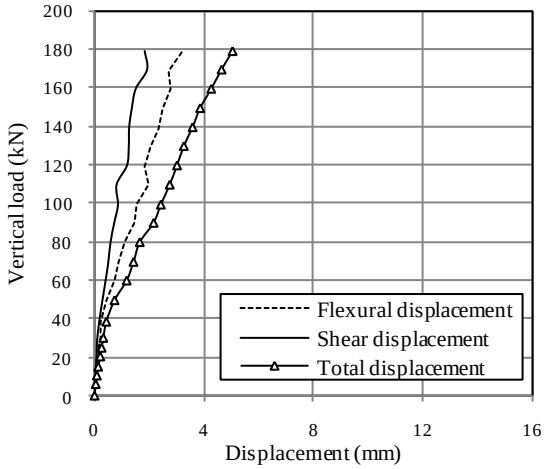

(c) Contributions of the flexural and shear displacement components to the total displacement

Figure 5.3 Specimen EW11: load-displacement behaviour patterns

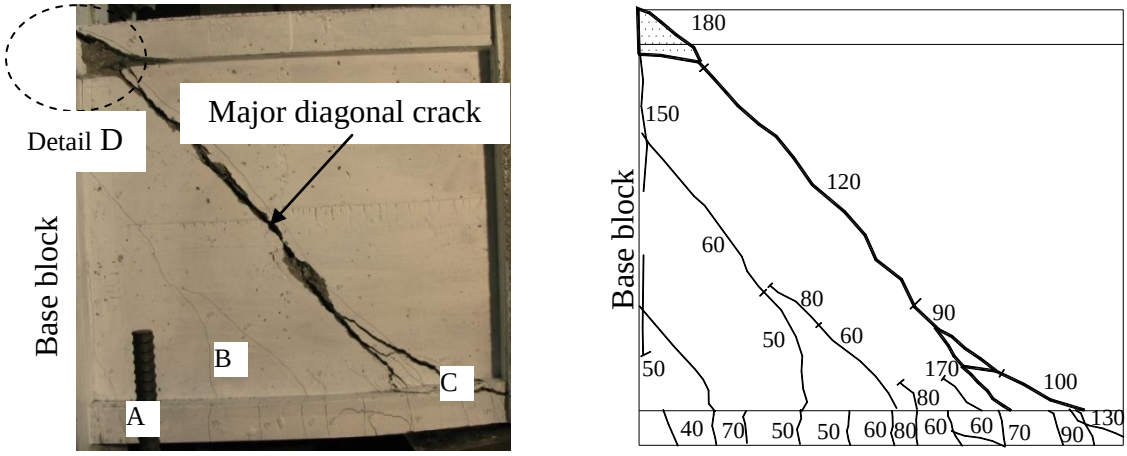

Figure 5.4 Specimen EW11: crack pattern at failure

It was observed that the portion of the specimen above the diagonal crack, along which failure took place, moved as a rigid body relative to the other part of the wall. Spalling of concrete in the compressive side was observed shortly after reaching the ultimate load. The specimen showed a reasonable ability to sustain load at this level and to undergo considerable plastic deformation after failure, and the test was terminated when the load dropped to 170 kN. The crack pattern and specimen form after failure are shown in Figure 5.4.

It was also observed that the rebars crossing the failure plane showed localised bending deformation during failure, see Detail D in Figure 5.5. The mode of failure for this specimen was considered to be shear by diagonal tension.

Figure 5.5 Detail D, bending of rebars crossing the diagonal tension failure plane

The strains recorded during the test are illustrated in Figure 5.6. For all walls in this investigation, the first yield load was determined from readings of the strain gauge attached the outermost tensile reinforcement at the wall base. The strain gauges on the tensile reinforcement (R6 and R5 in Figure 5.2a) detected yield when the applied load reached 130 kN, and the strain continued to increase linearly beyond this load level. On the other hand,

the response of rebars in the compressive boundary element (R1 and R2) remained linear, and the strain values indicated that yielding was not attained at any stage of behaviour, with a maximum recorded strain remaining below 0.001 in strain gauge R1, see Figure 5.6a. Although the central panel longitudinal reinforcement (R4) yielded at 160 kN, the transverse reinforcement (R7) showed low levels of strain, and it was initially under compression but became under little tension at loads higher than 140 kN, Figure 5.6b.

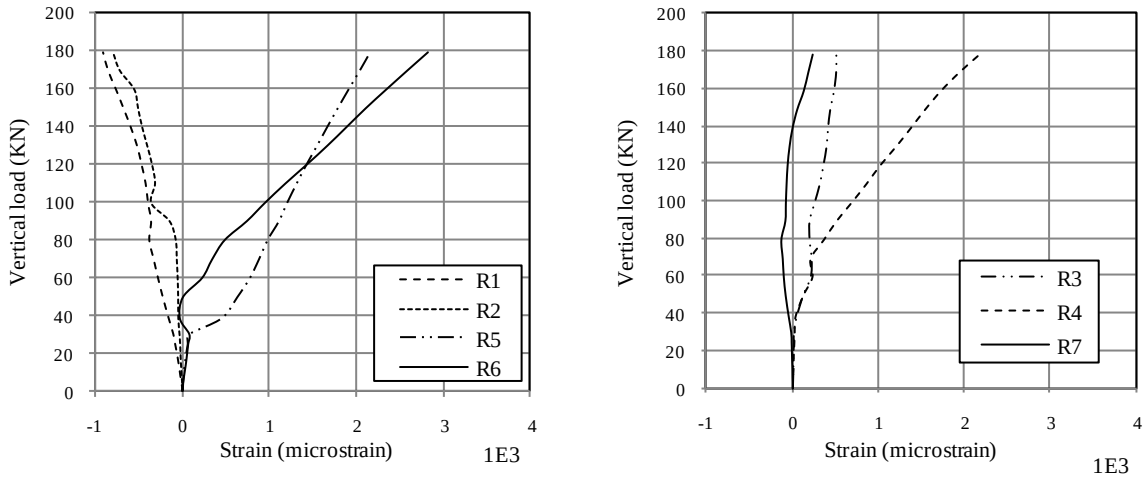

(a) Boundary elements (b) Central panel

Figure 5.6 Specimen EW11: strain development in rebars

B. Specimen EW12

This specimen was identical to the control specimen EW11 in geometric dimensions and reinforcement but a plate with 0.8 mm thickness was embedded centrally in the wall's cross-section.

The load-displacement behaviour patterns of the specimen are depicted in Figure 5.7. The first flexural crack appeared in the tensile boundary element at 60 kN load, which was 50% higher than that of the control specimen EW11. Soon after, several flexural cracks became clearly visible in the tensile boundary element. The first diagonal crack in the central panel appeared at 80 kN load. Additional loading produced not only new flexural cracks, but also

more diagonal cracks in the central panel. Some inclined cracks appeared near the point of load application at a load level of 150 kN. The first inclined crack widened and ran diagonally towards the compressive edge of the wall forming a main diagonal crack. At 210 kN load, another diagonal crack appeared parallel to the first diagonal crack and extended towards the compressive corner. It was noticed that flexural cracks had an average spacing of about 40 mm, while diagonal cracks had a wider average spacing close to 120 mm. Further load increments extended the diagonal cracks until they penetrated the compressive zone resulting in the formation of a diagonal tension failure plane.

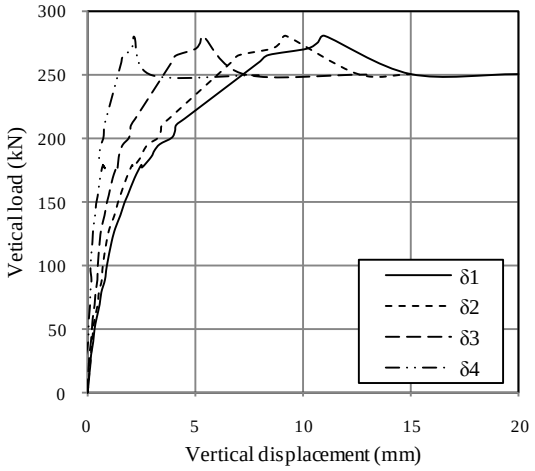

(a) Vertical displacements

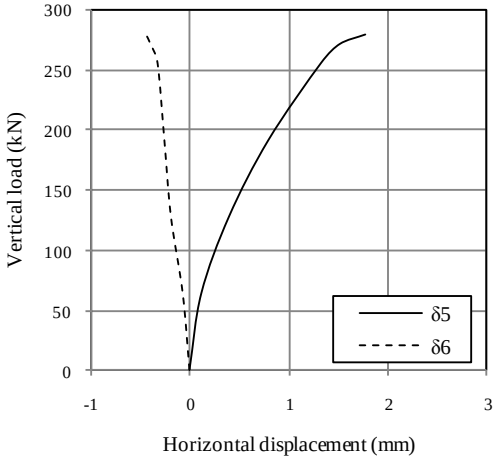

(b) horizontal displacements

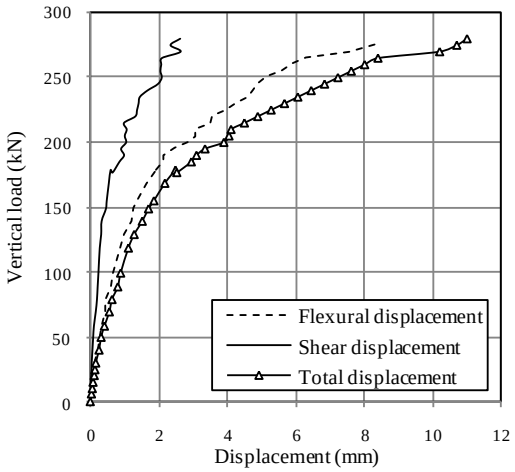

(c) Contributions of the flexural and shear displacement components to the total displacement

Figure 5.7 Specimen EW12: load-displacement behaviour patterns

As was observed in specimen EW11, the portion of the specimen above the diagonal crack**,** along which failure took place**,** moved as a rigid body relative to the other part of the wall. The wall failed when the lateral load reached 280 kN, which was 56% higher than that of control specimen EW11. The crack pattern and the form of the specimen after failure are shown in Figure 5.8.

Also, the reinforcement crossing the failure plane showed localised bending deformation during failure, which appeared after removing the loose concrete cover, without any evidence of slippage from the base block, see Figure 5.9.

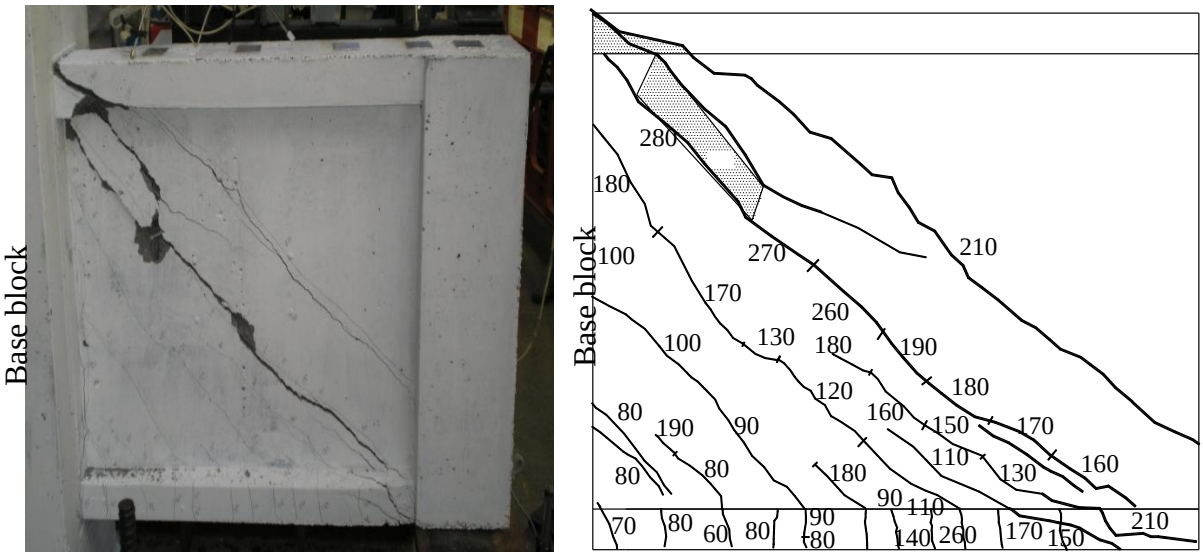

Figure 5.8 Specimen EW12: crack pattern at failure

No signs of debonding between the encased-plate and the surrounding concrete were observed during all loading stages prior to failure. At failure, debonding was observed causing plate buckling in the compressive zone of the central panel, Figure 5.9. The buckled plate caused the concrete cover to spall, resulting in significant loss of web thickness in the vicinity of buckled plate and causing a drop in load carrying capacity and eventually failure, see Figures 5.7a. The wall failed in shear by diagonal tension similar to

specimen EW11, and this implied that the use of encased-plate had no effect on the failure mode in specimen EW12.

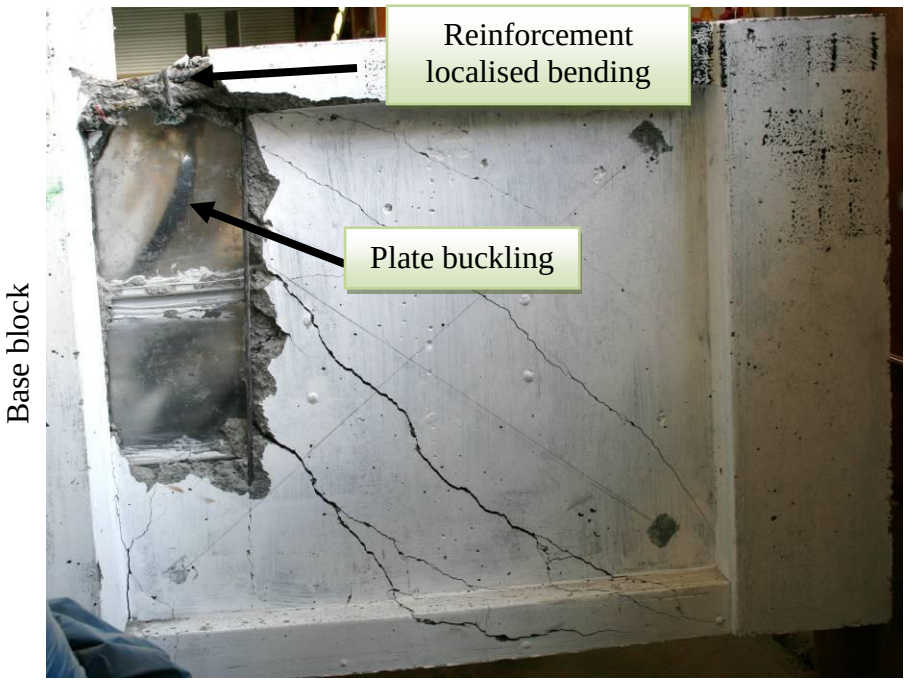

Figure 5.9 Specimen EW12: plate buckling and localised bending of reinforcement

Figures 5.10 and 5.11 present the strain development in the rebars and the encased-plate, respectively. Yielding of tensile reinforcement, R6 (Figure 5.2b), seemed to have developed when the applied load reached 190 kN. Furthermore, compression reinforcement, R1, in the boundary element yielded prior to failure, see Figure 5.10a. The same response was observed in the encased-plate as the maximum tensile and compressive strains remained below 0.0029 and 0.0022 in strain gauges P6 and P1 (Figure 5.2b) at failure, respectively, see Figure 5.11a. However, all the strain gauges on the rebars and the encased-plate in the central panel did not detect any yield until failure, Figures 5.10b and 5.11b.

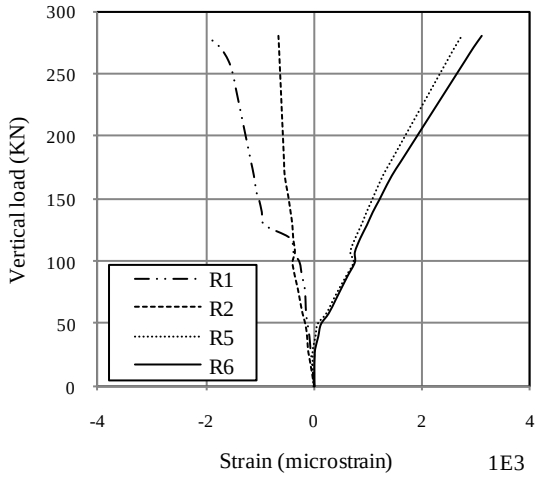

(a) Boundary elements

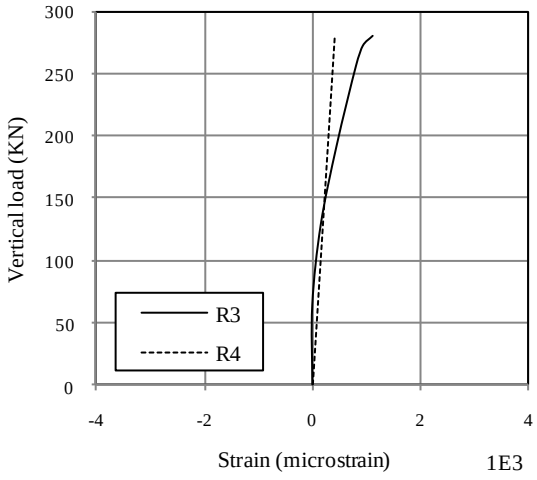

(b) Central panel

Figure 5.10 Specimen EW12: strain development in rebars

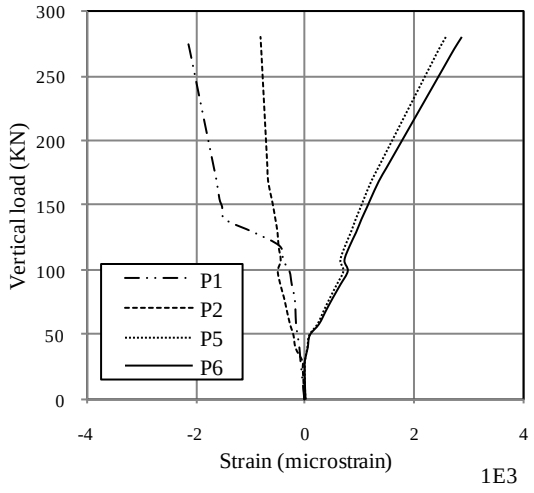

(a) Boundary elements

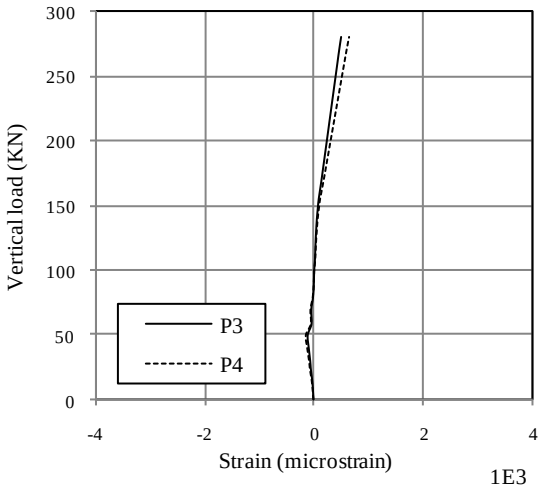

(b) Central panel

Figure 5.11 Specimen EW12: strain development in encased-plate

C. Specimen EW13

The only difference in design between specimens EW12 and EW13 was that the latter had a thicker plate (1.5 mm thick instead of 0.8 mm in specimen EW12).

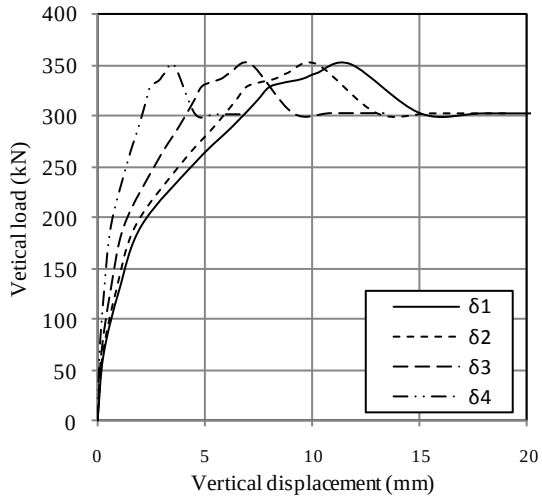

(a) Vertical displacements

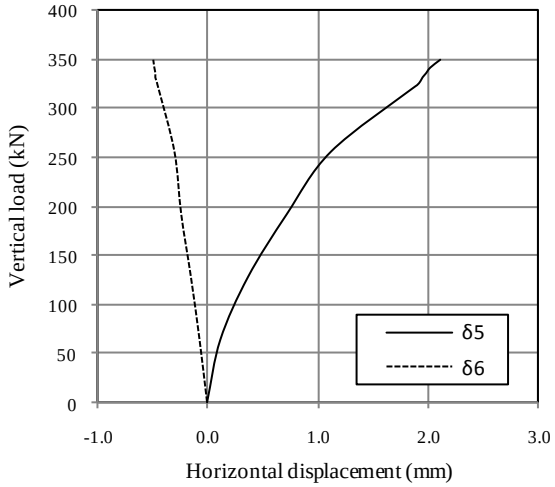

(b) horizontal displacements

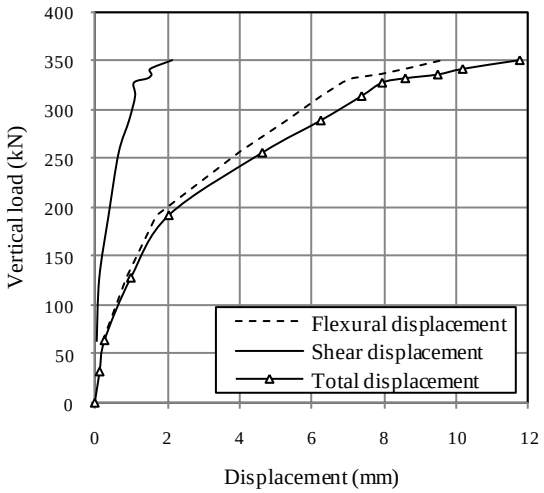

(c) Contributions of the flexural and shear displacement components to the total displacement

Figure 5.12 Specimen EW13: load-displacement behaviour patterns

The load-displacement behaviour patterns of the specimen are plotted in Figure 5.12. The flexural cracking of specimen EW13 was similar to EW12 as it started at 60 kN load. Subsequent loading resulted in the development and progression of flexural cracks in the tensile boundary element. Afterwards, when the applied load reached 100 kN, the flexural cracks penetrated the central panel. Additional flexural and shear (diagonal) cracks were observed with further load increments. Shear cracks ran diagonally and parallel to the first

inclined crack approaching the compression zone. A diagonal crack widened and its width continued to increase fast and became considerably bigger than other secondary diagonal cracks. Diagonal cracks were distributed evenly on the concrete surface with average spacing of about 100 mm. At a load of 350 kN, the specimen underwent failure with the formation of a diagonal tension failure plane. The crack pattern and specimen form after failure are plotted in Figure 5.13.

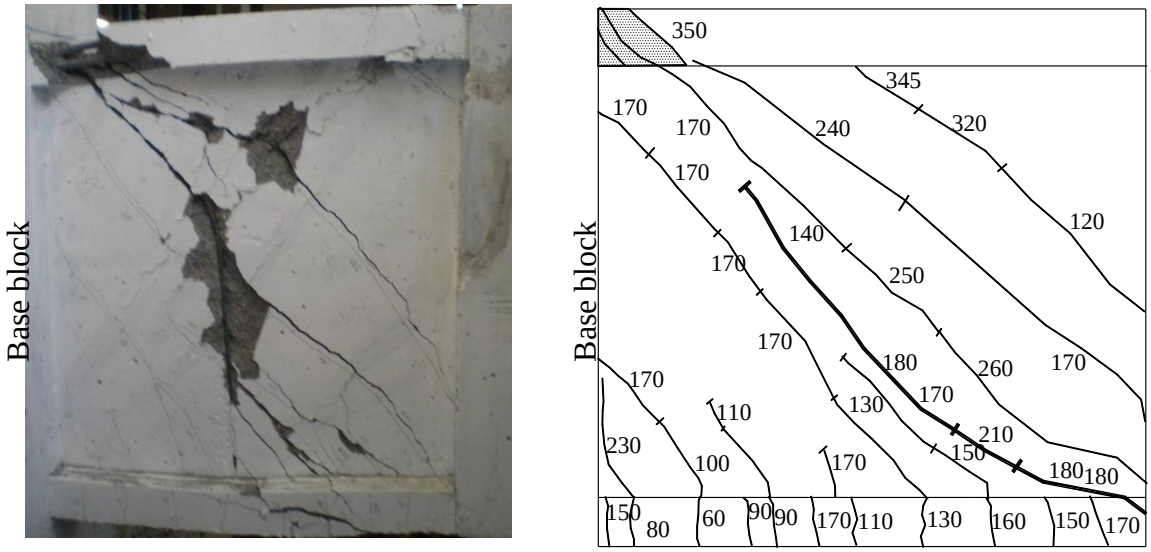

Figure 5.13 Specimen EW13: crack pattern at failure

As was observed in specimen EW12, no debonding between the encased-plate and the concrete was observed prior to failure. At failure, debonding was observed causing plate buckling and cover peeling leading to serious loss of web thickness in the vicinity of the buckled plate, causing a drop in load carrying capacity and overall failure, see Figures 5.12a and 5.14. Plate buckling was accompanied with buckling of stirrups and localised bending of reinforcement crossing the failure plane.

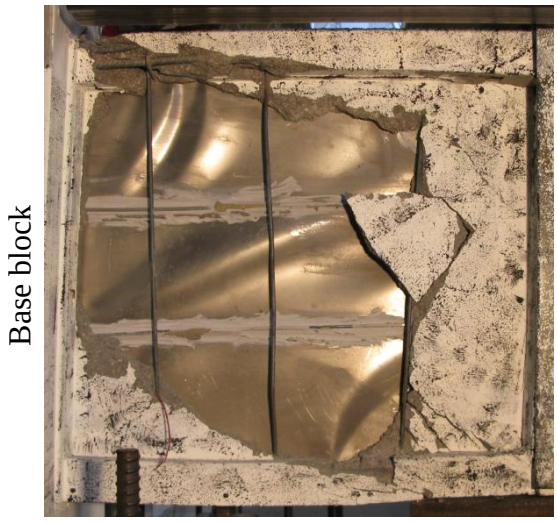

Figure 5.14 buckling of encased-plate and stirrups after failure

Figures 5.15 and 5.16 present the strain development in rebars and encased-plate in specimen EW13, respectively. The strain readings indicated that rebars in the tensile boundary element, R6 (Figure 5.2c), underwent yield at around 220 kN load, with a maximum recorded strain of about 0.0037 at failure, while compressive reinforcement yielded when the applied load reached 240 kN, Figure 5.15a. In contrast, central panel reinforcements did not yield untill failure took place with a maximum recorded strain of about 0.0011, Figure 5.15b.

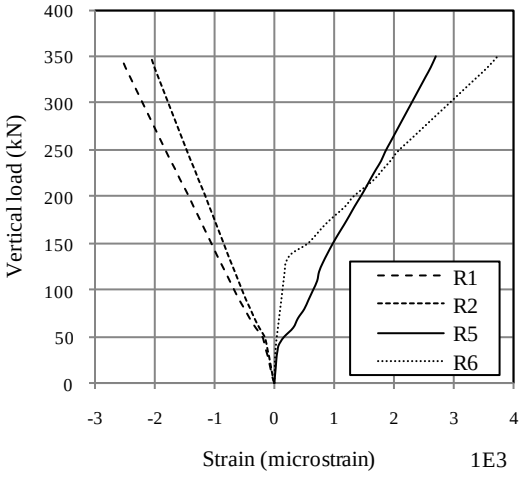

(a) Boundary elements

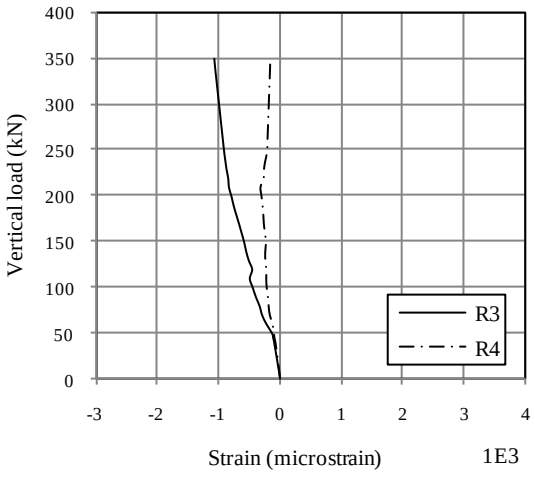

(b) Central panel

Figure 5.15 Specimen EW13: strain development in rebars

Figure 5.16a shows that the tensile yield of the plate developed at a load level of 280 kN with a maximum strain of 0.0029 at failure, while yield was observed in the compressive side at 320 kN load, with a maximum strain of 0.0023 at failure. However, plate strain gauges in the central panel did not detect yield till failure with a maximum strain of 0.0005, see Figure 5.15b. Gauge P7 (Figure 5.2c), which measured the transverse strain in the encased-plate, did not operate during the test

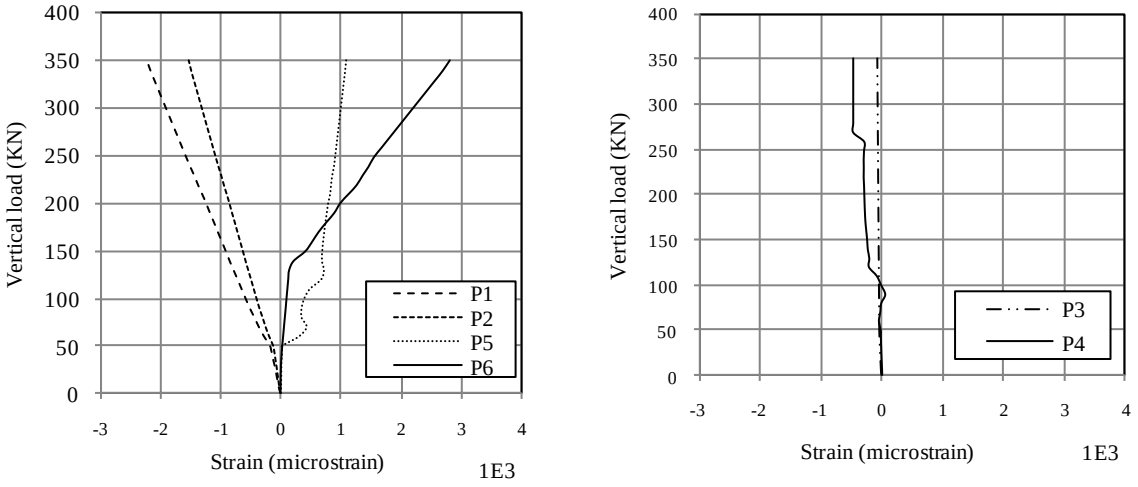

(a) Boundary elements (b) Central panel

Figure 5.16 Specimen EW13: strain development in encased-plate

D. Specimen EW21

This specimen had a rectangular cross-section and was conventionally-reinforced with a grid of longitudinal and transverse reinforcement as described in Section 4.5, and selected to act as a control specimen for the second group.

The load-displacement behaviour patterns of the specimen are presented in Figure 5.17. The first flexural crack was visible at 66 kN load in the tensile boundary element at point A in Figure 5.18. Extensive flexural cracking with average spacing of 50-75 mm became clear with further loading. The flexural cracks penetrated the central panel at a load level of 70 kN. Further load increments not only produced additional diagonal cracks, but also

extended and widened existing cracks. When the load reached 160 kN, several diagonal cracks formed and converged towards the compression edge of the wall. The crack pattern continued the same during the load range from 235 to 340 kN. Successive loading caused splitting and crushing of concrete cover in the extreme compressive edge of the specimen leading to overall failure at 365 kN- see detail B in Figure 5.19. The crack pattern and specimen form after failure are shown in Figure 5.18. The wall was considered to have failed in shear by diagonal compression.

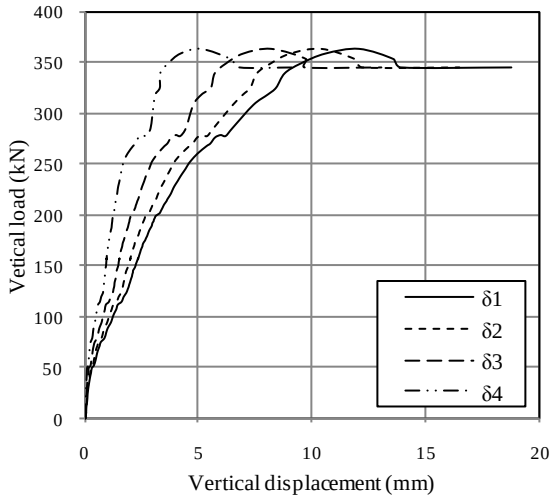

(a) Vertical displacements

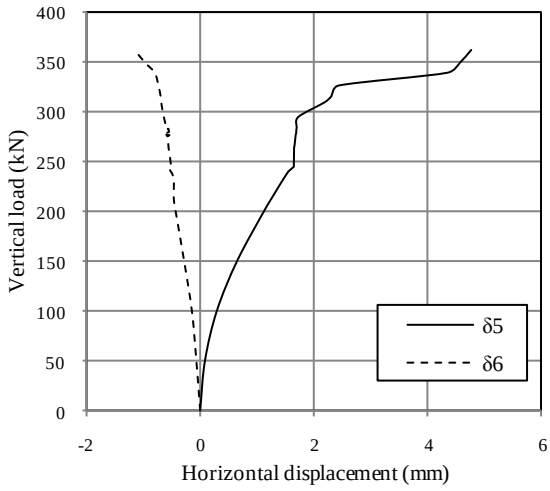

(b) horizontal displacements

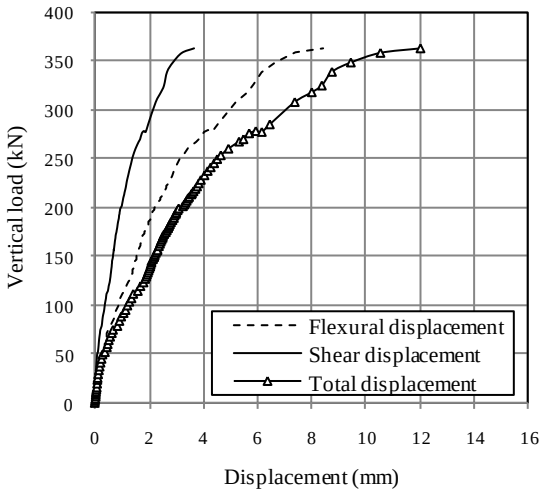

(c) Contributions of the flexural and shear displacement components to the total displacement

Figure 5.17 Specimen EW21: load-displacement behaviour patterns

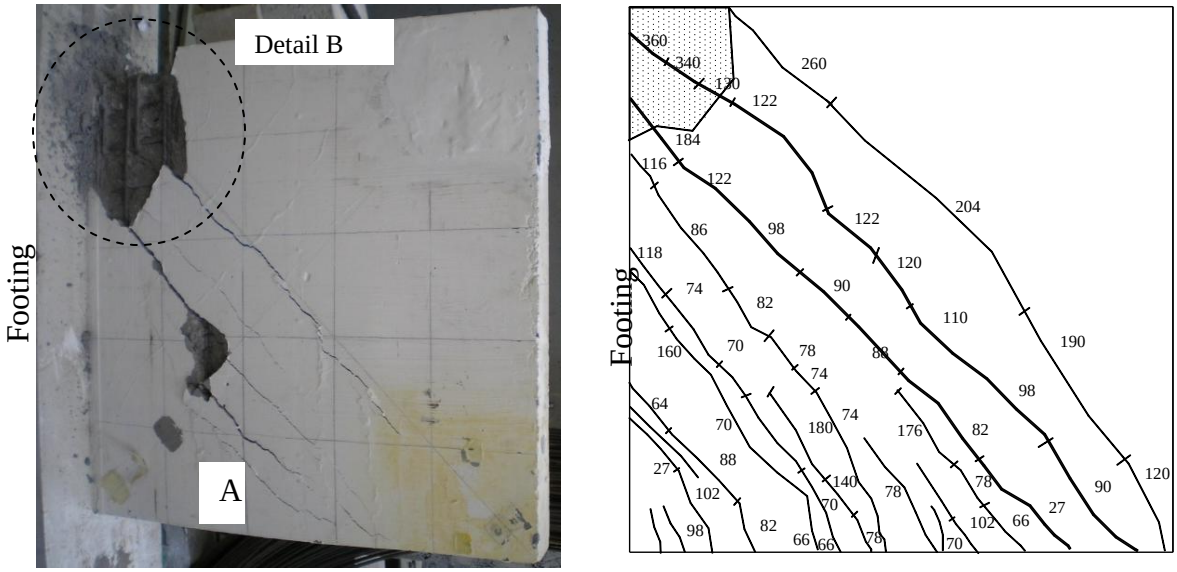

Figure 5.18 Specimen EW21: crack pattern at failure

Figure 5.19 Detail B, concrete crushing at compression zone

Strains in the longitudinal reinforcement of the boundary elements and the central panel are plotted against the vertical load in Figure 5.20. Yield of tensile reinforcement was detected at a load level of 175 kN. On the other hand, compressive reinforcement yielded at higher load (286 kN), with a maximum strain of around 0.002 at failure, see Figure 5.20a. All central panel rebars were subjected to tensile stresses and some of them yielded prior to failure as shown in Figure 5.20b.

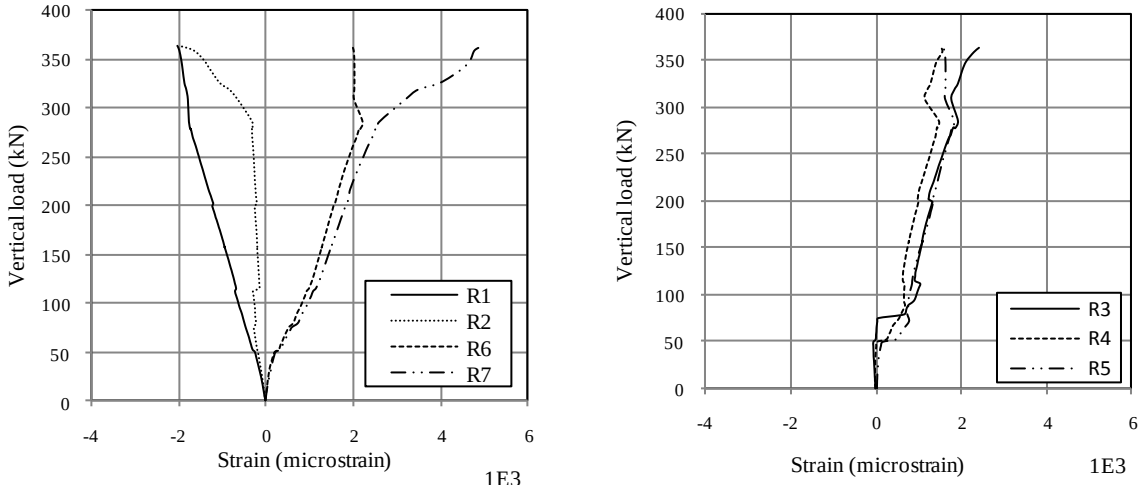

(a) Boundary elements (b) Central panel

Figure 5.20 Specimen EW21: strain development in rebars

E. Specimen EW22

Specimen EW22 had a rectangular cross-section and was identical to the control specimen EW21 in geometric dimensions and reinforcement layout but had a 0.8 mm thick plate.

The load-displacement behaviour patterns of the specimen are presented in Figure 5.21. The development of cracking in this specimen was almost identical to EW21 in the initial stage up to 70 kN. The first diagonal crack appeared in the central panel at 74 kN load, and subsequent loading resulted in development of scattered flexural cracks in the tensile boundary element with average spacing of about 35 mm. Afterwards, additional widely spread flexural and shear (diagonal) cracks were observed with further load increments. Shear cracks ran diagonally and parallel to the first inclined crack until they approached the compressive zone, but had an average crack width that was considerably higher than that of flexural cracks. Unfortunately, the connection between the wall and the footing started to crack parallel to the wall at 240 kN load, which might be attributed to the presence of some honeycombs in the connection region due to rebar congestion and inadequate vibration. At load level of 270 kN, full failure of the connection was observed with tensile reinforcement

and plate slippage from the footing. This was accompanied by large displacement at the top of tensile boundary element, δ5, see Figures 5.2b and 5.21b. At this time, the specimen suffered large displacement and no more load could be sustained. Failure was considered to be premature due to wall-footing connection failure. Neither debonding between the plate and concrete nor concrete crushing at the compressive edge was observed until the failure took place. The crack pattern and specimen form after failure are plotted in Figures 5.22 and 5.23.

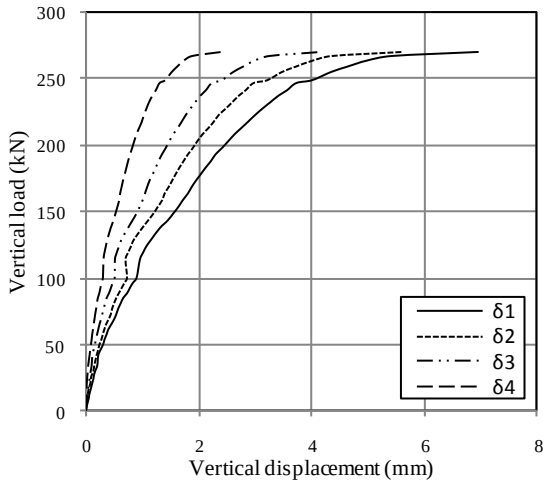

(a) Vertical displacements

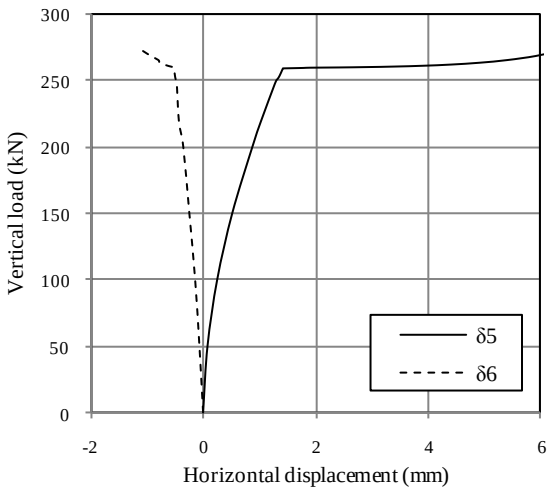

(b) horizontal displacements

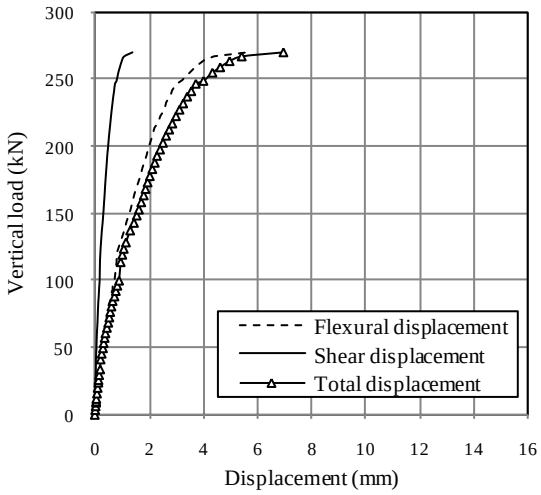

(c) Contributions of the flexural and shear displacement components to the total displacement

Figure 5.21 Specimen EW22: load-displacement behaviour patterns

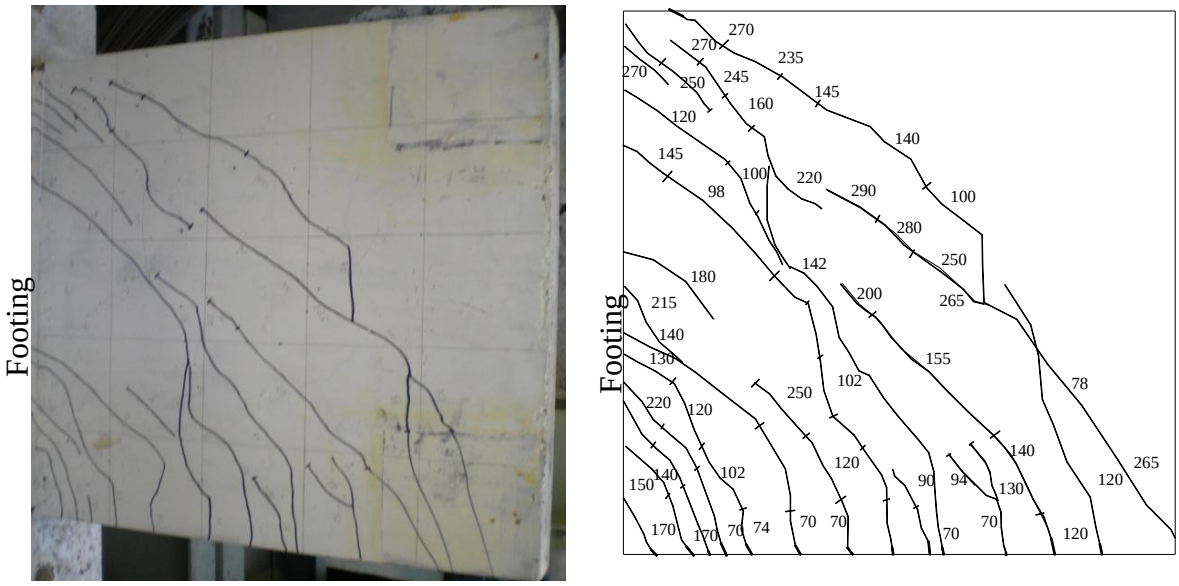

Figure 5.22 Specimen EW22: crack pattern at failure

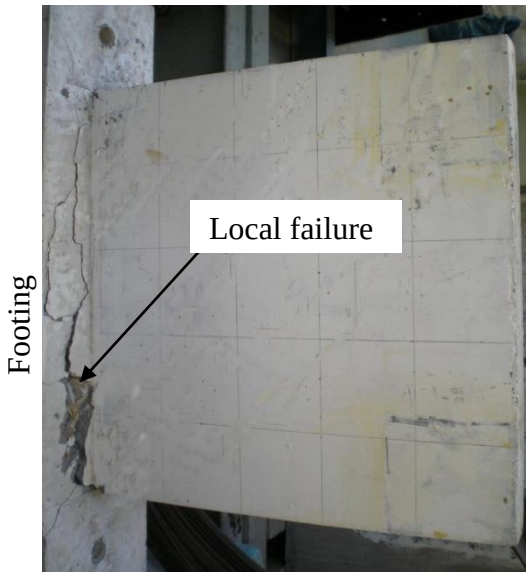

Figure 5.23 Premature failure of the specimen EW22

Fourteen strain gauges were attached to the rebars and the encased-plate to monitor strain development as shown in Figure 5.2e. Figure 5.24 depicts the strain development in the rebars of specimen EW22. Although the specimen failed prematurely, strain readings showed that yielding of tensile reinforcement was reached at 184 kN load, while compressive flexural reinforcement yielded at around 242 kN load. All central panel strain gauges showed linear response with small strain values remaining below 0.0013.

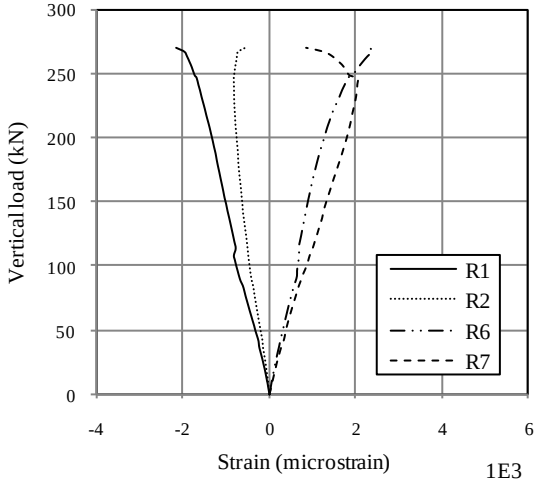

(a) Boundary elements

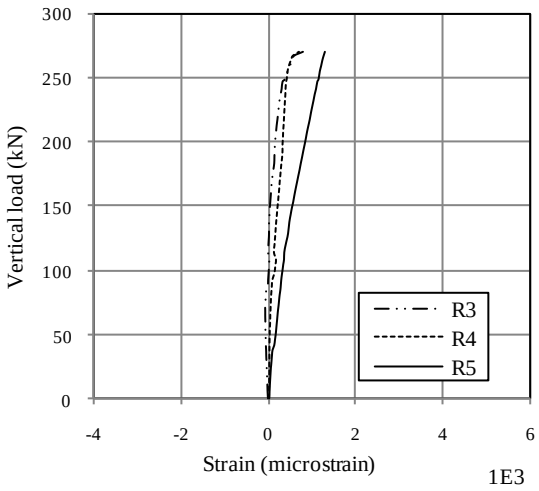

(b) Central panel

Figure 5.24 Specimen EW22: strain development in rebars

Measured strains in the encased-plate in wall EW22 are depicted in Figure 5.25. The figure shows the linear behaviour of the plate in the boundary elements until 250 kN load with yielding taking place almost at test termination. No yielding was observed in the encased-plate in the central panel with a maximum strain of about 0.0012 at 270 kN load.

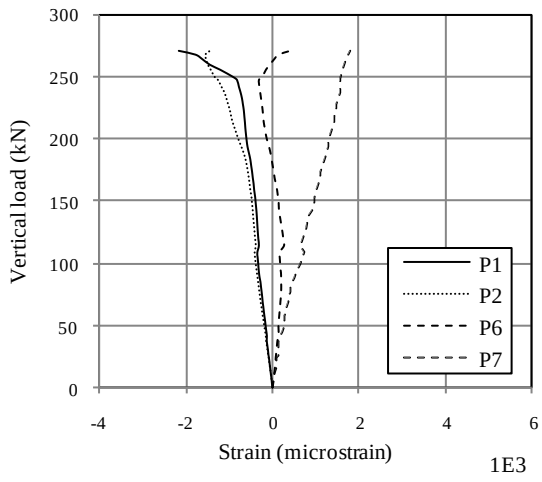

(a) Boundary elements

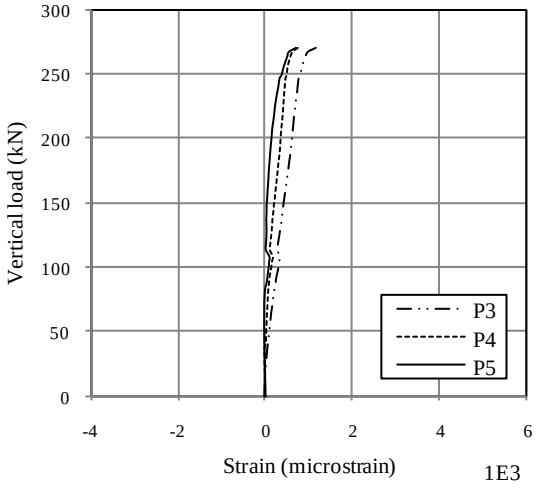

(b) Central panel

Figure 5.25 Specimen EW22: strain development in encased-plate

F. Specimen EW23

Specimen EW23 was identical to specimen EW22 but reinforced with a plate of 1.5 mm thickness instead of the 0.8 mm plate used in specimen EW22.

The load-displacement behaviour patterns are depicted in Figure 5.26. Unlike all other specimens, which were tested at around 28 days, this specimen was tested after 3 months.

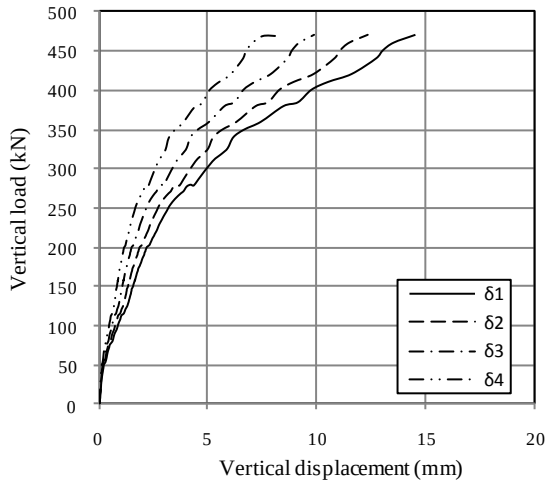

(a) Vertical displacements

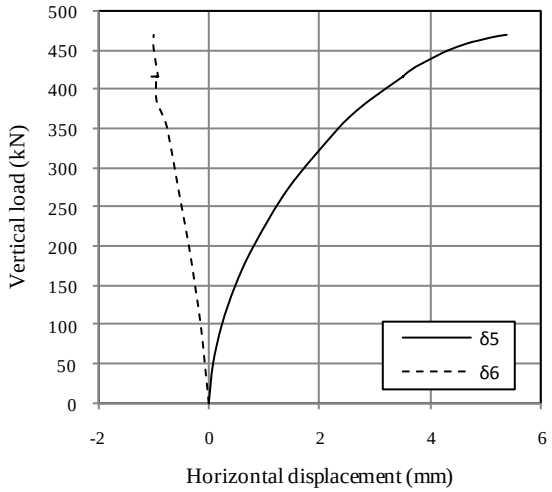

(b) horizontal displacements

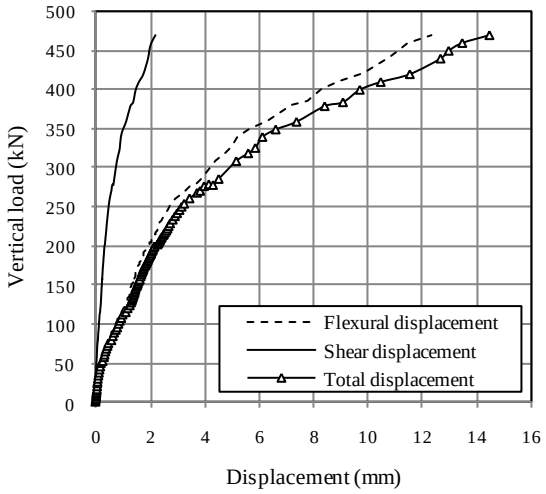

(c) Contributions of the flexural and shear displacement components to the total displacement

Figure 5.26 Specimen EW22: Load-displacement behaviour patters

The first flexural crack appeared vertically in the tensile boundary element at a load level of 100 kN. The first cracking load was substantially higher (51%) than that of specimen EW21, partly due to the difference in age at the time of testing which affects the concrete strength and splitting stress. Subsequent loading resulted in development of scattered flexural cracks in the tensile boundary element near the footing as shown in Figure 5.27. Afterwards, when the applied load reached 120 kN, the first inclined crack appeared in the central panel. Additional flexural and diagonal cracks were observed with further load increments. Shear cracks ran diagonally and parallel to the first inclined crack until they approached the compressive side.

Cracks were distributed on the concrete surface with average spacing of about 45 mm. At higher loads, some cracks appeared on the compressive boundary element in the area near the point of load application. At this stage, a vertical crack was also observed in the end section of the wall. As the load progressed further, a longitudinal crack initiated on the bottom edge of the wall, see Figure 5.28. Major shear cracks ran diagonally from the point of load application and penetrated the compressive zone. When the applied load reached 470 kN, the vertical crack in the wall end section extended until it reached the compressive edge of the wall, resulting in splitting of the wall in two parts with loud sound and a sharp drop in load carrying capacity was observed, see Figures 5.26a and 5.27. Debonding was clearly observed and caused plate buckling in the end section, see Figures 5.27 and 5.28.

No buckling was observed in compressive reinforcement while concrete crushing in the compressive zone was noted. The crack pattern and specimen form after failure are shown in Figures 5.27 and 5.28. Failure of this wall was localised due to stress concentration at the point of load application, leading to splitting of the wall end section.

Figure 5.27 Specimen EW23 after failure

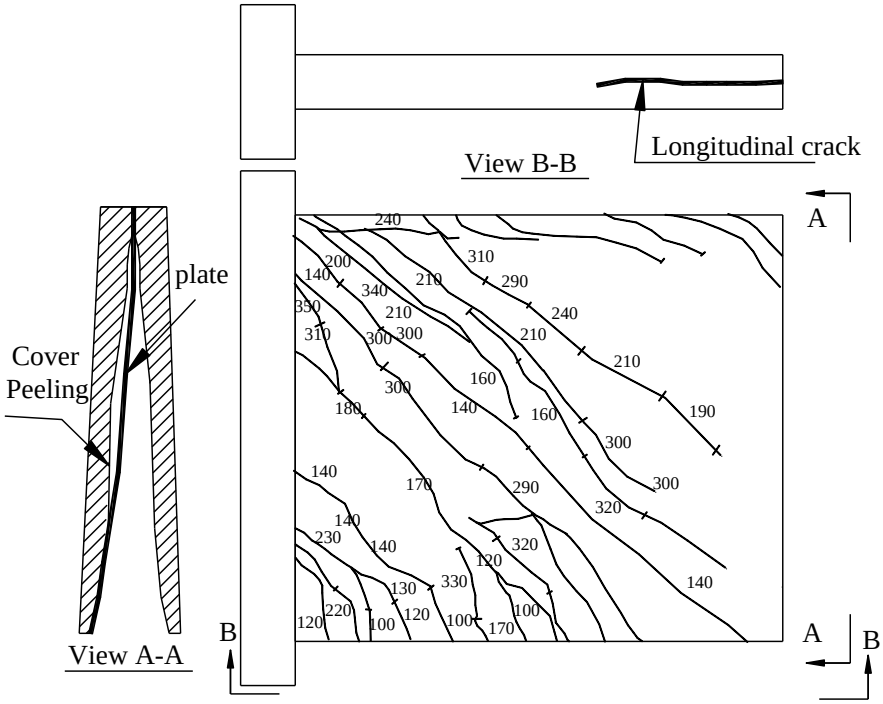

Figure 5.28 Specimen EW23: Crack pattern for specimen at failure

Figures 5.29 and 5.30 present the strain development in rebars and encased-plate in specimen EW23, respectively. Observations from strain readings indicated that tensile

reinforcement in the boundary element, R7, yielded at around 247 kN load, while compressive reinforcement, R1, yielded at 345 kN load, Figure 5.29a. In contrast, the central panel reinforcement behaved linearly until failure and did not experience yield, see Figure 5.29b. The readings of the strain gauges attached to the encased-plate were similar to those in the adjacent rebars, see Figure 5.30

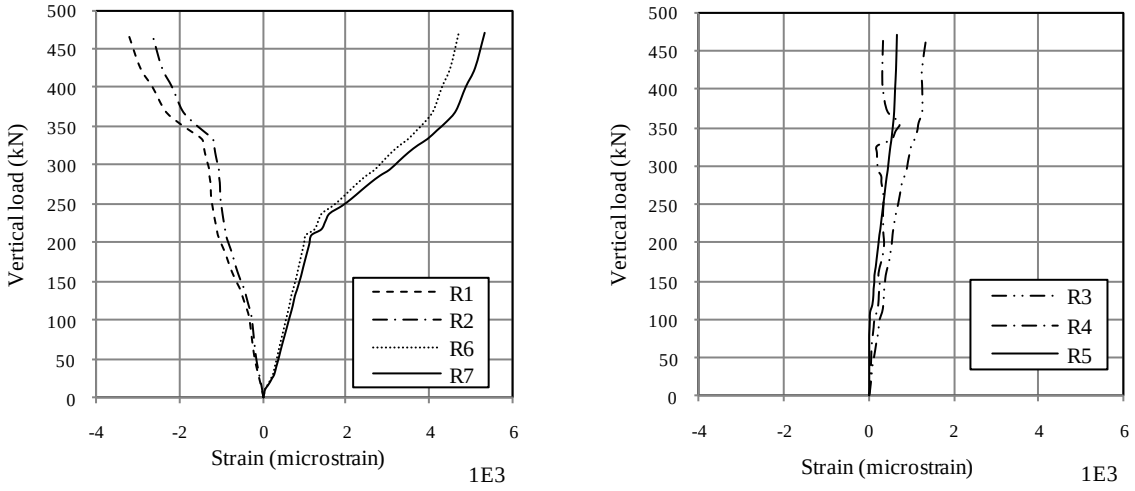

(a) Boundary elements (b) Central panel

Figure 5.29 Specimen EW23: Strain development in rebars

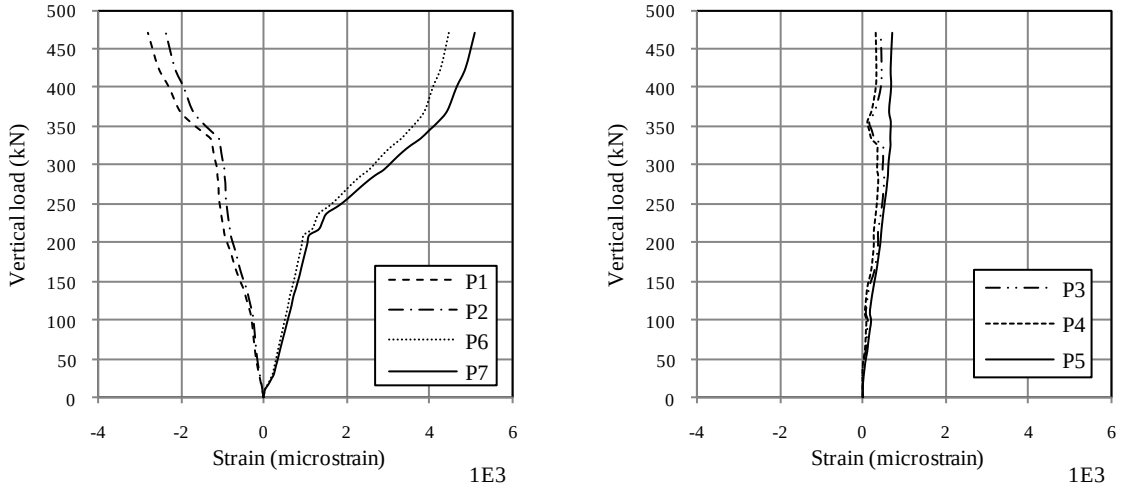

(a) Boundary elements (b) Central panel

Figure 5.30 Specimen EW23: Strain development in encased-plate

G. Specimen EW31

Specimen EW31 had a rectangular cross-section with height-to-width ratio of 1.67. The specimen was reinforced with a grid of rebars and a 1 mm thick plate. The specimen was designed to fail in flexure. The load-displacement behaviour patterns are depicted in Figure 5.31.

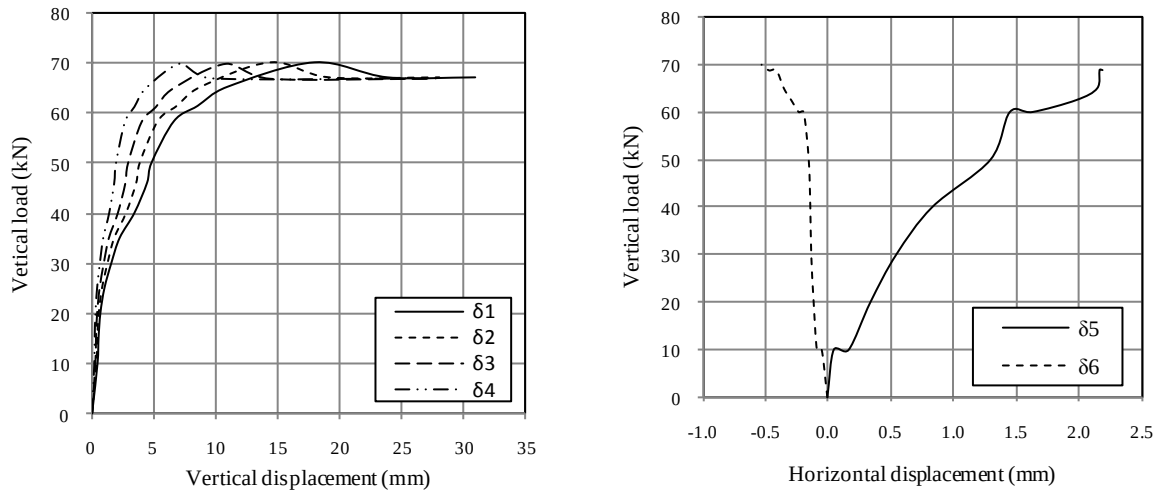

(a) Vertical displacements (b) horizontal displacements

Figure 5.31 Specimen EW31: load-displacement behaviour patterns

Flexural cracks started early in the tensile boundary element of the specimen after the application of 9 kN load. Further loading resulted in developing of additional vertical flexural cracks in the tensile boundary element with average spacing of about 100 mm. Increasing the vertical load caused the extension of flexural cracks vertically in the central panel and the first shear crack started at a load of 21 kN with a slight inclination towards the compressive side. Flexural cracks at the wall boundary were denser than cracks in the central panel area. When the load reached 28.5 kN, a major flexural crack appeared vertically in the wall near the footing, see Figure 5.32a. No new cracks were observed after a load level of 55 kN until failure. As the applied load was increased further, the major flexural crack penetrated the compressive edge of the wall. When the load reached 66.5 kN,

spalling of the concrete cover of the extreme compressive edge of the wall was clearly noticed with increases in the major flexural crack width up to 4 mm, see Figure 5.32. This led to the progressive failure of the compressive zone of the wall and the drop of the load carrying capacity of the specimen, see Figure 5.32b. The specimen failed when the vertical load reached 70 kN with a flexural mode of failure. The crack pattern and specimen form after failure are shown in Figure 5.33. No buckling or localised bending of rebars was observed at failure. Also, the plate did not show any debonding or buckling throughout the test.

(a) major flexural cracking (b) concrete crushing

Figure 5.32 Cracking of specimen EW31

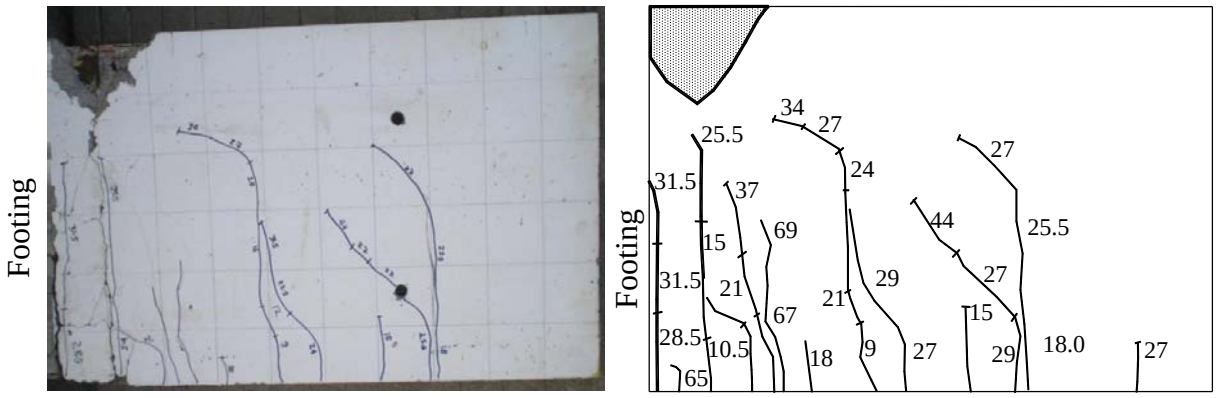

Figure 5.33 Crack pattern and specimen form after failure

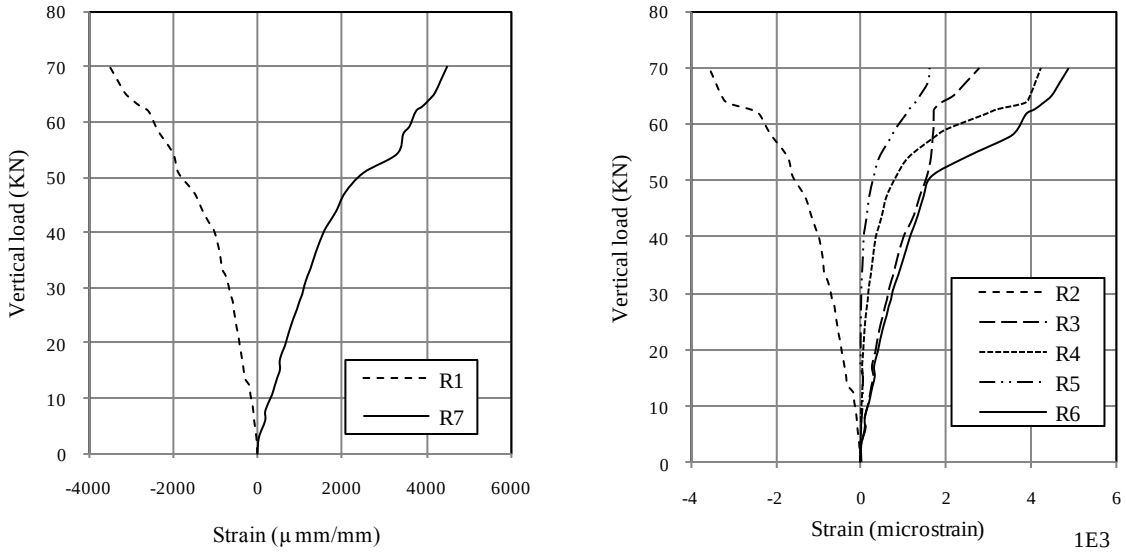

(a) Boundary elements (b) Central panel

Figure 5.34 Specimen EW31: Strain development in rebars

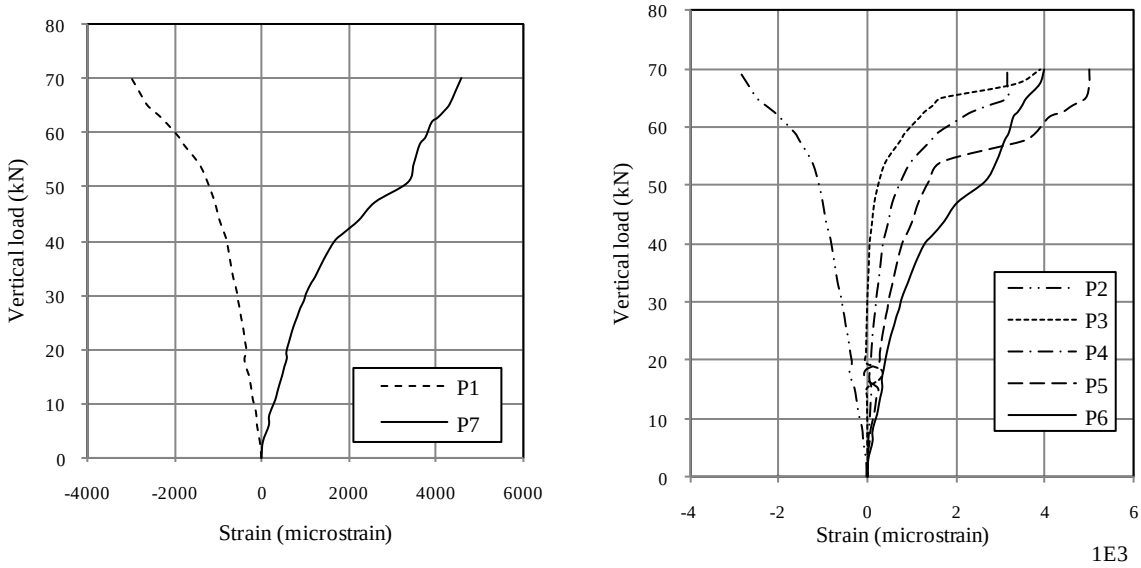

(a) Boundary elements (b) Central panel

Figure 5.35 Specimen EW31: Strain development in encased-plate

Figures 5.34 and 5.35 depict the strain development in the rebars and the encased-plate in specimen EW31, respectively. Figure 5.34a suggests that the tensile rebars yielded at 42 kN load, while compressive reinforcement yielded at the higher level of load of 51 kN. All strain gauges in central panel reinforcements showed linear response until the load reached

50 kN and most of them yielded at around 58 kN, see Figure 5.34b. Similarly, Figure 5.35a shows that the first yield at the tensile edge of the plate occurred at 42 kN load. All the strain gauges mounted to the plate except P2 detect tensile strains and most of them yielded before failure, see Figure 5.35b.

The main results obtained from the tests are summarised in Table 5.1 which contains the values of vertical load, F_v, the maximum vertical displacement at wall end, δ, the secant stiffness, K, and the drift index, γ, at (1) the start of flexural cracking; (2) the start of inclined cracking; (3) the first yield of the tensile reinforcement, (4) the first yield of the plate in the tension side, and (5) the ultimate limit state.

5.2.3 PIV results

The PIV technique was also used to monitor the full-field displacement of the specimens during the test. The technique was available for use with three specimens only; EW11, EW13 and EW23. The performance of the technique was assessed first by comparing the vertical displacement obtained from LVDT 1 (δ1) with the corresponding values obtained from the PIV technique as shown in Figure 5.36. The results show that the PIV measurement technique yielded a reasonable estimation of the vertical displacement when compared to the LVDT readings.

In order to investigate the principal strains on the concrete surface, a mesh comprising 210 patches were distributed across the images. The vector fields on the deformed shape of the specimens are plotted in Figure 5.37. The vector fields confirmed the formation of the diagonal tension failure plane in specimens EW11 and EW13 which failed in shear by diagonal tension and could not be seen in specimen EW23 which failed due to local failure at the point of load application.

The plots of the shear strain, minor and major principal strains at failure for specimens EW11 and EW23 are depicted in Figure 5.38. The shear and principal strains in specimen EW11 confirmed the formation of the diagonal tension failure plane, while those in specimen EW23 clearly show the formation of a main diagonal crack across the specimen and concrete crushing in the compression zone.

Table 5.1Principle experimental results of tested specimens at different load stages

Specimen		First group			Second group			Third group
		EW11	EW12	EW13	EW21	EW22	EW23	EW31
(1) start of flexural cracking	F_V (kN)	40.00	60.00	60.00	66.00	70.00	100.00	9.00
	δ (mm)	0.43	0.41	0.27	0.57	0.51	0.72	0.44
	K (kN/mm)	93.00	146.30	222.20	115.8	137.25	138.90	20.45
	γ (%)	0.057	0.055	0.04	0.08	0.07	0.10	0.04
(2) start of diagonal cracking	F_V (kN)	50.00	80.00	100.00	70.00	74.00	120.00	21.00
	δ (mm)	0.73	0.63	0.42	0.63	0.54	1.18	0.67
	K (kN/mm)	68.50	127.00	238.1	111.10	137.04	101.70	31.34
	γ (%)	0.097	0.084	0.056	0.084	0.072	0.16	0.067
(3)First yield of tensile rebars	F_V (kN)	130.00	190.00	220.00	175.00	184.00	247.00	42.00
	δ (mm)	3.28	3.10	3.07	2.63	2.13	3.09	4.35
	K (kN/mm)	39.64	61.30	71.70	66.54	86.40	79.94	10.07
	γ (%)	0.44	0.41	0.41	0.35	0.28	0.41	0.44
(4) First yield of plate in tension	F_V (kN)	--	190.00	280	--	270.00	247	42.00
	δ (mm)	--	3.10	6.26	--	6.97	3.09	4.35
	K (kN/mm)	--	61.30	44.72	--	38.74	79.94	10.07
	γ (%)	--	0.41	0.83	--	0.93	0.41	0.44
(5) Ultimate limit state	F_V (kN)	180.00	280.00	350.00	365.00	270.00*	470.00	70.00
	δ (mm)	5.06	11.00	11.77	12.05	6.97	14.50	18.00
	K (kN/mm)	35.60	25.46	29.73	30.29	38.74	32.42	3.89
	γ (%)	0.67	1.46	3.36	1.61	0.93	1.93	1.80

*Premature failure

- F_V= vertical load (kN)
- δ= maximum vertical displacement at wall end
- h_W= wall height (mm)
- K= secant stiffness (kN/mm)= F_V/ δ
- γ = drift index= 100*(δ/h_W)

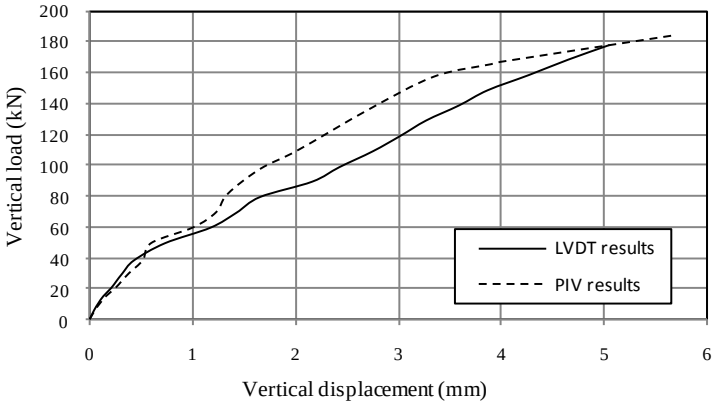

(a) Specimen EW11

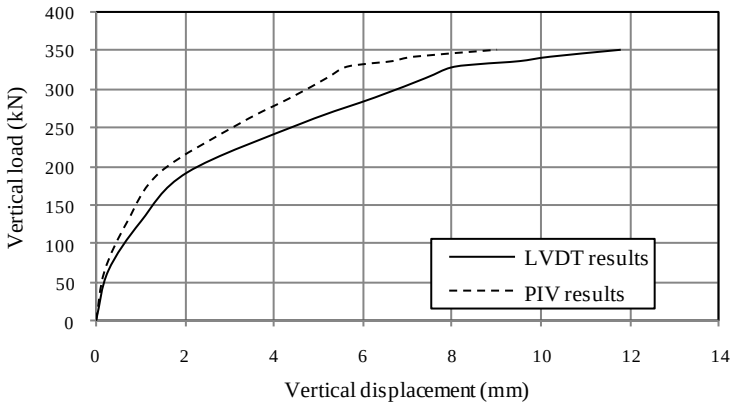

(b) Specimen EW13

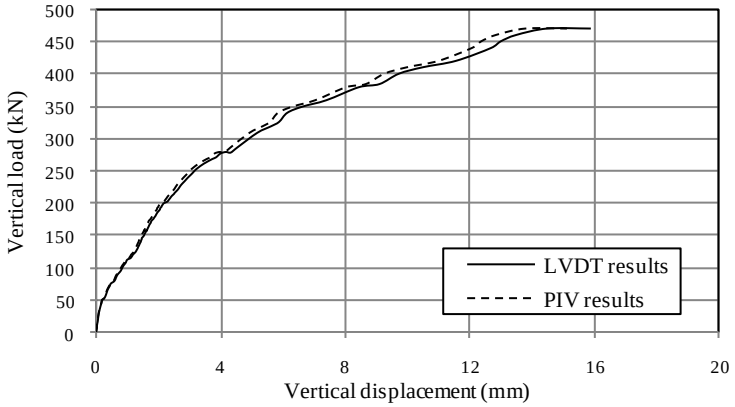

(c) Specimen EW23

Figure 5.36 Vertical load-displacement behaviour as obtained from LVDT measurement and PIV analysis

Deformed shape and displacement vector plots at failure

Specimen form at failure

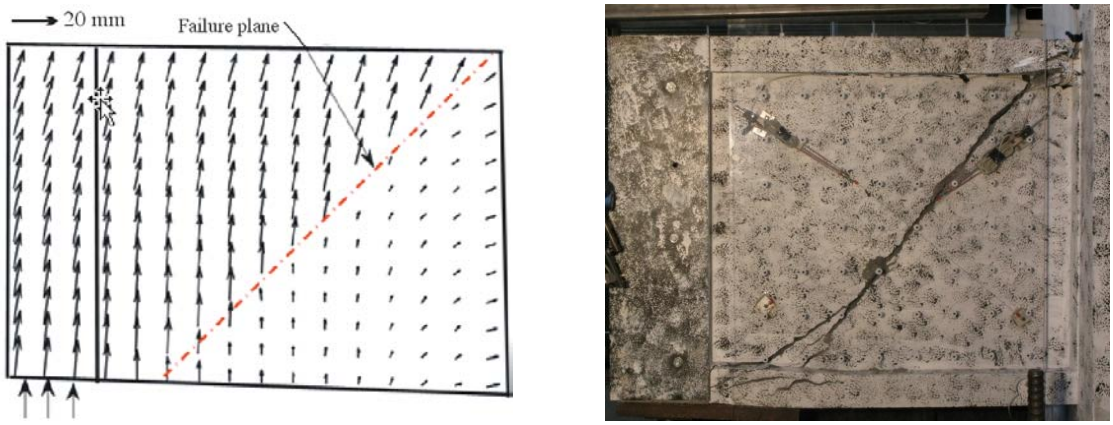

(a) Specimen EW11

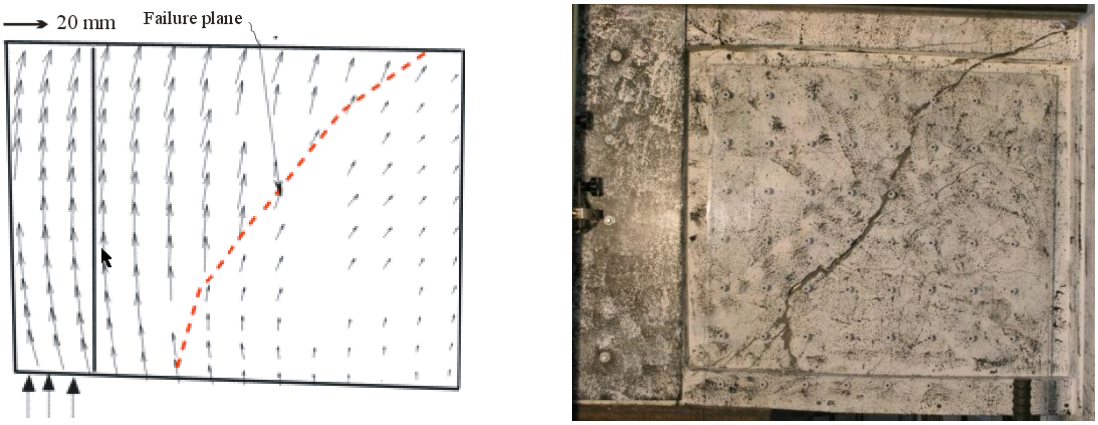

(b) Specimen EW13

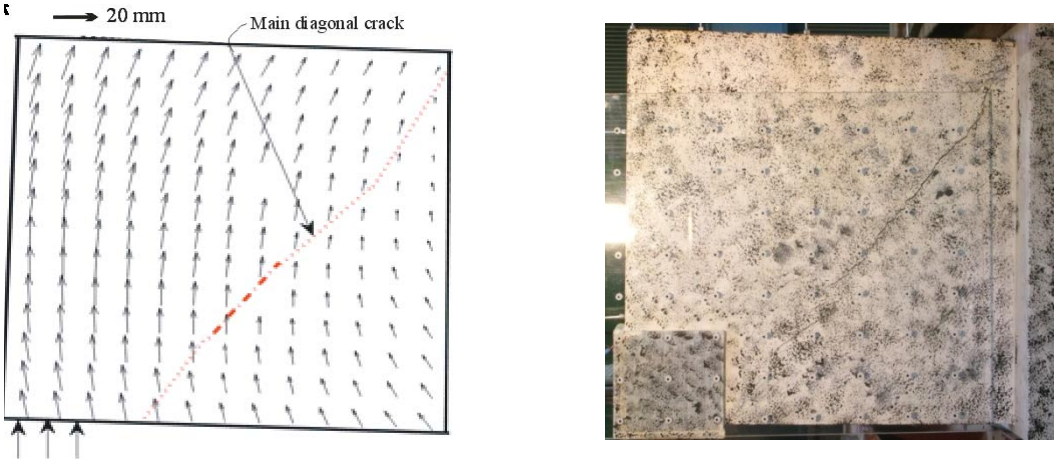

(C) Specimen EW23

Figure 5.37 Deformed shape and vector fields after failure

(1) Specimen EW11 (2) Specimen EW23

(a) specimen form at failure

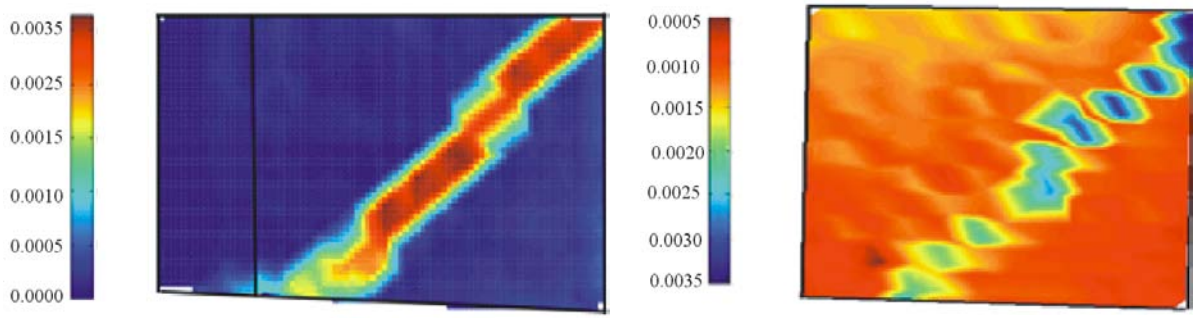

(b) Shear strains at failure

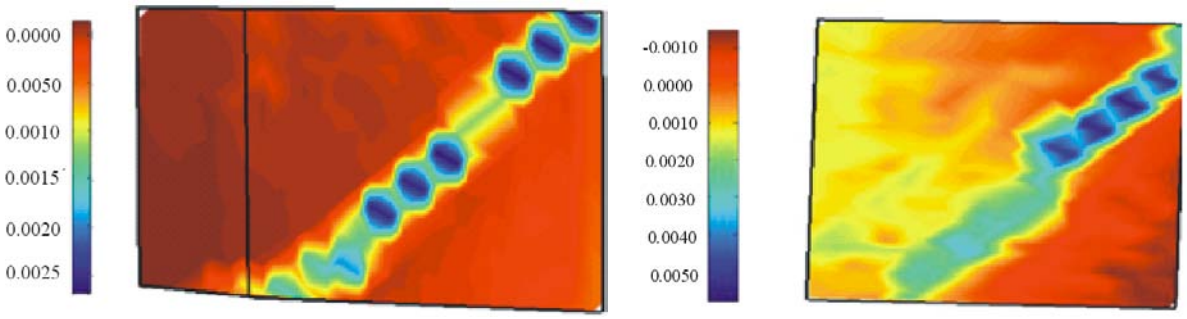

(c) Minor principal strains at failure

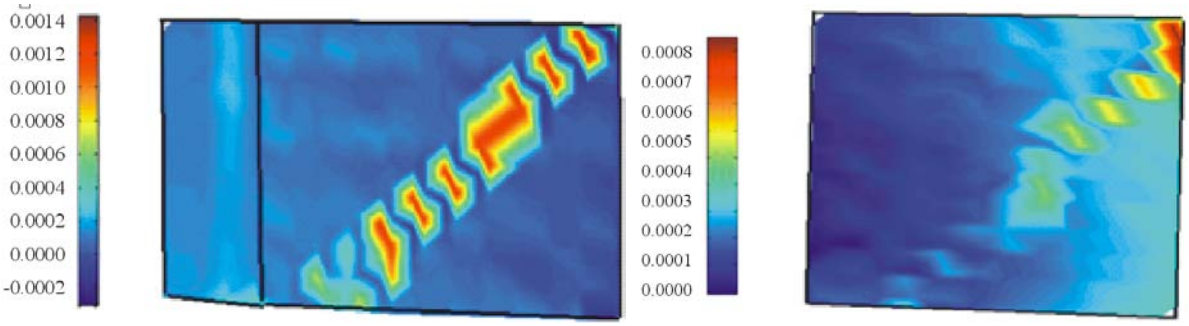

(d) Major principal strains at failure

Figure 5.38 Shear and principal strains obtained from the PIV analysis

5.3 Analysis and discussion of experimental results

This section contains a discussion of the experimental results obtained from testing the seven wall specimens. Out-of-plane displacements and base block and footing rotations were assessed to check the performance of the test rig. A comparative study of the mode of failure, deformation characteristics and load carrying capacity is presented in detail. Strain distribution in rebars and encased-plates was used to estimate the neutral axis depth and to assess the efficiency of composite action between the encased-plates and the rebars.

5.3.1 Out-of-plane displacements

A number of transducers were used to assess the out-of-plane displacement of specimen and base block and footing. Out-of-plane displacements may be caused by misalignment of specimens in the test rig or imperfections in specimens' construction. All out-of-plane displacements recorded were below 0.02% of specimen height, indicating they were insignificant and had a negligible effect on specimen behaviour.

5.3.2 Base block and footing rotation

In the test rig assembly, base block and footing rotation were unavoidable since the stiffness of the upper reaction beams and the prestressing rebars was not infinite. Three transducers were used to assess the displacement and rotation of the base block and the footing of the specimens during the test as described in Section 4.8.2. Since the rotation of the base block and footing was monitored during the test, its effect on all other displacements could be estimated and eliminated only after the test. Consequently, all the results presented in this chapter were prepared after eliminating the effect of the rotation of the base block and footing.

5.3.3 Strain compatibility between encased-plates and rebars

In an attempt to assess the efficiency of composite action between the encased-plates and the rebars, strain gauges were placed at almost the same level. Figure 5.39 plots the results of pairs of strain gauges positioned at the same location on the encased-plate and the rebars. The figure depicts a good match between strains in the encased-plate and the rebars, which reflects the efficiency of the used glue.

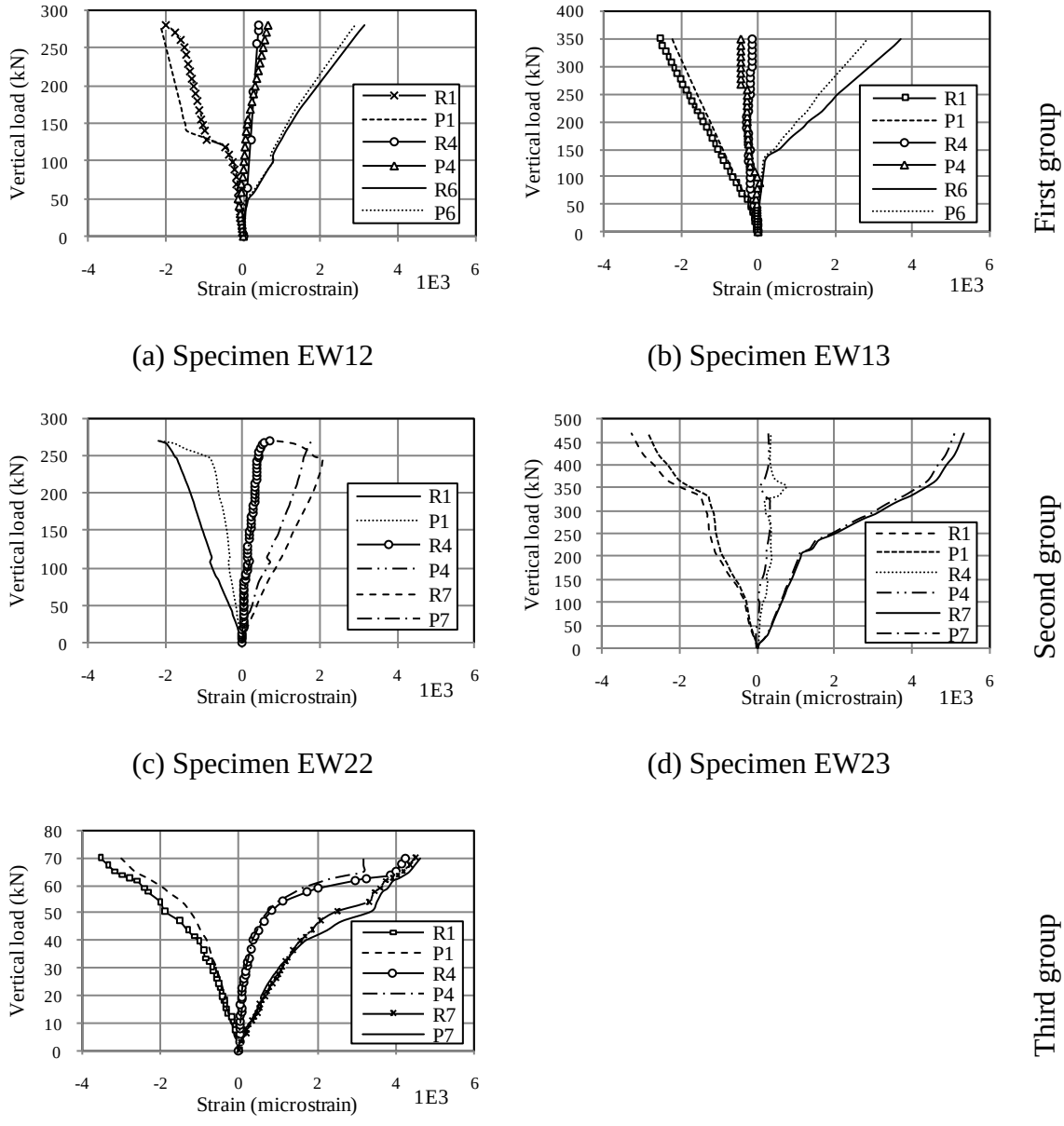

(a) Specimen EW12

(b) Specimen EW13

(c) Specimen EW22

(d) Specimen EW23

(e) Specimen EW31

Figure 5.39 Compatibility between strains in rebars and encased-plates

5.3.4 Strain distribution and neutral axis depth

The strain readings recorded during the test were used to plot the strain distribution along the wall width and to assess the variation of the neutral axis depth as the vertical load increased. Figure 5.40 shows the distribution of strain in the rebars and encased-plates along the wall width at different load increments. The neutral axis depth was estimated based on the strain distribution in rebars and encased-plate. Table 5.2 presents the values of the neutral axis depth as obtained from Figure 5.40 and the normalised values of neutral axis depth with respect to the wall width.

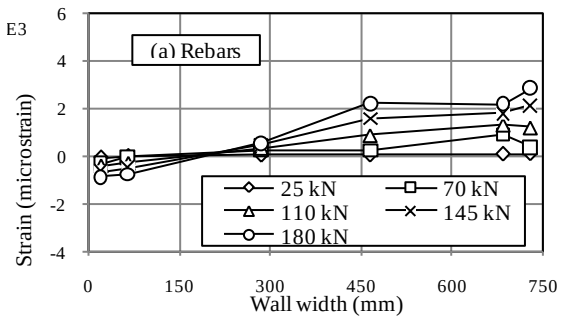

(a) Specimen EW11

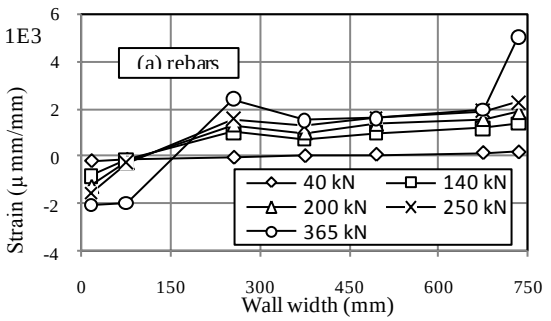

(b) Specimen EW21

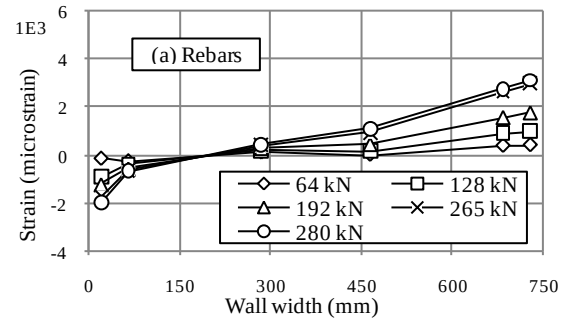

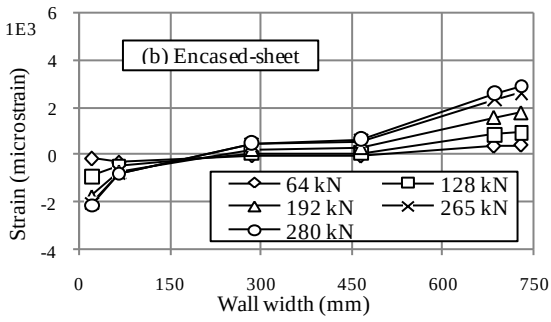

(c) Specimen EW12

Figure 5.40 Distribution of strains in rebars and encased-plates along wall width

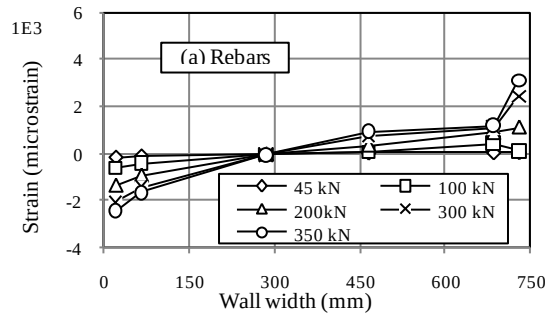

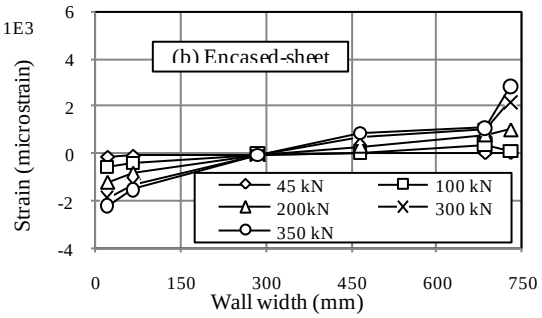

(c) Specimen EW13

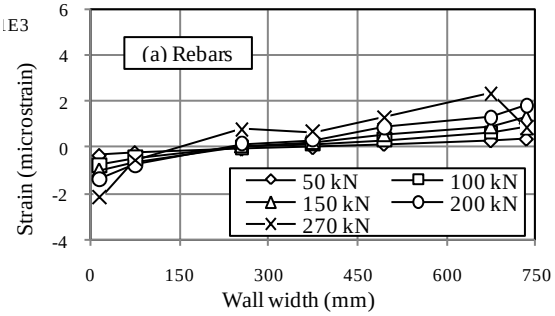

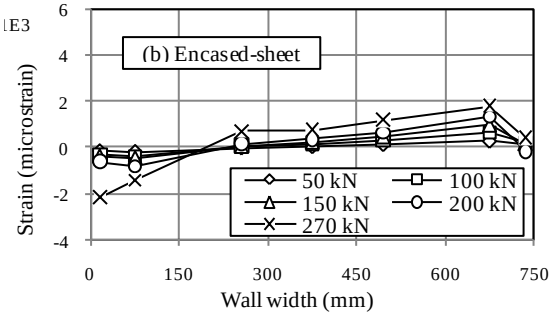

(d) Specimen EW22

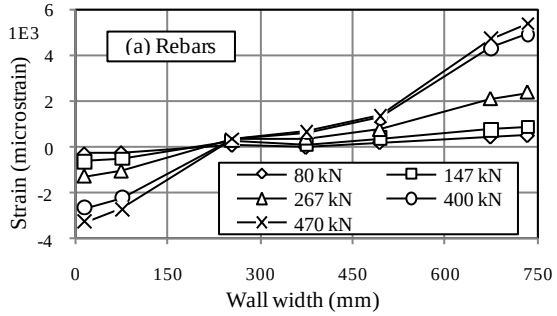

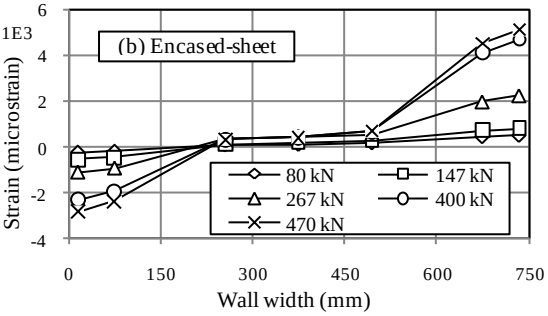

(e) Specimen EW23

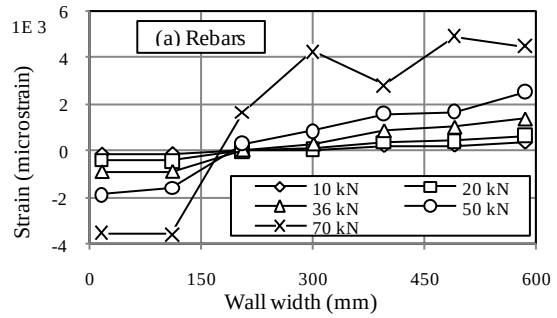

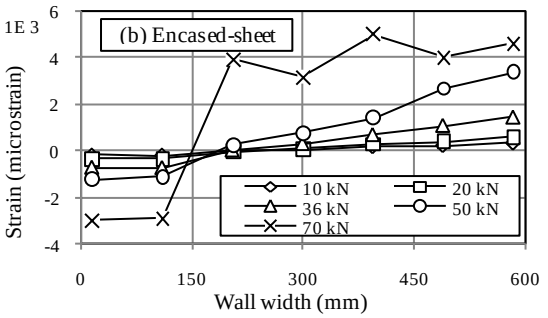

(f) Specimen EW31

Figure 5.40 Distribution of strains in rebars and encased-plates along wall width (cont.)

Table 5.2 Neutral axis depth of test walls

Specimen	Cross-section shape	Plate thickness (mm)	Neutral axis depth (mm)	Neutral axis depth/wall width
EW11	Flanged	0.00	178.00	0.24
EW12	Flanged	0.80	211.00	0.28
EW13	Flanged	1.50	290.00	0.38
EW21	Rectangular	0.00	85.00	0.11
EW22	Rectangular	0.80	205.00	0.27
EW23	Rectangular	1.50	245.00	0.33
EW31	Rectangular	1.00	205.00	0.34

Using the data in Table 5.2 and Figure 5.40, the following significant features can be observed:

- The neutral axis shifted away from the centre of wall's cross-section due to concrete cracking;
- Before first yield of reinforcement, the strains in the rebars and the encased-plates were directly proportional to the distance from the neutral axis, i.e. the assumption of plane section was valid, while after first yield the distribution of strain became nonlinear;
- As the vertical load increased, the depth of the neutral axis decreased slightly. The decrease in the neutral axis depth was attributed to the accumulation of plastic strains in the rebars and encased plates and widening of cracks;
- The use of encased-plates was associated with an increase in the depth of the neutral axis, i.e. as the plate thickness increased, the neutral axis depth increased.

5.3.5 Modes of failure

The term failure mode is used to describe the manner in which overall failure took place and the physical reasons behind it. The mode of failure of a structural wall depends on a number of factors such as geometrical dimensions, material properties, cross-sectional shape, details of reinforcement and boundary conditions.

A. Flexural failure

Flexural failure usually occurs in tall cantilever walls with high aspect (height-to-width) ratios. This type of failure takes place when the flexural capacity is much lower than the shear capacity. In the current test programme, flexural cracks appeared in the tensile boundary elements at a relatively small load [as marked by number 1 in Figure 5.41]. As the load progressed, additional flexural cracks penetrated the central panel and extended towards the compression zone [as marked by numbers 2 and 3]. The failure was characterised by excessive yielding of tension reinforcement and plate and widening of flexural cracks accompanied with crushing of concrete in the most compressed zone [as marked by number 4]. This mode of failure was observed in specimen EW31.

B. Shear failure

Three main types of shear-dominant failures are usually observed in reinforced concrete structural walls with low aspect ratio namely; diagonal tension, diagonal compression and sliding shear. Only diagonal tension and diagonal compression failures were observed in the test specimens.

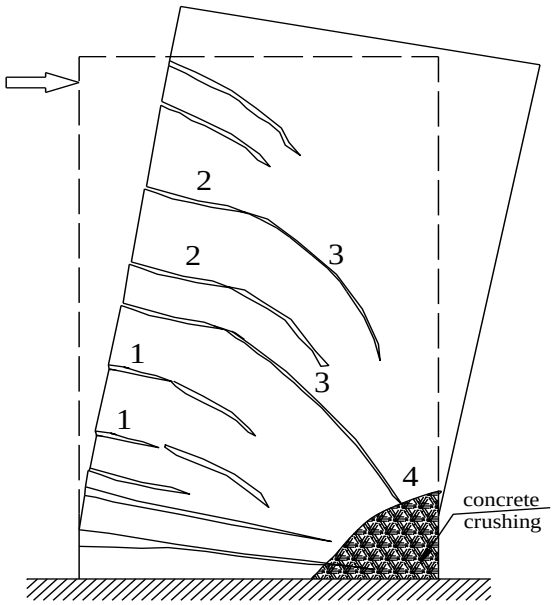

Figure 5.41 Flexural Failure of cantilever walls*

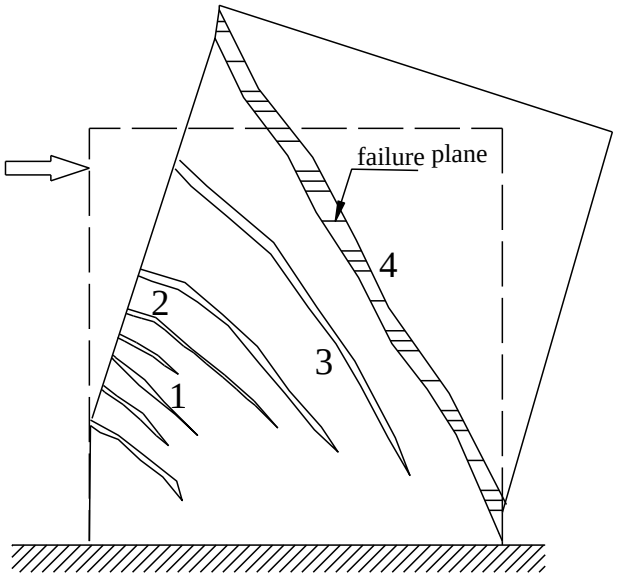

Figure 5.42 Diagonal tension failure

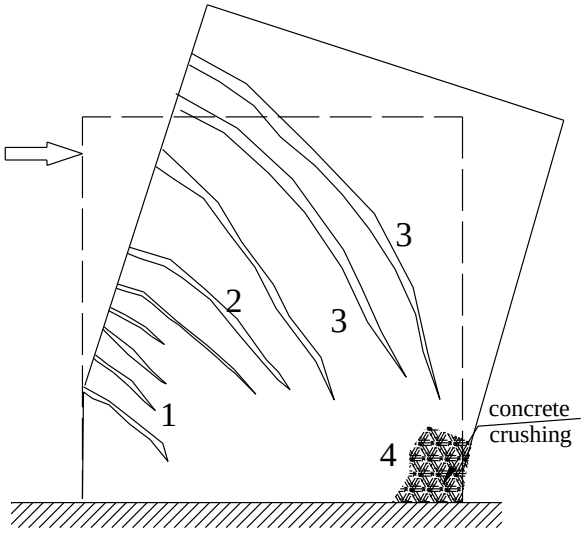

Figure 5.43 Diagonal compression failure

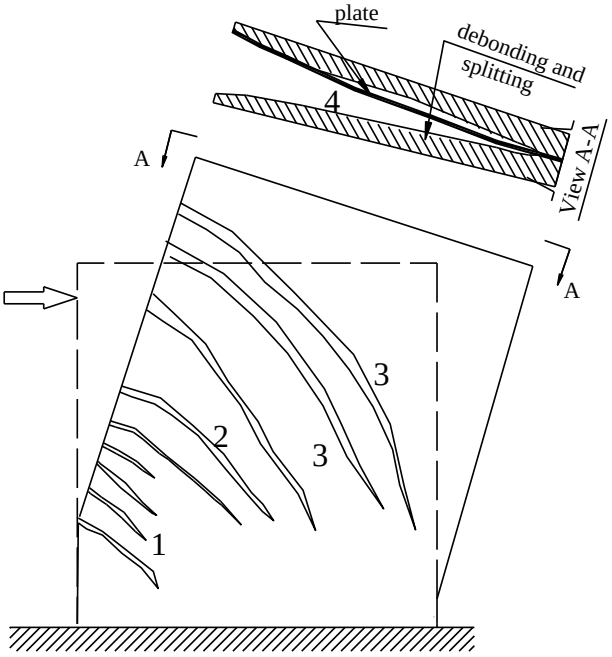

Figure 5.44 Local failure

*Numbers indicate events

i. Diagonal tension failure

Diagonal tension failure arises in concrete walls with low content of transverse reinforcement (stirrups) when a corner-to-corner failure plane is developed, see Figure

5.42. In the current study, flexural cracks first appeared in the tension side [as marked by number 1 in Figure 5.42]. As the load increased, additional cracks appeared and extended in the central panel (2 and 3) until the main diagonal crack formed and extended from the point of load application to the opposite corner (4), resulting in a diagonal failure plane which was accompanied by a drop in load carrying capacity. This mode of failure was observed in flanged specimen EW11 that was designed with low ratio of horizontal reinforcement (0.38%).

For encased-plate walls and after the achievement of the ultimate load, specimen failure was due to debonding of the plate from the surrounding concrete, leading to a significant loss of concrete cover in the central panel in the vicinity of the buckled plate. This mode of failure was observed in specimens EW11 and EW12. Encased-plates appeared to have no effect on the mode of failure.

ii. Diagonal compression failure

Diagonal compression is usually observed in walls with large flexural capacities and diagonal tension failure is suppressed by providing adequate transverse reinforcement (stirrups). In the current study, flexural cracks [as marked by number 1 in Figure 5.43] initiated in the tensile boundary element, then diagonal cracks (2 and 3) extended in the central panel and ran towards the compression edge of the wall, see Figure 5.43. The failure was characterised by the crushing of concrete in the extreme compression fibres (4). This mode of failure was observed in specimen EW21 which had a relatively high ratio of transverse reinforcement (1.2%).

C. Local failure

This mode of failure may occur in walls with a rectangular cross-section and is significantly affected by the form of load introduction at the free end of the wall. The presence of flanges

(boundary elements) and end beams provide clamping to the wall end, effectively preventing local failure. When this type of failure occurred in specimen EW23, it was associated with a debonding between the encased-plate and the concrete in the region of high stresses and the full capacity of the wall was not realised, Figure 5.44. This mode of failure is highly undesirable and should be avoided to achieve the full capacity of the walls.

5.3.6 Deformation characteristics

Evaluation of the effect of embedding steel plates inside concrete walls on the overall behaviour can be achieved by a comparative study of wall deformations. The next section discusses this effect on the vertical displacement, the elongation and shortening of boundary elements, the shear and flexural deformation components and on the secant stiffness and wall ductility.

A. Vertical Displacements

Figure 5.45 presents the load-vertical displacement behaviour of specimens tested in the first and second groups. The figure shows that the deformation response of the specimens was distinctly nonlinear after concrete cracking. The load-displacement behaviour can be divided into three distinct parts as shown in Figure 5.45a, and specimen EW12 was selected to describe the typical wall's behaviour. The first part and up to point (A) shows the linear uncracked response of the specimen. The second part started at point (A) with the initiation of flexural and shear cracks and was characterised by a sudden drop in stiffness. The last part of the curve started at point (B), which denotes the first yield of flexural tensile reinforcement and encased-plate, and was characterised by another drop in stiffness due to significant increases in displacement.

The effect of embedding steel plates was clear in reducing the value of vertical displacement at all stages of loading. This meant that the steel plate had played a major part in increasing the bending stiffness of the walls, and its contribution should be also taken in consideration when calculating the flexural capacity of the walls.

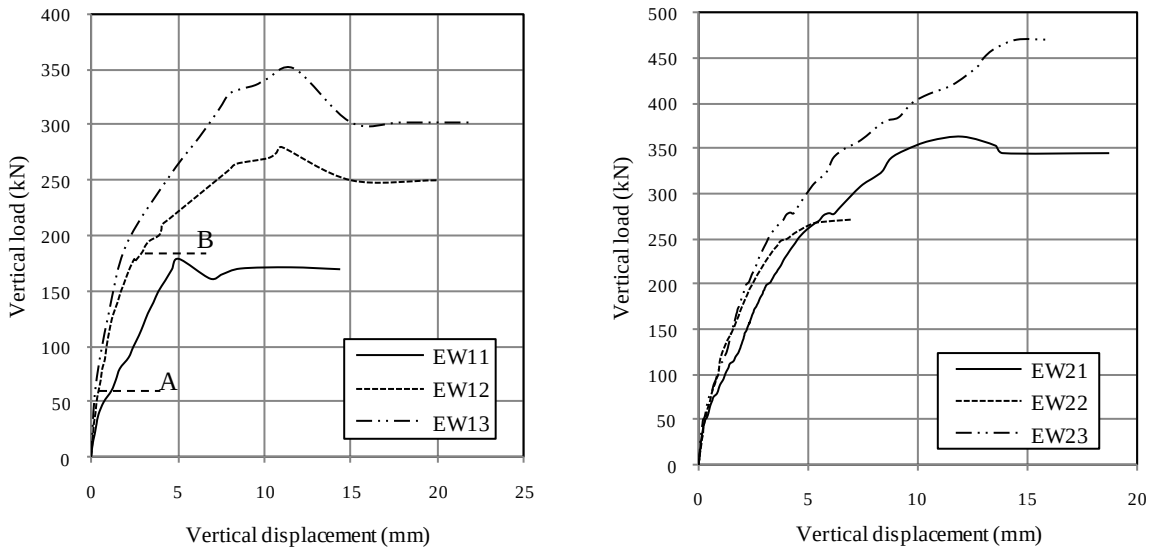

(a) First group (b) Second group

Figure 5.45 Load-vertical displacement behaviour of test specimens in the first and second groups

B. Elongation and shortening of boundary element

The elongation and shortening of boundary elements may be used to assess the effect of embedding steel plates in concrete walls since they provide useful indications on the shear distortion of the wall. As the value of vertical load increased, shortening and elongation of wall edges were clearly noticed. Figures 5.46 and 5.47 depict the load-horizontal displacement behaviour of walls' boundary elements for the specimens in the first and second groups, respectively. The figures show that with load increments, specimens tended to experience increasing extension of the tensile boundary elements, while the shortening of the compression boundary elements was much smaller. The extension of the wall on the

tension side was ascribed to the opening of flexural cracks, dilation of concrete and accumulation of plastic strains in the reinforcement and encased-plate. Figures 5.46 and 5.47 also suggest that the extension and shortening of the boundary elements of encased-plate walls were substantially lower than those of conventionally-reinforced walls essentially due to the increase in wall axial stiffness caused by encased-plates.

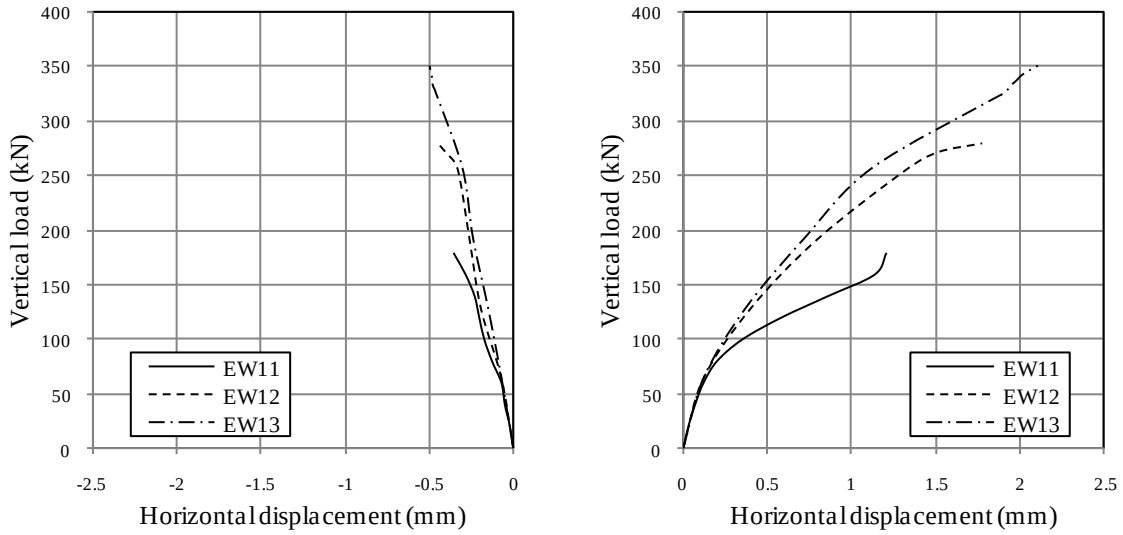

(a) shortening (b) extension

Figure 5.46 Vertical load-horizontal displacement curves for walls in the first group

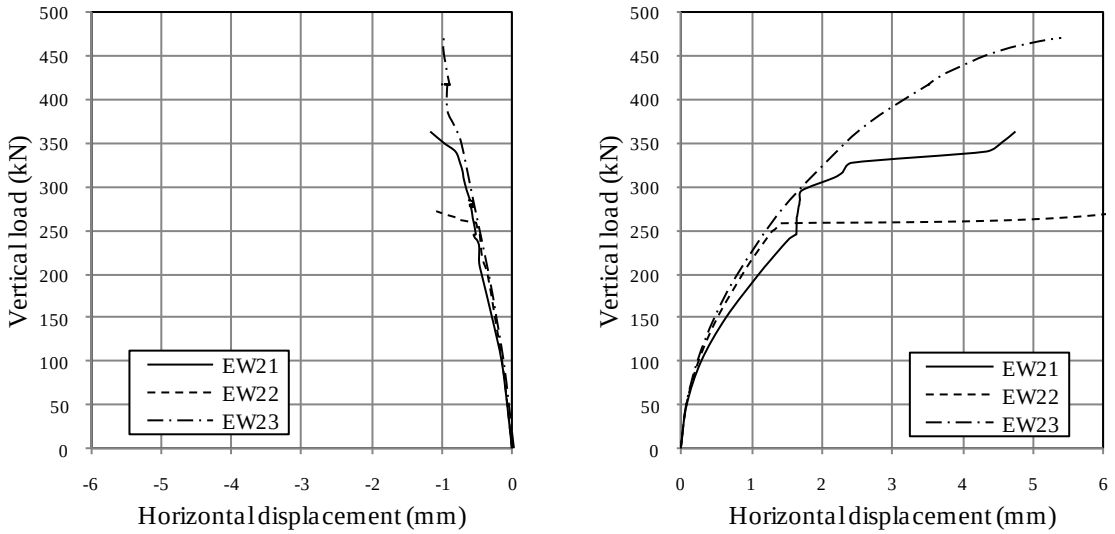

(a) shortening (b) extension

Figure 5.47 Vertical load-horizontal displacement behaviour for walls in the second group

Moreover, the values of the elongation and shortening of the boundary elements can be used to give an indication about the depth of the neutral axis (Lefas 1988). The greater the difference between the absolute values of elongation and shortening, the smaller the depth of neutral axis of the wall. Figure 5.48 shows a comparison of the difference between the absolute values of elongation and shortening with the vertical load. The figure clearly suggests that encased-plate walls had a smaller difference between the absolute values of elongation and shortening which implied that encased-plate walls had a greater neutral axis depth. This was compatible with the observations obtained from strain distribution as discussed in Section 5.3.4.

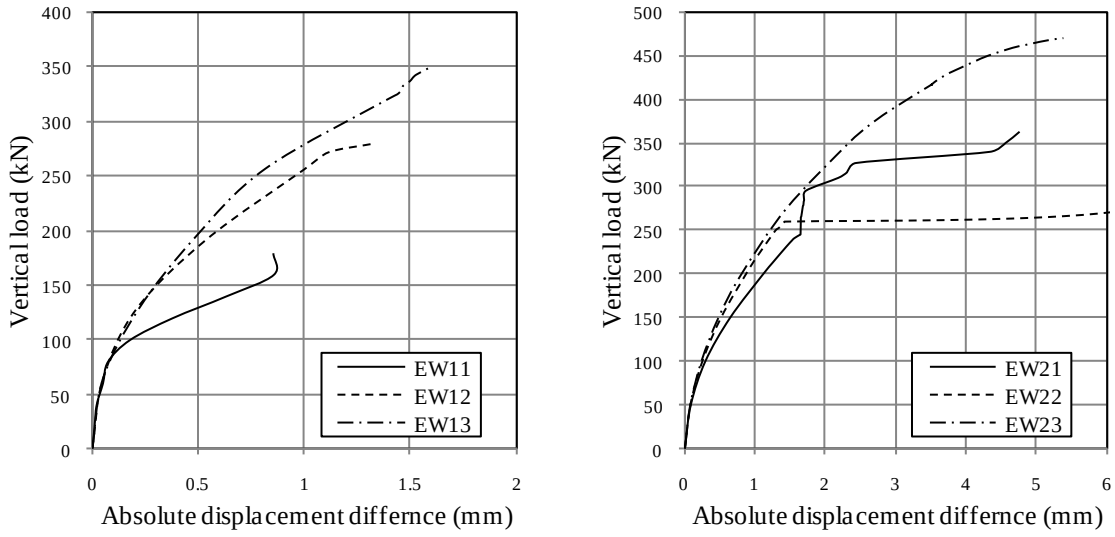

(a) First group (b) Second group

Figure 5.48 Comparison of the difference between the absolute values of elongation and shortening with the vertical load

C. Assessment of flexural and Shear deformation components

The displacement values obtained from the diagonal transducers were used to estimate the shear and flexural components of the total wall displacement. The total displacement at each wall end was decomposed into the flexural and shear components and depicted in

Figures 5.49 and 5.50 for the first and second group specimens, respectively. The figures suggest that flexural displacement was responsible for most of the vertical displacement. Also, encased-plate walls exhibited less shear distortion when compared to conventionally-reinforced walls. This result was consistent with results obtained from the elongation and shortening of the boundary elements.

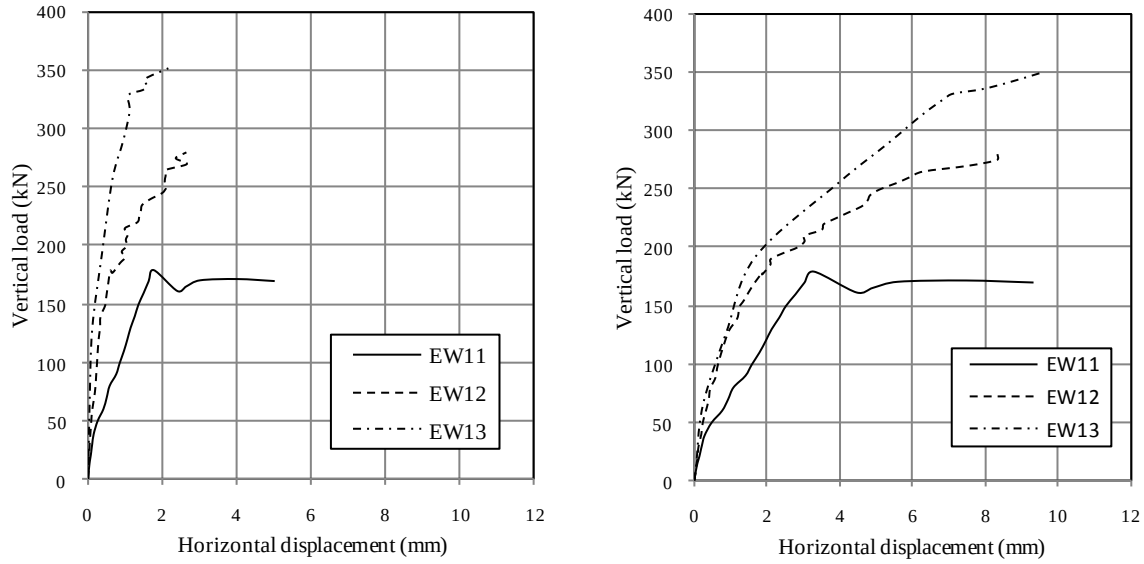

(a) Shear component (b) Flexural component

Figure 5.49 Displacement components behaviour of first group walls

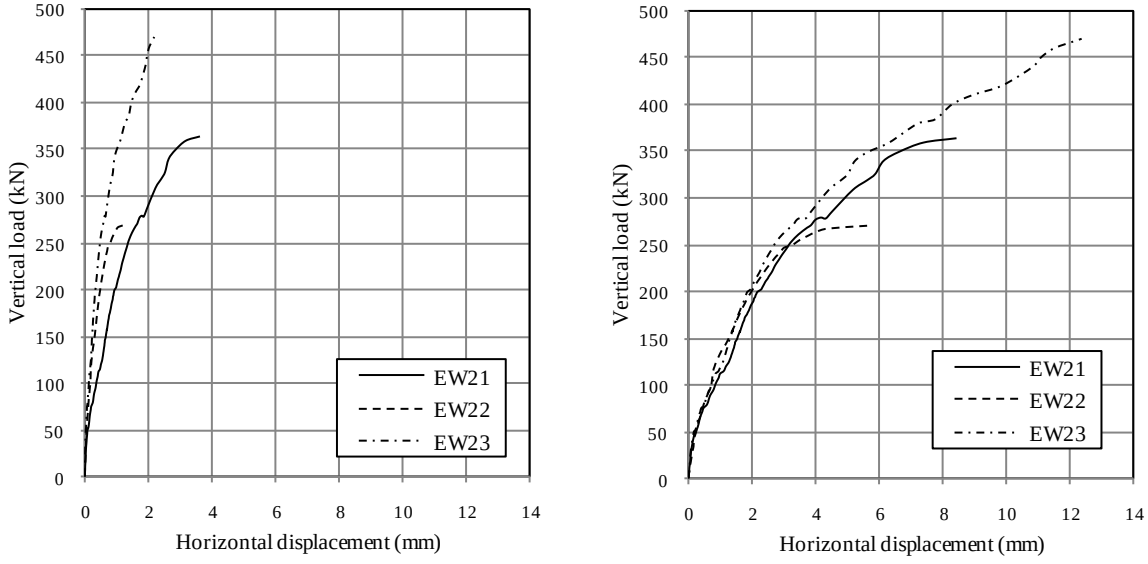

(a) Shear component (b) Flexural component

Figure 5.50 Displacement components behaviour of second group walls

D. Secant stiffness

Figure 5.51 plots the variation of the walls' secant stiffness against the vertical load for all test specimens. The figure shows that stiffness degradation was first observed after concrete cracking and became more pronounced after the yielding of flexural reinforcement and encased-plate. This observation was valid in all test specimens regardless of their mode of failure. The first part of the stiffness curve indicated the uncracked stage, in which the stiffness was not constant and was highly affected by the accuracy of the measuring devices, while near failure a significant decrease in the stiffness was observed with a trend to become almost horizontal. The values of secant stiffness at different loading stages and the ratio of stiffness relative to the control specimen are summarised in Table 5.3. The values in Table 5.3 indicate a significant average increase in secant stiffness of 59, 87 and 47% were noticed at flexural cracking, diagonal cracking and yielding of reinforcement, respectively when specimens were reinforced with plates. However, no enhancement was observed in stiffness at failure which attributed to the higher load and displacement attained by encased-plate specimens at failure.

E. Ductility

Ductility ratio is defined as the ratio of vertical displacement at ultimate load to vertical displacement at first yield of tensile reinforcement. Table 5.4 presents the vertical load at first yield of tensile reinforcement and the ductility ratio for all test specimens, while Figures 5.52 and 5.53 show a comparison of the vertical load at first yield of reinforcement and ductility ratio for specimens in the first and second groups, respectively.

Generally, embedding of steel plate inside the concrete wall had a noticeable effect in increasing the load at first yield, Figure 5.52. The values in Table 5.4 indicate significant increase in the vertical load at first yield of tensile reinforcement of 40 and 55% were

achieved when specimens were reinforced with plates. Also, embedding of steel plates was found to increase the value of the vertical displacement at failure, and hence the ductility ratio as indicated in Table 5.4. An increase of the ductility ratio from 1.41 to 3.78 in the first group and from 4.38 to 4.57 in the second group was associated with increasing the plate thickness from 0 to 1.5 mm.

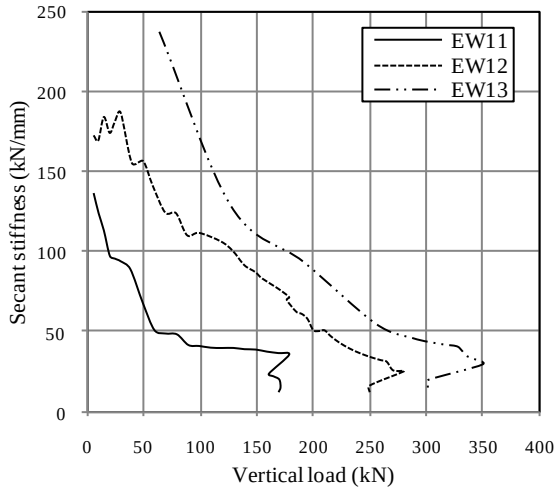

(a) First group

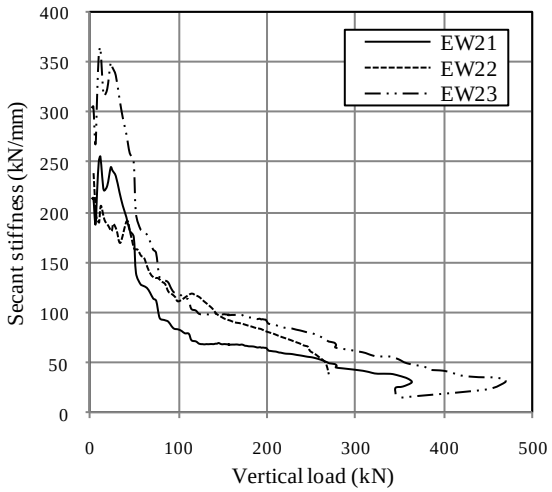

(b) Second group

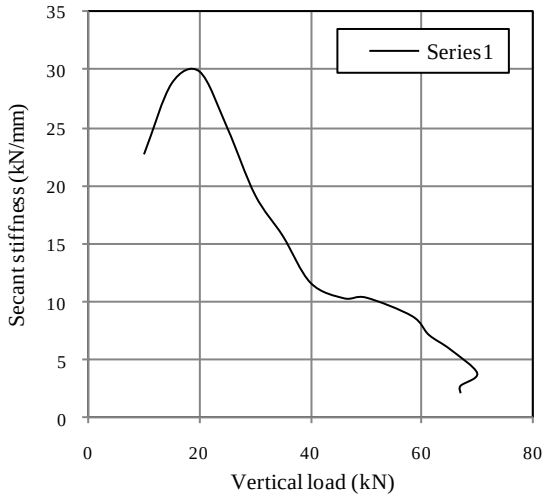

(c) Third group

Figure 5.51 Variation of secant stiffness with vertical load for test specimens

Table 5.3 Calculated values of secant stiffness

Specimen	Secant stiffness at flexural cracking (kN/mm)	Stiffness ratio relative to control specimen (%)	Secant stiffness at diagonal cracking (kN/mm)	Stiffness ratio relative to control specimen (%)	Secant stiffness at yielding of rebar (kN/mm)	Stiffness ratio relative to control specimen (%)	Secant stiffness at ultimate (kN/mm)	Stiffness ratio relative to control specimen (%)
EW11	93.00	100.00	68.50	100.00	39.64	100.00	35.60	100.00
EW12	146.30	157.31	127.00	185.40	61.30	154.64	25.46	71.52
EW13	222.20	238.92	238.10	347.59	71.70	180.88	29.73	83.51
EW21	115.80	100.00	111.10	100.00	66.54	100.00	30.29	100.00
EW22	137.25	118.52	137.04	123.35	86.40	129.85	38.74	127.90
EW23	138.90	119.95	101.70	91.54	79.94	120.14	32.42	107.03

Table 5.4 First yield load and ductility ratio

Specimen	Plate thickness (mm)	First yield load (kN)	First yield load relative to control specimen (%)	Ductility ratio (mm/mm)	Ductility ratio relative to control specimen
EW11	0.00	130.00	100.00	1.41	100.00
EW12	0.80	190.00	146.16	3.54	251.06
EW13	1.50	220.00	169.24	3.78	268.08
EW21	0.00	175.00	100.00	4.38	100.00
EW22*	0.80	184.00	134.24	3.04	69.41
EW23	1.50	247.00	141.15	4.57	104.33

*Premature failure

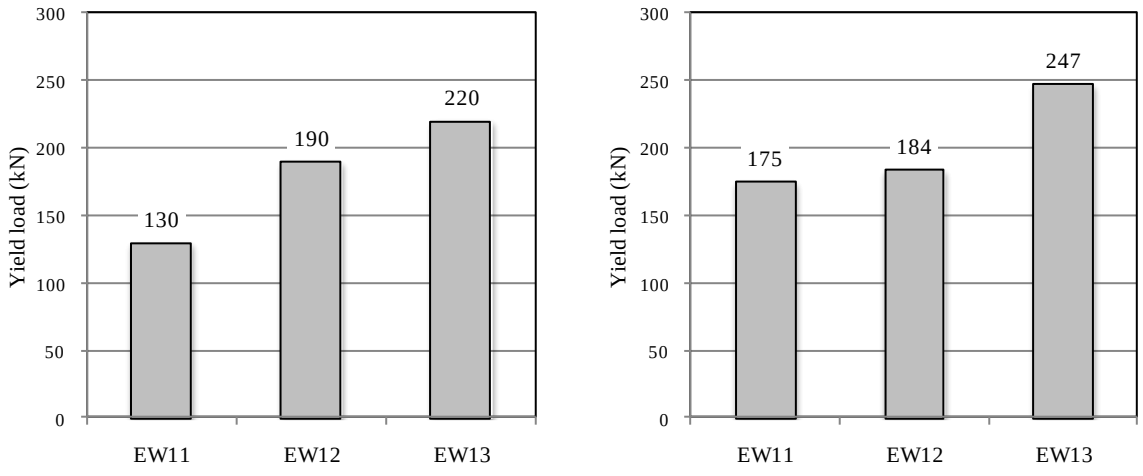

(a) First group (b) Second group

Figure 5.52 Comparison of vertical load at first yield of tensile reinforcement

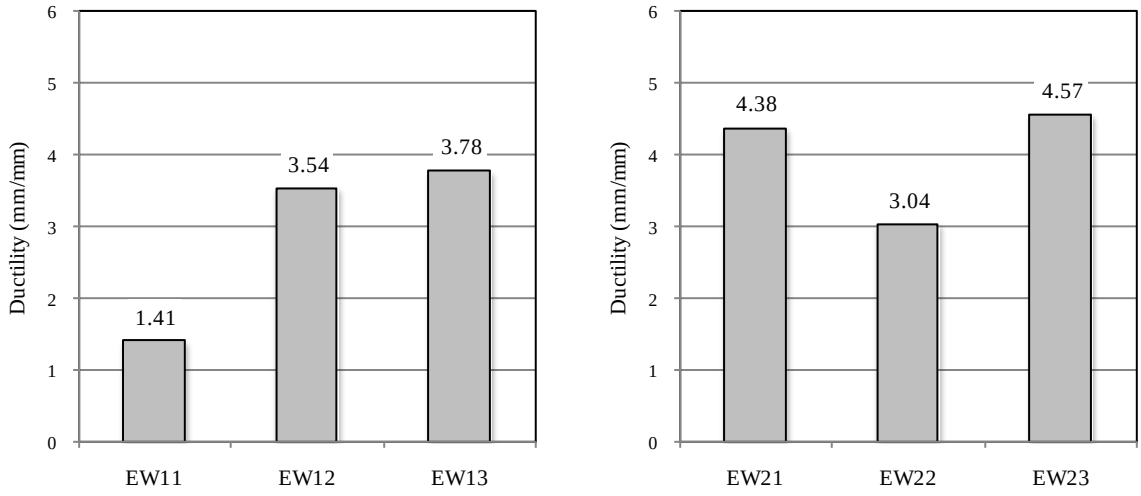

(a) First group (b) Second group

Figure 5.53 Comparison of ductility ratio values attained by test specimens

5.3.7 Load carrying capacity

Table 5.5 summarises the values of ultimate load achieved for the test specimens, while Figure 5.54 shows a comparison of the ultimate load values for the test specimens in the first and second groups. The figure clearly shows that increasing the plate thickness caused significant increases in the load carrying capacity. For the first group, a load carrying capacity enhancement of the order of 55.6% and 94.6% with respect to the conventionally-reinforced specimen EW11 were obtained with walls reinforced with plates of 0.8 and 1.5 mm thickness, respectively. In the second group, specimen EW22 could not be included in this comparison as it failed prematurely, while specimen EW23 achieved an enhancement of about 29% in strength due to the use of 1.5 mm thick plate. The reason behind the low enhancement of load carrying capacity is attributed to the local failure of the specimen as described in Section 5.2.2.

Table 5.5 Values of ultimate load for all test specimens

Specimen	Plate thickness (mm)	Ultimate load (kN)	Ultimate load relative to control specimen (%)
EW11	0.00	180.00	100.00
EW12	0.80	280.00	155.60
EW13	1.50	350.00	194.60
EW21	0.00	365.00	100.00
EW22*	0.80	270.00	74.00
EW23	1.50	470.00	128.80
EW31	1.00	70.00	----

* premature failure

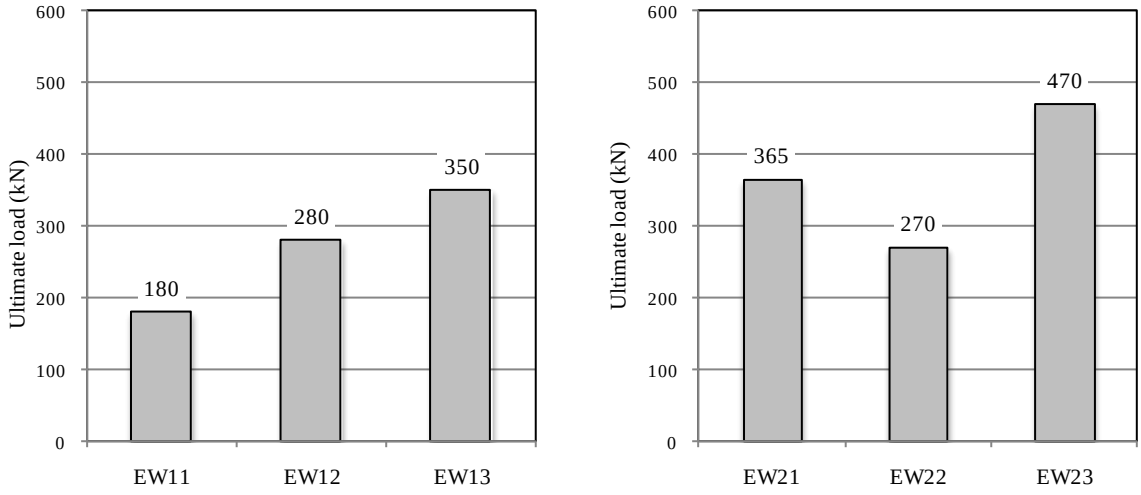

(a) First group (b) Second group

Figure 5.54 Comparison of ultimate load values

5.4 Summary

This chapter presents a detailed description of the results of testing the seven structural wall specimens described in the preceding chapter. The results including the overall wall displacements, the strains in rebars and encased-plates, the crack patterns and the behaviour under applied load to failure were presented in detail. The chapter also includes a final discussion section to cover the overall behaviour, the modes of failure and deformation characteristics.

Chapter 6 Numerical modelling of encased-plate composite walls behaviour

6.1 Overview

This chapter describes the development and validation of a finite element model that simulates the behaviour of encased-plate composite walls. The nonlinear finite element analysis was carried out using Abaqus (version 6.8); a commercial software package with a wide range of applications. Abaqus consists of three main products: Abaqus/Standard, Explicit and CAE. Only CAE interface was used for creating, submitting, monitoring analyses and post processing the results.

The reliability of the finite element model was demonstrated through three case studies (Lefas 1988, Marsono 2000 and Baglin 1998) involving isolated structural walls, coupled walls and encased-plate composite beams, respectively, in addition to the experimental results obtained in this study and discussed in Chapters 3 and 5.

Following successful validation, the model was used to conduct a parametric study to assess the effect of variables which were thought to have a considerable influence on the behaviour of encased-plate composite structural walls.

6.2 Modelling strategy

Generally, concrete can be modelled using two-dimensional plane elements or three-dimensional solid elements, while rebars can be modelled using either a discrete, embedded or smeared model. In order to produce a realistic model, concrete was modelled using three-dimensional solid elements and discrete approach was used to model the rebars.

The modelling of encased-plate structural walls went through five main steps namely; geometric modelling, consideration of material constitutive models, introduction of boundary conditions, load application and nonlinear solution.

6.2.1 Geometric modelling

The first step in finite element modelling is the topological description of the structure's geometric features. The finite element idealisation for walls tested under pure in-plane shear and lateral loading is depicted in Figure 6.1, and includes all physical parts of the walls. The walls were discretised such that each element was bounded by some reinforcement to avoid numerical instability and sensitivity to mesh density.

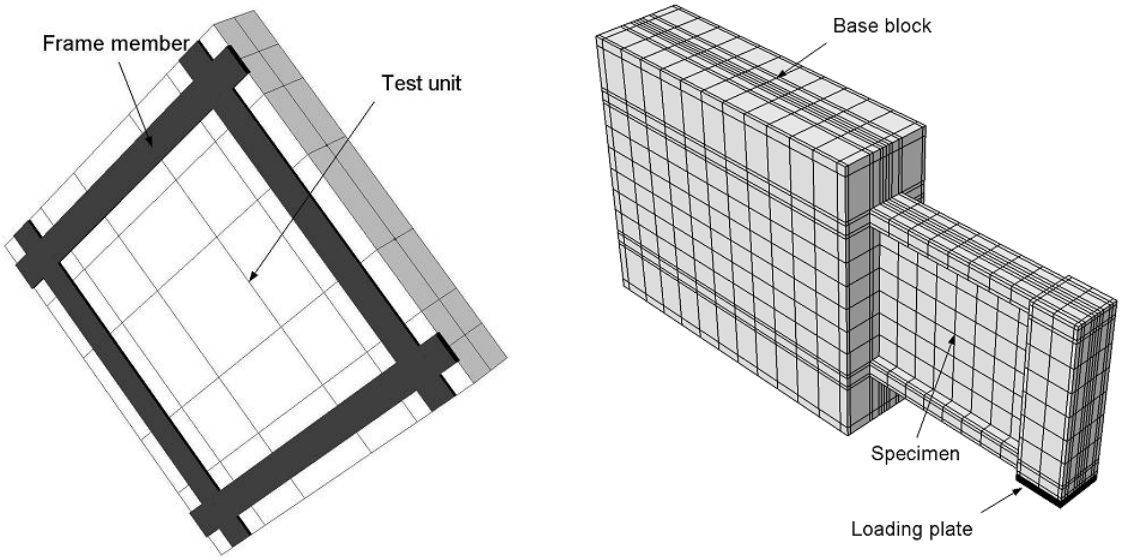

(a) Walls tested under in-plane shear (b) Walls tested under lateral loading

Figure 6.1 Finite element idealisation of walls

A. Element types

Abaqus provides a wide range of element types suitable for non-linear problems. The element types selected in the analysis were obtained from an initial sensitivity study, which assessed the predicted performance against that observed experimentally. Figure 6.2 shows

the behaviour of wall EW21 obtained experimentally and predicted numerically using different element types. The results shown in Figure 6.2a suggested that the analysis was sensitive to concrete element type, and three dimensional, 8-node linear brick, reduced integration element (**C3D8R**) was found to be efficient in modelling concrete and gave the best correlation with the experimental results, while Figure 6.2b showed that 2-node linear displacement beam element with six degrees of freedom at each node (**B31)** can be used to model the rebars. In this initial sensitivity study, the rebars were modelled using beam elements B31 while concrete elements were being modified and concrete was modelled using solid element C3D8R while rebars elements were being modified. Since the encased-plate transmits in-plane forces only and has no bending stiffness, a three dimensional, 4-node membrane element with reduced integration (**M3D4R**) was used to model the encased-plates.

For small wall specimens tested under pure in-plane shear, the frame members were modelled using three dimensional, 2-node linear displacements, hybrid truss elements (**T3D2H**). This element type was selected to match the experimental setup, as the frame members were not contributing to the load carrying capacity and only resisted axial loading which was transferred to the test unit at the common nodes, see Figure 6.1a.

For walls tested under lateral loading, the steel plate used for applying the load was also included in the finite element model and modelled using **C3D8R** element type, see Figure 6.1b. The presence of this plate was important to have a stable analysis and prevent stress concentration at the loading area. The geometry and node ordering of the selected element types are shown in Figure 6.3.

B. Mesh density

Increasing mesh density is known to result in both better accuracy and higher analysis costs due to the increased number of nodes and elements, and hence number of equilibrium

equations. In order to deliver the best balance between accuracy and cost, a mesh density optimisation study was carried out on a typical specimen, EW21. Three mesh densities were selected, involving 3830, 7164 and 18172 elements, representing coarse, medium and fine mesh, respectively as shown in Figure 6.4 and summarised in Table 6.1.

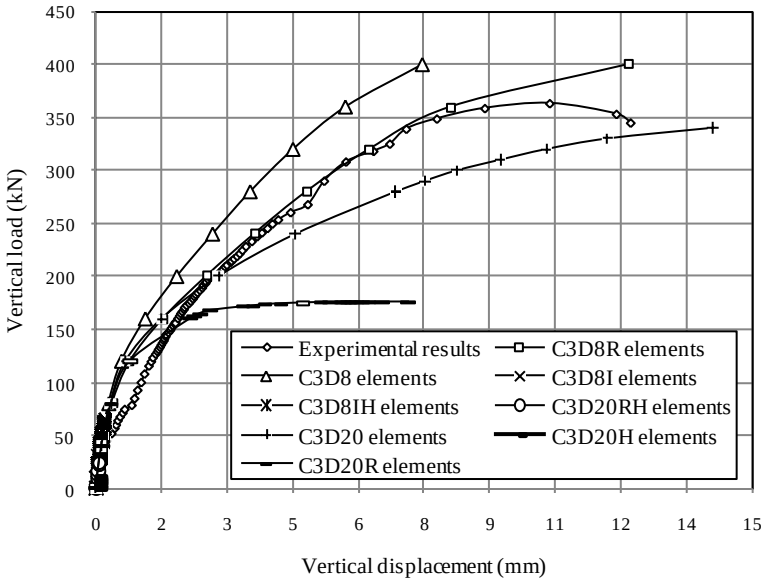

(a) Effect of concrete element type*

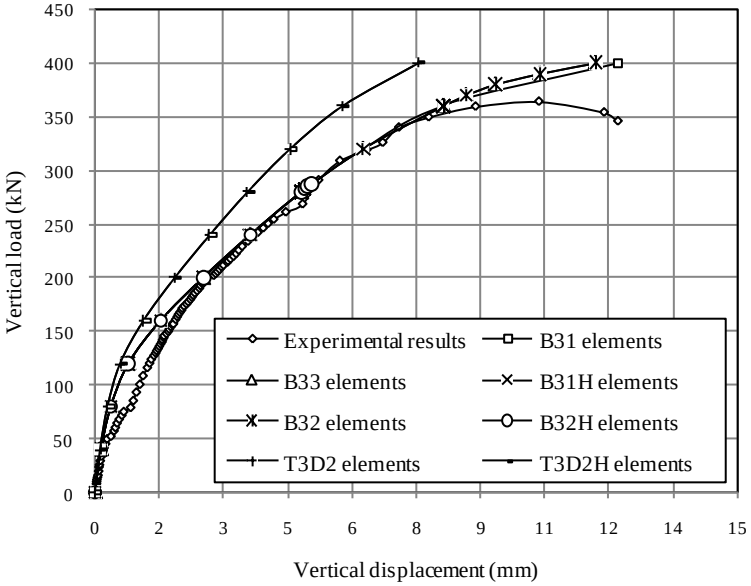

(b) Effect of steel element type*

Figure 6.2 Sensitivity analysis for element type

* Note

C3D8	is 8-node linear brick element	B33	is 2-node cubic beam element
C3D20	is 20-node quadratic brick element	T3D2	is 2-node linear displacement element
B31	is 2-node linear beam	H	hybrid for compressible material
B32	is 3-node quadratic beam	R	reduced integration to form element stiffness
		I	incompatible mode to improve bending

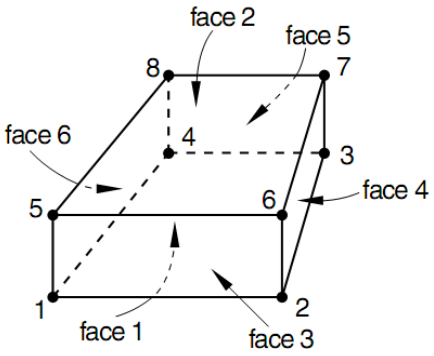

(a) 3D Solid element **C3D8R**

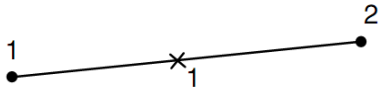

(b) Beam element **B31**

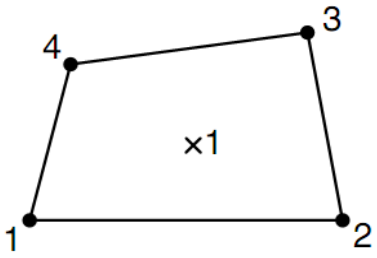

(c) Membrane element **M3D4R**

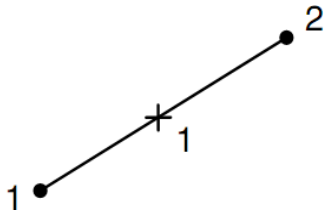

(d) Truss element **T3D2H**

Figure 6.3 Geometry and node ordering for the element types used in analysis

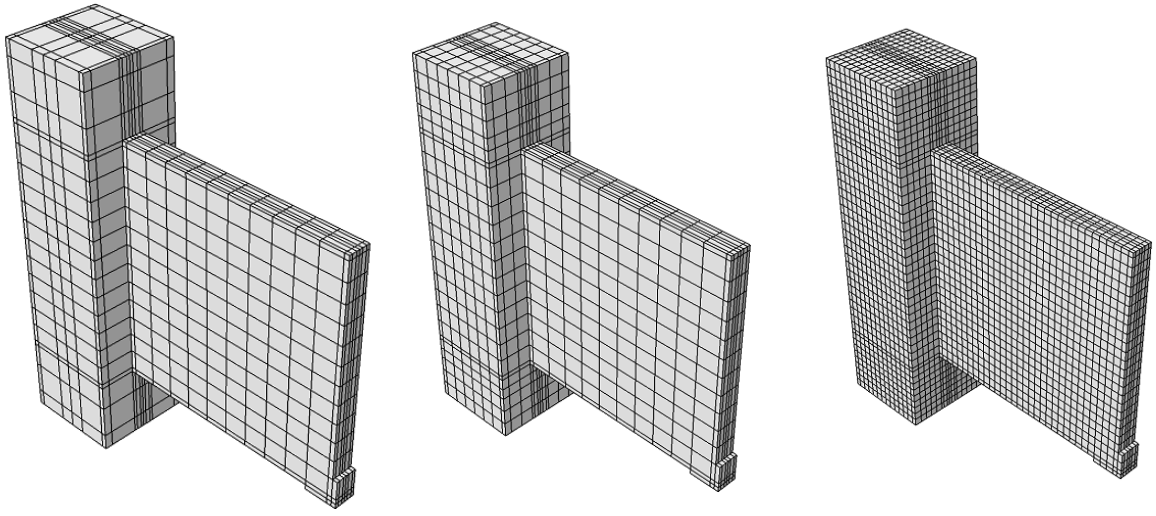

(a) Coarse mesh with 100 × 100 mm concrete element size

(b) Medium mesh with 50 × 50 mm concrete element size

(c) Dense mesh with 25 × 25 mm concrete element size

Figure 6.4 Mesh configurations, sensitivity to element size

Table 6.1 Sensitivity to element size

Mesh density	Coarse	Medium	Fine
Approximate concrete element size (mm)	100 × 100	50 × 50	25 × 25
Concrete element type	C3D8R		
Reinforcement element type	B31		
Number of nodes	2926	4234	17593
Number of concrete elements	2238	4342	14896
Number of rebar elements	1592	2822	3276
Total number of elements	3830	7164	18172

The results obtained from this study are depicted in Figure 6.5 in the form of load-displacement behaviour. The results showed that the mesh density played a key role in the numerical modelling of concrete structures when reinforcement was modelled as discrete elements. The fine mesh showed softer behaviour compared to models with medium and coarse meshes. Fine meshing provided several elements with little or no reinforcement. The Abaqus Users Manual (2008) discussed this numerical problem and stated that "*In cases with little or no reinforcement, the specification of a postfailure stress-strain relation introduces mesh sensitivity in the results, in the sense that the finite element predictions do not converge to a unique solution as the mesh is refined because mesh refinement leads to narrower crack bands".* To overcome this problem and to reduce computational time, a coarse mesh with average concrete element size of 100 × 100 mm was selected and designed such that each concrete element bounded by an element of reinforcement.

6.2.2 Constitutive models of materials

In general, the main causes for nonlinear behaviour of reinforced concrete structures are concrete cracking and reinforcement plastic properties. Creep, shrinkage and temperature can also be considered as sources of nonlinearity, but in the current study only time-independent parameters were considered in the finite element modelling.

A. Reinforcement and encased-plate model

The elastic-perfectly-plastic approach was used to present the stress-strain constitutive relationship for both rebars and the encased-plates. This behaviour is presented as bilinear curve and it was assumed to be identical under tension and compression, see Figure 6.6. Abaqus requires input of the modulus of elasticity, E_s, Poisson's ratio, v, and the yield stress, f_y, to define the material uniaxial stress-strain relationship, see Figure 6.7. The stress-strain behaviour, as obtained from the uniaxial tension tests, was implemented in the finite element model. Perfect bond was assumed between thee encased-plates and the surrounding concrete. This assumption was compatible with the observations made during experimental testing as discussed in Chapters 3 and 5, and the analysis methodology presented in Chapter 7.

In all numerical simulations, a specimen was considered to be failed when excessive deformations were obtained and no further increases in applied load was achieved, similarly to that considered in the experimental investigation.

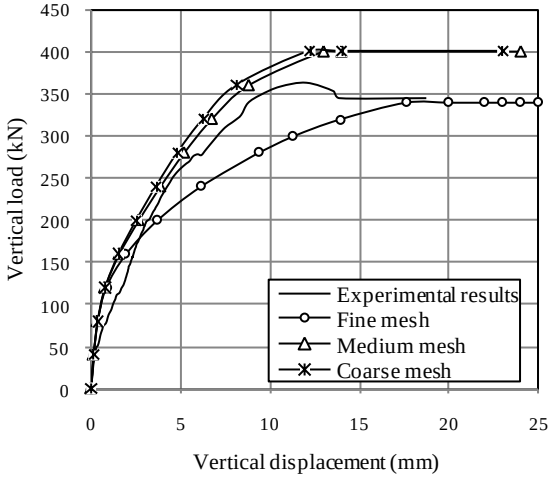

Figure 6.5 Sensitivity of analysis to mesh density

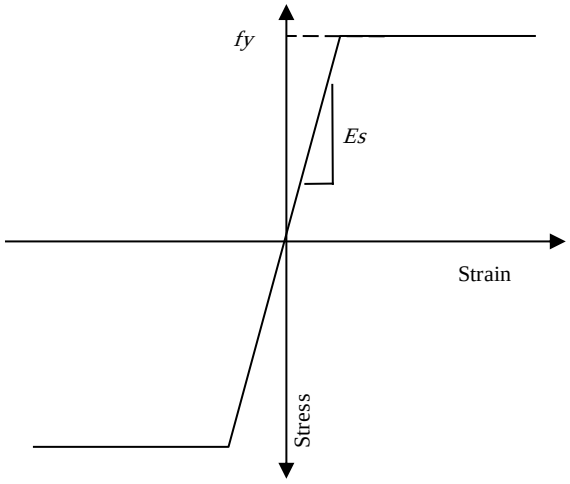

Figure 6.6 Stress-strain behaviour for steel reinforcement and encased-plate

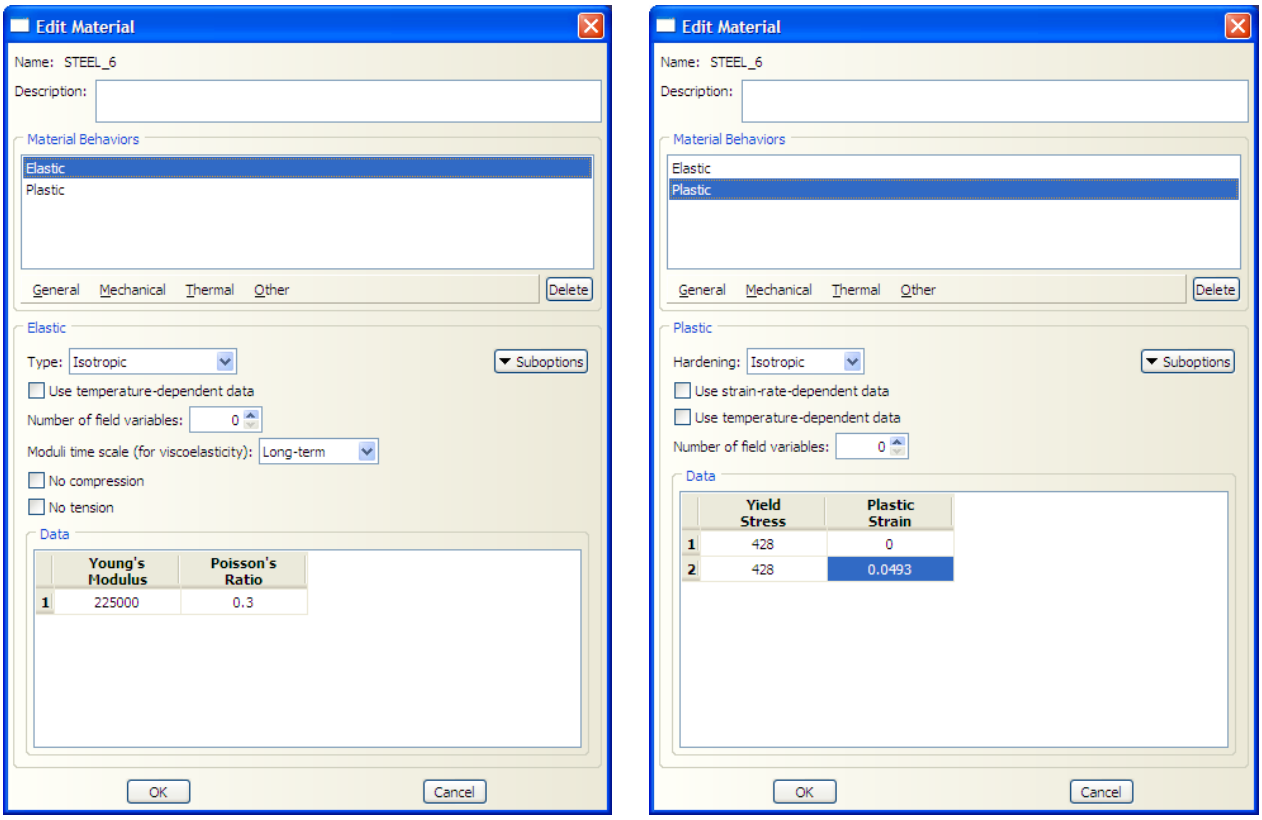

Figure 6.7 Input of reinforcement properties in a typical analysis

B. Concrete model

Abaqus offers two concrete modelling approaches; smeared cracking and damage plasticity models. In the current study, the damage plasticity model was used in the finite element analysis. The basic features of the model are discussed in detail through this section.

i. Mechanical behaviour

The concrete damaged plasticity model offers a general capability for modelling concrete material in reinforced concrete structures and implements a mix of isotropic damaged elasticity, isotropic tensile and compressive plasticity concepts. The model considers the effects of irrevocable damage incorporated with the failure mechanisms that take place in concrete under moderately low confining pressures (less than four or five times the uniaxial

compressive strength). The primary failure mechanisms of concrete are tensile cracking and compressive crushing.

The uniaxial tensile and compressive behaviour of concrete characterised by the damaged plasticity model are displayed in Figure 6.8. The behaviour of concrete under uniaxial tension has a linear elastic trend until the initiation of micro-cracking, followed by softening response leading to strain localisation in the concrete structure. Under uniaxial compression the behaviour is similar until the point of initial yield, $f`_{co}$. In the plastic regime, the response is typically characterised by stress hardening followed by strain softening beyond the ultimate stress, $f`_c$.

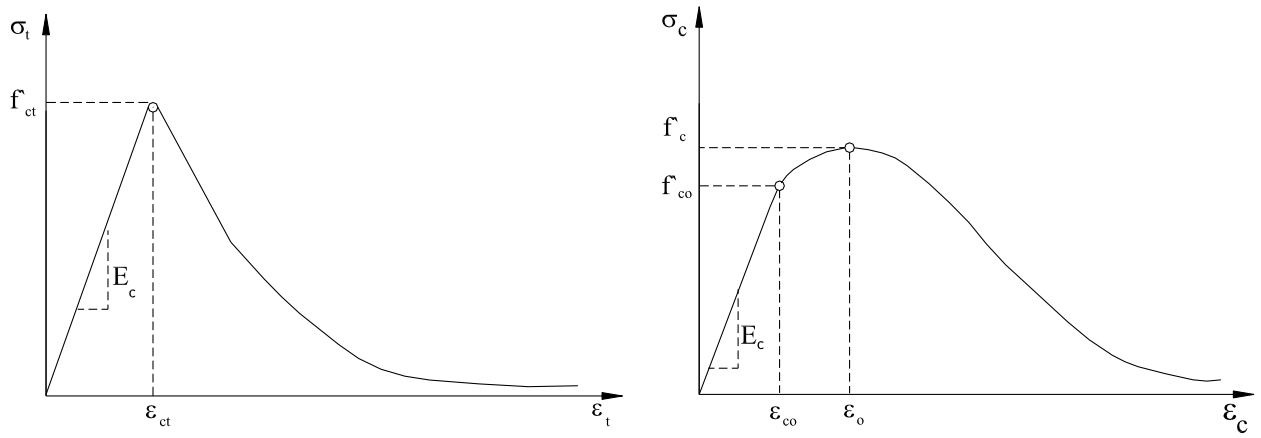

(a) Tension (b) Compression

Figure 6.8 Behaviour of concrete under uniaxial loading

The concrete properties are defined through two steps; first the elastic properties including the modulus of elasticity, E_c, and Poisson's ratio, v, are defined, then the plastic behaviour including plastic softening is characterised, see Figures 6.9.

The data required to define the concrete uniaxial stress-strain behaviour was generated from the equation proposed by Eurocode 2 (2008) as shown in Figure 6.10. However, the values of concrete strength and modulus of elasticity were obtained from testing of concrete cubes

and cylinders as described in Chapters 3 and 4. Figure 6.10 describes the relation between the compressive stress, σ_c, and shortening strain, ε_c, and described by the following equation:

$$\sigma_c = \frac{f_c'\left(k\eta - \eta^2\right)}{1+(k-2)\eta} \qquad 6.1$$

where:

$f`_c$ is the mean value of concrete cylinder compressive strength, $\eta = \frac{\varepsilon_c}{\varepsilon_o}$, $K$=1.05 $\frac{E_c \varepsilon_{c1}}{f`_c}$

ε_o is the strain at peak stress, E_c is the secant modulus of elasticity of concrete.

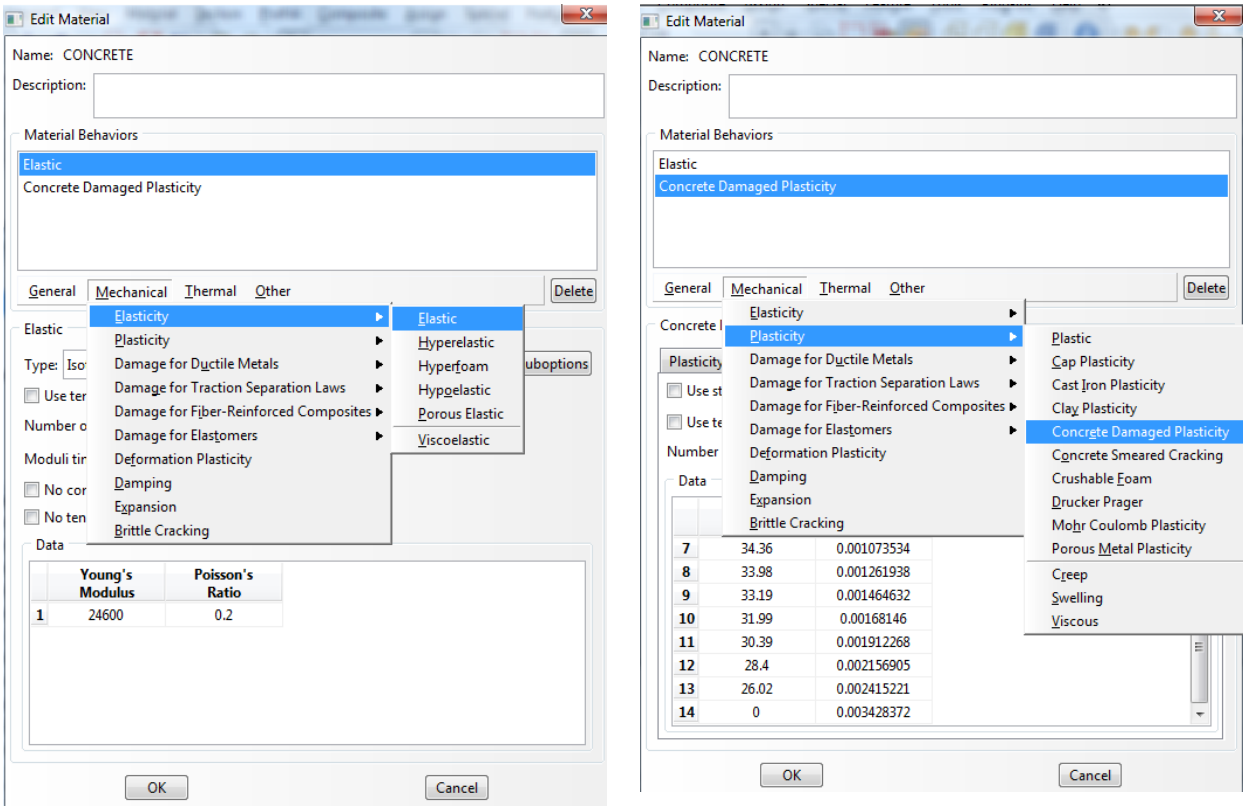

Figure 6.9 Description of concrete properties in Abaqus/CAE

ii. Plasticity parameters

Five parameters are required to define the plastic damage concrete model which uses a yield condition based on the yield function initially developed by Lubliner *et al* .(1989) and latter modified by Lee and Fenves (1998). The values of the five parameters were obtained

from previous studies and a sensitivity analysis was then carried out to assess the effect of each parameter as described below.

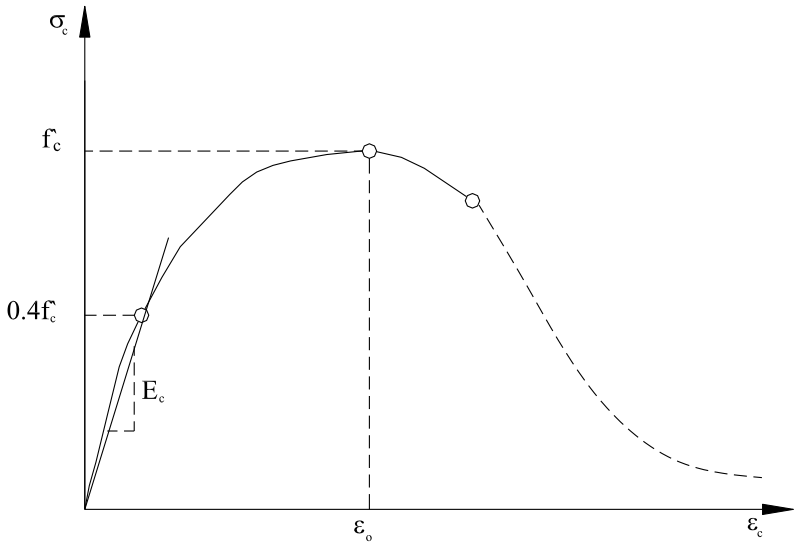

Figure 6.10 Schematic representation of the stress-strain behaviour of concrete as proposed by Eurocode 2 (2008)

a. Dilation angle ψ

Dilation angle is the ratio between the rate of volumetric strain and the rate of shear strain. Typical dilation angle values for concrete range from 12° (Vermeer and de Borst 1984) to 37° (Nielsen 1984).

b. Flow potential eccentricity (ϵ)

This parameter defines the rate at which the hyperbolic flow potential of the Drucker-Prager hyperbolic function approaches the asymptote (the flow potential tends to a straight line as the eccentricity tends to be zero).

c. Biaxial compressive yield ratio (σ_{b0}/σ_{c0})

This parameter indicates the ratio of compressive yield stress to initial uniaxial compressive yield stress. Typical values of this parameter for concrete are in the range from 1.10 to 1.16 (Abaqus Users Manual 2008).

d. Parameter K_c

The value of parameter K_c is to be determined considering a yield surface in the deviatoric plane and can be defined as the ratio of the second stress invariant on the tensile meridian, $q_{(TM)}$, to that on the compressive meridian, $q_{(CM)}$, at initial yield for any given value of the pressure P such that the maximum principal stress is negative. Typical yield surfaces are shown in Figure 6.11 on the deviatoric plane and in Figure 6.12 for plane stress conditions. Typical values of K_c range from 0.5 to 1.

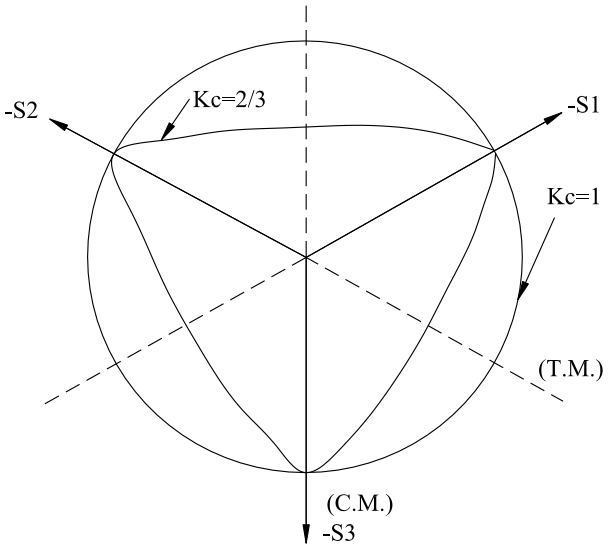

Figure 6.11 Yield surfaces in the deviatoric plane, corresponding to different values of K_c

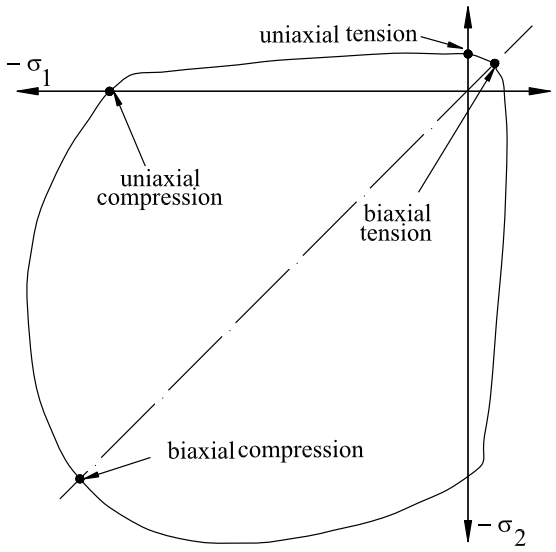

Figure 6.12 Yield surface in plane stress

e. Viscosity parameter (μ)

This parameter is used for the visco-plastic regularisation of the concrete constitutive equations implemented in Drucker-Prager model (Abaqus Users Manual 2008). The technique of a visco-plastic regularisation of the constitutive equations is used to overcome convergence difficulties due to the softening behaviour and stiffness degradation.

iii. Calibration of model parameters

The parameters in the concrete constitutive model were determined using experimental data wherever possible. The parameters that could not be determined directly from experimental data, including dilation angle, ψ, flow potential eccentricity, ϵ, biaxial compressive yield ratio, σ_{b0}/σ_{c0}, the parameter K_c and the viscosity parameter ,μ, were given values from data available in the literature. A multidimensional parametric study was then conducted whereby the results of numerical analyses with assumed values for the concrete parameters were compared with experimental observations. The study also helped quantify the likely effect of the values of the five parameters on the analysis of composite walls. The results of the study when compared to the experimental results of specimen EW21 are described below.

Sensitivity to dilation angle (ψ)

Lee and Kuchma (2007) and Lee *et al.* (2008) suggested a value for the dilation angle, ψ, of 37°. The sensitivity of numerical solution was investigated by setting the values of ϵ, σ_{b0}/σ_{c0}, K_c *and* μ according to Abaqus default values while changing the value of ψ between 12° and 50°. The numerical results depicted in Figure 6.13a show that ψ has a significant effect on the analysis results, with a low value resulting in premature termination of analysis, and a high value leads to substantial increase in stiffness. An excellent agreement between experimental and numerical results was achieved using a dilation angle of 37°, and this value was used in all subsequent numerical analyses.

Sensitivity to flow potential eccentricity (ϵ)

The flow potential eccentricity has a small positive value of around 0.1, meaning that the material has almost the same dilation angle over a wide range of confining pressure values. Increasing the value of ϵ provides more curvature to the flow potential, making ψ increase rapidly as the confining pressure decreases. Values of ϵ that are significantly less than the

default value (0.1) were reported to lead to convergence problems (Abaqus Users Manual 2008). No data was available about the value of this parameter in the literature and the selected value was obtained after performing a sensitivity study. The value of ϵ was changed from 0.001 to 10 while setting the values of ψ, σ_{b0}/σ_{c0}, K_c and μ according to Abaqus default values , and the parameter seems to be effective in calibrating the numerical modelling of shear-critical structures, see Figure 6.13b. Larger values of ϵ increase stiffness, and a value of 3 seemed to lead to reasonable results. This value was selected for all subsequent analyses.

Sensitivity to biaxial compressive yield ratio (σ_{b0}/σ_{c0})

In this parametric study, the value of σ_{b0}/σ_{c0} was varied from 1 to 6, around the default value of 1.16 while setting the values of ψ, ϵ, K_c and μ according to Abaqus default values. The numerical results shown in Figure 6.13c reveal that the analysis is not sensitive to the value of this parameter. Therefore, the default value was used in the proposed model.

Sensitivity to Parameter K_c

The value of this parameter was changed from 0.5 to 1.0 while setting the values of ψ, ϵ, σ_{b0}/σ_{c0} and μ according to Abaqus default values. The numerical model was insensitive to the value of this parameter as shown in Figure 6.13d. The failure mode and peak load remained without change during the simulations. The default value (0.667) was used in all subsequent analyses.

Sensitivity to Viscosity parameter (μ)

According to Figure 6.13e, the viscosity parameter is effective for stiffness calibration, but affects strength predictions insignificantly. A small value of μ improves the rate of convergence of the model in the softening regime. A value of 0 was selected for μ as suggested by the Abaqus Users Manual (2008).

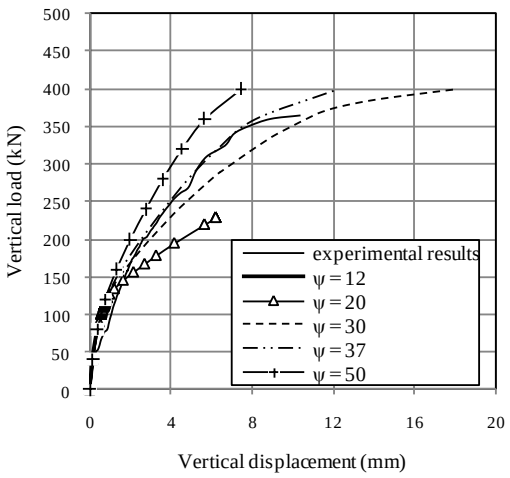

(a) Dilation angle (ψ)

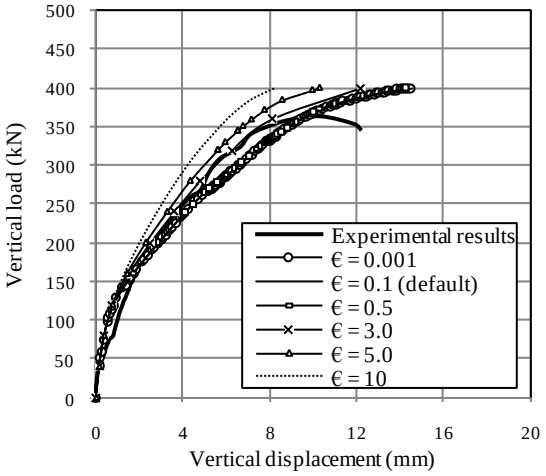

(b) Flow potential eccentricity ($€$)

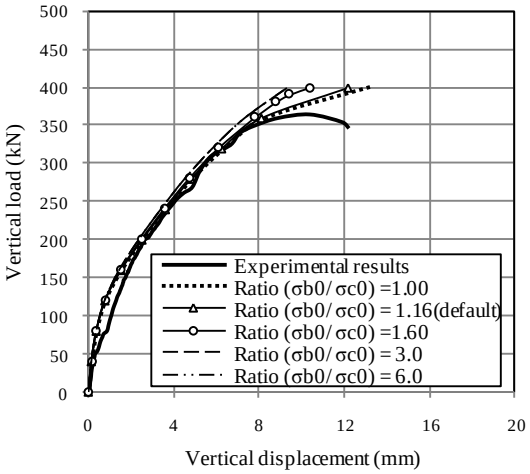

(c) Biaxial compressive yield ratio(σ_{b0}/σ_{c0})

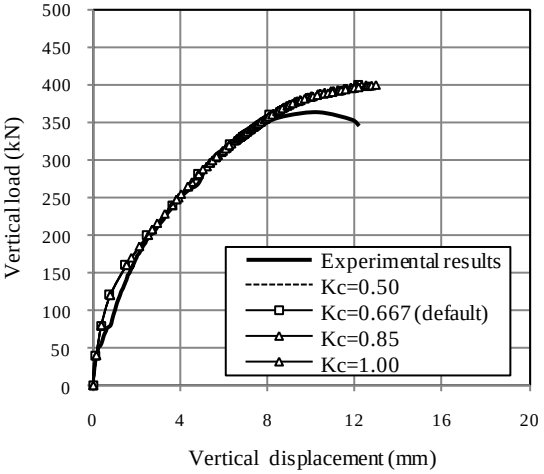

(d) Parameter K_c

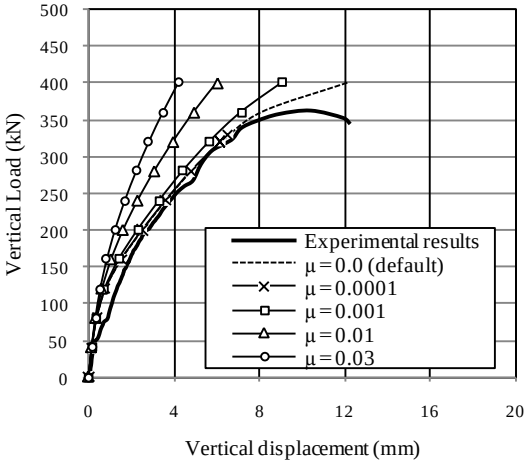

(e) Viscosity parameter (μ)

Figure 6.13 Sensitivity of numerical predictions to the values of concrete model parameters

6.2.3 Boundary conditions

A. Wall specimens tested under lateral loading

For the first group of specimens, the base block nodes below the upper reaction beams were restrained in the horizontal and vertical directions, closely simulating the test conditions, Figure 6.14a, while for the second and third groups, selected nodes were restrained to approach the boundary conditions provided experimentally, Figure 6.14b. In both cases, all specimens' nodes were restrained in the third direction to improve numerical stability.

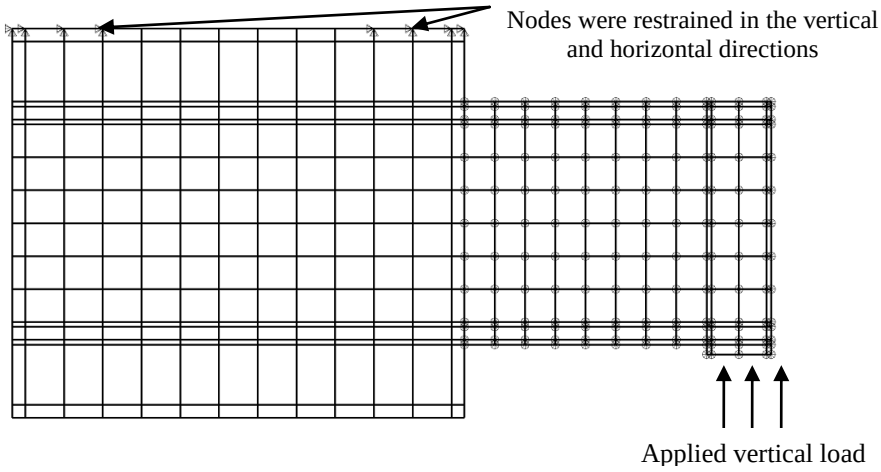

(a) First group specimens

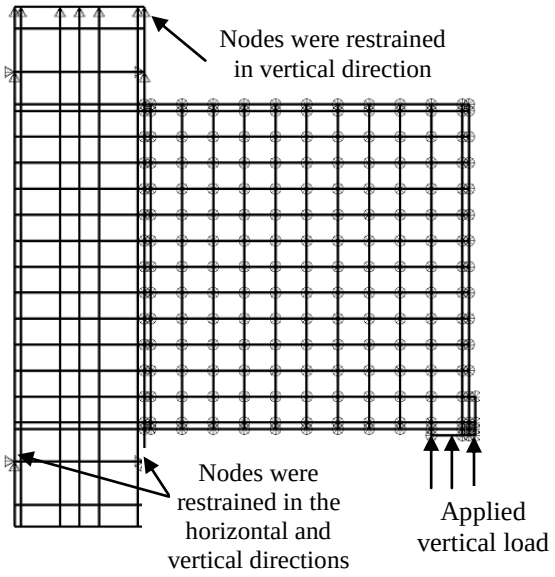

(b) Second and third groups of specimens

Figure 6.14 Details of boundary conditions for walls tested under lateral loading

B. Wall units tested under pure in-plane shear

Appropriate boundary conditions have been assigned in order to simulate the corner hinges and the mechanism behaviour of frame members so that they do not contribute to the load carrying capacity. In order to closely simulate the test conditions, test units were restrained near the bottom corner and the load was applied vertically at the diagonally opposite corner, see Figure 6.15.

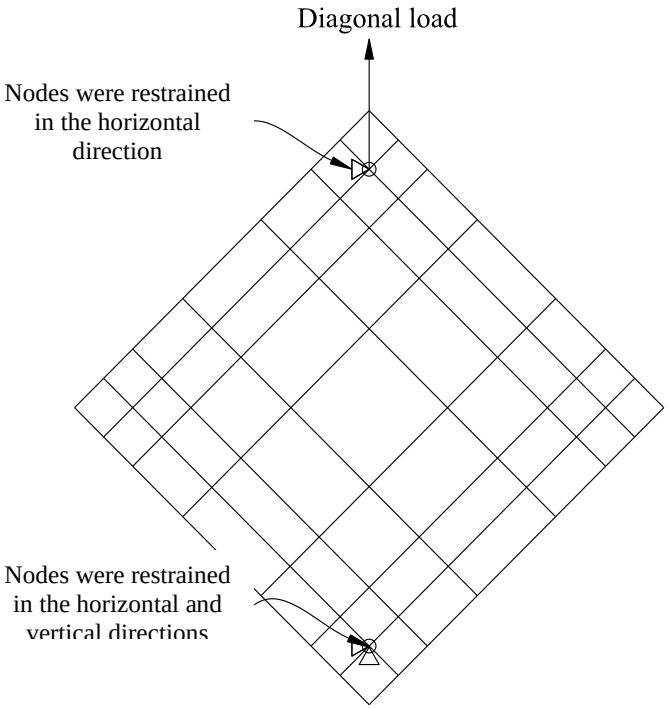

Figure 6.15 Boundary condition details for wall units tested under pure in-plane shear

6.2.4 Load application and nonlinear solution

The applied load was divided into a number of small increments to ensure correct modelling of the behaviour. Abaqus/CAE usually requires several iterations to determine an acceptable solution for each load increment. At the end of each increment, the stiffness matrix of the model is updated to reflect the nonlinear changes in stiffness before proceeding to the next increment. Newton's method is used in solving the nonlinear equilibrium equations. Since high degree of nonlinearity was expected in the response

including the possibility of unstable regimes as the concrete cracks, the automatic stabilisation option was used. This option was used to overcome the instability of the analysis due to severe nonlinearity.

6.3 Model validation

It is important to have sufficient confidence that the proposed finite element model can accurately simulate the true behaviour of the tested walls. The accuracy of the model can be verified if the following predictions closely matched the experimental results:

- Load-displacement behaviour,
- Ultimate load carrying capacity and crack pattern, and
- Strain development in the reinforcement and the encased-plate.

In order to validate the finite element model:

- ✓ Case studies were carried out on a number of structural wall specimens and encased-plate beams. Since no detailed research material was available in the literature on encased-plate structural walls, the proposed model was validated against experimental results of conventionally-reinforced isolated and coupled wall specimens and encased-plate simply-supported beams. Thirteen wall specimens built and tested by Lefas (1988) with different geometrical and material properties and tested under combined lateral and axial loading, a coupled wall specimen tested by Marsono (2000) and a shear-critical encased-plate simply-supported beam tested by Baglin (1998) were selected for these case studies.
- ✓ Moreover, the proposed model was validated against the experimental results of the wall units and wall specimens described in Chapters 3 and 5.

6.3.1 Case studies

A. Case studies details

The details of the specimens selected for the case studies are presented in this section. Geometric dimensions, material properties and reinforcement layouts are briefly described.

i. Isolated structural walls

The specimens tested by Lefas (1988) presented the critical storey component of a structural wall system in a multi-storey building. The geometry and reinforcement details of the walls are shown in Figure 6.16 and Table 6.2. All the walls considered in this investigation had a rectangular cross-section with height-to-width ratio varying from 1 to 2, and were divided into two types; Type I walls were 750 mm wide × 750 mm high × 70 mm thick , and Type II walls were 650 mm wide × 1300 mm high × 65 mm thick. Table 6.2 summarises the reinforcement ratios, axial loads and concrete properties. Lateral and axial loads were applied on the upper beams (1150 mm long × 150 mm deep × 200 mm thick), while the lower beams (1150 mm long × 300 mm deep × 200 mm thick) was used to clamp the specimens to the laboratory test floor, simulating a rigid footing, see Figure 6.16.

The specimens were reinforced with a grid of 8 and 6.25 mm diameter high strength bars in the vertical and horizontal directions, respectively. In order to provide additional confinement for the boundary elements, additional stirrups with 4 mm diameter were provided. The mechanical properties of the reinforcement are given in Table 6.3.

The mesh configurations, load application and boundary conditions used in the finite element analyses are shown in Figures 6.17.

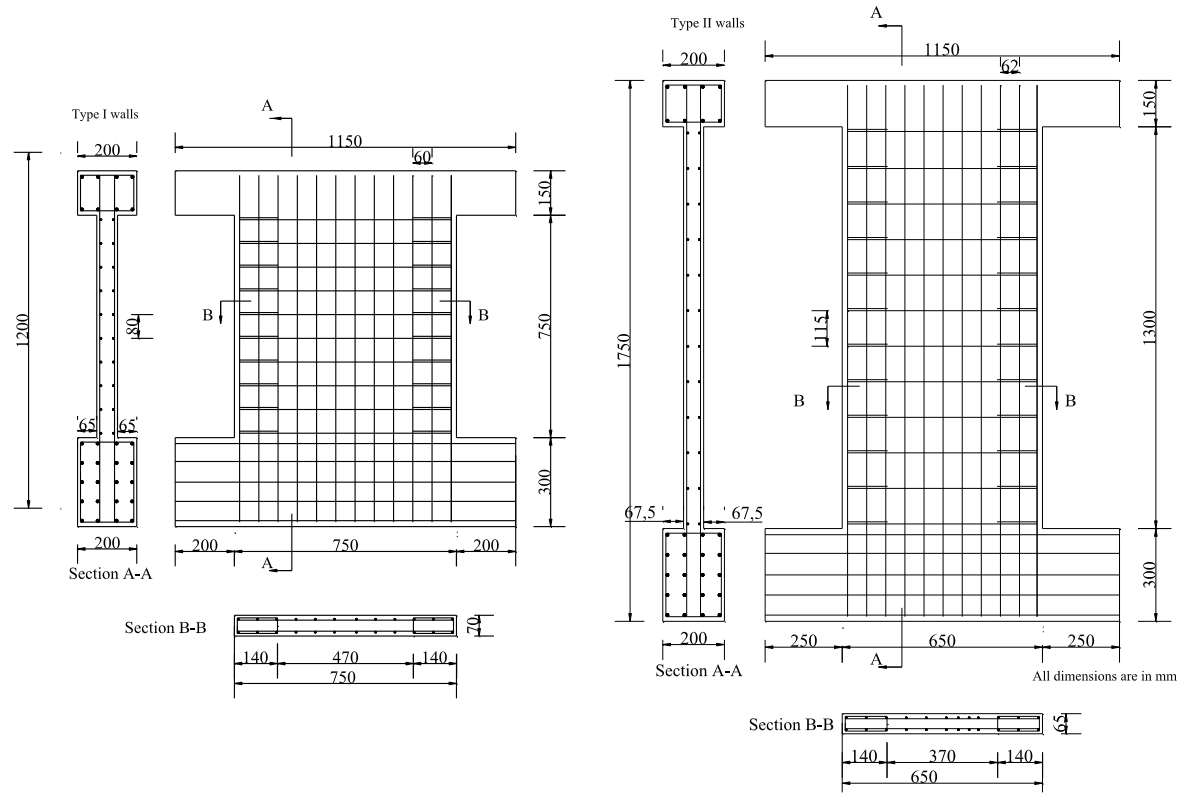

Figure 6.16 Geometry and reinforcement details of walls tested by Lefas (1988)

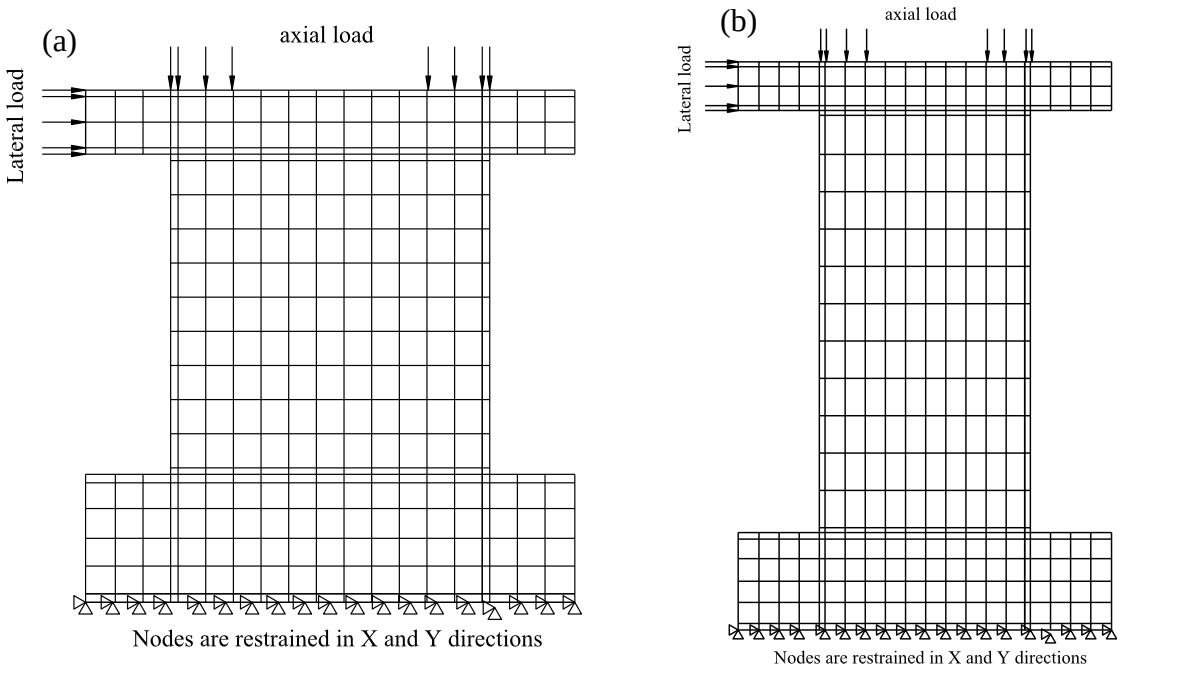

Figure 6.17 Numerical models of (a) type I and (b) type II walls tested by Lefas (1988)

Table 6.2 Details of isolated walls tested by Lefas (1988) and a comparison between the experimental and numerical analysis results

Type	Specimen	Reinforcement percentage				Cube strength f_{cu}, MPa	Axial load (kN)	Ultimate lateral load (kN)		experimental to analytical ultimate load (V_{test} /$V_{analysis}$)
		ρ_{hor}, (%)	ρ_{ver}, (%)	ρ_{flex}, (%)	ρ_s, (%)			Experiment (V_{test})	Numerical ($V_{analysis}$)	
Type I	SW1l	1.10	2.40	3.10	1.20	52.3	0	260	280	0.93
	SWl2	1.10	2.40	3.10	1.20	53.6	230	340	312	1.08
	SW13	1.10	2.40	3.10	1.20	40.6	355	330	348	0.94
	SW14	1.10	2.40	3.10	1.20	42.1	0	265	297	0.89
	SW15	1.10	2.40	3.10	1.20	43.3	185	320	305	1.05
	SW16	1.10	2.40	3.10	1.20	51.7	460	355	370	0.96
	SWl7	0.37	2.40	3.10	1.20	48.3	0	247	229	1.07
Type II	SW2l	0.80	2.50	3.30	0.90	42.8	0	127	140	0.91
	SW22	0.80	2.50	3.30	0.90	50.6	182	150	133	1.13
	SW23	0.80	2.50	3.30	0.90	47.8	343	180	200	0.90
	SW24	0.80	2.50	3.30	0.90	48.3	0	120	110	1.09
	SW25	0.80	2.50	3.30	0.90	45.0	325	150*	180	0.83
	SW26	0.40	2.50	3.30	0.90	30.1	0	123	120	1.03
								Average		0.99
								Standard deviation (SD)		0.09
								Coefficient of variation (CoV)		0.01

Note:
ρ_{flex}= ratio of main flexural reinforcement to gross concrete area of edge element;
ρ_{hor}= ratio of horizontal reinforcement to gross concrete area of vertical direction of wall web;
ρ_{ver} = ratio of vertical web reinforcement to gross concrete area of horizontal section of wall web;
ρ_s= ratio of effective volume of confinement reinforcement to the volume of the core.

* Premature failure

Table 6.3 Mechanical properties of reinforcement

Bar diameter (mm)	Yield stress (N/mm^2)	Ultimate strength (N/mm^2)
8	470	565
6.25	520	520
4	420	490

ii. Coupled structural walls

Isolated structural walls in tall buildings are normally connected together by coupling beams at regular heights forming what is known as coupled walls. A coupled wall Model 1 tested by Marsono (2000) was selected to further validate the numerical model. The model consisted of two symmetrical walls (1500 mm high × 350 mm wide × 40 mm thick) connected together with a series of coupling beams (50 mm high × 100 mm wide × 30 mm thick), and constructed from concrete with characteristic cube compressive strength value of 40 N/mm^2. The coupled walls were connected to a stiff base of 200 mm thickness and 300 mm depth. The walls were reinforced with a grid of 6 mm diameter high tensile bars in both directions with a yield stress of 406 N/mm^2. The geometric details and the reinforcement layout are given in Figure 6.18. The mesh configuration, load application and boundary conditions used in the finite element analysis are shown in Figure 6.19.

iii. Encased-plate simply supported beams

Simply-supported encased-plate beam 7S4 tested by Baglin (1998) was used as a further case study. The beam was designed to fail in shear with a flexural capacity set at a much higher level than shear capacity. The beam compression reinforcement comprised two 16 mm diameter high strength bars with a yield stress of 487 N/mm^2. Two 32 mm diameter high strength bars with 442 N/mm^2 yield stress were used as main tension reinforcement. The beam was constructed from concrete with characteristic cube compressive strength value of 40 N/mm^2 and was further reinforced with a 4 mm thick mild steel plate with yield stress of 239 N/mm^2. The encased-plate had profiled cut-outs along its bottom edge to

provide anchorage against slippage, which was ignored in the numerical model. Beam details and finite element idealisation are given in Figures 6.20 and 6.21, respectively.

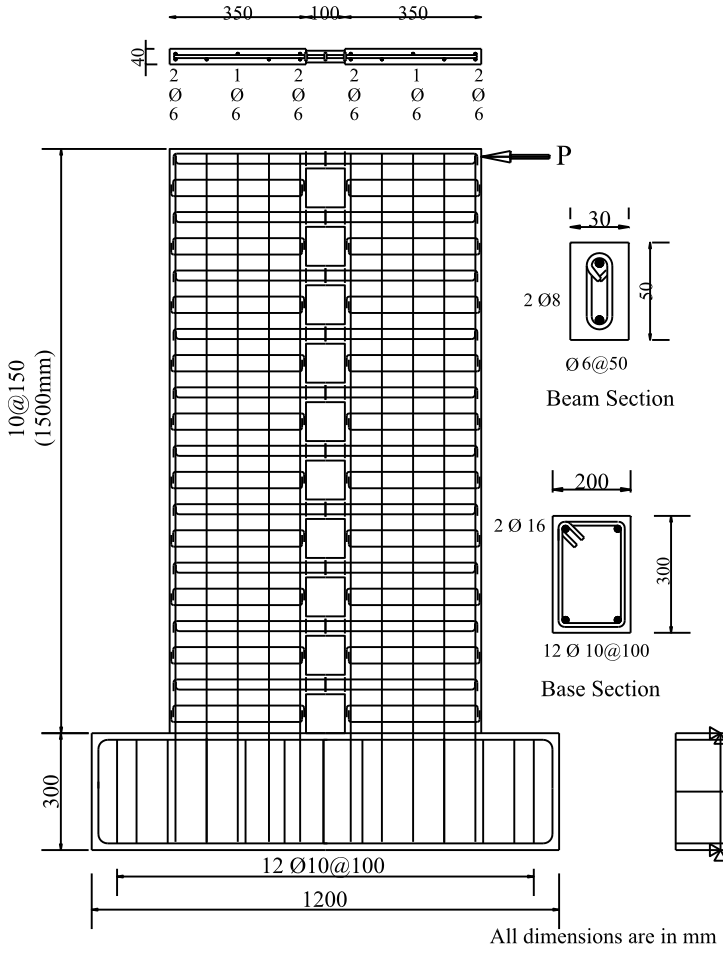

Figure 6.18 Geometry and reinforcement details of coupled structural wall Model1 tested by Marsono (2000)

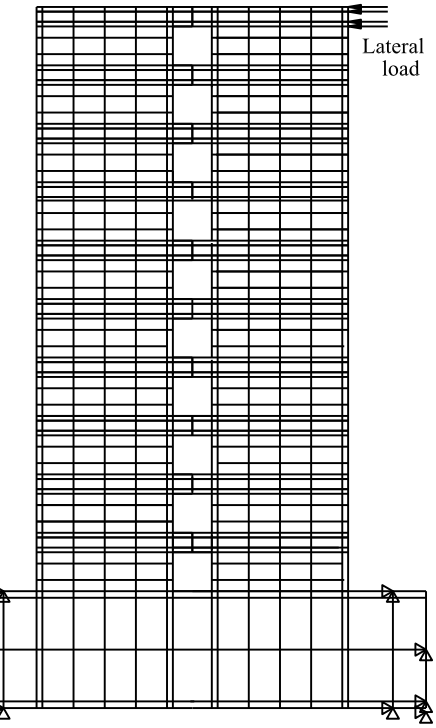

Figure 6.19 Numerical model of coupled wall Model 1 tested by Marsono (2000)

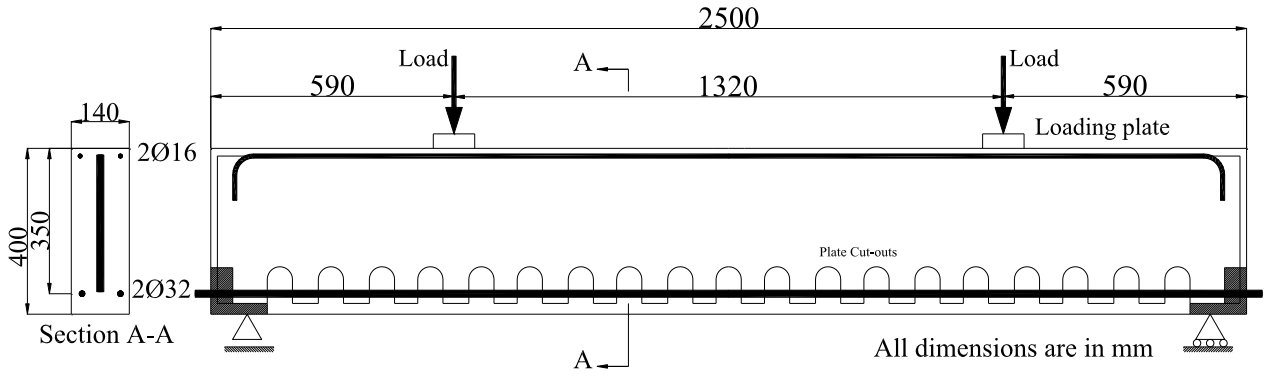

Figure 6.20 Geometry and reinforcement details of encased-plate beam S74 tested by Baglin (1998)

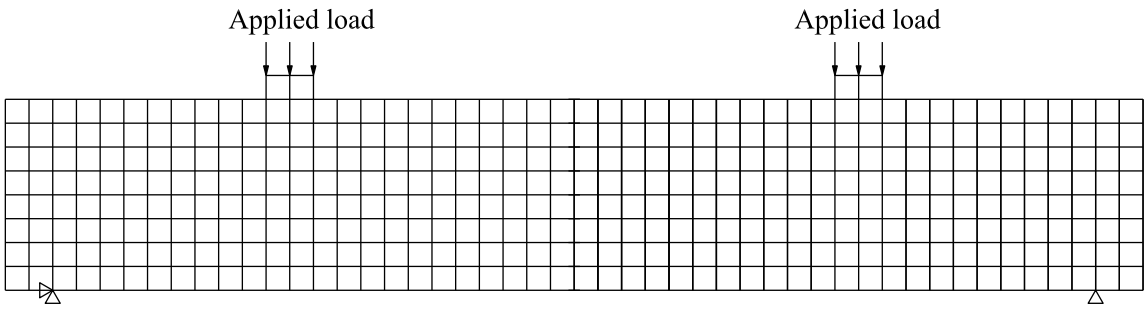

Figure 6.21 Numerical model of beam 7S4 tested by Baglin (1998)

B. Results and discussion

i. Isolated structural walls

A comparison between the experimentally obtained and numerically predicted load-displacement behaviour of specimens SW11, SW16, SW21 and SW23 is given in Figure 6.22a-d. The figures show that the proposed model was able to accurately trace the behaviour of isolated walls till failure. The predictions of the ultimate capacity were also compared to the experimental failure loads and listed in Table 6.2. The last column in the table presents the ratio of the experimental, V_{test}, to analytical results, $V_{analysis}$, (V_{test} / $V_{analysis}$). The average ratio of V_{test} /$V_{analysis}$ was 0.99 with a coefficient of variation (CoV) of 0.01 and a standard deviation (SD) of 0.09. These results indicated the reasonable success of the finite element model in simulating the behaviour of conventionally-reinforced walls.

Abaqus does not enable the direct graphical visualisation of crack development in concrete damage plasticity model. However, the analysis assumes that crack initiation takes place when the maximum principal plastic strain is greater than zero. The direction of cracks can be obtained from the direction of maximum principal plastic strains. This approach was used to investigate the crack propagation in the walls. Figure 6.23 presents the crack pattern as obtained experimentally and predicted numerically at failure for specimen SW23.

The figure shows the close agreement achieved in this case and in most walls tested by Lefas (1988).

ii. Coupled shear wall

With respect to the coupled wall Model 1 tested by Marason (2000), the finite element model yielded a reasonable prediction of overall behaviour, see Figure 6.22e, and ultimate strength (39.28 kN) compared well with the experimental failure load (36 kN).

iii. *Encased-plate simply-supported beams*

The load-displacement behaviour of encased-plate simply-supported beam 7S4 is compared to laboratory observations in Figure 6.22f .The comparison shows that the model predictions closely matched the ultimate load; however, the model considerably overestimated the beam stiffness. This overestimation is probably due to the assumption of full bond between the plate and concrete, which ignores the slip at plate-concrete interface. Also, a good agreement between the experimental and numerical crack patterns was obtained as shown in Figure 6.24.

6.3.2 Experimental results

All the wall units tested under pure in-plane shear presented in Chapter 3 and the wall specimens tested under lateral loading presented in Chapters 4 and 5 were modelled numerically. The numerical predictions were compared to the experimental results including the load-displacement behaviour, the ultimate load, the development of crack patterns and the strain propagation in the rebars and encased-plates.

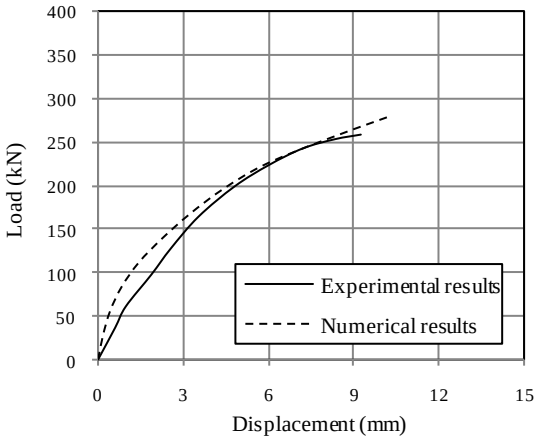

(a) Specimen SW11 (Lefas 1998)

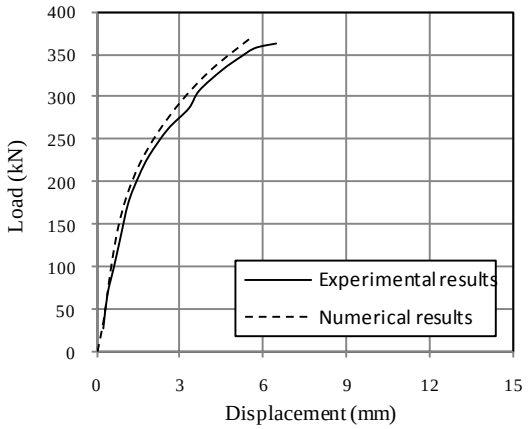

(b) Specimen SW16 (Lefas 1998)

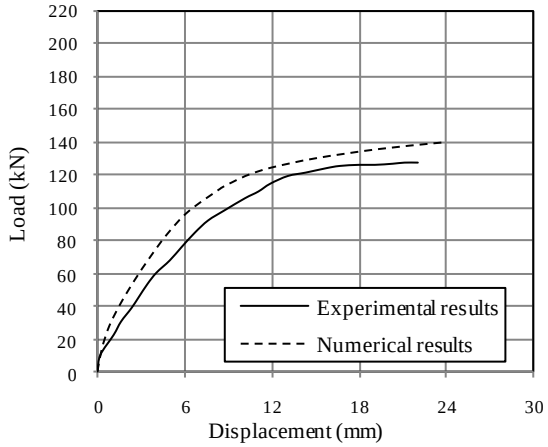

(c) Specimen SW21 (Lefas 1998)

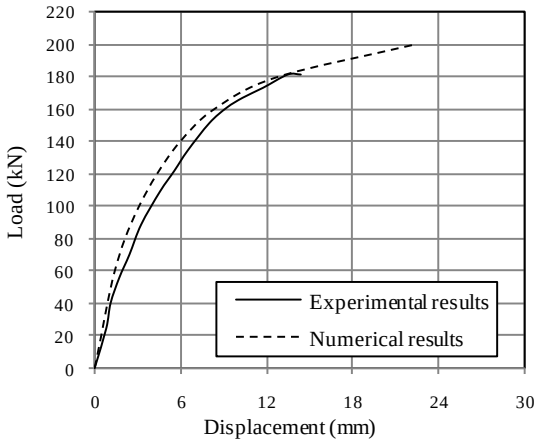

(d) Specimen SW23 (Lefas 1998)

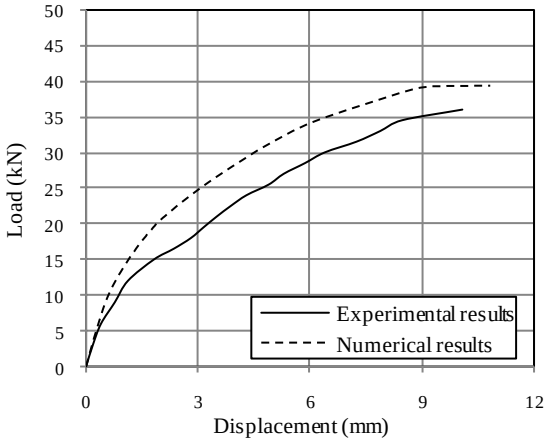

(e) Model 1 (Marsono 2000)

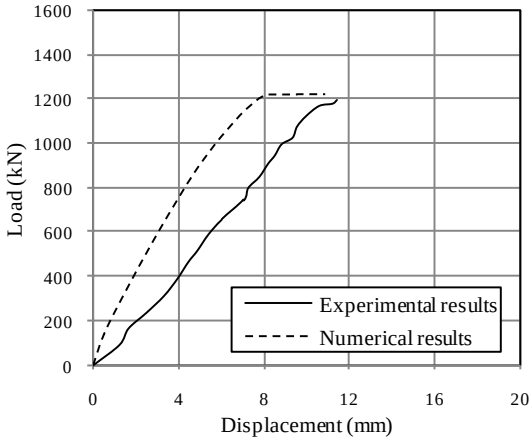

(f) Beam 7S4 (Baglin 1998)

Figure 6.22 The load-displacement behaviour for study case specimens as obtained experimentally and predicted numerically

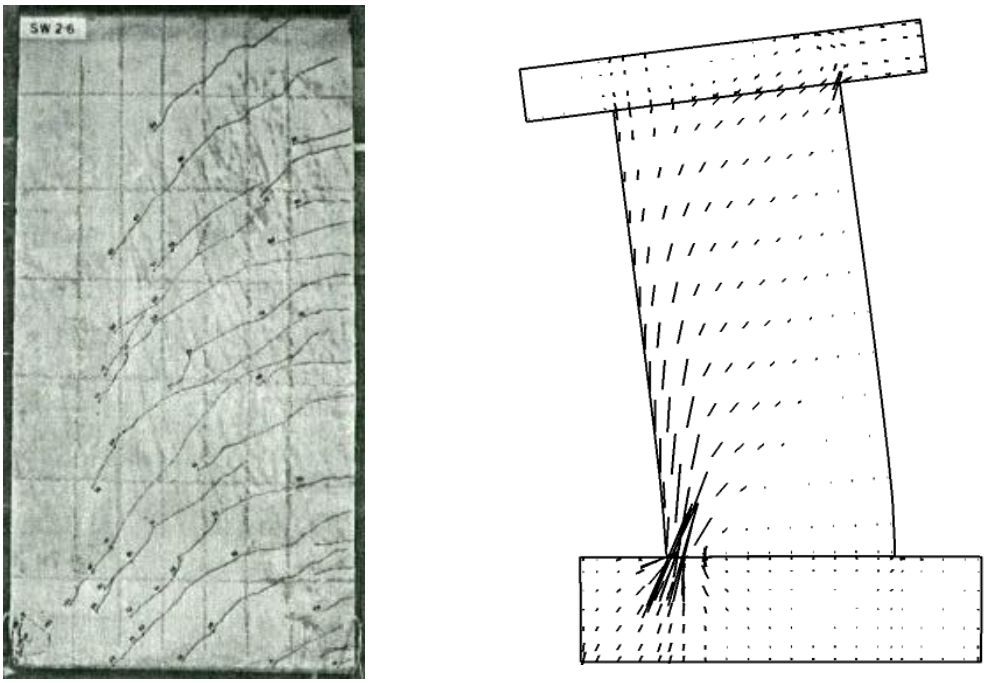

Figure 6.23 Crack pattern and deformed shape at failure of specimenSW23 tested by Lefas (1988) as obtained experimentally and predicted numerically

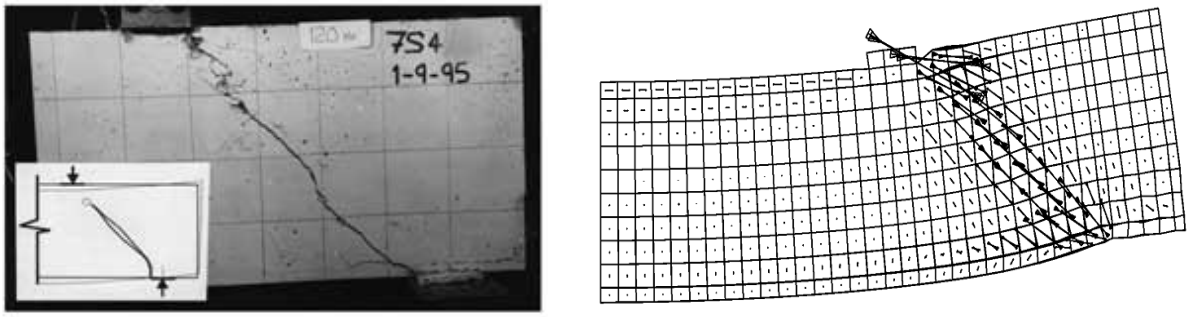

Figure 6.24 Crack pattern and deformed shape at failure of beam 7S4 tested by Baglin (1998) as obtained experimentally and predicted numerically

A. Load-displacement behaviour

The load-displacement behaviour of the specimens as obtained experimentally and predicted numerically is displayed in Figures 6.25 and 6.26. The figures show that the

numerical model could accurately predict the load-displacement behaviour of the specimens. The main features of numerical results are:

- In all cases, the initial stiffness of the simulation was consistent with the experimental values.

- For wall units tested under pure in-plane shear, the numerical model underestimated the stiffness of the units, which could be attributed to the simplicity adopted in modelling the frame members that ignores the slip at the connecting bolts and the corner pins.

- For wall specimens tested under lateral load, the model predicted slightly higher the post-cracking stiffness compared with the test data. This is thought to be a consequence of the inability of the concrete damage plasticity model to accurately simulate the load transferred through open cracks, the assumption of full bond between the encased-plate and concrete and the disregard of time-dependant displacements such as creep in the numerical model.

- The experimental softening behaviour of the specimens in post ultimate load was not tracked in the numerical simulation, possibly due to the assumption that the concrete is isotropic with complete softening uniformly distributed in all directions.

- The numerical model was not able to trace the behaviour of unit P8 that failed prematurely due to extensive damage of concrete cover, early plate buckling and formation of diagonal tension field. In this case, the numerical model was able to sustain higher loads compared to the experimental results.

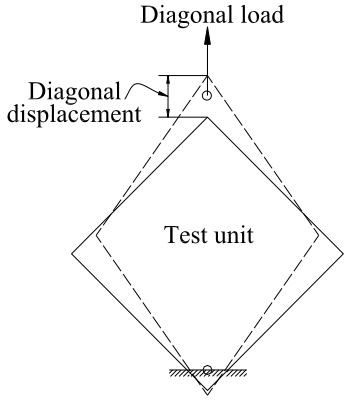

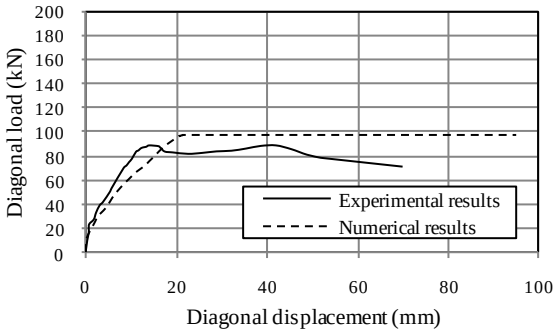

(a) Unit P1

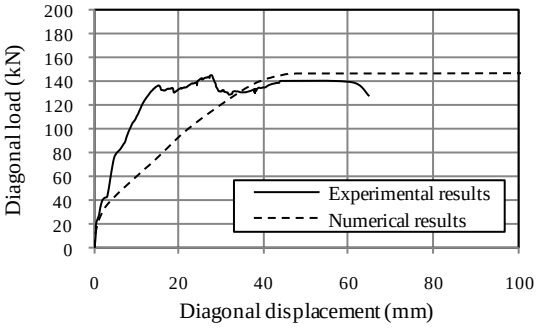

(b) Unit P2

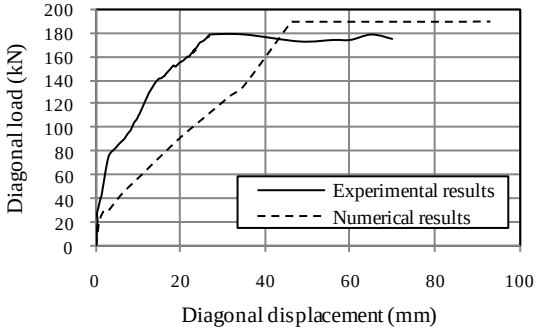

(c) Unit P3

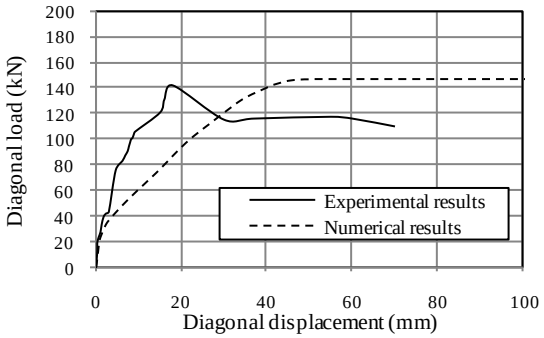

(d) Unit P4

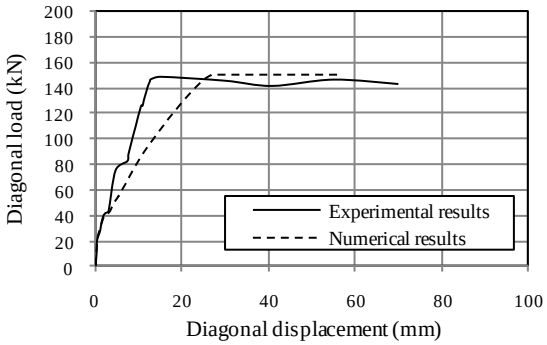

(e) Unit P5

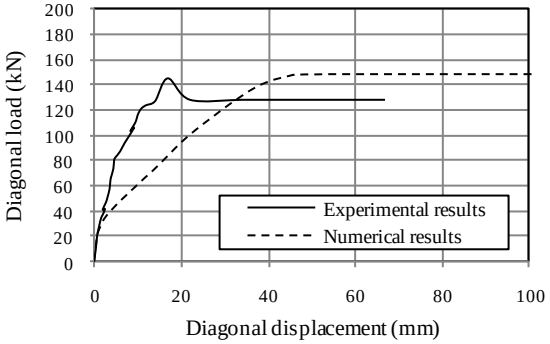

(f) Unit P6

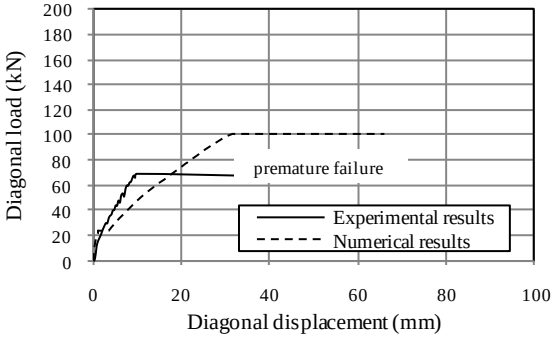

(g) Unit P8

Figure 6.25 Comparison between the experimental and the numerical diagonal load-diagonal displacement behaviour of wall units tested under pure in-plane shear

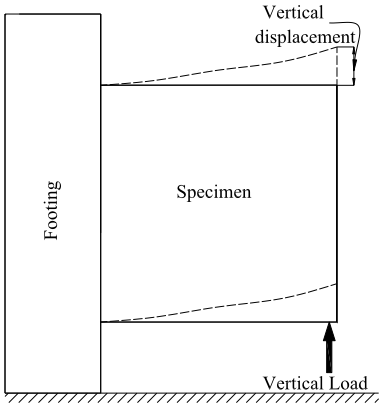

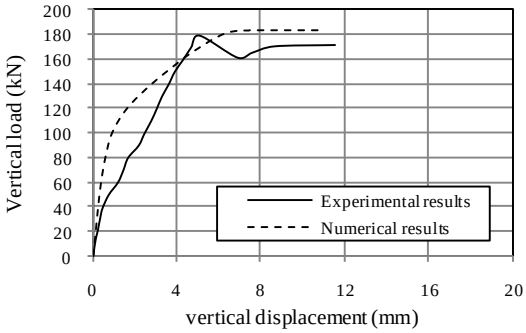

(a) Specimen EW11

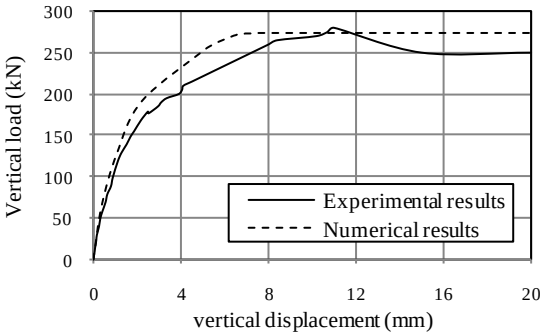

(b) Specimen EW12

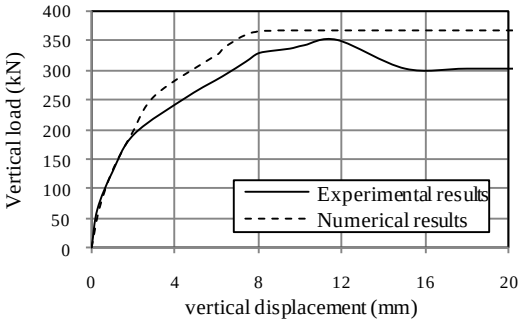

(c) Specimen EW13

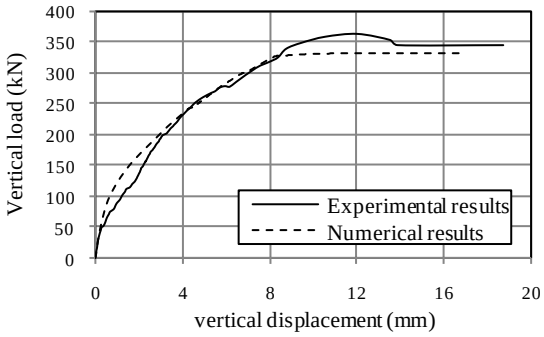

(d) Specimen EW21

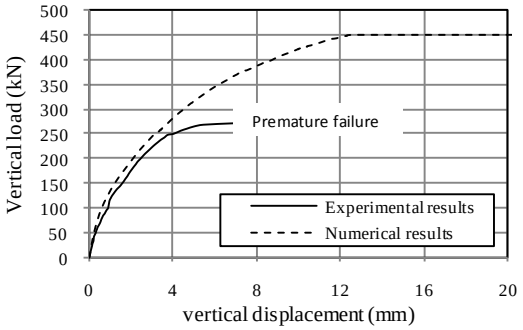

(e) Specimen EW22

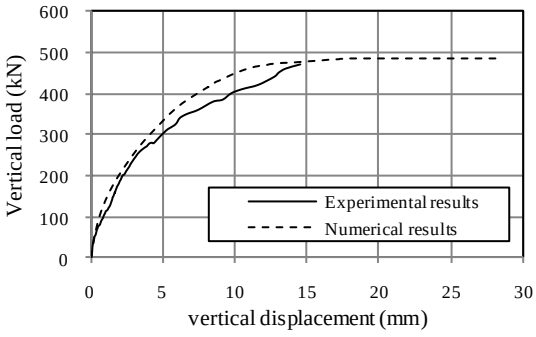

(f) Specimen EW23

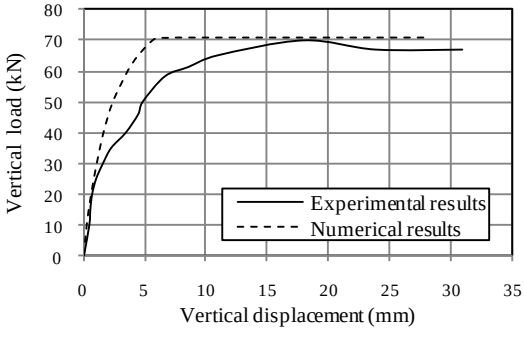

(g) Specimen EW31

Figure 6.26 Comparison between the experimental and the numerical load-displacement behaviour of specimens tested under lateral loading

B. Ultimate load

A comparison of the ultimate load values of the specimens obtained experimentally and predicted numerically is presented in Figure 6.27 and Table 6.4. The values in the table indicate that the numerical models yielded realistic predictions of the ultimate load values and a good agreement was achieved between the two sets of the results for all cases except that of unit P8 and specimen EW22, both failed prematurely as described in Chapters 3 and 5. Also, the numerical results for specimen EW23 compared well with the experimental results although it failed locally. The average ratio of experimental to analytical failure loads were 0.97 and 0.99 with coefficients of variation (CoV) of 0.001 and 0.003 and standard deviations (SD) of 0.03 and 0.06 for wall units tested under pure in-plane shear and wall specimens tested under lateral loading, respectively. These results are a further evidence of the effectiveness of the proposed model in tracing the behaviour of encased-plate composite walls.

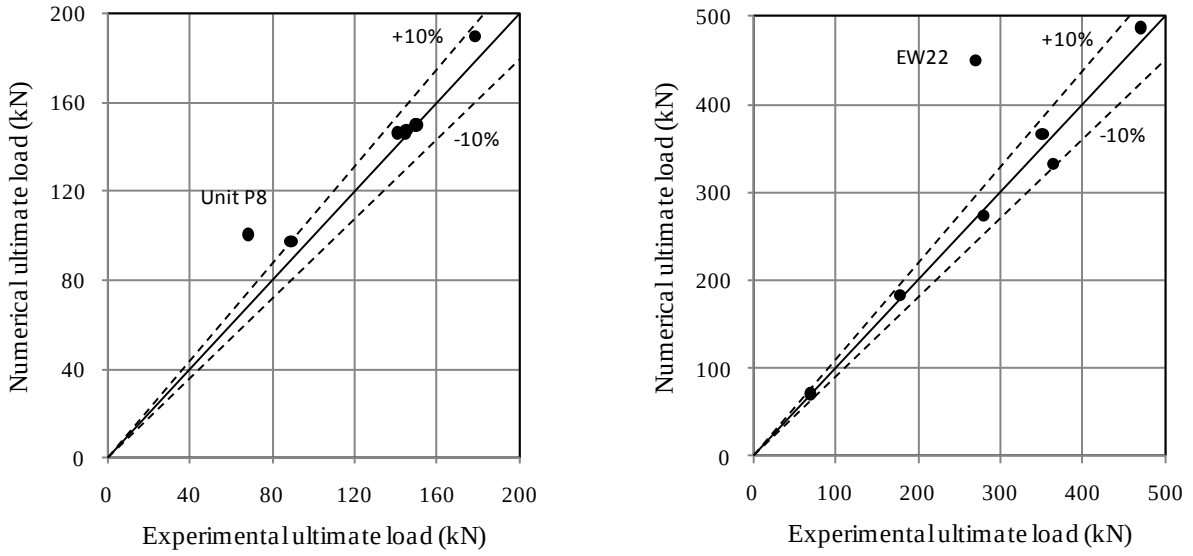

(a) Wall units tested under pure in-plane shear (b) Wall specimens tested under lateral loading

Figure 6.27 Comparison of ultimate load values predicted numerically with the corresponding experimental data

Table 6.4 Numerical predictions and experimental values of ultimate load

(a) Wall units tested under pure in-plane shear

Specimen	Diagonal ultimate load (kN)		experimental to analytical ultimate load (V_{test} / $V_{analysis}$)
	Experimental (V_{test})	Numerical ($V_{analysis}$)	
P1	89.20	97.60	0.91
P2	144.32	146.60	0.98
P3	178.70	189.80	0.94
P4	141.01	146.60	0.96
P5	149.32	150.20	0.99
P6	144.99	147.80	0.98
P7	149.96	150.00	1.00
P8*	68.28	100.60	0.68^{x}
*Premature failure	Mean		0.97
^{x}Excluded from statistical analysis	Standard deviation(SD)		0.03
	Coefficient of variation (CoV)		0.001

(b)Wall specimens tested under lateral loading

Specimen	Ultimate load (kN)		experimental to analytical ultimate load (V_{test} / $V_{analysis}$)
	Experimental (V_{test})	Numerical ($V_{analysis}$)	
EW11	180.00	183.20	0.98
EW12	280.00	273.92	1.02
EW13	350.00	365.44	0.96
EW21	365.00	332.00	1.10
EW22*	270.00	450.00	0.6^{x}
EW23	470.00	487.00	0.97
EW31	70.00	70.80	0.99
*Premature failure	Mean		0.99
^{x}Excluded from statistical analysis	Standard deviation(SD)		0.06
	Coefficient of variation (CoV)		0.003

C. Crack patterns

Figure 6.28 shows typical development of cracking for specimen EW11 at different loading stages as predicted numerically. A flexural crack appeared vertically in the tensile boundary element at a vertical load of 65 kN, which was 9% higher than the experimental load, Figure 6.28a. This was followed by several flexural cracks spreading on the tensile boundary element and extending diagonally in the central panel, Figure 6.28b and c. With further increases in vertical load, tensile reinforcement yielding was associated with independent diagonal cracks spreading over the central panel and penetrating the compressive zone, until total specimen failure, Figures 6.28c and d. The predicted crack pattern matched well with the experimentally observed behaviour.

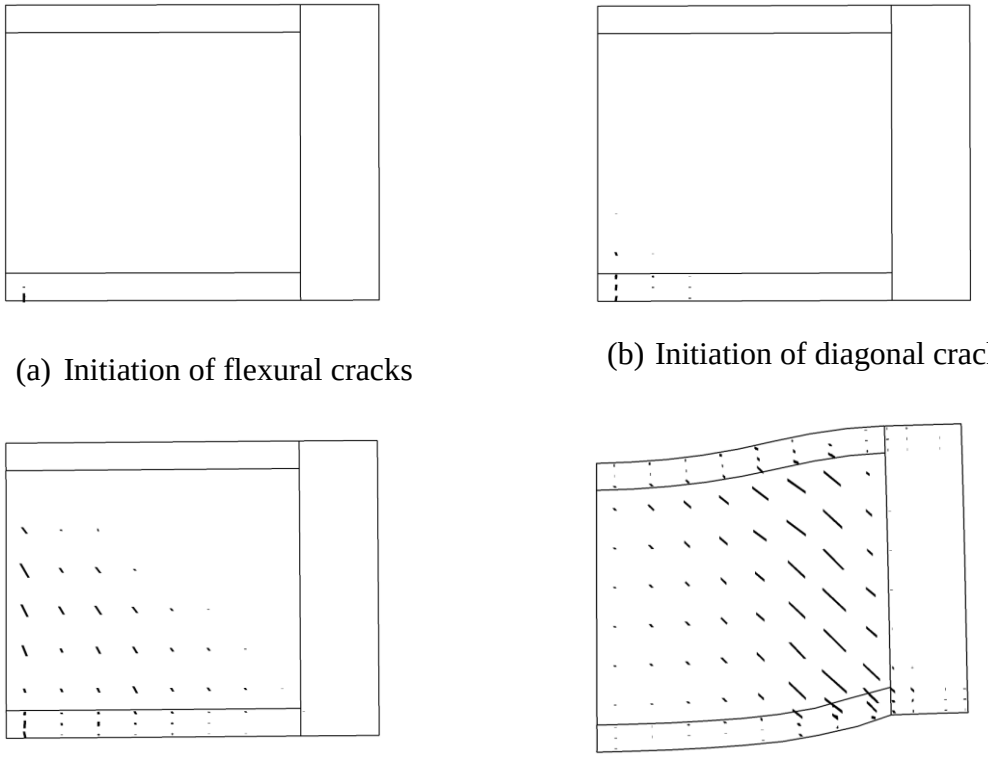

(a) Initiation of flexural cracks

(b) Initiation of diagonal crack

(c) Yielding of tensile reinforcement

(d) Failure

Figure 6.28 Evolution of crack pattern in Specimen EW11

The crack patterns obtained from the experiments and the analyses of all wall specimens and unit P2 are illustrated in Figure 6.29. For specimens EW11, EW12 and EW13, which failed in shear by diagonal tension, concrete crushing in the most compressive zone was observed in the numerical results as obtained experimentally. On the other hand, concrete crushing could be predicted in specimens EW21 and EW31 which failed in shear and flexure, respectively, see Figures 6.29e and h. The crack patterns predicted numerically for specimens EW22 and EW23 were different from those observed experimentally since specimen EW22 failed prematurely and the failure mode of specimen EW23 could not be traced numerically since the specimen failed locally at the point of load application as discussed in Chapter 5.

D. Reinforcement strains

Figure 6.30 depicts the strain propagation predicted by the numerical simulation in the rebars and encased-plates for all wall specimens tested under lateral loading. Overall, the numerical simulation was capable of capturing the experimentally observed strain trends for the entire loading range. These results present another validity evidence of the proposed finite element model.

6.3.3 Main findings of validation study

The proposed finite element modelling technique was used to study the behaviour of a wide range of concrete structures ranging from structural walls, shear-critical encased-plate simply-supported beams and encased-plate composite walls. Based on the results discussed in Section 6.3, the proposed numerical model appears to be able to accurately predict the behaviour of these structural types. Consequently, it will be used to represent the behaviour of encased-plate composite walls within a parametric study that covers a wide variation of parameters that are thought to influence the performance of composite walls.

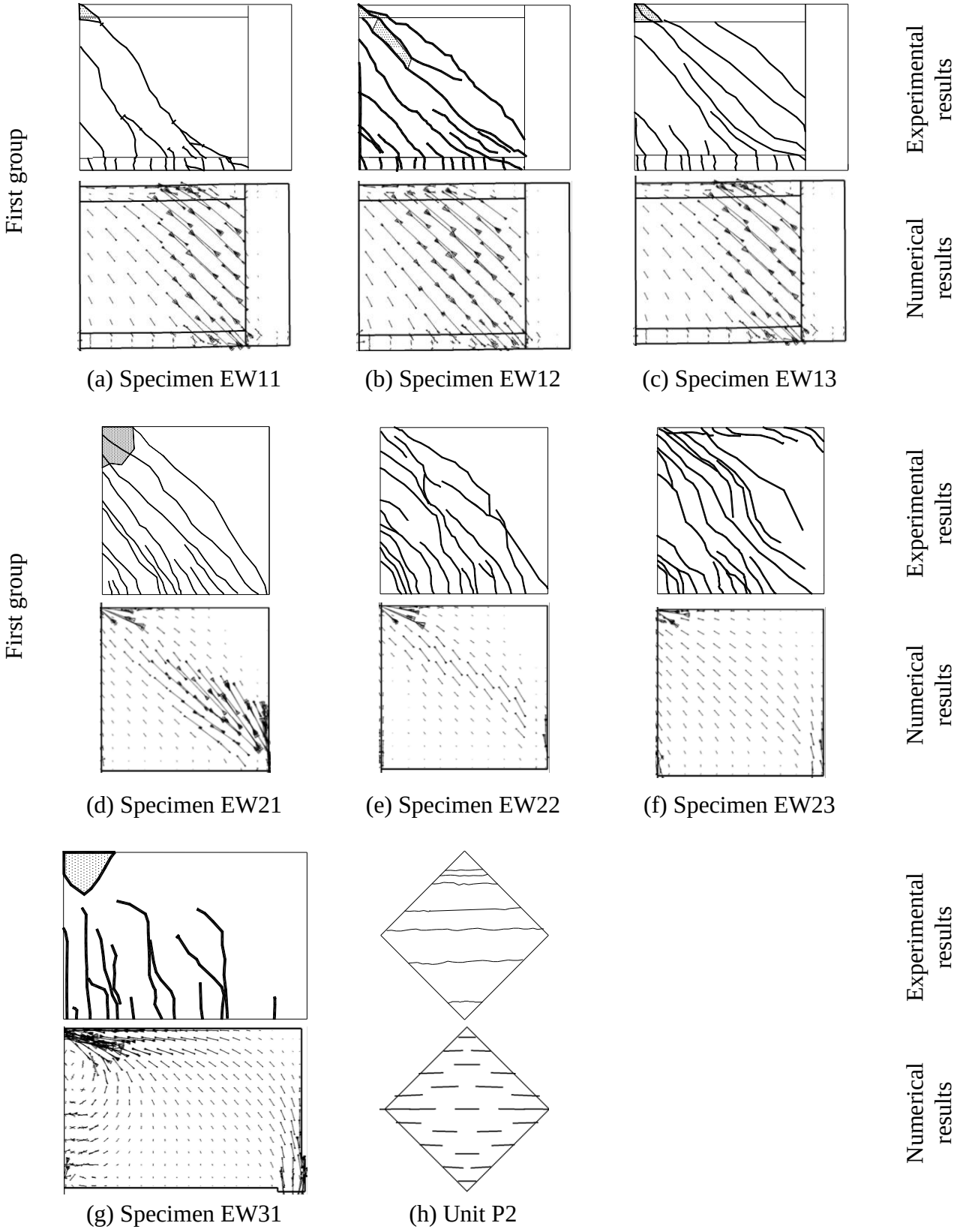

Figure 6.29 Sketches of crack patterns as obtained experimentally and predicted numerically at failure

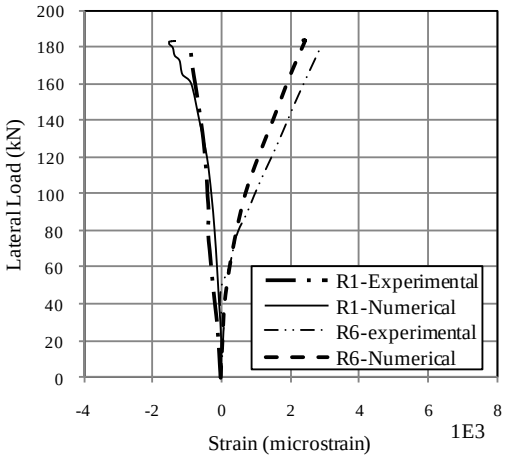

(1) Specimen EW11

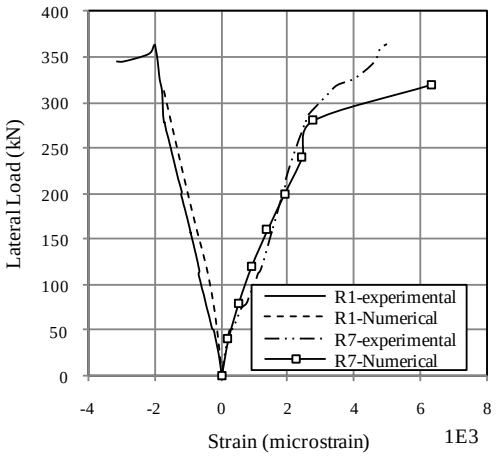

(2) Specimen EW21

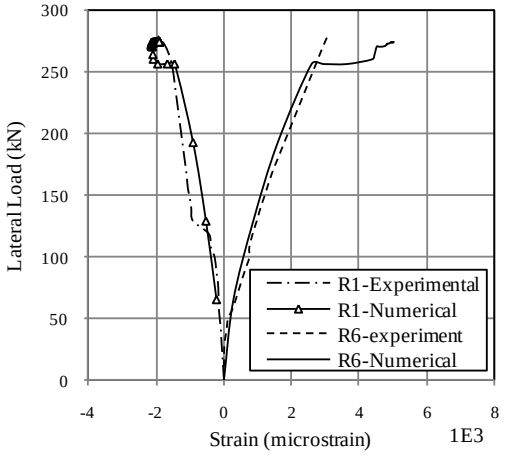

(a) Rebars

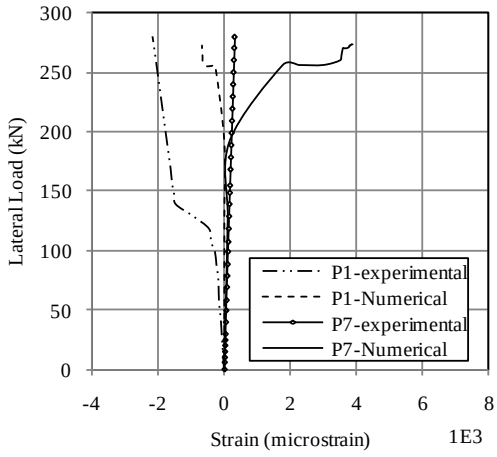

(b) Encased-plate

(3) Specimen EW12

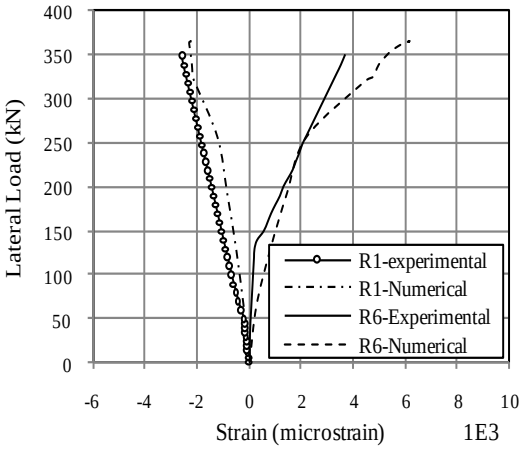

(a) Rebars

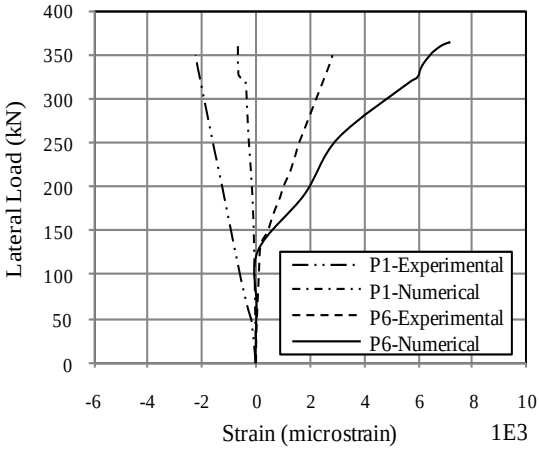

(b) Encased-plate

(4) Specimen EW13

Figure 6.30 Experimental and predicted strain profiles in reinforcement and encased-plate

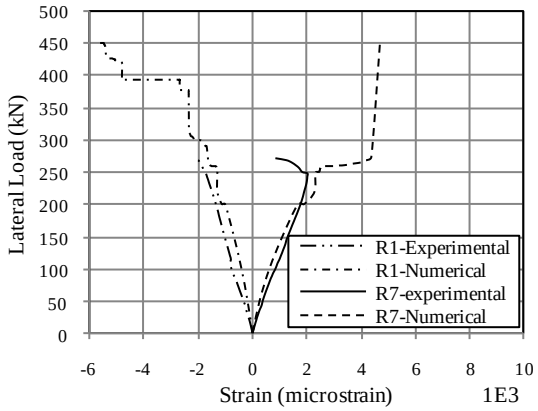

(a) Rebars

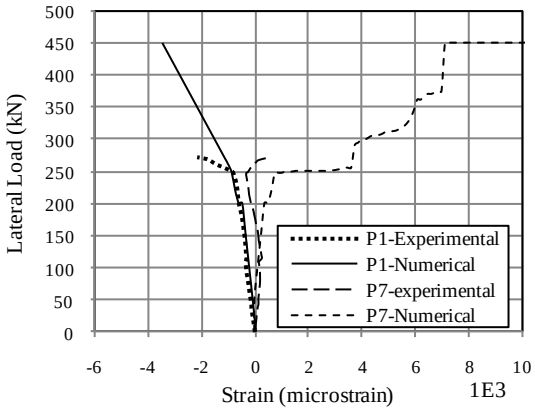

(b) Encased-plate

(5) Specimen EW22

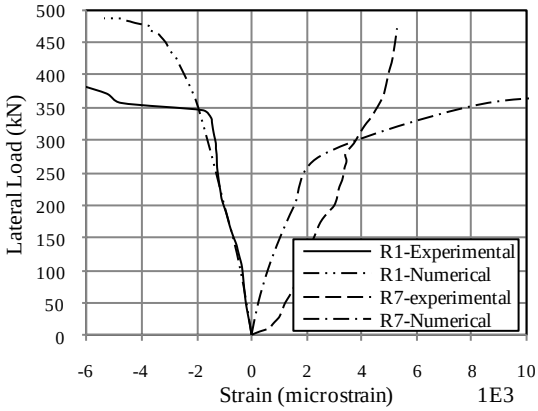

(a) Rebars

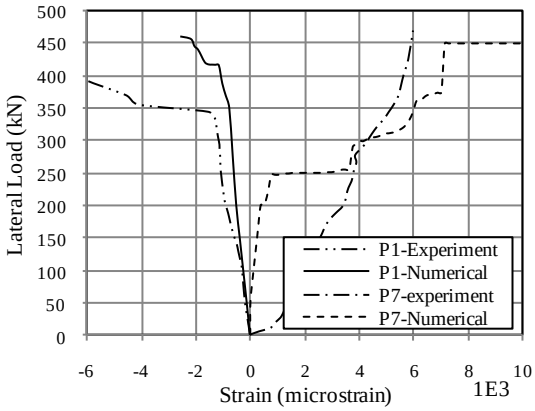

(b) Encased-plate

(5) Specimen EW23

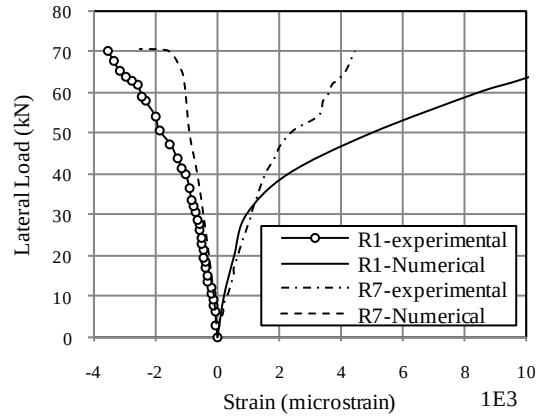

(a) Rebars

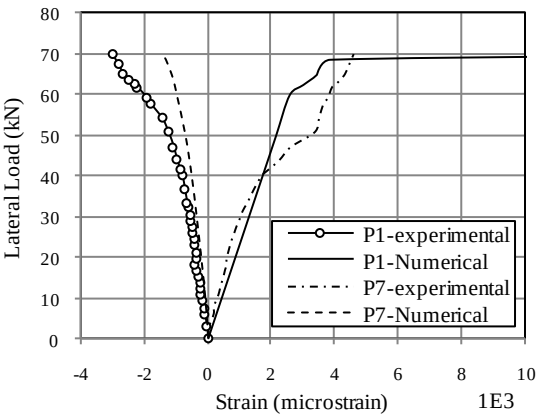

(b) Encased-plate

(7) Specimen EW31

Figure 6.30 Experimental and predicted strain profiles in reinforcement and encased-plate (cont.)

6.4 Parametric study

6.4.1 Introduction

Since experimental testing of concrete structures is time-consuming and expensive, finite element modelling could be used to simulate their behaviour and produce large amounts of useful data on the effect of different parameters on their performance. A number of hypothetical conventional and encased-plate composite walls with larger capacities and dimensions than those built and tested experimentally were modelled and analysed using the proposed numerical model. The parametric study comprised 57 hypothetical walls with different combinations of wall geometry, plate size and reinforcement layout, and comparisons of behaviour concentrated on the load-displacement behaviour, initial stiffness, ultimate load and cracking pattern. The parameters considered in the study included (a) aspect ratio, 0.5-3, (b) plate thickness, 0-4 mm, (c) axial loading, 0-0.2 of the uniaxial compressive strength of the wall's cross-section, (d) concrete strength, 25-80 N/mm^2, (e) longitudinal reinforcement of central panel, 0.31-4%, (f) transverse reinforcement of central panel (stirrups), 0.38-4%, and (g) longitudinal reinforcement of boundary elements, 1-4%.

6.4.2 Details of the numerical models

The numerical model of specimen EW12 was selected as a reference in the design of the parametric study. In order to reduce the number of required models, boundary element size, wall thickness, stiff beam and base block size were kept constant in all models. The numerical models were divided into three series, S-EW, Q-EW and C-EW, representing short, squat and cantilever walls with aspect ratios of 0.5, 1 and 3, respectively. Each model was constructed with a stiff beam with 200 mm square cross-section and a base block with dimensions of 1400 mm length × 1200 mm depth × 400 mm width.

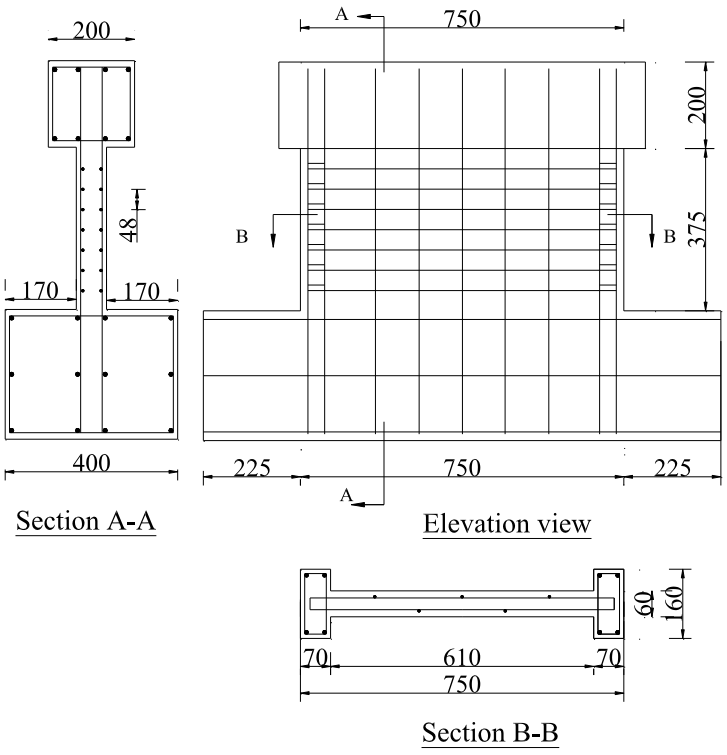

(a) Series S-EW

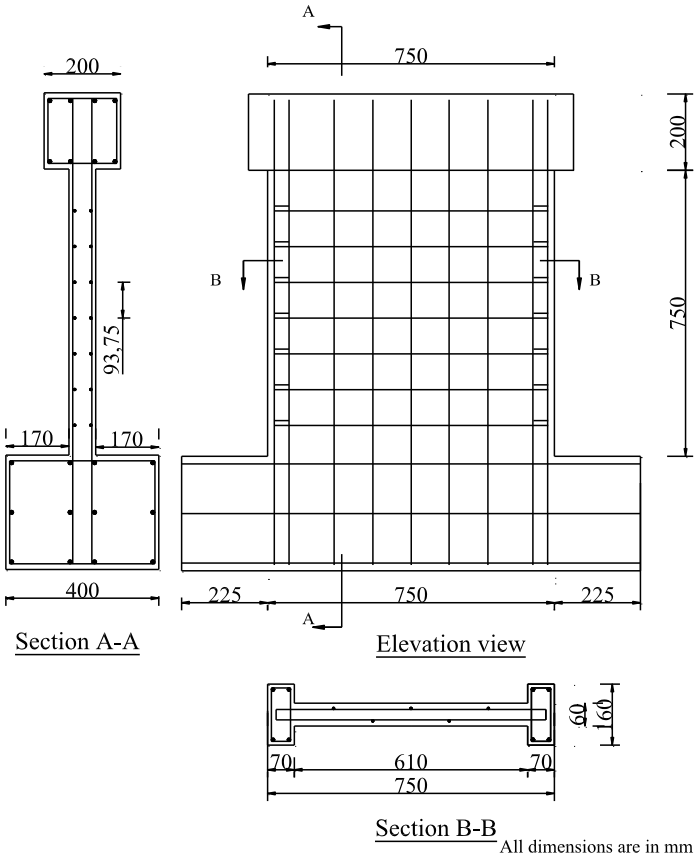

(b) Series Q-EW

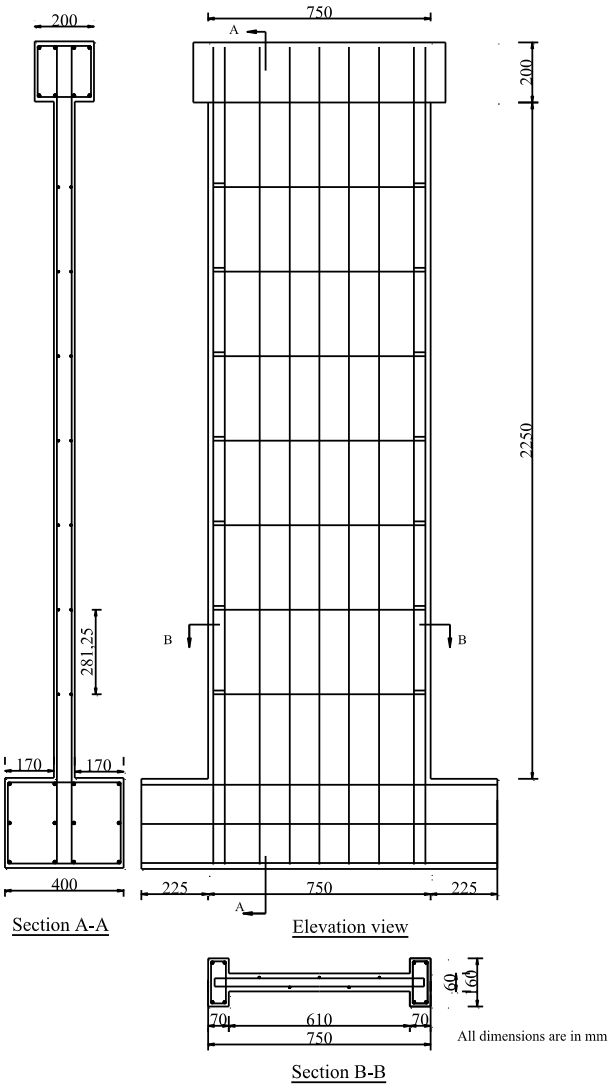

(c) Series C-EW

Figure 6.31 Dimensions and reinforcement details of the hypothetical walls

The overall wall width was fixed at 750 mm, while the height was either 375, 750 or 2250 mm for the three model series, respectively. The dimensions and reinforcement layout of the models are given in Figure 6.31, while Figure 6.32 presents a perspective view of the finite element meshes adopted.

Each model series was further divided into six categories according to the plate thickness, central panel longitudinal reinforcement, central panel stirrups, concrete strength, axial

loading and boundary elements longitudinal reinforcement. The details and reinforcement ratios of the hypothetical walls considered in the study are summarised in Table 6.5.

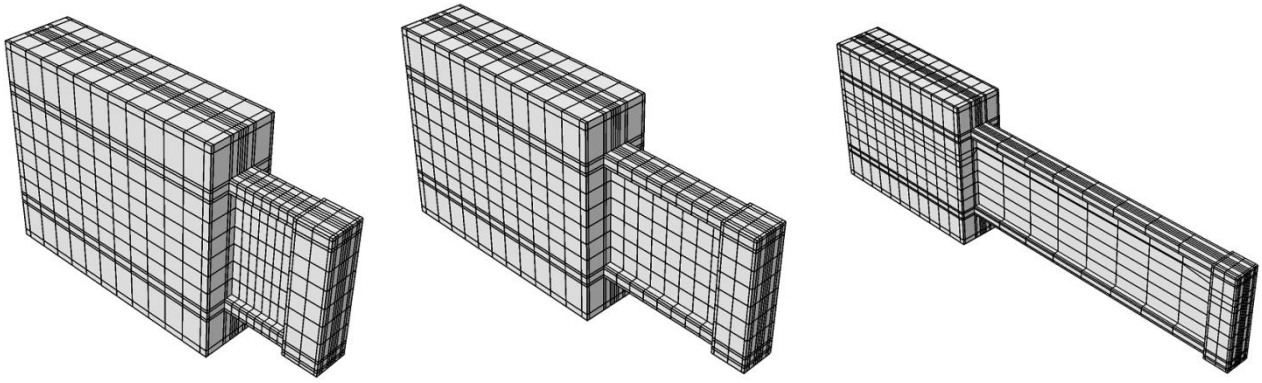

(a) Series S-EW (b) Series Q-EW (c) Series C-EW

Figure 6.32 A perspective view of the finite element meshes for the modelling of hypothetical walls

Table 6.5 Details of hypothetical walls used in parametric study

Category	Specimen	Plate thickness (mm)	Central panel reinforcement		Concrete strength (N/mm^2)	Axial load ratio	Boundary element longitudinal reinforcement ratio (%)	Main parameter
			Longitudinal (%)	Transverse ρ_t (%)				
(1)	A1	0.0	0.31	0.38	40	0.0	4.0	Plate thickness
	A2	0.8	0.31	0.38	40	0.0	4.0	
	A3	1.5	0.31	0.38	40	0.0	4.0	
	A4	2.0	0.31	0.38	40	0.0	4.0	
	A5	3.0	0.31	0.38	40	0.0	4.0	
	A6	4.0	0.31	0.38	40	0.0	4.0	
(2)	A7	0.8	1.0	0.38	40	0.0	4.0	Central panel longitudinal reinforcement
	A8	0.8	2.0	0.38	40	0.0	4.0	
	A9	0.8	4.0	0.38	40	0.0	4.0	
(3)	A10	0.8	0.31	1.0	40	0.0	4.0	Central panel stirrups
	A11	0.8	0.31	2.0	40	0.0	4.0	
	A12	0.8	0.31	4.0	40	0.0	4.0	
(4)	A13	0.8	0.31	0.38	25	0.0	4.0	Concrete strength
	A14	0.8	0.31	0.38	60	0.0	4.0	
	A15	0.8	0.31	0.38	80	0.0	4.0	
(5)	A16	0.8	0.31	3.0	40	0.1	4.0	Axial load ratio
	A17	0.8	0.31	3.0	40	0.2	4.0	
(6)	A18	0.8	0.31	0.38	40	0.0	1.0	Boundary element longitudinal reinforcement
	A19	0.8	0.31	0.38	40	0.0	2.0	

6.4.3 Effects of parameters

A. Aspect ratio

Previous studies (Irwin 1984; Lefas 1988; Penelis and Kappos 1997; Raongjant 2007) suggested that the failure behaviour of structural walls with different aspect ratios differed significantly. Short walls with aspect ratios less than 1 were more susceptible to shear failure, while squat walls could fail in flexure or shear depending on the reinforcement layout. Appropriately designed cantilever walls with aspect ratios greater than 2 were expected to fail in a predominantly flexural mode. The aspect ratio was varied in the current study from 0.5 to 3 to investigate its effects on the response of encased-plate composite walls.

The models were constructed from concrete with characteristic cube compressive strength value of 40 N/mm^2 and were reinforced with a 0.8 mm thick steel plate and provided with the same ratios of reinforcement in the boundary elements (4%) and the central panel (0.31 and 0.38% in the longitudinal and transverse directions, respectively). The numerical load-displacement behaviour of the three basic models with different aspect ratios and subjected to lateral loading only is presented in Figure 6.33.

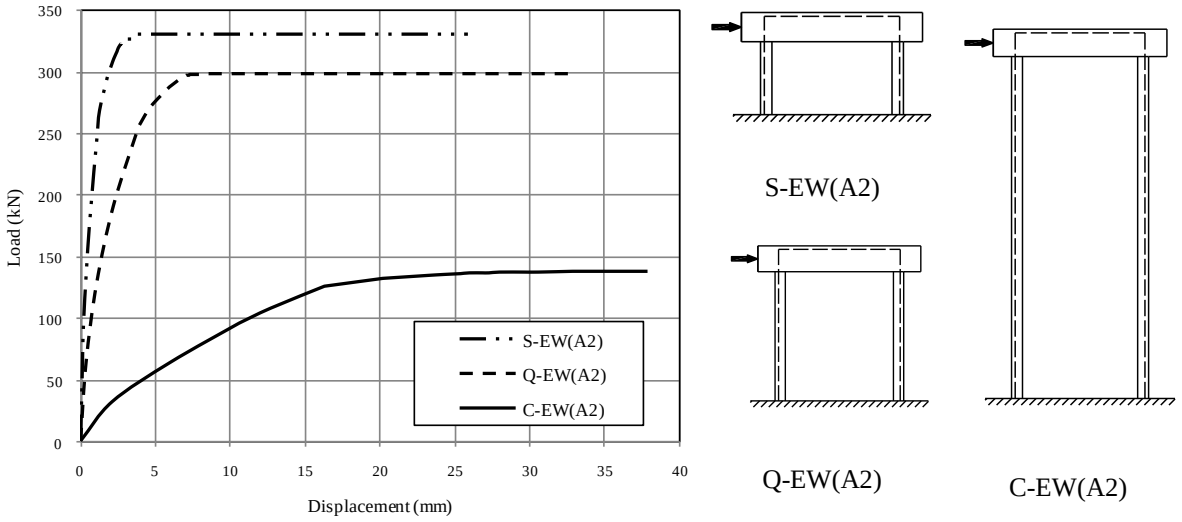

Figure 6.33 Load-displacement behaviour of walls with different aspect ratios

Figure 6.33 suggests that the aspect ratio is an important parameter affecting the behaviour of encased-plate composite walls. The initial stiffness and ultimate load are highly affected by increasing the aspect ratio as depicted in Figure 6.34, which illustrates the influence of aspect ratio on initial stiffness and ultimate load values. Cantilever wall failed under lower lateral loads and demonstrated comparatively lower initial stiffness compared to squat and short walls. The initial stiffness of cantilever wall was 8.8 and 2.7% of that of squat and short walls, respectively. The corresponding ratios of ultimate load were 46 and 41%, respectively.

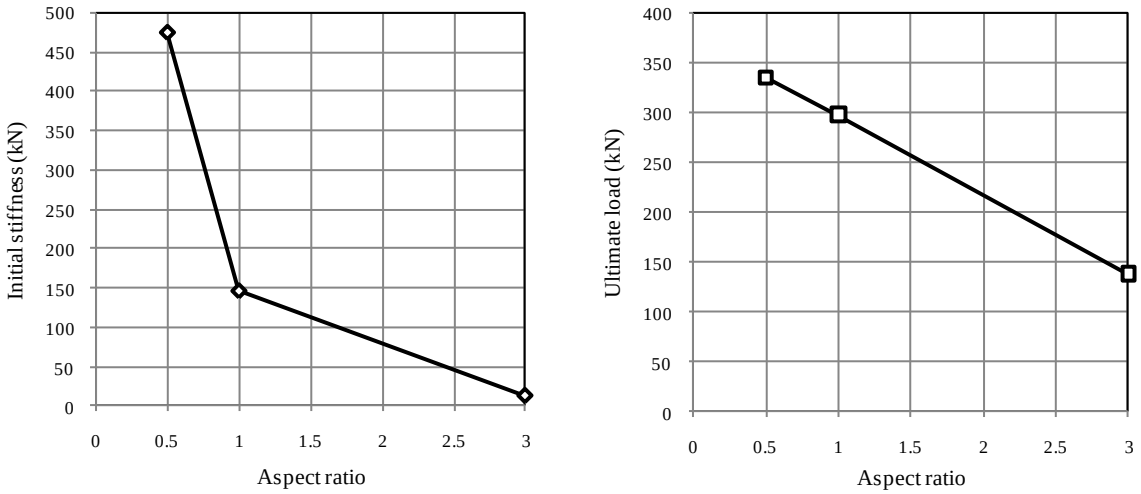

(a) Initial stiffness (b) Ultimate load

Figure 6.34 Influence of aspect ratio on initial stiffness and ultimate load values

The crack patterns of the walls are displayed in Figure 6.35. The figure was used to predict the mode of failure for the model walls. Cantilever walls experienced large flexural deformations with tensile yielding of encased-plate and tensile reinforcement. The mode of failure was characterised by extensive flexural cracking and concrete crushing in the most compressive zone. Squat walls failure was characterised by the formation of flexural cracking in the tensile boundary element and formation of diagonal tension failure plane as observed in the experimental testing of specimen EW12, while short wall failure, as

suggested by the numerical crack pattern, was associated with flexural cracking and concrete crushing forming what is known as diagonal compression failure.

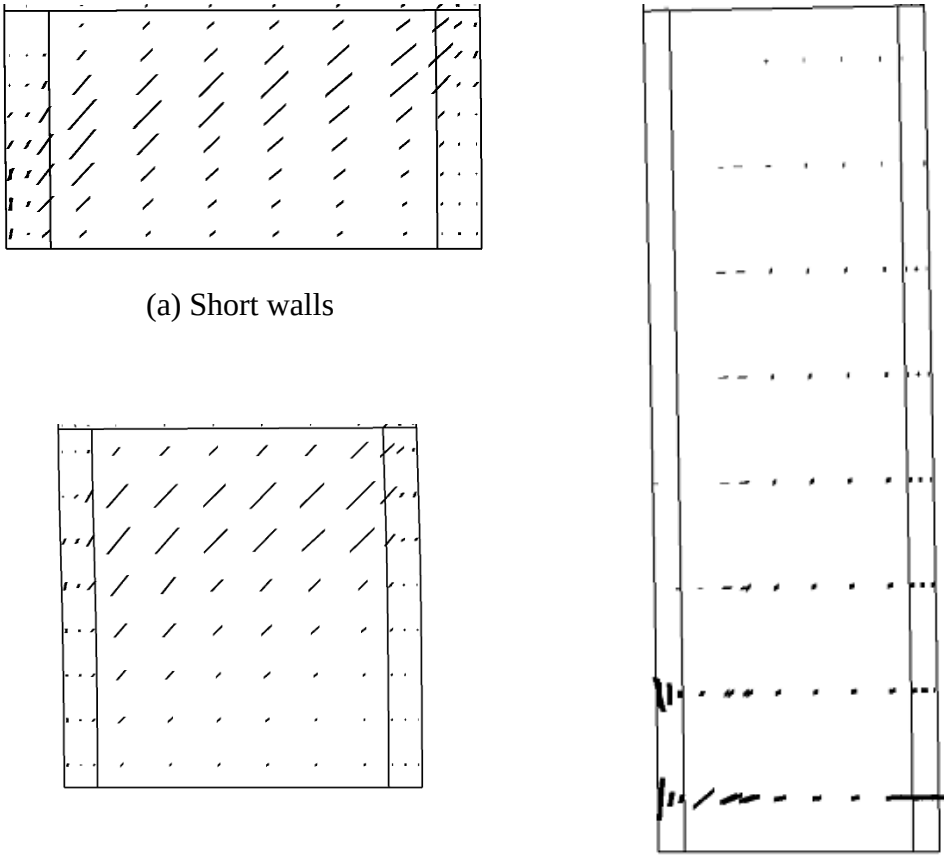

(a) Short walls

(b) Squat walls

(c) Cantilever walls

Figure 6.35 Crack pattern in basic walls at failure

B. Plate thickness

The strength of encased-plate structural walls reinforced with plates of different thickness was assessed. The walls were constructed from concrete with characteristics cube compressive strength value of 40 N/mm^2 and were provided with the same ratios of reinforcement in the boundary elements (4%) and the central panel (0.31 and 0.38% in the longitudinal and transverse directions, respectively). The plate thickness was varied from 0 to 4 mm, which was greater than the range investigated experimentally.

Figure 6.36 plots the variations of initial stiffness for short, squat and cantilever walls against plate thickness. Results including the initial stiffness, ultimate load and the ratio of the initial stiffness and ultimate load relative to those of the control walls (conventionally-reinforced walls, S-EW(A1), Q-EW(A1) and C-EW(A1) for short, squat and cantilever model series, respectively) are also summarised in Table 6.6.

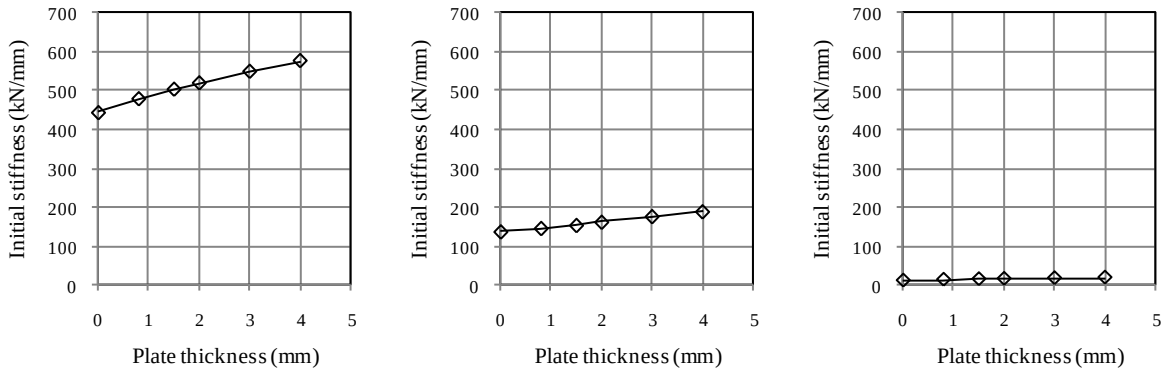

(a) Short walls (b) Squat walls (c) Cantilever walls

Figure 6.36 Variation of predicted values of initial stiffness with plate thickness

In all cases, the initial stiffness increased with larger plate thickness. The increase was more significant in cantilever walls and reduced gradually as the aspect ratio decreased. For example, cantilever wall C-EW (A6), reinforced with a 4 mm thick plate, could achieve a 74% increase in the initial stiffness when compared to a wall without a plate. The stiffness increase dropped to 36 and 29% in squat wall, Q-EW (A6), and short wall, S-EW(A6), respectively. These results indicate that encased-plates were effective in contributing to the flexural stiffness of structural walls.

The load-displacement behaviour of walls reinforced with different plate thickness values is presented in Figure 6.37. The figure suggests that the post-cracking stiffness was

considerably increased with the use of thicker plates. The variation in ultimate load with plate thickness is also presented in Figure 6.38.

Table 6.6 Values of initial stiffness and ultimate load

Wall type	Plate thickness	Initial stiffness (kN/mm)	Initial stiffness relative to control (%)	Ultimate load (kN)	Ultimate load relative to control (%)
Short	0.0	444.00	100.00	206.07	100.00
	0.8	479.00	107.88	327.02	158.74
	1.5	503.00	113.29	446.00	216.50
	2.0	519.00	116.89	496.10	240.78
	3.0	548.00	123.42	634.01	307.77
	4.0	575.00	129.50	651.03	316.02
Squat	0.0	138.00	100.00	183.20	100.00
	0.8	146.50	106.16	298.19	162.84
	1.5	154.00	111.59	366.14	200.00
	2.0	162.00	117.39	398.12	217.49
	3.0	176.00	127.54	398.11	217.49
	4.0	188.00	136.23	398.02	217.49
Cantilever	0.0	10.60	100.00	109.13	100.00
	0.8	12.95	122.17	138.24	126.83
	1.5	14.40	135.85	154.88	142.09
	2.0	15.30	144.34	155.11	142.20
	3.0	17.00	160.38	155.20	142.20
	4.0	18.50	174.53	155.15	142.20

Figure 6.38 and Table 6.6 show that increasing plate thickness has a considerable effect on the strength of encased-plate composite walls as expected. Plate contribution in load carrying capacity was more pronounced in short walls than in squat and cantilever walls. With reference to Table 6.6, short wall S-EW (A5), reinforced with a 3 mm thick plate, achieved 208% increase in ultimate load when compared to conventionally-reinforced wall, S-EW (A1). However, this increase dropped to 117 and 42% in squat and cantilever walls, respectively. These results imply that the use of encased-plates is more effective in short walls which are expected to fail in shear. This result agrees well with the improvements

achieved from using of encased-plates in shear-critical simply-supported and coupling beams (Baglin 1998; Lam 2006).

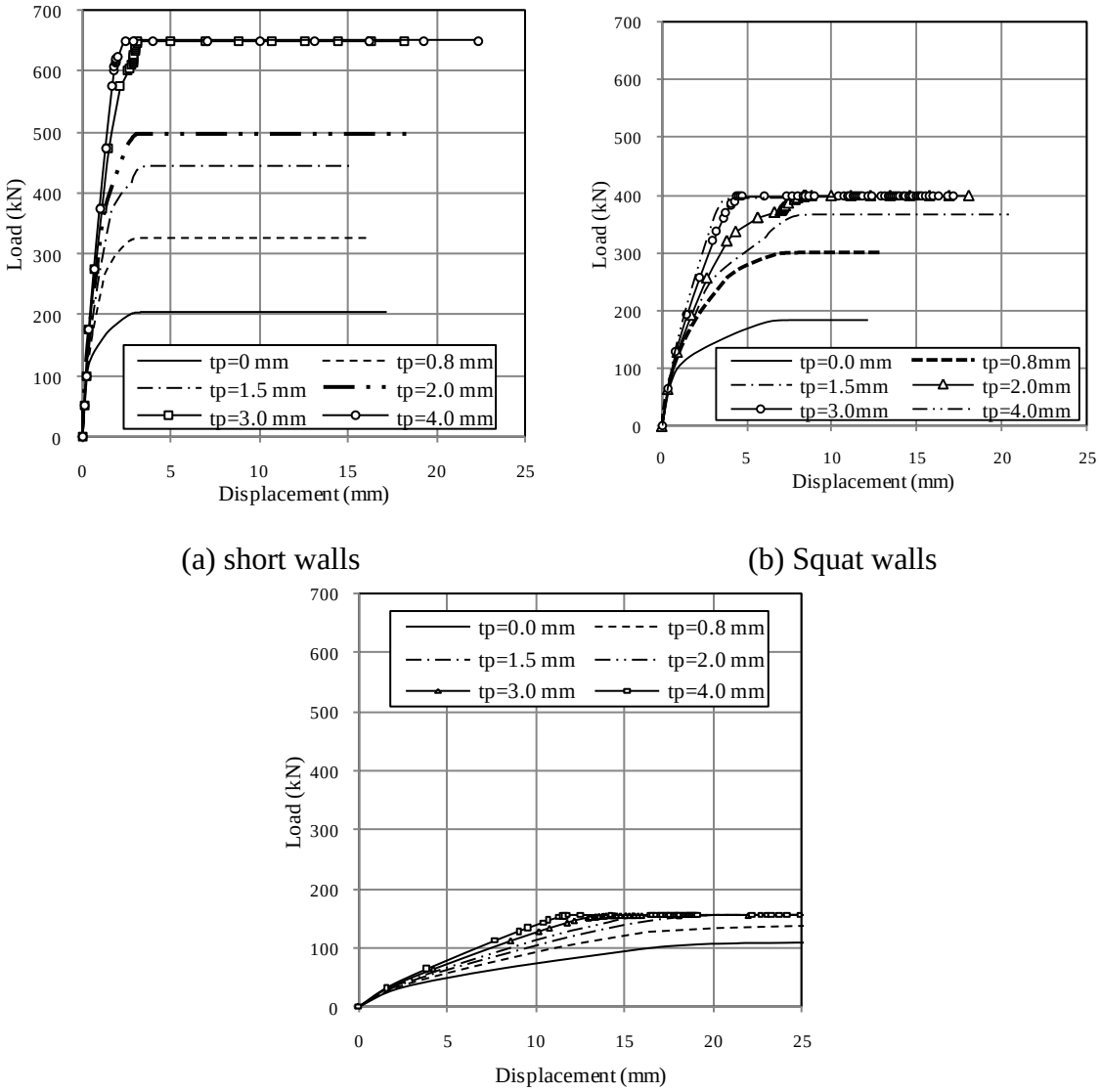

(a) short walls (b) Squat walls

(c) Cantilever walls

Figure 6.37 Load-displacement behaviour of walls with different plate thickness

Figure 6.38 also shows that the considerable increase in the load carrying capacity continued until an optimal plate thickness was used; which was 3, 2 and 1.5 mm for short, squat and cantilever walls, respectively. Further increases in plate thickness, above the optimal value, resulted in only a nominal increase in the ultimate strength, which could be attributed to the moment capacity of the wall cross-section reaching the maximum value.

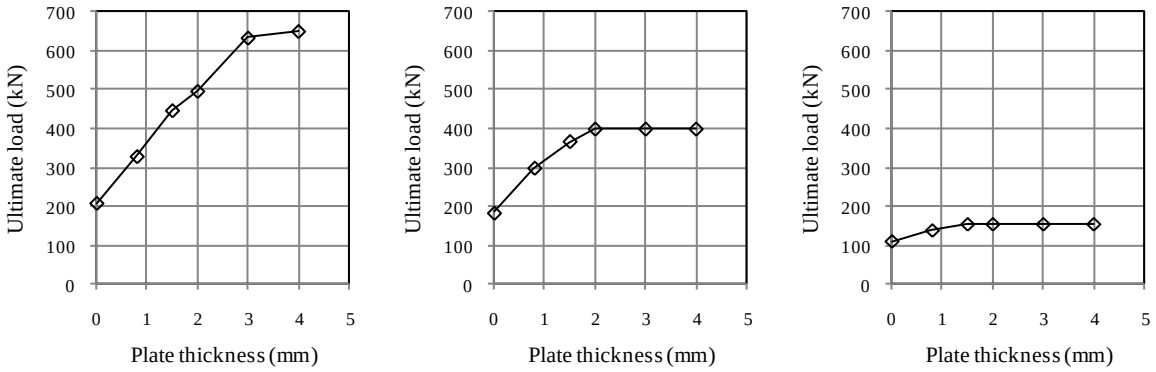

(a) Short walls (b) Squat walls (c) Cantilever walls

Figure 6.38 Variation of predicted values of ultimate load with plate thickness

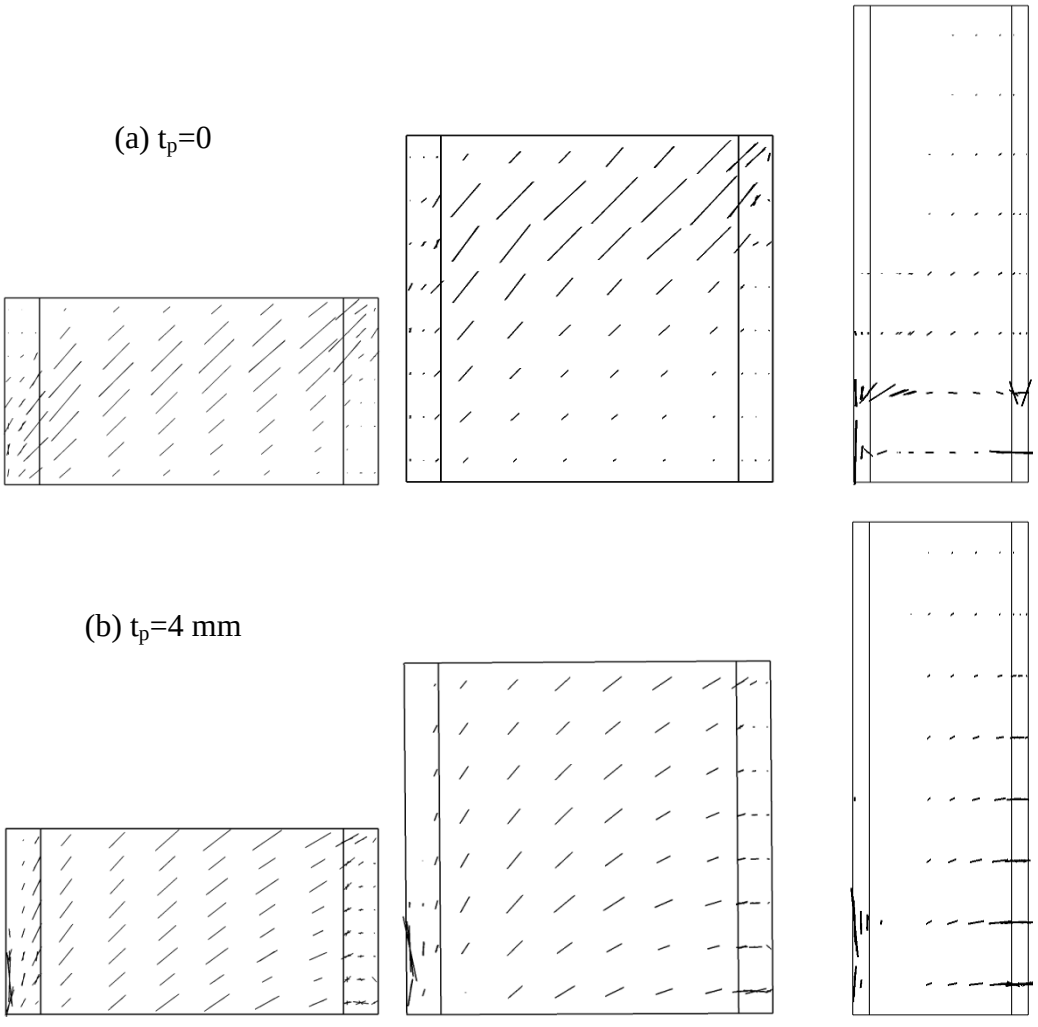

Short walls Squat walls Cantilever walls

Figure 6.39 Crack pattern at failure for (a) a conventionally-reinforced walls and (b) walls reinforced with thick plates

The crack patterns at failure for walls conventionally-reinforced and reinforced with thick plates (t_p=4.00 mm) are further depicted in Figure 6.39. It can be observed that using thick plates has no effect on either the cracking pattern or the failure mode, which is consistent with the experimental observations.

C. Axial load ratio

Three levels of axial load were selected in the study to investigate their effect on the behaviour of encased-plate composite walls. These values corresponded to 0.0, 0.1 and 0.2 of the uniaxial compressive strength of the wall's cross-section, which was equal to 0.85 × the cube compressive strength × the gross cross-sectional area of the wall. The three load levels represented the amount of axial loads resulting from the structure's self weight and the imposed loads at the wall's base of a single storey, a medium-rise and a high-rise building, respectively (Lefas 1988).

The considered walls were constructed from concrete with characteristic cube compressive strength value of 40 N/mm^2 and were provided with the same plate thickness (0.8 mm) and the same ratios of reinforcement in the boundary elements (4%) and the central panel (0.31 and 0.38% in the longitudinal and transverse directions, respectively).

The axial load was first applied to the boundary elements of the walls, and then the lateral load was applied incrementally to the stiff beams. A comparison of load-displacement behaviour of walls with different axial load ratios is displayed in Figure 6.40, while Figures 6.41 and 6.42 plot the variations of predicted initial stiffness and ultimate load values against the axial load ratio, respectively. Table 6.7 summarises the values of initial stiffness and ultimate load values for walls with different axial load ratios. The results suggest that axial loads have a considerable effect on the ductility of all wall types, i.e. walls with higher axial load ratios showed stiffer behaviour. Walls subjected to high level of axial loading (0.2) achieved 38, 103 and 38% increase in the initial stiffness when compared to

walls subjected to lateral loading only for short, squat and cantilever walls, respectively, see Figure 6.41. Similarly, load carrying capacity enhancements of 22, 29 and 27% were achieved with respect to walls subjected to lateral loading only for short, squat and cantilever walls, respectively where the axial load ratio was equal to 0.2. The enhancement could be attributed to the fact that the axial load increasing the neutral axis depth, leading to a delay in the occurrence of concrete crushing, and thus further increasing the wall capacity (Lefas 1988; Lefas *et al.* 1990). However, experimental evidence is still required to check the accuracy of these results since axial loading may initiate plate buckling early and lead to a premature failure of the encased-plate composite walls. The initiation of flexural cracks was also affected by the presence of axial loading such that walls without axial loads cracked first.

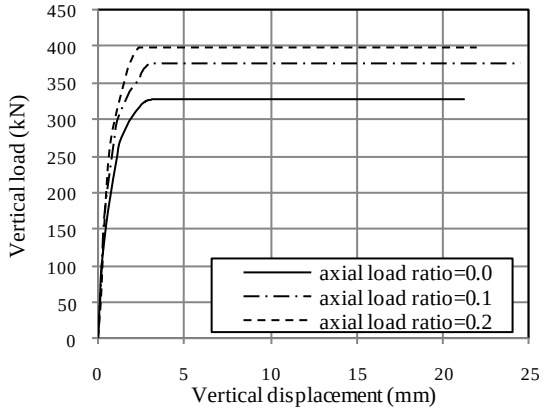

(a) short walls

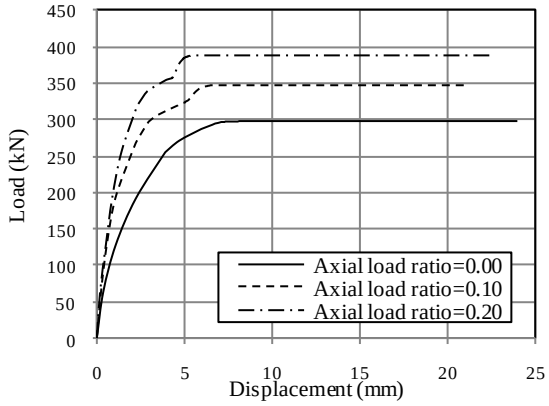

(b) Squat walls

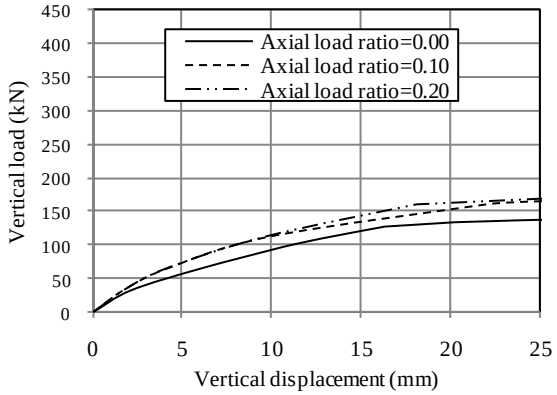

(c) Cantilever walls

Figure 6.40 Load-displacement behaviour of walls with different axial load ratios

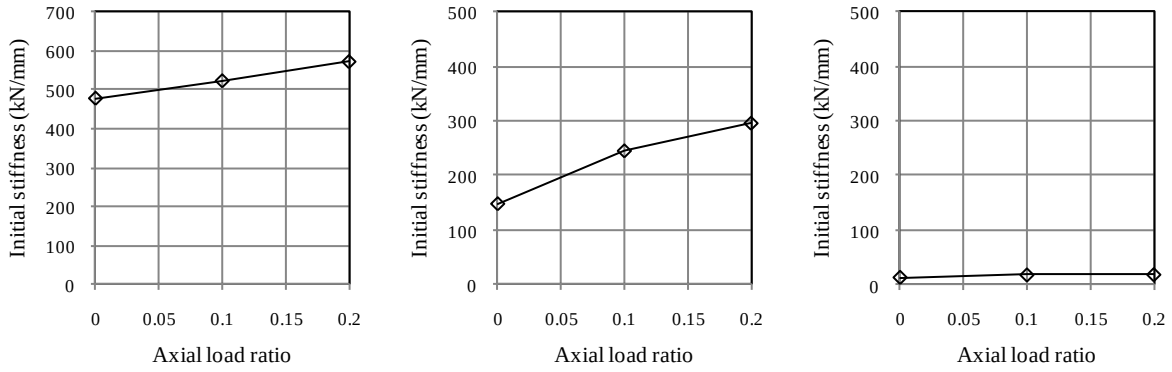

(a) Short walls (b) Squat walls (c) Cantilever walls

Figure 6.41 Variation of predicted values of initial stiffness with axial load ratios

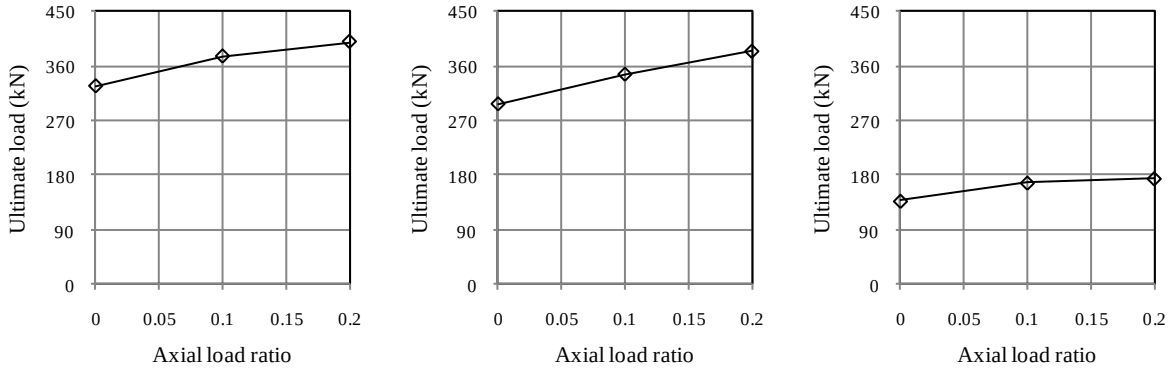

(a) Short walls (b) Squat walls (c) Cantilever walls

Figure 6.42 Variation of predicted values of ultimate load with axial load ratios

Table 6.7 Values of initial stiffness and ultimate load for walls with different axial load ratio

Wall type	Axial load ratio	Initial stiffness (kN/mm)	Initial stiffness relative to control (%)	Ultimate load (kN)	Ultimate load relative to control (%)
Short	0.0	479.00	100.00	327.00	100.00
	0.1	524.51	126.02	376.00	114.98
	0.2	574.33	137.99	400.00	122.32
Squat	0.0	146.53	100.00	298.00	100.00
	0.1	245.30	167.41	347.00	116.44
	0.2	296.80	202.55	385.00	129.19
Cantilever	0.0	12.95	100.00	138.00	100.00
	0.1	17.40	134.36	168.00	121.74
	0.2	17.90	138.22	175.10	126.88

D. Concrete strength

In order to study the effect of increasing concrete compressive strength, four hypothetical walls for each wall type were modelled and analysed. The walls were constructed from concrete with characteristic cube strength values of 25, 40, 60 and 80 N/mm^2, respectively, and were provided with the same plate thickness (0.8 mm) and the same ratios of reinforcement in the boundary elements (4%) and the central panel (0.31 and 0.38% in the longitudinal and transverse directions, respectively).

Figure 6.43 shows the load-displacement behaviour of walls with varying concrete strength. The figure suggests that concrete strength has a negligible effect on the initial and the post-cracking stiffness of the considered walls. For example, the initial stiffness of walls constructed from high strength concrete (80 N/mm^2) achieved only 0.3, 8 and 0.1% increase in the initial stiffness when compared to walls constructed from relatively low strength concrete (25 N/mm^2) for short, squat and cantilever walls, respectively.

The increase in concrete strength should have an effect on the crushing strength of the wall web and boundary elements, which can affect the failure loads of walls failed by diagonal compression (web crushing) as observed numerically in short walls, see Table 6.8 and Figure 6.45 which draws a comparison of ultimate load values for walls with different values of concrete strength.

Squat walls which are expected to fail in shear by diagonal tension, as confirmed experimentally, failed due to the formation of a diagonal tension failure plane. Thus, the increase in concrete strength could affect the initiation of the main diagonal crack, but should not have a significant effect on the ultimate load.

For cantilever walls, yielding of longitudinal reinforcement and encased-plates are responsible for initiating wall failure, and hence concrete strength should have no

significant effect on the strength of such walls, see Figure 6.43c. In all cases, however, the increase in concrete strength has a small effect in delaying the initiation of flexural cracks.

The predictability of the numerical simulations could be improved significantly if the effect of plate buckling was included in the numerical model, which was ignored since plate buckling was not observed during tests up to peak load, and hence this could be considered as one of the limitations of the proposed numerical modelling.

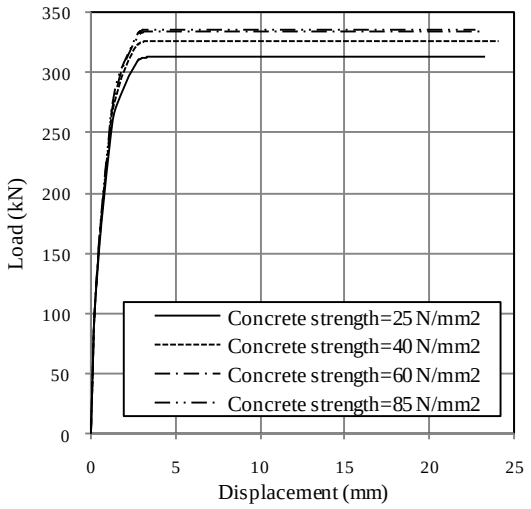

(a) short walls

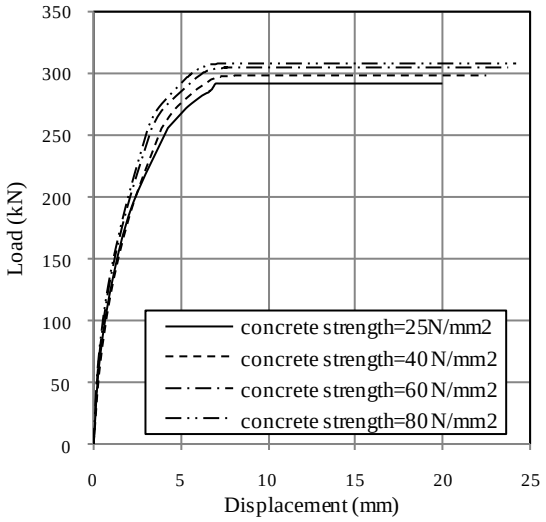

(b) Squat walls

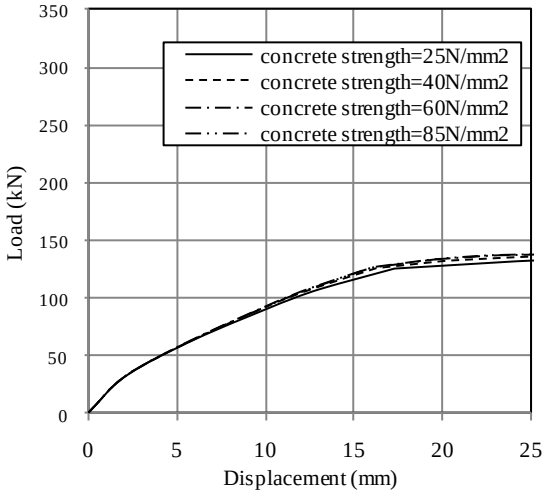

(c) Cantilever walls

Figure 6.43 Load-displacement behaviour of walls with different concrete strength

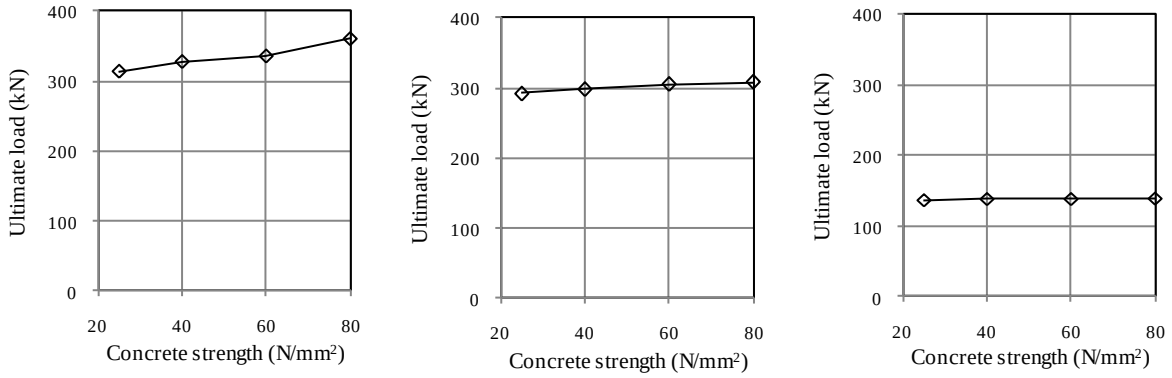

(a) Short walls (b) Squat walls (c) Cantilever walls

Figure 6.44 Variation of predicted values of ultimate load with concrete strength

Table 6.8 Values of initial stiffness and ultimate load for walls with different concrete strength

Wall type	Concrete strength (N/mm^2)	Initial stiffness (kN/mm)	Initial stiffness relative to control (%)	Ultimate load (kN)	Ultimate load relative to control (%)
Short	25	477.66	100.00	313.00	100.00
	40	479.00	100.28	327.00	104.47
	60	479.00	100.28	335.00	107.03
	80	479.00	100.28	360.00	111.02
Squat	25	163.00	100.00	292.00	100.00
	40	164.95	101.20	298.00	102.05
	60	175.00	107.36	305.00	104.45
	80	176.00	107.98	308.00	105.48
Cantilever	25	12.92	100.00	137.00	100.00
	40	12.93	100.08	138.80	101.31
	60	12.93	100.08	138.80	101.31
	80	12.93	100.08	139.52	101.84

E. Longitudinal reinforcement of central panel

The ratio of the central panel's longitudinal reinforcement was varied from 0.31 to 4%, and the load-displacement behaviour of walls with different ratios is displayed in Figure 6.45. Table 6.9 summarises the values of ultimate load for walls with different ratios of longitudinal reinforcement in central panel. In all cases, central panel longitudinal reinforcement showed no considerable effect on the initial stiffness; however, the effect in

decreasing the post-cracking ductility was clear. Further, the central panel's longitudinal reinforcement does have a significant effect on the load carrying capacity as depicted in Figure 6.46. Increasing the ratio of longitudinal reinforcement in central panel from 0.31 to 4% resulted in an increase in the ultimate load by 11, 20 and 12% for short, squat and cantilever walls, respectively. This result agrees with the behaviour of conventionally-reinforced walls found experimentally (Gupta 1996; Dabbagh 2005).

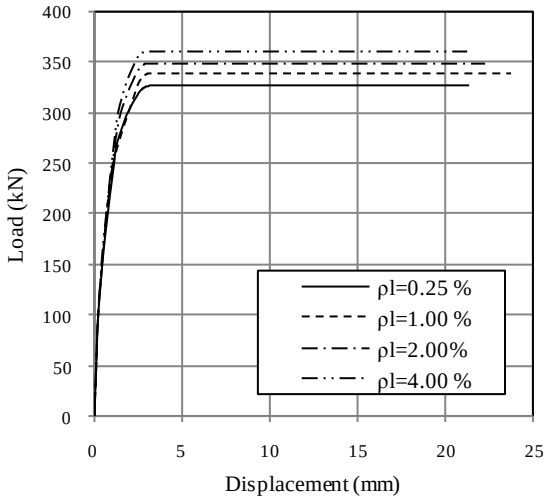

(a) short walls

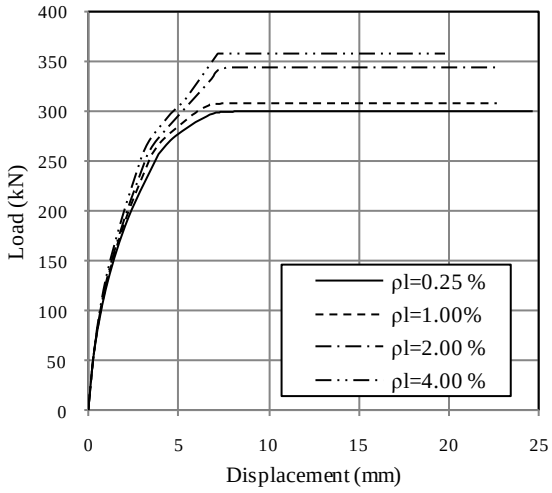

(b) Squat walls

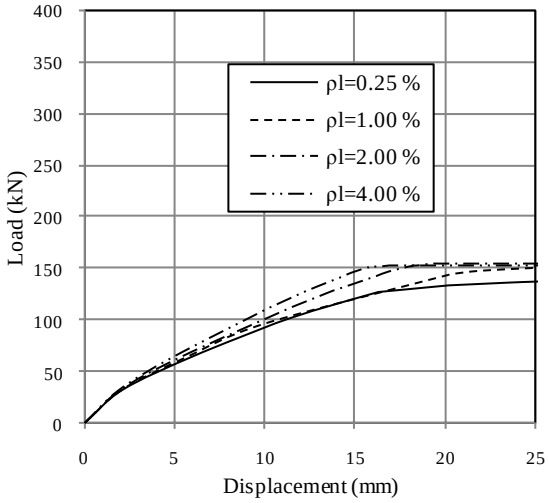

(c) Cantilever walls

Figure 6.45 Load-displacement behaviour of walls with varying ratios of central panel longitudinal reinforcement

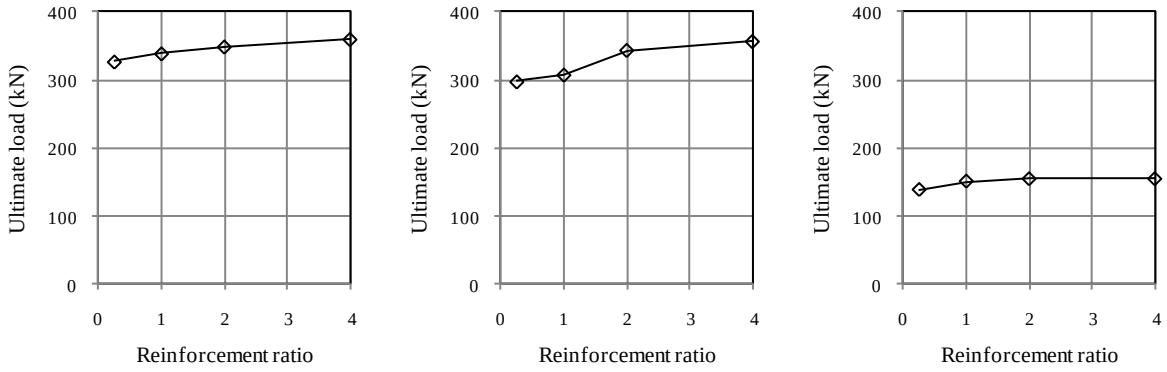

(a) Short walls (b) Squat walls (c) Cantilever walls

Figure 6.46 Variation of predicted values of ultimate load for walls with different ratios of longitudinal reinforcement in the central panel

Table 6.9 Values of ultimate load for walls with different ratios of longitudinal reinforcement in central panel

Wall type	Longitudinal reinforcement in central panel (%)	Ultimate load (kN)	Ultimate load relative to control (%)
Short	0.31	327.02	100.00
	1	339.00	103.67
	2	349.00	106.73
	4	360.00	110.09
Squat	0.31	298.19	100.00
	1	308.00	103.36
	2	344.00	115.44
	4	357.00	119.80
Cantilever	0.31	138.24	100.00
	1	150.50	109.06
	2	154.00	111.59
	4	154.00	111.59

F. Transverse reinforcement of central panel (stirrups)

The ratio of central panel's horizontal reinforcement (stirrups) was varied from 0.38 to 4%, with the high percentage representing the upper limit allowed by Eurocode 2 (2008). The load-displacement behaviour of walls with different ratios of central panel stirrups is depicted in Figure 6.47, while Figure 6.48 shows the associated variation in ultimate load

values. Table 6.10 summarises the values of the ultimate load for walls with different ratios of longitudinal reinforcement in central panel. The results suggest that central panel horizontal reinforcement (stirrups) does not have a significant effect on either the initial stiffness or the load carrying capacity of encased-plate composite walls as well documented for conventionally-reinforced walls (Lefas *et al.* 1990).

The ultimate load of walls with higher ratio of transverse reinforcement in the central panel (4%) was 4, 5 and 1% higher than those reinforced with low ratios (0.38%) for short, squat and cantilever walls, respectively, see Figure 6.48. This trend suggests that there is no rationale behind providing more than the minimum horizontal reinforcement in the design of encased-plate composite walls, while it is still needed to provide lateral support to the encased-plate and to reduce concrete shrinkage.

Table 6.10 Values of ultimate load for walls with different ratios of longitudinal reinforcement in central panel

Wall type	Transverse reinforcement in central panel (%)	Ultimate load (kN)	Ultimate load relative to control (%)
Short	0.38	327.02	100.00
	1	333.00	101.83
	2	338.00	103.36
	4	340.00	103.98
Squat	0.38	298.19	100.00
	1	305.00	102.35
	2	310.00	104.03
	4	312.00	104.70
Cantilever	0.38	138.24	100.00
	1	138.24	100.00
	2	139.00	100.72
	4	139.00	100.72

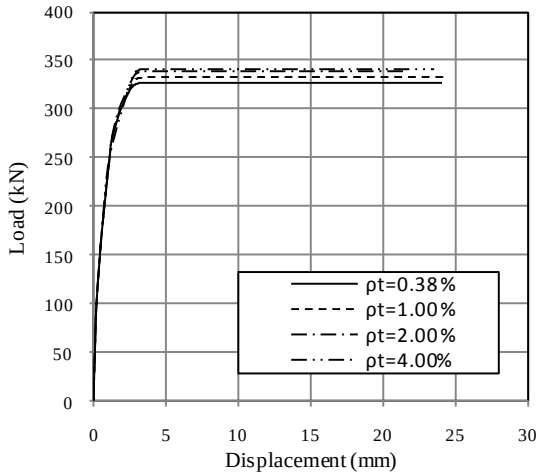

(a) short walls

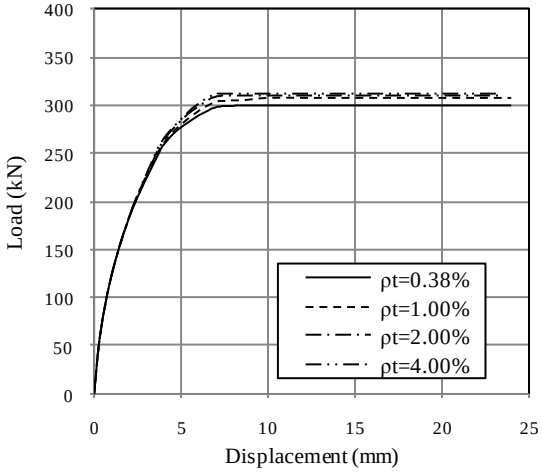

(b) Squat walls

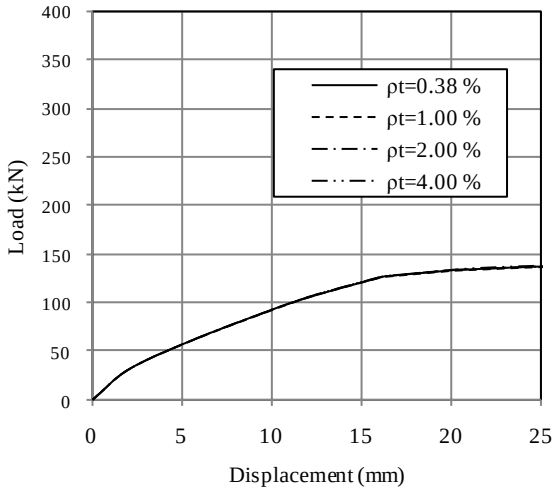

(c) Cantilever walls

Figure 6.47 Load-displacement behaviour of walls with different ratios of horizontal reinforcement in central panel

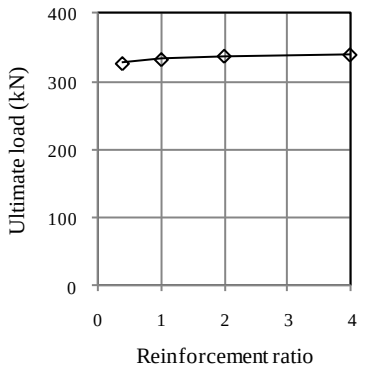

(a) Short walls

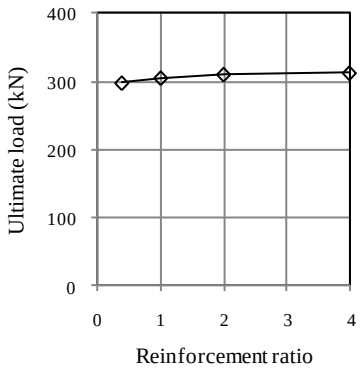

(b) Squat walls

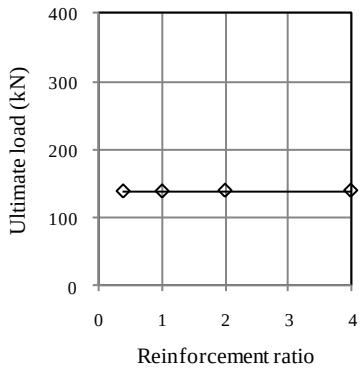

(c) Cantilever walls

Figure 6.48 Variation in predicted values of ultimate load values with different ratios of horizontal reinforcement in central panel

G. Longitudinal reinforcement of boundary elements

The ratio of longitudinal reinforcement in boundary elements was varied between 1 and 4%, and the resulting load-displacement behaviour is depicted in Figure 6.49. Table 6.11 summarises the values of initial stiffness and ultimate load values for walls with different ratios of longitudinal reinforcement in boundary elements, while Figures 6.50 and 6.51 show the variations of initial stiffness and ultimate load with the ratio of longitudinal reinforcement in the boundary element, respectively.

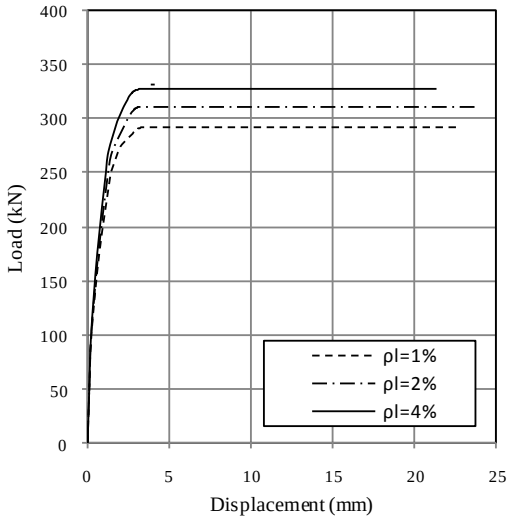

(a) short walls

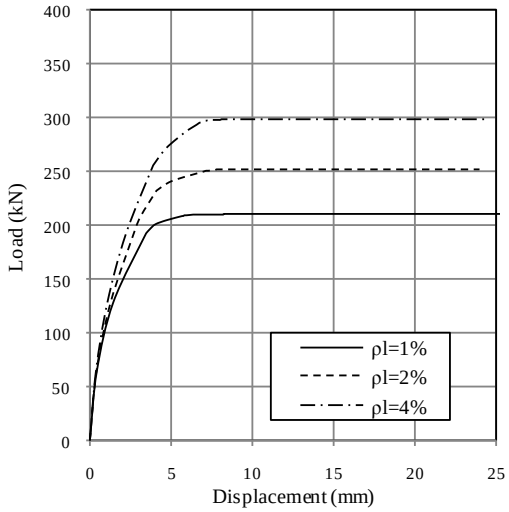

(b) Squat walls

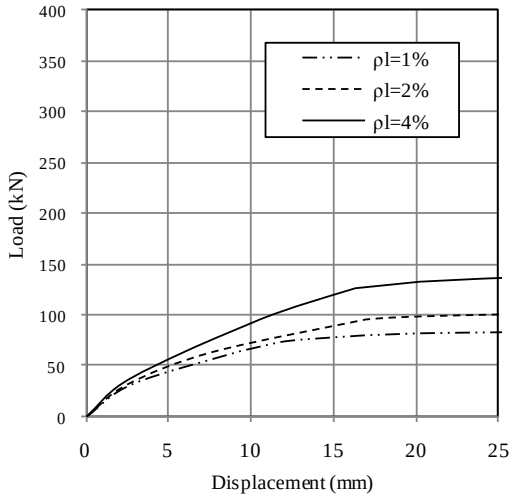

(c) Cantilever walls

Figure 6.49 Load-displacement behaviour of walls with different ratios of boundary element longitudinal reinforcement

Table 6.11 Values of initial stiffness and ultimate load for walls with different ratios of longitudinal reinforcement in boundary elements

Wall type	Longitudinal reinforcement in boundary elements (%)	Initial stiffness (kN/mm)	Initial stiffness relative to control (%)	Ultimate load (kN)	Ultimate load relative to control (%)
Short	1	449.52	100.00	292.00	100.00
	2	462.61	102.91	310.00	106.16
	4	479.00	106.56	327.02	111.99
Squat	1	119.74	100.00	210.00	100.00
	2	130.39	108.89	252.00	120.00
	4	146.50	122.35	298.19	141.90
Cantilever	1	9.08	100.00	83.20	100.00
	2	10.57	116.41	104.30	125.36
	4	12.93	142.40	138.24	166.17

The figures suggest that increasing the longitudinal reinforcement in the boundary elements has an effect on increasing the initial stiffness of the walls, especially in cantilever walls. Increasing the ratio of longitudinal reinforcement in boundary elements from 1 to 4% achieved 7, 22 and 42% increase in the initial stiffness for short, squat and cantilever walls, respectively, see Figure 6.50. Moreover, it has a clear effect on increasing the post-cracking stiffness especially in cantilever walls.

Also, the load carrying capacity increased considerably by increasing the longitudinal reinforcement ratio in boundary elements in all cases. Increasing the ratio of longitudinal reinforcement in boundary elements from 1 to 4% achieved 12, 42 and 66% increase in the ultimate load for short, squat and cantilever walls, respectively, see Figure 6.51. This result implies that boundary element reinforcement contributes to both the shear and flexural

strength values of encased-plate composite walls. Not much difference was observed in the crack pattern as the ratio of longitudinal reinforcement in boundary elements increased.

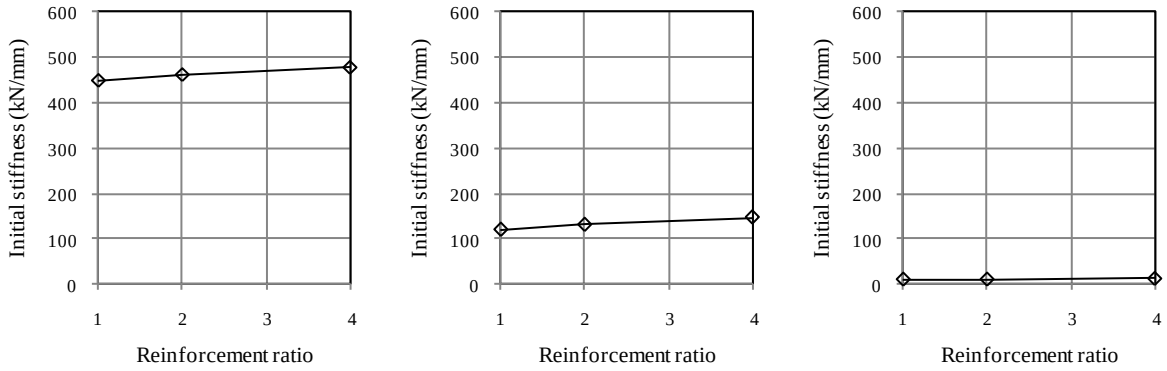

(a) Short walls (b) Squat walls (c) Cantilever walls

Figure 6.50 Variation in predicted values of initial stiffness with varying ratios of longitudinal reinforcement in boundary elements

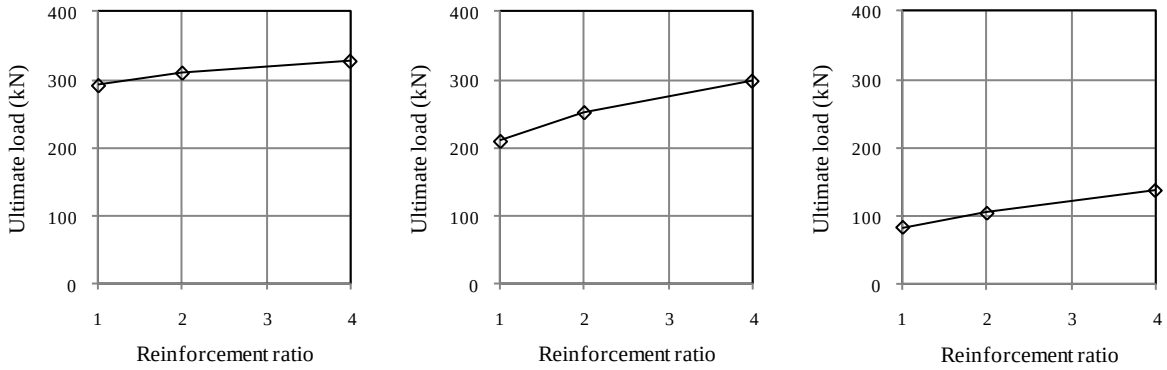

(a) Short walls (b) Squat walls (c) Cantilever walls

Figure 6.51 Variation in predicted values of ultimate load with varying ratios of longitudinal reinforcement in boundary elements

6.4.4 Conclusions

This chapter presented a numerical model that was able to simulate the behaviour of encased-plate composite walls. The accuracy of the model was validated against a wide range of concrete structures. The model was used to investigate the behaviour of encased-plate composite walls within a parametric study that covered a wide variation of parameters

that were thought to influence their performance. The main conclusions of the parametric study may be summarised as follows:

1. The initial stiffness and ultimate load of encased-plate composite walls were significantly reduced by increasing the walls' aspect ratios.
2. The initial stiffness and load carrying capacity increased for walls reinforced with thicker plates. The plate contribution to the load carrying capacity is more pronounced in short walls than in squat and cantilever walls.
3. Axial loads considerably decreased the ductility of encased-plate composite walls, but led to a considerable improvement in the load carrying capacity.
4. Central panel longitudinal reinforcement had a negligible effect on the initial stiffness of composite walls. However, the effect in decreasing the post-cracking ductility was clear. Further, the central panel's longitudinal reinforcement had a significant effect on increasing the load carrying capacity.
5. The horizontal reinforcement of central panel (stirrups) had a little effect on the initial stiffness and the load carrying capacity of encased-plate composite walls, which suggests that there is no rationale behind providing more than the minimum horizontal reinforcement in the design of such walls, while it would be required to provide lateral support to the encased-plate and to reduce concrete shrinkage.
6. Increasing the longitudinal reinforcement in the boundary elements had an effect on increasing the initial stiffness of all wall types, and it had a clear effect in increasing the load carrying capacity of encased-plate composite walls.

Chapter 7 Nonlinear analysis of conventionally-reinforced and encased-plate composite walls

7.1 Introduction

Structural walls are employed in both low-rise buildings and higher structures, where the predominant actions include both shear and flexure (Paulay and Priestley 1992, Gulec *et al.* 2008, Paulay *et al.* 1982). While the walls' flexural resistance is now well understood (Warner *et al.* 1989), the ACI 318-08 method on the shear design of walls still relies on empirical expressions derived from experimental testing of deep beams (Hwang *et al.* 2001). For this reason, better analysis methods that can accurately predict the shear strength of structural walls are needed (Farvashany *et al.* 2008, Gulec *et al.* 2009, Kassem and Elsheikh 2010).

Significant attention was devoted to estimate the shear capacity of structural walls using nonlinear analytical models. Including those based on the softened truss model developed by Mau and Hsu (1987) and modified by Gupta and Rangan (1998), and the softened strut-and-tie model proposed by Hwang *et al.* (2001). Although the latter model is reported to accurately predict the shear transmission mechanism and shear failure behaviour of structural walls (Yu and Hwang 2005), the model cannot predict wall deformation. This feature has been addressed in the softened truss model, which provides a more complete evaluation of structural walls strength and behaviour (Mansour *et al.* 2004).

The first truss model concept was developed by Ritter in 1899 (Ritter 1899 as cited in Hsu 1993), in which reinforced concrete elements subjected to shear stresses develop diagonal cracks at an angle inclined to the steel rebars. The diagonal cracks split the concrete into a series of diagonal struts, which resist compressive stresses along their axis and tensile

stresses perpendicular to it. The rebars, assumed to resist axial tension, form with the concrete struts a truss action to resist the applied shear. The inclination of concrete struts was initially assumed at 45° to the rebars and this assumption led to 50% overestimation of short walls' shear strength (Kong 2003). Later, three major developments were proposed including the variable-angle truss model (Lampert and Thurlimann 1968), the compression field theory (Collins 1973) and the softened truss model (Vecchio and Collins 1981). The softened truss model is widely believed to provide a reasonable representation of shear strength, behaviour and failure mode of squat and short walls (Hsu and Mo 1985; Gupta and Rangan 1998; Kong 2003; Mansour *et al.* 2004). However, the strut cracking angle used in the softened truss calculations is not based on experimental or analytical evidence, and its estimation requires cycles of trial and error (Gupta and Rangan 1998), which make the analysis tedious and unsuitable for practical design.

The softened truss model further limits the value of the cracking angle between upper and lower bounds in what is termed the fixed angle solution. Earlier assessment of this technique reported a number of drawbacks including inaccurate predictions of failure mode (Yu and Hwang 2005). With the fixed angle solution, the concrete softening feature does not have an impact on the prediction of shear strength of walls with low steel reinforcement content or with height-to-width ratio below 0.5 (Yu and Hwang 2005). Addressing these shortfalls would be expected to improve the method's estimates and widen its range of application.

This chapter proposes a new strut cracking angle based on regression analysis of the reported shear capacity values of 100 structural walls subjected to both monotonic and cyclic loading. The analysis pays particular attention to parameters expected to influence

the walls' shear capacity including the geometric properties, reinforcement ratios, internal stresses and concrete strength.

Having validated the proposed analysis method, a mathematical model is developed to predict not only the ultimate shear strength, but also the deformation behaviour of encased-plate structural walls throughout their post-cracking loading history.

7.2 Softened truss model

The softened truss model is based on the compression field theory proposed by Collins (1973), according to which the web of the structural wall may be visualised as an assembly of smaller reinforced concrete elements. Typical walls consist of two boundary elements simulating columns or cross walls and a central panel. The isolated web element, A, shown in Figure 7.1, is under lateral shear force, *V*, and has reinforcement in the longitudinal, *L*, and transverse, *t*, directions with an assumed smeared crack type. The longitudinal and transverse directions coincide with the wall's vertical and horizontal directions, respectively.

The element stresses are analysed by the principle of stress transformation. The three effective stress components including normal stresses, σ_L, σ_t, and shear stress, τ_{Lt}, are shown in their positive directions in Figure 7.1b. After cracking, the concrete is split into a series of diagonal struts making an angle α to the longitudinal direction. The diagonal struts and the longitudinal and transverse rebars form a truss that is expected to resist the applied shear and normal loads. Under loading, the strut develops compressive stress, σ_d, along its axis and tensile stress, σ_r, perpendicular to it (Figure 7.1c). Since the concrete strut is assumed to be free of shear (Gupta and Rangan 1998) , σ_d and σ_r are considered the concrete principal stresses. The principal stresses σ_d and σ_r can then be replaced by

components in the longitudinal and transverse directions to coincide with the stresses in the rebars. Analysis of element A can proceed by considering the equilibrium, strain compatibility and stress-strain relationships of concrete and steel.

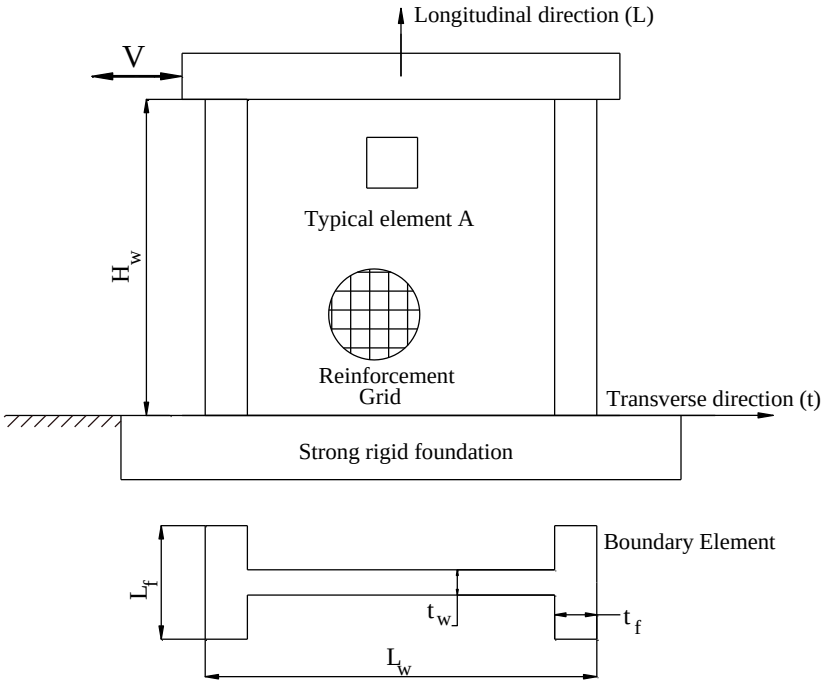

(a) Front elevation and cross-sectional views

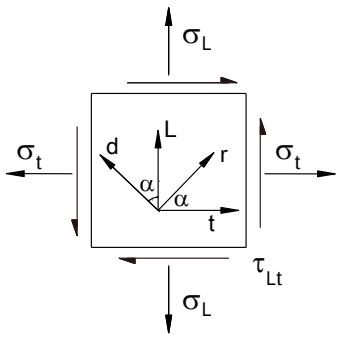

(b) Applied stresses on element A

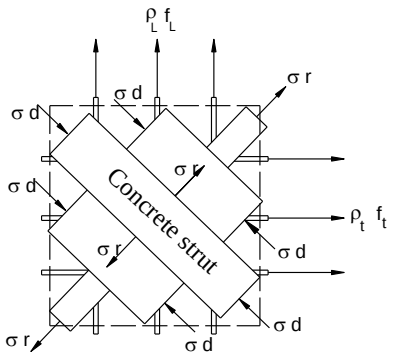

(c) Concrete struts within element A

Figure 7.1 Schematic views of a typical structural wall with an isolated wall element

7.2.1 Equilibrium and compatibility

Equilibrium of wall element A (Figure 7.1c) in *L* and *t* directions results in the following equations. It is assumed that the rebars can only resist axial stresses and therefore any dowel action is ignored (Hsu 1993).

$$\sigma_L = \sigma_d \cos^2\alpha + \sigma_r \sin^2\alpha + \rho_L f_L \tag{7.1}$$

$$\sigma_t = \sigma_d \sin^2\alpha + \sigma_r \cos^2\alpha + \rho_t f_t \tag{7.2}$$

$$\tau_{Lt} = (-\sigma_d + \sigma_r) \cos\alpha \sin\alpha \tag{7.3}$$

In Equations 7.1 to 7.3, f_L, f_t are the average stresses in rebars in *L* and *t* directions, respectively, and ρ_L, ρ_t are the corresponding average reinforcement ratios. By assuming a uniform state of stress in the wall's web, the relationship between the shear force, *V*, and the average shear stress in the horizontal plane, τ_{Lt}, can be expressed as follows (Gupta and Rangan 1998) :

$$V = \tau_{Lt} t_w d_w \tag{7.4}$$

where t_w is the web thickness, d_w is the horizontal length of the wall between the centres of boundary elements. In the absence of boundary elements, d_w is assumed to be equal to 0.8 L_w (Gupta and Rangan 1998), where L_w is the length of the wall (refer to Figure 7.1a).

Similar to stresses, the transformation of strains into the *L* and *t* directions results in the following compatibility equations (Hsu 1993):

$$\varepsilon_L = \varepsilon_d \cos^2\alpha + \varepsilon_r \sin^2\alpha \tag{7.5}$$

$$\varepsilon_t = \varepsilon_d \sin^2\alpha + \varepsilon_r \cos^2\alpha \tag{7.6}$$

$$\gamma_{Lt} = 2(\varepsilon_r - \varepsilon_d) \cos\alpha \sin\alpha \tag{7.7}$$

where ε_L, ε_t, ε_d and ε_r are the average normal strains in *L*, *t*, *d* and *r* directions, respectively, γ_{Lt} is the average shear strain in the *L*-*t* coordinate system. By assuming that the boundary elements resist the flexural stresses and the effect of the flexural stresses on the web shear behaviour is ignored, the deflection of the wall top, Δ, can be calculated from the shear strain using the following relationship (Gupta and Rangan 1998):

$$\Delta = \gamma_{Lt} H_w \tag{7.8}$$

where H_w is the wall height (refer to Figure 7.1a)

7.2.2 Constitutive models for concrete

Due to the presence of lateral tensile strain in the inclined concrete struts, the compression behaviour is assumed to follow the stress-strain relationships for softened concrete as given by Zhang and Hsu (1998) and expressed as:

$$\sigma_d = -\zeta f_c' \left[2\left(\frac{-\varepsilon_d}{\zeta\varepsilon_0}\right) - \left(\frac{-\varepsilon_d}{\zeta\varepsilon_0}\right)^2 \right] \qquad \text{for } -\varepsilon_d \le \zeta\varepsilon_0 \tag{7.9-a}$$

$$\sigma_d = -\zeta f_c' \left[1 - \left(\frac{-\varepsilon_d/\zeta\varepsilon_0 - 1}{2/\zeta - 1}\right)^2 \right] \qquad \text{for } -\varepsilon_d > \zeta\varepsilon_0 \tag{7.9-b}$$

where f'_c is the compressive cylinder strength of concrete in N/mm^2, ε_0 the strain at peak stress of a standard concrete cylinder, taken as $\varepsilon_0 = 0.002$ (Hsu 1993), ε_d the average normal strain in *d* direction and ζ the softening coefficient defined as (Yu and Hwang 2005):

$$\zeta = \frac{5.8}{\sqrt{f_c'}\sqrt{1+400\ \varepsilon_r}} \le \frac{0.9}{\sqrt{1+400\,\varepsilon_r}} \tag{7.9-c}$$

Under tension, the relationship between the principal stress, σ_r, and the principal strain, ε_r, is (Gupta and Rangan 1998):

$$\sigma_r = E_c \varepsilon_r \qquad \text{for } 0 \le \varepsilon_r \le \varepsilon_{ct} \qquad (7.10\text{-a})$$

$$\sigma_r = f'_{ct} \frac{(\varepsilon_{ut} - \varepsilon_r)}{(\varepsilon_{ut} - \varepsilon_{ct})} \qquad \text{for } \varepsilon_{ct} \le \varepsilon_r \le \varepsilon_{ut} \qquad (7.10\text{-b})$$

$$\sigma_r = 0 \qquad \text{for } \varepsilon_r > \varepsilon_{ut} \qquad (7.10\text{-c})$$

where f'_{ct} is the tensile strength of concrete in N/mm^2, taken equal to $0.4\sqrt{f'_c}$, $\varepsilon_{ct} = f'_{ct}/E_c$, E_c is modulus of elasticity of concrete and ε_{ut} the ultimate tensile strain, taken as 0.002, beyond which the tensile stress becomes zero (Gupta and Rangan 1998).

7.2.3 Constitutive models for steel rebars

The stress-strain behaviour of reinforcing steel is assumed to be elastic-perfectly-plastic. Therefore,

$$f_s = E_s \varepsilon_s \qquad \text{for } 0 < \varepsilon_s < \varepsilon_y \qquad (7.11\text{-a})$$

$$f_s = f_y \qquad \text{for } \varepsilon_s \ge \varepsilon_y \qquad (7.11\text{-b})$$

where f_s and ε_s are the average stress and strain of steel rebars, respectively. They become f_L, ε_L and f_t, ε_t when applied to longitudinal and transverse steel, respectively. f_y and ε_y are the yield stress and strain of steel rebars and E_s is the modulus of elasticity of steel rebars.

7.2.4 Solution algorithm

The analysis of the softened truss model to predict the shear strength of walls involves 16 unknowns: V, σ_L, σ_t, τ_{Lt}, σ_d, σ_r, f_L, f_t, α, ζ,Δ, ε_r, ε_d, ε_L, ε_t, and γ_{Lt}. Thirteen equations have already been described including eight equilibrium and compatibility equations, and five related to the constitutive laws of materials. The indeterminacy degree can be reduced by

specifying strain, ε_d, for each load stage, and calculating the longitudinal stress, σ_L, from the applied vertical load, N, and the wall cross-sectional area, A:

$$\sigma_L = N/A \tag{7.12}$$

In order to provide the remaining required condition to make the analysis possible, Gupta and Rangan (1998) proposed that if the wall was infinitely restrained from movement in the transverse direction, strain ε_t would be 0, giving the upper bound solution for the cracking angle, α. On the other hand if the wall was assumed to be free to move in the transverse direction, stress σ_t would be 0, giving the lower bound solution. Gupta and Rangan (1998) proposed that the value of the cracking angle be limited between the upper and lower bound solutions, and calculated according to the following expression which gave the fixed angle solution:

$$\alpha = tan^{-1}(d_w/H_w) \tag{7.13}$$

where H_w is the wall height. The fixed angle solution ignores the effects of applied loads, concrete strength and reinforcement ratios. Earlier assessment of the solution concluded that it led to inaccurate predictions of failure mode (Yu and Hwang 2005). This solution hence represents a weak point in an otherwise sound analysis method for structural walls, and it anticipated that if a more realistic value of the strut cracking angle, α, could be developed, the overall accuracy of the softened truss model would be improved. The following represents an attempt to address this problem.

7.3 Regression analysis of experimental data

The results of tests involving 100 structural wall specimens were reviewed and categorised (69 walls with flanges and 31 rectangular walls). The failure load results of the selected

structural wall specimens were gathered from Hirosawa (1975), Barda *et al.* (1977), Cardenas *et al.* (1980), Oesterle *et al.* (1984), Maier and Thurliamann (1985), Lefas *et al.* (1990), Kabeasawa and Hiraishi (1993), Mo (1993), Gupta (1996) and Dabbagh (2005). All the specimens were one-storey isolated concrete walls, symmetrically reinforced with horizontal and vertical steel rebars without any diagonal reinforcement. The selected walls in the study cover both walls subjected to both axial and lateral loads (68 walls) and walls subjected to only lateral loading (32 walls). The walls were tested using either monotonically increasing load in one direction (54 walls) or cyclically loaded in the plane of the wall (46 walls).

The extracted data was used in a regression analysis to determine a suitable value of the cracking angle, α. The study was based on the expected statistical association between the cracking angle and a number of parameters thought likely to influence its value, including geometric dimensions, reinforcement ratios, concrete strength and applied axial stresses.

For each wall specimen, the value of the cracking angle that provided a match between the analytical and experimental shear strengths was recorded. In order to arrive at generic values of the cracking angle suitable for future structural wall design, the statistical association between the cracking angle values and several parameters related to concrete strength, f'_c, longitudinal stresses, N/A, geometric dimensions, A, d_w, H_w, L_w and reinforcement ratios, ρ_L, ρ_t, was assessed. The cracking angle values were further assessed against the crack propagation maps, in cases where the maps were available, to ensure compatibility with the experimental results. Some of the results are shown in Table 7.1 and Figures 7.2 and 7.3.

Table 7.1 Coefficients of determination (r^2) of the association between the cracking angle and parameters related to concrete strength, longitudinal stresses, geometric dimensions and reinforcement ratios

Parameter	Coefficients of determination,r^2, for walls under lateral and axial loading	Coefficients of determination, r^2 ,for walls under lateral loading only
f_c'	0.09	0.61
$\sqrt{f_c'}$	0.12	0.61
N/A	0.46	--- [a]
$N/(f_c' * A)$	0.01	--- [a]
$N/(\sqrt{f_c'} * A)$	0.56	--- [a]
d_w/H_w [b]	0.75	0.16
L_w/H_w	0.72	0.19
$\rho_L f_{yL}/\rho_t f_{yt}$	0.32	0.39
$\sqrt{f_c' + \rho_t f_{yt}}$	0.73	0.65
$1+(\rho_t f_{yt}/f_c')$	0.03	0.01
$\left(\frac{H_w}{d_w}\right)\left(N/A\sqrt{f_c'}\right)^{0.1}$	0.87 [c]	--- [a]
$\sqrt{f_c'} + (\rho_L / f_{yL}/(\rho_t / f_{yt})^{0.1})$	0.10	0.91 [d]

Note:

[a] values are not applicable

[b] fixed angle solution (Gupta and Rangan 1998)

[c] value for parameter x_1 in Figure 7.4 a

[d] value for parameter x_2 in Figure 7.4 b

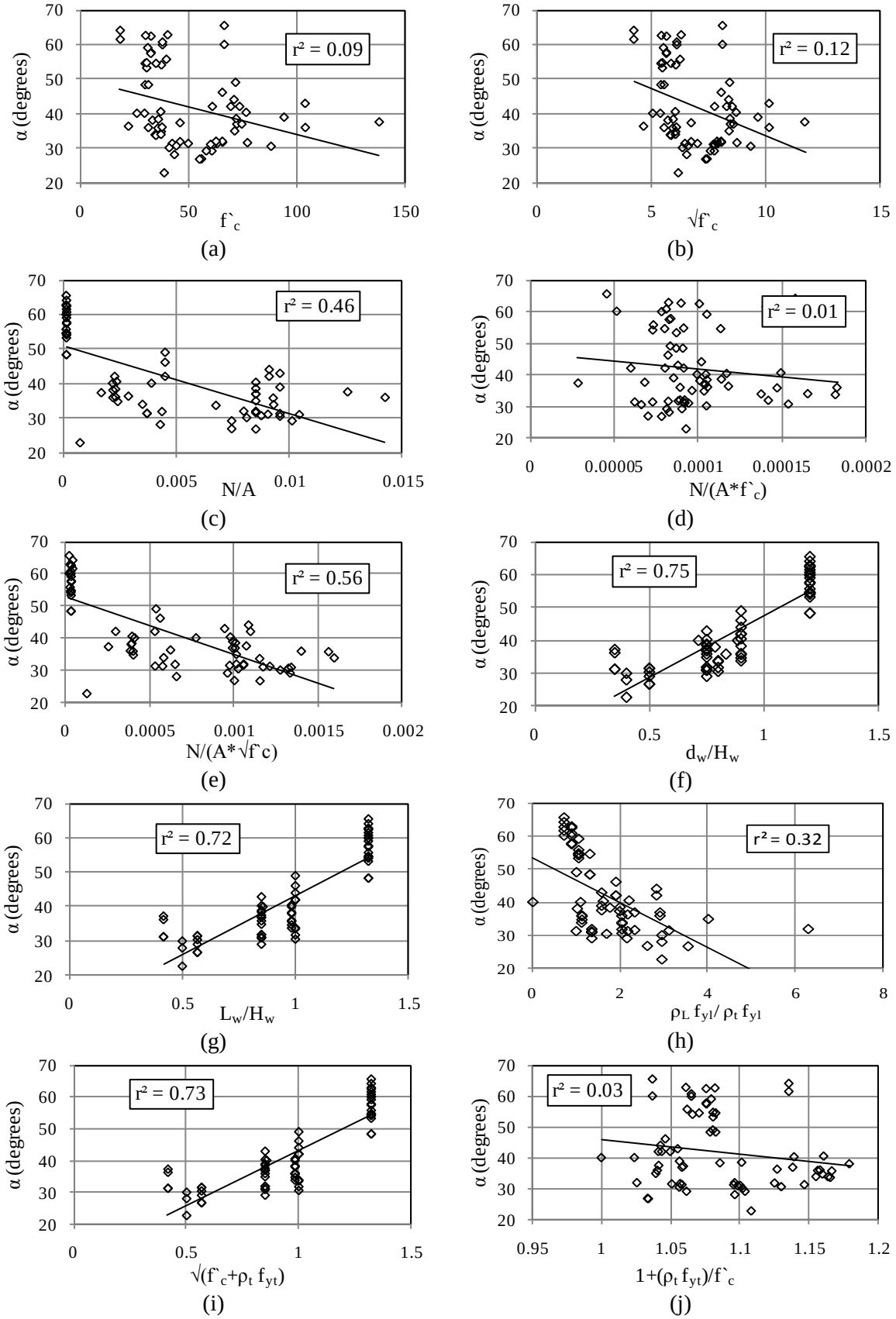

Figure 7.2 Correlation between the cracking angle and a number of studied parameters for walls subjected to lateral and axial loading

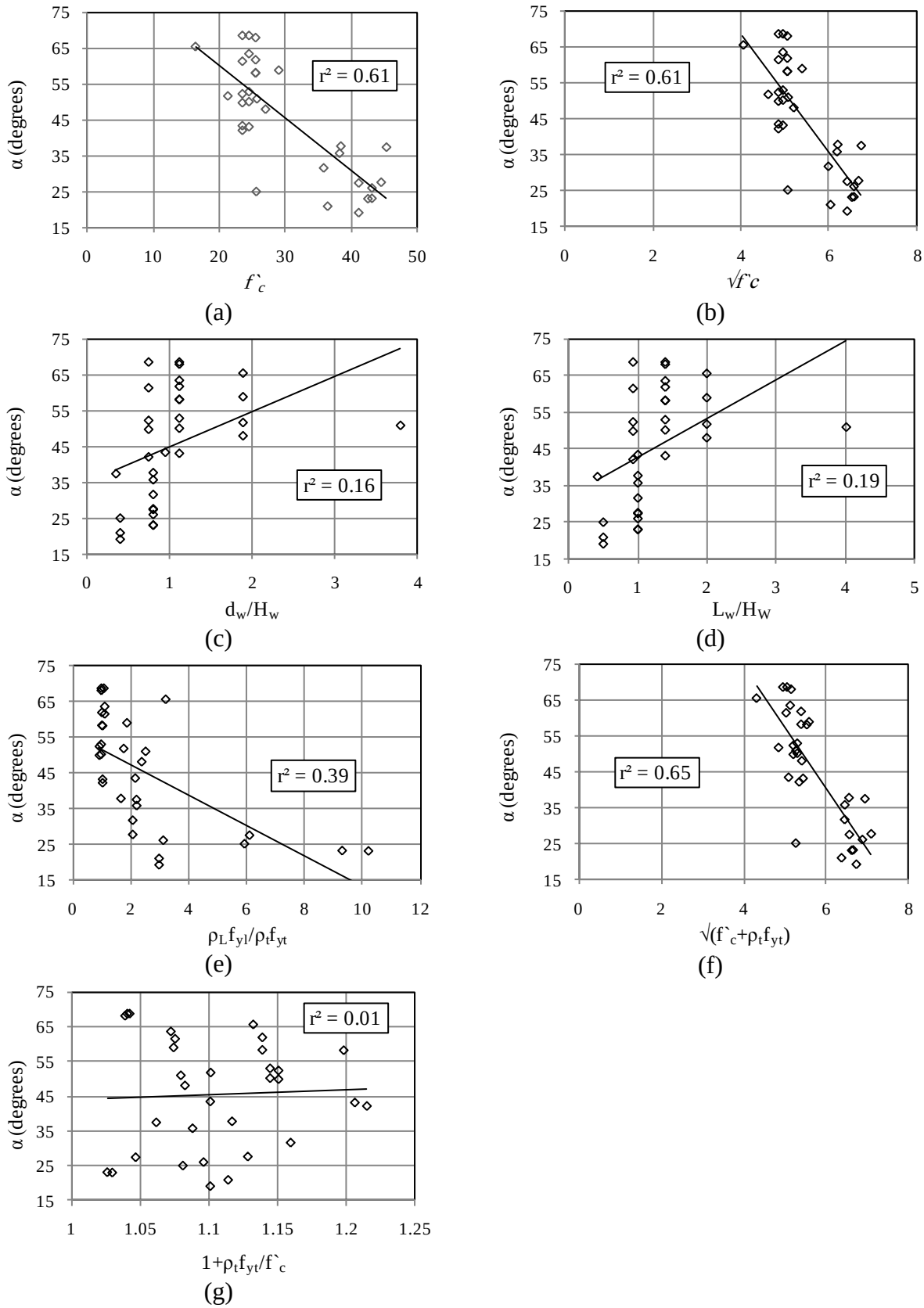

Figure 7.3 Correlation between the predicted cracking angle and a number of studied parameters for walls subjected to lateral loading only

The results show that the association between α and d_w/H_w assumed in the fixed angle solution is strong ($r^2 = 0.75$) for walls under combined lateral and axial loading but not for walls under lateral loads only, where r^2 reduces to 0.16 (see Figures 7.2f and 7.3c). For the first group of walls, a stronger association ($r^2 = 0.87$) was found when the axial stresses, *N/A*, and the concrete strength, f'_c, were also considered, see Figure 7.4a. Including the parameter *N/A* was only possible for walls under combined axial and lateral loading. On the other hand, considering the effect of the concrete strength, f'_c, and the reinforcement ratios, ρ_L, ρ_t, resulted in strong association ($r^2 = 0.91$) with the cracking angle, α, for walls subjected to lateral loads only, Figure 7.4b. These results led to the following two equations giving the values of the cracking angle, α, in degrees for the two types of structural wall considered, respectively.

For walls subjected to lateral and axial loading:

$$\alpha = 57.16x_1^2 - 117.6x_1 + 87.10 \tag{7.14}$$

$$\text{where } x_1 = \left(\frac{H_w}{d_w}\right)\left(\frac{N}{A\sqrt{f'_c}}\right)^{0.1}$$

For wall subjected to lateral loading only:

$$\alpha = -7.339x_2^2 - 65.74x_2 - 87.67 \tag{7.15}$$

$$\text{where } x_2 = \sqrt{f'_c} + \frac{\rho_l / f_{yl}}{\left(\rho_t / f_{yt}\right)^{0.1}}$$

In Equations 7.14 and 7.15, H_w and d_w are in mm, N is in kN, A is the cross-sectional area in mm^2, f'_c, f_{yL} and f_{yt} are in N/mm^2.

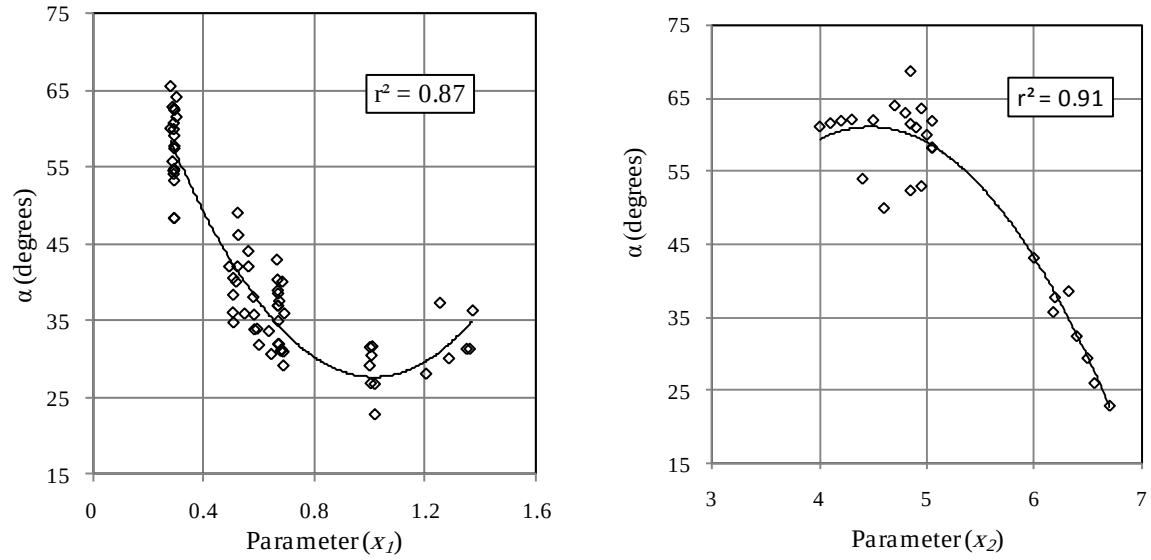

(a) Walls subjected to both lateral and axial loads (b) Walls subjected to lateral loads only

Figure 7.4 Correlation between the cracking angle, α, and two wall parameters x_1 and x_2 defined in Equations 7.14 and 7.15

7.4 Verification of proposed cracking angle

A method of analysis based on the softened truss model and incorporating the proposed cracking angle was used to predict the behaviour and failure loads of the 100 structural walls for which the experimental results are available in the literature. The analysis was used to predict the shear capacity, the load-displacement behaviour and the cracking angle of each wall.

7.4.1 Shear capacity

The shear capacity predictions of the new method were compared to the experimental failure loads for the 100 test specimens and the results are listed in Table 7.2. The details of the walls are listed in columns 1 to 10 in Table 7.2 while columns 11 to 13 present the ratio of the experimental to analytical results (V_{test} / $V_{analysis}$) according to the fixed angle solution, the proposed solution and the ACI (2008) method, respectively. The average ratio of experimental to analytical (V_{test} / $V_{analysis}$) results was 1.09 with a coefficient of variation

(CoV) of 0.03 and a standard deviation (SD) of 0.16 for the proposed analysis method, see Figure 7.5a. This exercise was repeated with the softened truss model incorporating the cracking angle values proposed by Gupta and Rangan (1998), (Equation 7.13), and the average, CoV and SD values were 1.24, 0.14, 0.38, respectively, see Figure 7.5b. Using the shear capacity predictions made by the ACI (2008), which were included for the sake of completeness, the average, CoV and SD values obtained were 1.23, 0.08, 0.28, see Figure 7.5c. The low average V_{test} / $V_{analysis}$ ratio achieved with the proposed method is promising and indicative of the effectiveness of the proposed method.

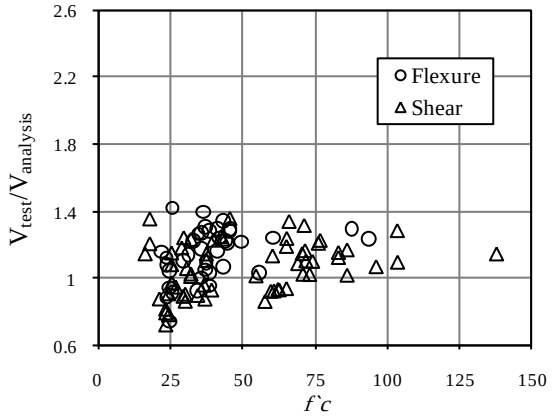

(a) The proposed method

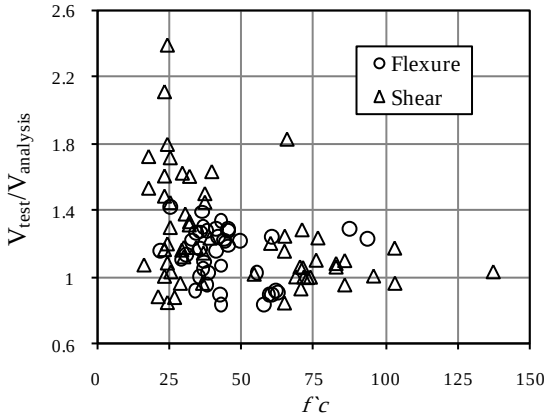

(b) The fixed angle solution

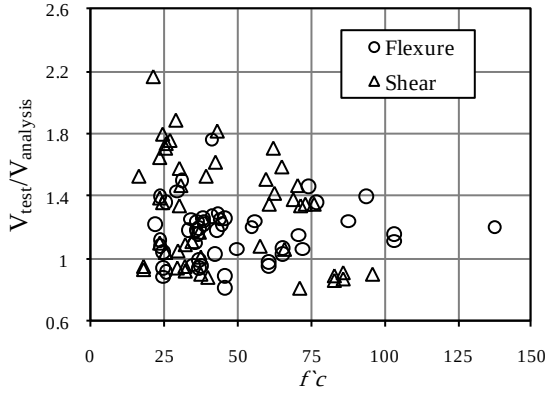

(C) The ACI (2008) method

Figure 7.5 Ratios between experimental failure loads, V_{test} ,and maximum capacity predictions, $V_{analysis}$, made by (a) the proposed method, (b) the fixed angle solution proposed by Gupta and Rangan (1998), and (c) the ACI (2008) method

Table 7.2 Comparison of theoretical and experimental shear strengths

Specimen	H_w x L_w x t (cm)	L_f x t_f (cm)	f'_c (MPa)	ρ_L %	f_{yL} (MPa)	ρ_t %	f_{yt} (MPa)	N (KN)	V_{test} (KN)	V_{test} / $V_{analysis}$		
										Fixed angle	Proposed	ACI
(1)	(2)	(3)	(4)	(5)	(6)	(7)	(8)	(9)	(10)	(11)	(12)	(13)
Tests by Oesterle *et al*. (1984)												
B5[C]	457x190.5x10.2	30.5x31	45.30	1.37	444.4	0.63	444.4	0	761.3	1.28[F]	1.28[F]	1.34
B6[C]	457x190.5x10.2	30.5x31	21.8	1.37	440.9	0.63	440.9	929	824.4	1.15[F]	1.15[F]	1.35
B7[C]	457x190.5x10.2	30.5x31	49.4	1.37	458.2	0.63	458.2	1192	979.6	1.21[F]	1.21[F]	1.42
B8[C]	457x190.5x10.2	30.5x31	42.0	1.37	447.8	1.38	447.8	1192	976.9	1.24[F]	1.24[F]	1.22[F]
F2[C]	457x190.5x10.2	91x10.2	45.6	1.25	430.6	0.63	430.6	1186	886.7	1.19[L]	1.36[F]	1.35
Tests by Maier and Thurliamann (1985)												
S1	120x118x10	40x10	36.9	1.16	574.0	1.03	574.0	433.0	680.0	1.05[F]	1.05[F]	1.06[F]
S2	120x118x10	40x10	35.4	1.16	574.0	1.03	574.0	1653.0	928.0	1.00[F]	1.00[F]	1.03[F]
S3	120x118x10	40x10	36.7	2.46	530.0	1.03	574.0	424.0	977.0	0.96[X]	0.96	1.08
s4	120x118x10	10x23.6	32.9	1.05	574.0	1.03	574.0	262.0	392.0	1.22[F]	1.22[F]	1.19[F]
S5[C]	120x118x10	40x10	37.3	1.16	574.0	1.03	574.0	416.0	701.0	1.09[F]	1.09[F]	1.10[F]
S6	120x118x10	40x10	35.6	1.13	479.0	0.57	537.0	416.0	667.0	1.17[F]	1.17[F]	1.18[F]
S7[C]	120x118x10	40x10	34.1	1.13	555.0	1.01	555.0	1657.0	836.0	0.92[F]	0.92[F]	0.95[F]
S9[C]	120x118x10	10x11.8	29.2	0.98	560	0	0	260	342	1.10[F]	1.10[F]	1.71
S10	120x118x10	10x17.9	31.0	2.00	496.0	0.98	496.0	262.0	670.0	1.14[F]	1.14[F]	1.18[F]
Tests by kabeyasawa and Hiraishi.(1993)												
NW-1	300x170x8	20x20	93.6	0.84	1187	0.53	1001	1764	1468.0	1.29[F]	1.29[F]	1.25[F]
NW-2	200x170x8	20x20	55.5	0.65	848	0.25	1001	1764	714.0	1.23[F]	1.23[F]	1.43
NW-3	300x170x8	20x20	54.6	0.88	593	0.25	753	1372	784.0	1.03[F]	1.03[F]	1.50
NW-4	300x170x8	20x20	60.3	1.07	593	0.49	753	1568	900.0	1.01[X]	1.01	1.24
NW-5	300x170x8	20x20	65.2	1.15	1187	0.49	753	1372	1056.0	1.20[X]	1.13	1.40
NW-6	300x170x8	20x20	103.3	0.84	1187	0.53	753	1568	1670.0	1.24[X]	1.24	1.40[F]
W08	200x170x8	20x20	137.5	0.84	848	0.53	1079	1764	1719.0	1.17[X]	1.29	1.24[F]
W12	200x170x8	20x20	70.8	1.42	848	0.35	1079	2313	1254.0	1.03[X]	1.14	1.51
N1	200x170x8	20x20	65.1	1.34	339	0.21	792	1568	1100	0.84[X]	0.93	1.59
N2	200x170x8	20x20	71.8	1.54	565	0.53	792	1568	1378.0	0.93[X]	1.02	1.38
N3	200x170x8	20x20	103.4	1.54	848	0.53	792	1568	1696.0	1.00[X]	1.10	1.35
N4	200x170x8	20x20	76.7	1.54	848	0.49	792	2617	1158.0	0.96[X]	1.09	1.47
N5	300x170x8	20x20	74.1	1.69	1187	0.72	792	1568	1411.0	1.23[X]	1.23	0.81
N6	200x170x8	20x20	71.5	1.84	1158	0.92	792	1568	1498.0	1.00[X]	1.10	1.09
N7	200x170x8	20x20	76.1	2.17	1469	1.34	792	1568	1639.0	1.05[X]	1.16	0.92
N8	200x170x8	20x20	62.6	1.00	2147	0.74	810	1568	1049.0	1.10[X]	1.21	0.95
W35X[C]	200x170x8	20x20	60.8	1.00	1187	0.74	810	1764	1054.0	0.90[F]	0.93	0.95[F]
W35H[C]	200x170x8	20x20	57.7	1.00	1187	0.74	810	1921	958.0	0.90[F]	0.92	0.89[F]
W30H[C]	200x170x8	20x20	62.2	1.00	1187	0.74	810	1862	1020.0	0.83[F]	0.86	0.96[F]
P35H[C]	200x170x8	20x20	59.7	1.00	1187	0.74	810	1470	1011.0	0.92[F]	0.93	0.94[F]
MW35H[C]	200x170x8	20x20	93.6	0.84	1187	0.53	810	1666	1468.0	0.89[F]	0.92	1.25[F]
Tests by Lefas *et al*. (1990)												
SW11	75x75x7	-----	44.5	2.49	470.0	1.10	520.0	0.0	260.00	1.21[F]	1.21[F]	1.18[F]
SW12	75x75x7	-----	45.6	2.49	470.0	1.10	520.0	230.0	340.00	1.29[F]	1.29[F]	1.24[F]
SW13	75x75x7	-----	34.5	2.49	470.0	1.10	520.0	355.0	330.00	1.26[F]	1.26[F]	1.22[F]
SW14	75x75x7	-----	35.8	2.49	470.0	1.10	520.0	0.00	265.00	1.27[F]	1.27[F]	1.24[F]
SW15	75x75x7	-----	36.8	2.49	470.0	1.10	520.0	185.0	320.00	1.30[F]	1.30[F]	1.27[F]
SW16	75x75x7	-----	43.9	2.49	470.0	1.10	520.0	460.0	355.00	1.22[F]	1.22[F]	1.16[F]
SW17	75x75x7	-----	41.1	2.49	470.0	0.37	520.0	0.00	247.00	1.16[F]	1.16[F]	1.76
SW21	130x65x6.5	-----	36.4	2.62	470.0	0.80	520.0	0.00	127.00	1.39[F]	1.39[F]	1.36[F]
SW22	130x65x6.5	-----	43.0	2.62	470.0	0.80	520.0	182.0	150.00	1.34[F]	1.34[F]	1.29[F]
SW24	130x65x6.5	-----	41.1	2.62	470.0	0.80	520.0	0.00	120.00	1.29[F]	1.29[F]	1.26[F]
SW25	130x65x6.5	-----	38.3	2.62	470.0	0.80	520.0	32.5	150.00	1.28[F]	1.28[F]	1.22[F]
SW26	130x65x6.5	-----	25.6	2.62	470.0	0.40	520.0	0.00	123.00	1.42[F]	1.42[F]	1.4[F]
Tests by Yoshizaki (1973) as reported by Hirosawa (1975)												
165-1-56-2[C]	86x80x6	-----	23.50	0.22	433	0.23	433	0.00	102.00	2.92[L]	1.12[F]	1.12[F]
166-1-56-8[C]	86x80x6	-----	23.50	0.73	433	0.82	433	0.00	147.00	1.48[L]	1.08[F]	1.08[F]
167-1-88-4[C]	86x80x6	-----	23.50	0.44	433	0.41	433	0.00	135.00	2.11[L]	0.81	0.94
168-1-88-8[C]	86x80x6	-----	23.50	0.73	433	0.82	433	0.00	159.00	1.61[L]	0.88[F]	0.88[F]
169-1-88-12[C]	86x80x6	-----	23.50	1.17	433	1.17	433	0.00	175.00	1.16[L]	0.71	0.90

Table 7.2 Comparison of theoretical and experimental shear strengths (cont.)

Specimen	H_w x L_w x t	L_f x t_f	f'_c	ρ_L	f_{yL}	ρ_t	f_{yt}	N	V_{test}	V_{test} / $V_{analysis}$		
	(cm)	(cm)	(MPa)	%	(MPa)	%	(MPa)	(KN)	(KN)	Fixed angle	Proposed	ACI
(1)	(2)	(3)	(4)	(5)	(6)	(7)	(8)	(9)	(10)	(11)	(12)	(13)
Tests by Yoshizaki (1973) as reported by Hirosawa (1975) (cont.)												
170-2/3-36-2 [C]	86x120x6	-----	24.50	0.24	433	0.23	433	0.00	160.00	2.39[L]	1.04[F]	1.04[F]
171-2/3-36-8 [C]	86x120x6	-----	24.50	0.78	433	0.82	433	0.00	235.00	1.08	0.94[F]	0.94[F]
172-2/3-52-4 [C]	86x120x6	-----	24.50	0.44	433	0.41	433	0.00	220.00	1.79	0.90	1.01
173-2/3-52-8 [C]	86x120x6	-----	24.50	0.78	433	0.82	433	0.00	260.00	1.20	0.78	0.88
174-2/3-52-12 [C]	86x120x6	-----	24.50	1.17	433	1.17	433	0.00	275.00	0.84	0.74[F]	0.93
175-1/2-27-2 [C]	86x120x6	-----	25.50	0.22	433	0.23	433	0.00	199.00	3.25	0.91[F]	0.91[F]
176-1/2-27-8 [C]	86x120x6	-----	25.50	0.8	433	0.82	433	0.00	322.00	1.45	0.97	0.81[F]
178-1/2-42-8 [C]	86x120x6	-----	25.50	0.8	433	0.82	433	0.00	382.00	1.71	1.15	0.95
179-1/2-42-12 [C]	86x120x6	-----	25.50	1.17	433	1.17	433	0.00	422.00	1.30	1.08	1.05
Tests by Gupta (1996)												
S-2	100x100x75	37.5x10	65.1	1.06	545	0.52	578	610	719.6	1.19[X]	1.15	1.47
S-3	100x100x75	37.5x10	69	1.06	545	0.52	578	1230	850.7	1.09[X]	1.00	1.34
S-5	100x100x75	37.5x10	73.1	1.61	533.2	0.52	578	610	790.2	1.02[X]	0.99	1.58
S-6	100x100x75	37.5x10	70.5	1.61	533.2	0.52	578	1230	970	1.15[X]	1.06	1.53
S-7	100x100x75	37.5x10	71.2	1.06	545	1.06	545	610	800	1.32[X]	1.28	1.17
S-F	100x100x75	37.5x10	60.5	1.06	545	0.52	578	310	486.6	1.24[F]	1.24[F]	1.26[F]
Tests by Mo (1993)												
HN4-1[C]	65 x 86 x 7	17 x 8	32.2	0.72	302	0.81	302	13.6	205	1.33[X]	1.02	0.99[F]
HN4-2 [C]	65 x 86 x 7	17 x 8	32.2	0.72	302	0.81	302	13.6	247	1.60[X]	1.23	1.2[F]
HN4-3 [C]	65 x 86 x 7	17 x 8	32.1	0.72	302	0.81	302	13.5	202	1.31[X]	1.01	0.98[F]
HN6-1 [C]	65 x 86 x 7	17 x 8	29.5	0.72	443	0.81	302	12.4	255	1.16[X]	0.89	1.11
HM4-1 [C]	65 x 86 x 7	17 x 8	37.5	0.72	302	0.81	302	13.5	223	1.45[X]	1.10	1.07[F]
HM4-2 [C]	65 x 86 x 7	17 x 8	37.5	0.72	302	0.81	302	13.5	231	1.50[X]	1.14	1.11[F]
HM4-3 [C]	65 x 86 x 7	17 x 8	39.9	0.72	302	0.81	302	12.0	250	1.63[X]	1.23	1.2[F]
LN4-1 [C]	65 x 86 x 7	17 x 8	18	0.58	302	0.81	302	13.0	193	1.53[X]	1.21	1.03[F]
LN4-2 [C]	65 x 86 x 7	17 x 8	18	0.58	302	0.81	302	13.0	217	1.72[X]	1.36	1.15[F]
LN4-3 [C]	65 x 86 x 7	17 x 8	29.7	0.58	302	0.81	302	12.5	203	1.62[X]	1.24	1.06[F]
LN6-1 [C]	65 x 86 x 7	17 x 8	30.7	0.58	443	0.81	302	12.9	246	1.38[X]	1.06	1.06
LN6-2 [C]	65 x 86 x 7	17 x 8	30.2	0.58	443	0.81	302	12.7	200	1.12[X]	0.86	0.87
LN6-3 [C]	65 x 86 x 7	17 x 8	30.2	0.58	443	0.81	302	12.7	210	1.17[X]	0.90	0.91
LM6-1 [C]	65 x 86 x 7	17 x 8	39.3	0.58	443	0.81	302	11.8	219	1.23[X]	0.93	0.9
LM6-2 [C]	65 x 86 x 7	17 x 8	37	0.58	443	0.81	302	13.4	205	1.14[X]	0.87	0.86
LM6-3 [C]	65 x 86 x 7	17 x 8	34.5	0.58	443	0.81	302	12.5	210	1.17[X]	0.89	0.89
LM4-3 [C]	65 x 86 x 7	17 x 8	66	0.58	302	0.81	302	11.9	227	1.83[X]	1.34	1.16[F]
Tests by Barda (1977)												
B1-1	95.5x190.5x10.2	61x10.2	29.00	0.73	543.00	0.44	496.10	0.00	1217.30	0.96[X]	1.18	1.82
B2-1	95.5x190.5x10.2	61x10.2	16.40	1.26	552.00	0.44	499.60	0.00	977.60	1.07[X]	1.14	1.62
B3-2[c]	95.5x190.5x10.2	61x10.2	27.00	0.97	545.10	0.44	513.40	0.00	1107.20	0.87[X]	0.94	1.65
B6-4[c]	95.5x190.5x10.2	61x10.2	21.30	0.75	496.80	0.44	496.80	0.00	875.60	0.88[X]	0.87	1.39
B7-5[c]	47.5x190.5x10.2	61x10.2	25.70	0.96	531.30	0.41	501.60	0.00	1138.60	1.03[X]	0.97	1.80
B8-5[c]	190.5x190.5x10.2	61x10.2	23.50	0.96	527.90	0.48	496.10	0.00	884.80	1.00[X]	0.79	1.36
Tests by Cardenas *et al*. (1980)												
SW7	190.5x190.5x7.6	-----	43.10	0.02	448.50	0.00	414.0	0.00	518.7	0.83[F]	1.23	1.71
SW8	190.5x190.5x7.6	-----	42.50	0.03	448.50	0.00	465.8	0.00	569.3	0.90[F]	1.25	1.04
SW9	190.5x190.5x7.6	-----	43.1	2.87	448.5	1.00	414.0	0.00	678.7	1.07[F]	1.07[F]	1.04
SW-11	190.5x190.5x7.6	-----	38.2	1.64	448.5	0.75	448.5	0.00	608.9	0.95[F]	0.95[f]	1.36[F]
SW-12	190.5x190.5x7.6	-----	38.4	1.64	448.5	1.00	448.5	0.00	657.8	1.03[F]	1.03[F]	1.46[F]
Tests by Dabbagh (2005)												
SW1[c]	100x100x75	37.5x10	86	2.52	536.0	0.45	536.0	1200	992.0	0.95[x]	1.02	1.89
SW2[c]	100x100x75	37.5x10	86	3.22	498.0	1.34	498.0	1200	1190.0	1.10[x]	1.17	1.53
SW3[c]	100x100x75	37.5x10	96	2.82	498.0	0.75	536.0	1200	1107.0	1.00[x]	1.07	1.76
SW5[c]	100x100x75	37.5x10	83	3.22	498.0	0.45	536.0	1200	1134.0	1.06[x]	1.12	2.17
SW6[c]	100x100x75	37.5x10	83	2.95	498.0	0.94	498.0	1200	1141.0	1.08[x]	1.15	1.74
							Number of samples				100	
							Average strength ratio			1.24	1.09	1.23
							Standard Deviation (SD)			0.38	0.16	0.28
							Coefficient of Variation (CoV)			0.14	0.03	0.08

[C] Cyclic Loading
[F] Predicted as failing in flexure
[L] Lower bound solution
[X] Fixed solution

7.4.2 Load-displacement behaviour

The majority of cases demonstrated reasonable match between the recorded and predicted load-displacement behaviour based on the proposed cracking angle. Typical examples are presented in Figure 7.6 including specimen B1-1 tested by Barda *et al.* (1977) and specimen S-5 tested by Gupta (1996). Flanged Specimen S-5 was tested under combined lateral and axial loading while specimen B1-1 was subjected to lateral loading only. The figure, which shows the lateral deflection at the top of the two walls, depicts that the proposed analysis method can reasonably trace the nonlinear behaviour of structural walls up to the point of failure.

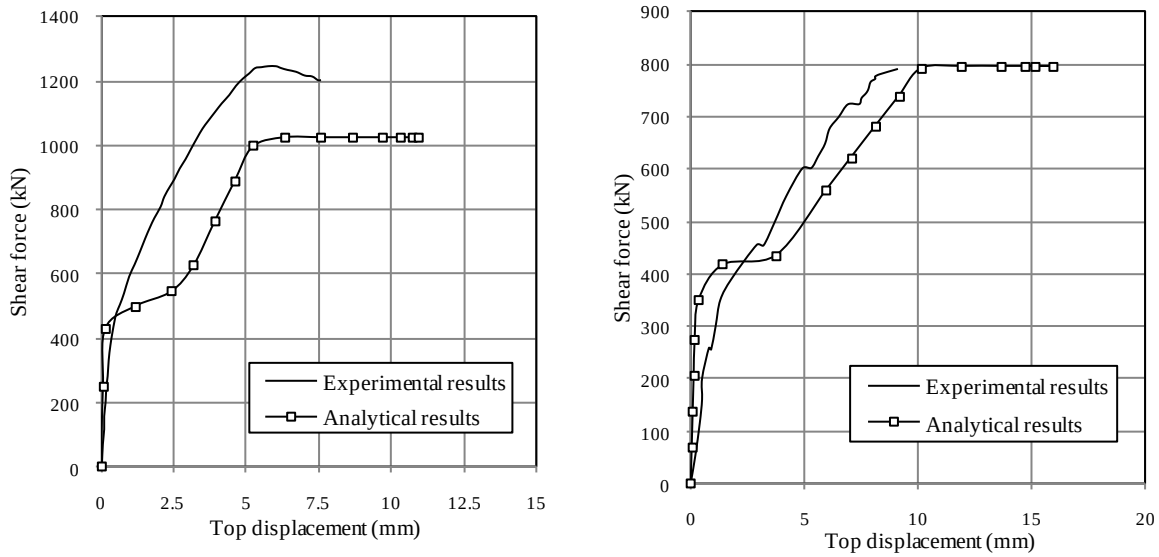

(a) Specimen B1-1 (Barda *et al.* 1977) (b) Specimen S-5 (Gupta 1996)

Figure 7.6 The load-displacement behaviour of two structural wall specimens as measured experimentally and predicted using the new method

7.4.3 Cracking angle values

As a further assessment of the proposed cracking angle equations, their predictions of the values of α were compared to those reported in the literature. This exercise was limited to the walls for which the cracking pattern was reported. Two typical samples including

specimen B3-2 tested by Barda *et al.* (1977) and specimen S-3 tested by Gupta (1996) are selected and the cracking pattern is shown in Figure 7.7. The Figure also represents the directions of the main cracks according to experimental results, new proposed cracking angle and fixed angle solution. It can be seen that the new proposed cracking angles matched well the experimental cracking map indicating the effectiveness of the proposed solution.

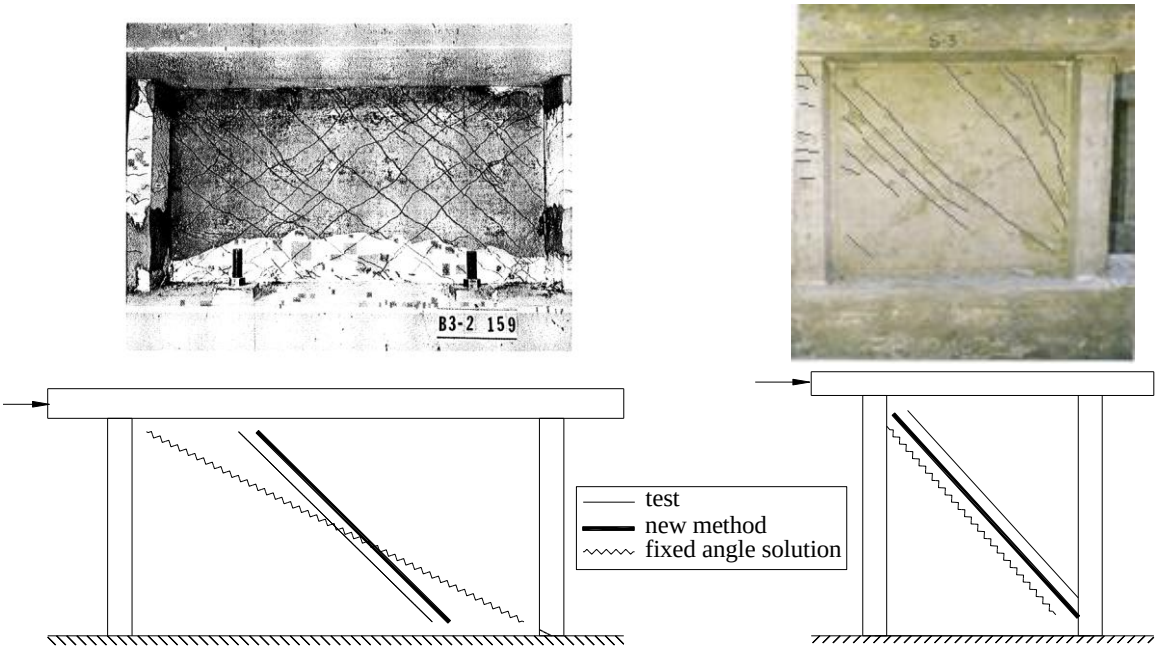

(a) Specimen B3-2 tested by Barda *et al.* (1977) (b) Specimen S-3 tested by Gupta (1996)

Figure 7.7 Comparison between the cracking angles for two structural walls as found experimentally and predicted using the new proposed method and the fixed angle solution

7.5 Applicability of the proposed method

Based on the verification results discussed in Section 7.4, the proposed analysis method was found to offer reasonable predictions when applied to the 100 structural walls reported in the literature. In the next section, the applicability of the proposed method with particular reference to variations in a number of parameters such as cross-sectional shape, concrete strength, steel reinforcement content and loading scheme, is assessed.

7.5.1 Cross-sectional shape

Figure 7.8 represents the effect of the walls' cross sectional shape on the ability of the method to predict the shear capacity, for flanged and rectangular walls. From the data presented in Table 7.2 for flanged walls, the values of the shear strength ratios V_{test} / $V_{analysis}$ have an average of 1.09, coefficient of variation (CoV) of 0.02 and standard deviation (SD) of 0.14, while the corresponding values for rectangular walls are 1.10, 0.04 and 0.2, respectively. This result implies that the softened truss model with the newly proposed cracking angle can predict the shear capacity of flanged walls slightly more accurately than rectangular walls. This may be attributed to the additional confining effect caused by the presence of boundary elements, which results in reducing the concrete softening effect and limiting the cracking and extension of the walls (Mansour *et al.* 2004).

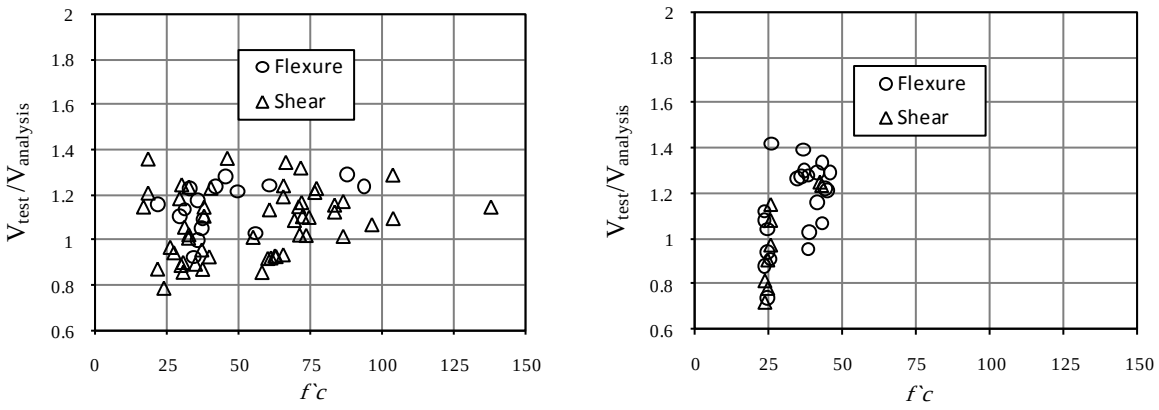

(a) Flanged walls (b) Rectangular walls

Figure 7.8 Variation of shear strength ratio as a function of concrete strength, $f`_c$, according to the proposed method for flanged walls and rectangular walls

7.5.2 Concrete strength

Figure 7.5a illustrates the variation of the shear strength ratios V_{test} / $V_{analysis}$ with concrete strength for the examined walls. The concrete strength for the walls reported in this investigation varied from 16.4 to 137.5 N/mm^2. Accordingly, it can be concluded that the

proposed analysis method could be used to predict the shear capacity of structural walls made with ordinary and high strength concrete with reasonably acceptable accuracy.

7.5.3 Reinforcement content

The variation of the shear strength ratio with the longitudinal, ρ_L, and transverse, ρ_t, steel ratios for the 100 wall specimens considered is shown in Figure 7.9. The figure shows that the proposed analysis method could be considered valid within a wide range of steel ratios from 0.22 to 3.2% and from 0.21 to 1.4% in the longitudinal and transverse directions, respectively.

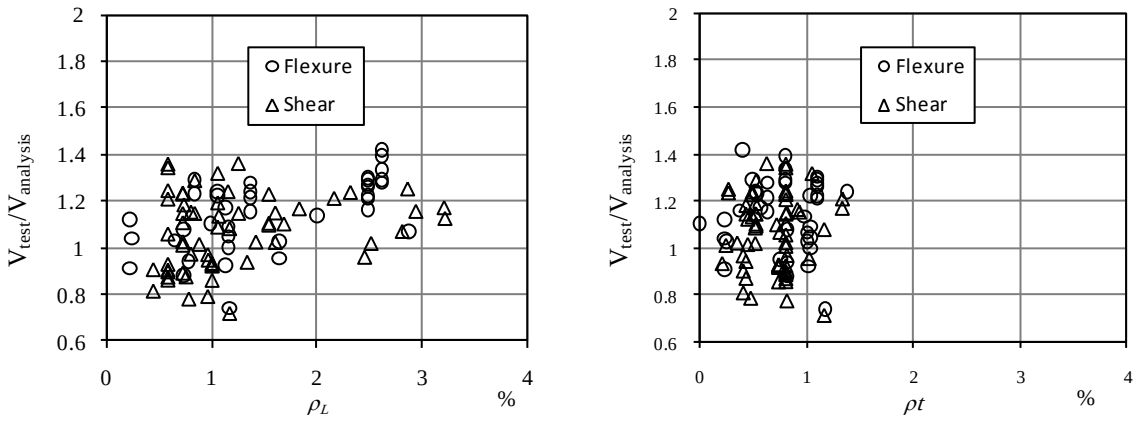

(a) The longitudinal direction (b) The transverse direction

Figure 7.9 Variation of shear strength ratio with reinforcement ratio in the longitudinal and transverse directions

7.5.4 Loading scheme

Figure 7.10 illustrates the effect of loading scheme on the shear strength ratios (V_{test} / $V_{analysis}$) as a function of concrete strength. The results included in Table 7.2 show that the values of the shear strength ratio V_{test} / $V_{analysis}$ have an average of 1.06, coefficient of variation (CoV) of 0.02 and standard deviation (SD) of 0.15 for walls tested under cyclic loading, while the corresponding values for monotonic loading are 1.12, 0.03 and 0.17,

respectively. These results show that the shear strength predictions for walls cyclically loaded are slightly more accurate than for walls monotonically loaded. One possible reason is that cyclically loaded walls usually suffer from extensive damage more than monotonically loaded walls and hence they have lower shear strengths. The accuracy of the results could be improved further if the cyclic constitutive models of concrete and steel were implemented.

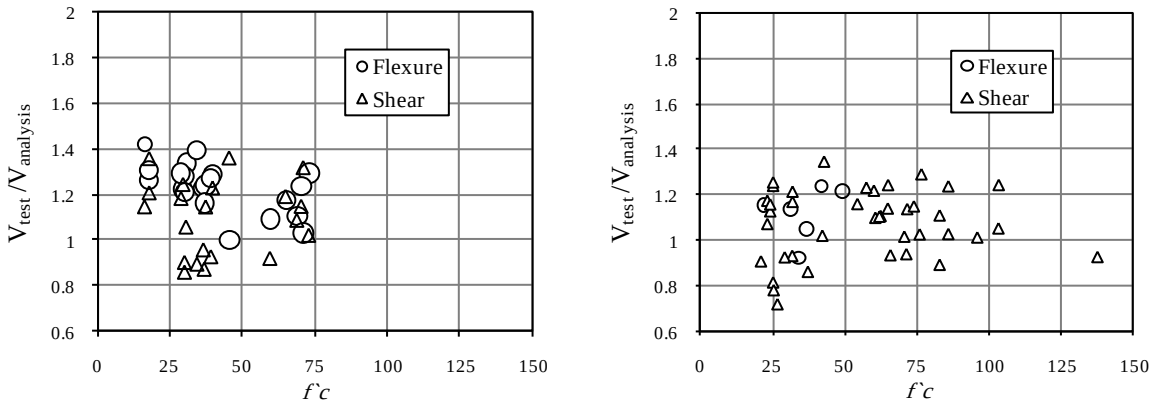

(a) Monotonic loading (b) Cyclic loading

Figure 7.10 Effect of loading scheme on wall shear strength predictions

7.6 Analysis of encased-plate composite walls

7.6.1 Introduction

Having validated the proposed analysis method against the experimental results of the 100 wall specimens available in the literature, the proposed method was slightly modified to include the contribution of the encased-plate. The proposed analysis method, discussed in detail in the current section, is able to predict not only the shear strength, but also the deformation behavior throughout the post-cracking loading history. Moreover, the analysis method can be used to predict the mode of failure based on a comparison between the flexural and shear strength values of the composite wall.

Before proceeding with the analysis method, two basic assumptions should be made. First, the proposed method assumes full composite action between the encased-plate and concrete, thus no relative displacement takes place during all stages of loading. This assumption is consistent with the experimental observations from testing of wall units under pure in-plane shear and wall specimens tested under lateral loading. Second, plate buckling is assumed to have a negligible effect on the behaviour of encased-plate composite walls and therefore composite walls are able to develop their full strength.

7.6.2 Proposed analysis method

Figure 7.11a represents a general view of an encased-plate composite wall, in which the web of the wall may be visualised as an assembly of smaller reinforced concrete elements. Each element is reinforced with a grid of steel rebars in the longitudinal, *L*, and transverse, *t*, directions and an encased-plate as given in Figure 7.11b. A typical composite element, A, is subjected to in-plane shear stresses leading to development of diagonal cracks.

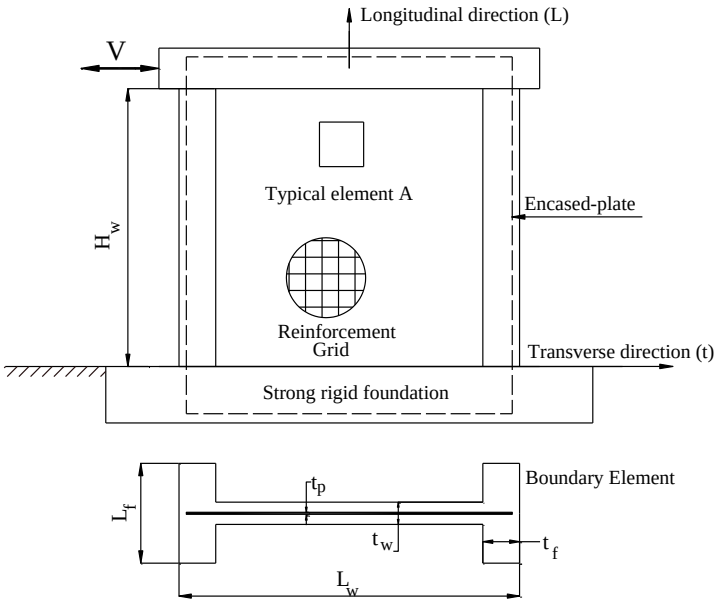

(a) Front elevation and cross-sectional views of an encased-plate composite wall

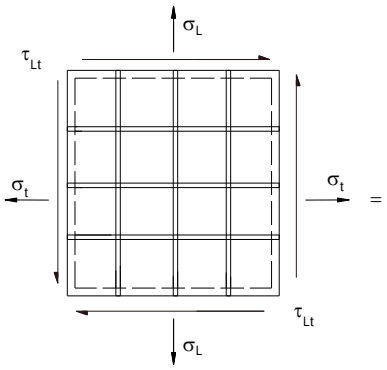

(b) Encased-plate composite element A

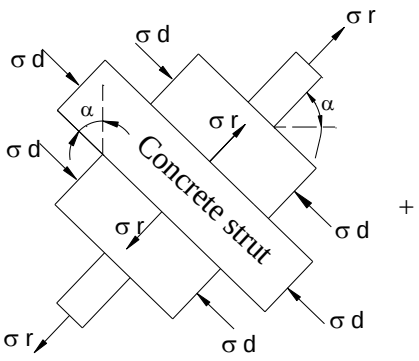

(c) Concrete struts

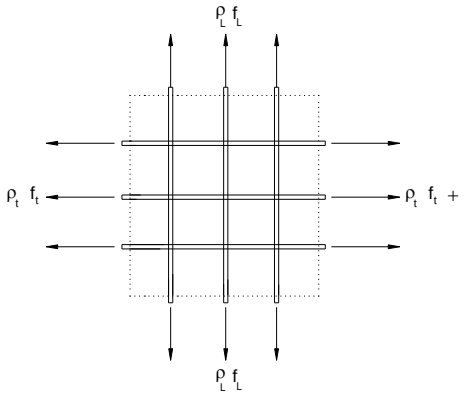

(d) Steel rebars

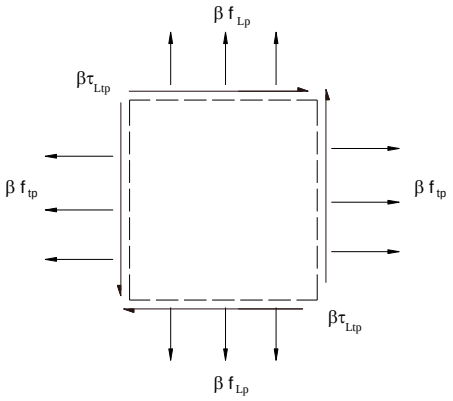

(e) Encased-plate

Figure 7.11 Schematic views of a typical encased-plate composite wall with an isolated wall element

After cracking, the concrete is split by diagonal cracks into a series of concrete struts that are inclined at an angle α with respect to the longitudinal axis (Figure 7.11c). The diagonal concrete struts, the longitudinal and transverse steel rebars (Figure 7.11d) and the encased-plate (Figure 7.11e) form a truss that is capable of resisting the applied shear stresses.

The element stresses are analysed by the principal of stress transformation by considering the equilibrium, strain compatibility and stress-strain relationships of concrete, steel rebars and encased-plate as described for conventionally-reinforced walls.

A. Equilibrium and compatibility

Equations 7.1 to 7.3 require some modifications to include the contribution of the encased-plate. The longitudinal and transverse steel rebars provide the smeared stresses $\rho_L f_L$ and $\rho_t f_t$, (Figure 7.12d) in the longitudinal and transverse directions, respectively, while the encased-plate produces tensile stresses βf_{Lp} and βf_{tp} in the longitudinal and transverse directions, respectively in addition to shear stress of $\beta \tau_{Ltp}$ (Figure 7.12e), where β is the ratio of plate thickness to the central panel thickness, $\beta = t_p / t_w$.

$$\sigma_L = \sigma_d \cos^2\alpha + \sigma_r \sin^2\alpha + \rho_L f_L + \beta f_{Lp} \tag{7.16}$$

$$\sigma_t = \sigma_d \sin^2\alpha + \sigma_r \cos^2\alpha + \rho_t f_t + \beta f_{tp} \tag{7.17}$$

$$\tau_{Lt} = (-\sigma_d + \sigma_r) \cos\alpha \sin\alpha + \beta \tau_{Ltp} \tag{7.18}$$

In Equations 7.16 to 7.18, σ_L, σ_t are normal stresses in the composite element, A, in L and t directions, respectively; τ_{Lt} is the average shear stress in L-t coordinate system; f_{Lp}, f_{tp} are the average normal stresses in the encased-plate in L and t directions, respectively; t_p and t_w

are the plate thickness and the central panel thickness, and τ_{Ltp} is the shear stress in the encased-plate.

It is important to limit the value of the shear stress resisted by the encased-plate. Subedi (1989) suggested that the shear stress assumed to be resisted by the encased-plate should not exceed 0.5 f_{yp} ,where f_{yp} is the yield stress of the plate. Also, the shear stress should not exceed $G\ \gamma_{Lt}$, where G is the shear modulus, $G = E_p/2(1+v)$,; γ_{Lt} the average shear strain in the composite element; E_p the plate's modulus of elasticity and v is the Poisson's ratio, taken as 0.3.

Equations 7.4 to 7.8 can still be applied to determine the average normal strains in *L*, *t*, *d* and *r* directions; the average shear strain in the *L*-*t* coordinate system and the average wall shear stress and strain.

B. Constitutive models

Equations 7.9 to 7.11 can be used to define the constitutive models for concrete in compression and tension and for steel rebars. Two equations are still needed to describe the constitutive models of the plate. The equations assume that the plate behaviour is elastic-perfectly-plastic with no strain-hardening.

$$f_s = E_p\, \varepsilon_s \qquad \text{for } 0 < \varepsilon_s < \varepsilon_{yp} \tag{7.19-a}$$

$$f_s = f_{yp} \qquad \text{for } \varepsilon_s \geq \varepsilon_{yp} \tag{7.19-b}$$

where f_s and ε_s are the stress and strain of the plate, respectively. They become f_{Lp}, ε_L and f_{tp} , ε_t when applied to longitudinal and transverse directions, respectively. f_{yp} and ε_{yp} are the yield stress and strain of the plate, and E_p is the modulus of elasticity of steel plate. These

set of equations represent an approximation of plate behaviour that ignores the effect of Poisson's ratio and was used to simplify the solution procedures.

C. Solution algorithm

Equation 7.12 can be used to determine the longitudinal stress, which is equal to zero for the walls under consideration since no axial load was applied. Finally, the new cracking angle presented by Equation 7.15 is used to calculate the angle α. A computer program was developed to solve the set of equations and to derive the load-displacement behaviour of the composite walls. The solution procedure is illustrated in the form of a flow chart in Figure 7.12.

D. Verification of proposed analysis method

The results obtained from testing of wall units under pure in-plane shear and wall specimens under lateral loading were used to verify the reliability of the proposed analysis method. The analysis was used to predict the shear capacity and the load-displacement behaviour of each specimen.

i. Shear capacity

The shear strength of tested walls was calculated using the analytical model presented above, while the flexural strength was calculated using the conventional analysis of reinforced concrete sections subjected to uniaxial bending moments. The smaller of the two values was taken as the predicted strength. The proposed method was used to estimate the strength of the conventionally-reinforced and encased-plate specimens discussed in Chapters 3 and 5.

The main features of the walls are listed in columns 1 to 7 in Table 7.3, while columns 8 and 9 present the experimental and the predicted strength values of the specimens and column 10 shows the ratio $V_{test} / V_{analysis}$.

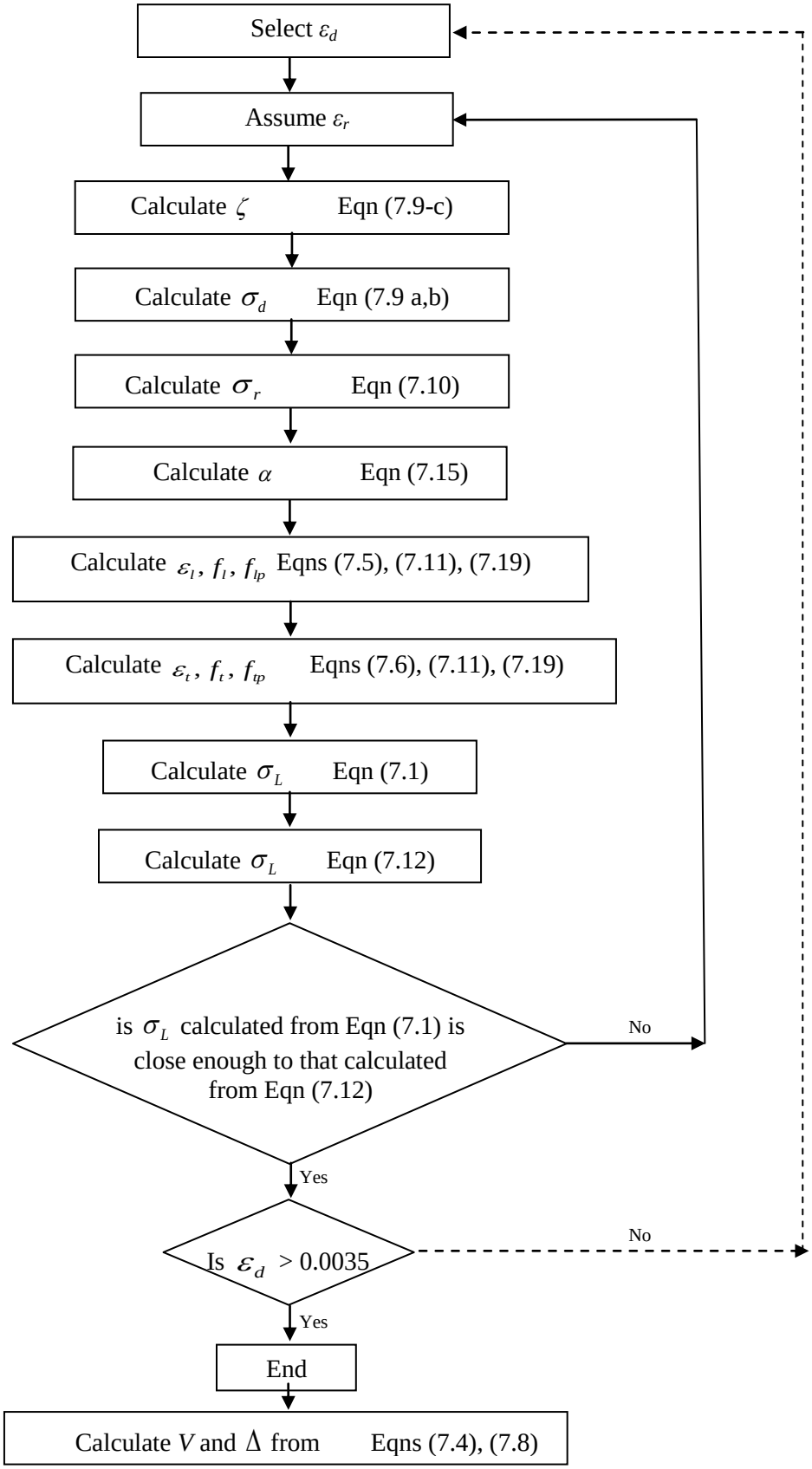

Figure 7.12 A flow chart of the solution procedures

Table 7.3 Comparison of theoretical and experimental shear strengths

(a) Wall units

Wall unit	Effective dimensions			Reinforcement		f_{cu} (N/mm^2)	V_{test} (kN)	$V_{analysis}$ (kN)	$V_{test}/V_{analysis}$
	Length (mm)	width (mm)	thickness (mm)	Plate thick. (mm)	Rebars				
(1)	(2)	(3)	(4)	(5)	(6)	(7)	(8)	(9)	(10)
P2	305	305	60	0.8	2Ø6	38.10	102.05	109.90	0.93
P3	305	305	60	1.5	2Ø6	34.20	126.4	142.50	0.89
P4	305	305	60	0.8	2Ø6	24.90	99.71	100.90	0.99
P5	305	305	60	0.8	2Ø6	71.40	105.59	102.60	1.03
P6	305	305	60	0.8	3Ø6	38.30	102.53	115.40	0.89
P7	305	305	60	0.8	4Ø6	37.90	106.04	127.70	0.83
P8*	305	305	40	0.8	2Ø6	34.40	48.28	78.60	0.61[x]

* Premature failure

[x] Excluded from statistical analysis

Average strength ratio	0.93
Standard Deviation (SD)	0.07
Coefficient of Variation (CoV)	0.01

(b) Structural walls

Wall specimen	Central panel dimensions			Reinforcement			V_{test} (kN)	$V_{analysis}$ (kN)	$V_{test}/V_{analysis}$
	Length (mm)	Width (mm)	Thick. (mm)	ρ_{long}, (%)	ρ_{trans}, (%)	Plate thick. (mm)			
(1)	(2)	(3)	(4)	(5)	(6)	(7)	(8)	(9)	(10)
EW11	750	610	60	0.31	0.38	0	180.00	184.6	0.97
EW12	750	610	60	0.31	0.38	0.8	280.00	283.4	0.99
EW13	750	610	60	0.31	0.38	1.5	350.00	343.0	1.02
EW21	750	750	70	0.63	1.18	0	365.00	360.3	1.01
EW22*	750	750	70	0.63	1.18	0.8	270.00	429.2	0.63[x]
EW23	750	750	70	0.63	1.18	1.5	470.00	470.0	1.00
EW31	1000	600	45	0.93	1.26	1	70.00	68.7[F]	1.02

* Premature failure

[x] Excluded from statistical analysis

[F] Flexural failure

Average strength ratio	1.01
Standard Deviation (SD)	0.02
Coefficient of Variation (CoV)	0.001

The values in Table 7.3 indicate that the proposed analysis method yielded realistic predictions of the ultimate load values and good agreement was achieved between the two sets of the results for all cases except that of unit P8 and specimen EW22, both of which failed prematurely as described in Chapters 3 and 5. Also, the analytical results for specimen EW23 compared well with the experimental results although it failed locally. The average ratio of experimental to analytical (V_{test} / $V_{analysis}$) results was 0.93, CoV=0.01 and SD=0.07 for wall units tested under pure in-plane shear, see Figure 7.13a. This exercise was repeated for wall specimens tested under lateral loading, and the average, CoV and SD values were 1.01, 0.001, 0.02, respectively, see Figure 7.13b. The low average of the V_{test} / $V_{analysis}$ ratio achieved with the proposed method is promising and indicates the effectiveness of the proposed analysis method.

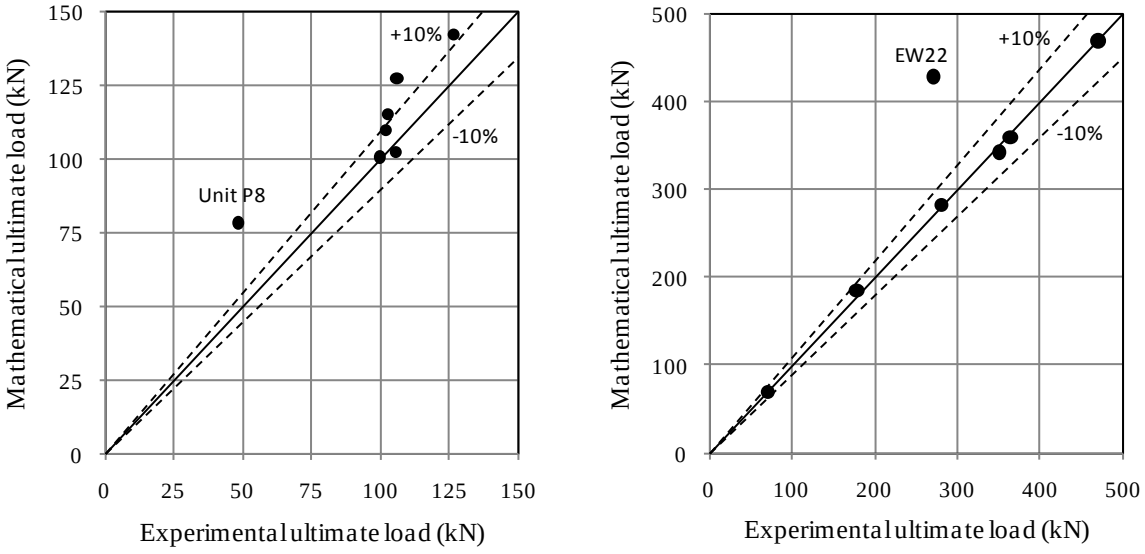

(a) Wall units (b) Structural walls

Figure 7.13 Comparison of ultimate load predicted mathematically with the corresponding experimental data

ii. Load-displacement behaviour

The proposed method was also used to predict the load-displacement behaviour of the wall specimens tested under lateral loading. Figure 7.14 presents a comparison of the load-

displacement behaviour of all tested specimens that failed in shear as obtained experimentally and predicted using the proposed method. The predicted load-displacement behaviour of conventionally reinforced concrete walls, EW11 and EW21, compared well with the recorded load-displacement behaviour. Also, it can be observed that the predicted load-displacement behaviour of flanged specimens EW12 and EW13was more accurate than in rectangular walls, EW22 and EW23 which implies that the proposed analysis method can predict the behaviour of encased-plate composite flanged walls more accurately than rectangular walls. The figure also depicts that the proposed analysis method can reasonably trace the nonlinear behaviour of conventionally and encased-plate composite walls up to the ultimate load level and beyond.

iii. Cracking angle

Figure 7.15 depicts the typical crack patterns of wall units tested under pure in-plane shear and that for wall specimens tested under lateral loading at failure. The figure suggests that, in all cases, the presence of the encased-plate has no significant effect on the direction of the cracking angle. For wall units tested under in-plane shear, the value of the cracking angle was almost the same (45° with the wall edge) in all cases for conventionally-reinforced unit (unit P1) and encased-plate units (units P2 and P3), Figure 7.15a-c. Therefore, the value of 45° was used to calculate the shear strength of the wall units. For wall specimens tested under lateral loading, not much difference was observed in the cracking angle in each group, see Figure 7.15d-i. This result implies that Equation 7.15, which was used in conventional walls to calculate the cracking angle, can still be used in the analysis of composite walls. It is worth noting that the analysis was sensitive to the value of the strut cracking angle and a proper value should be used to obtain reasonable results of walls' shear strength.

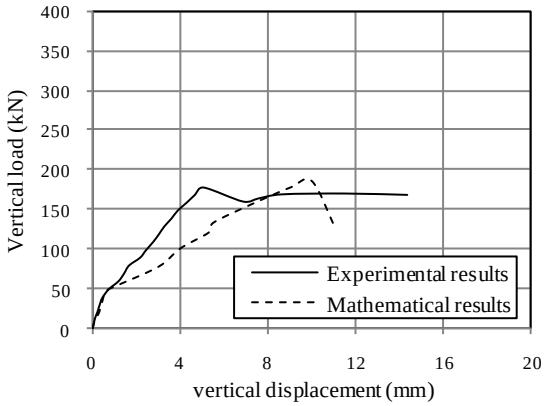

(a) Specimen EW11

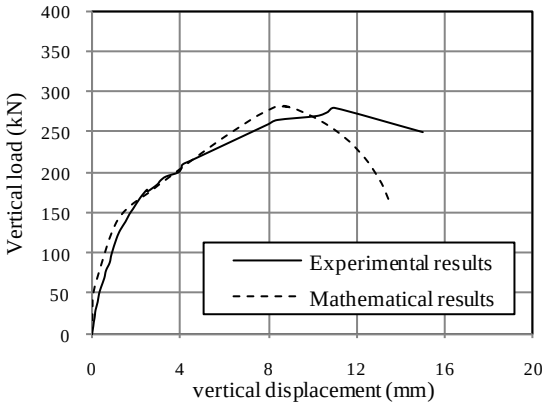

(b) Specimen EW12

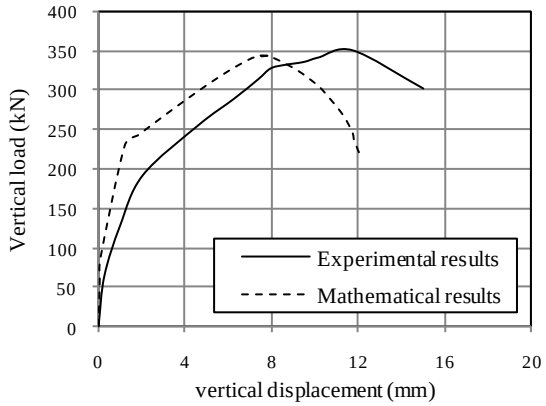

(c) Specimen EW13

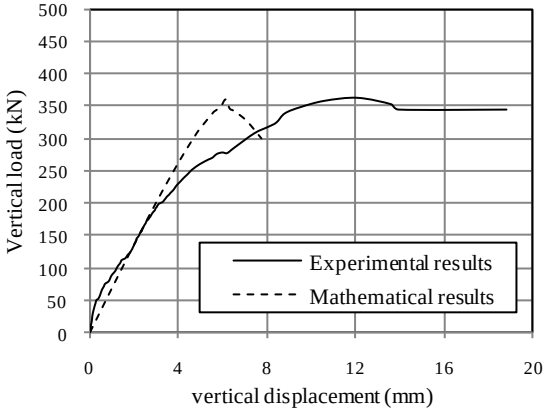

(d) Specimen EW21

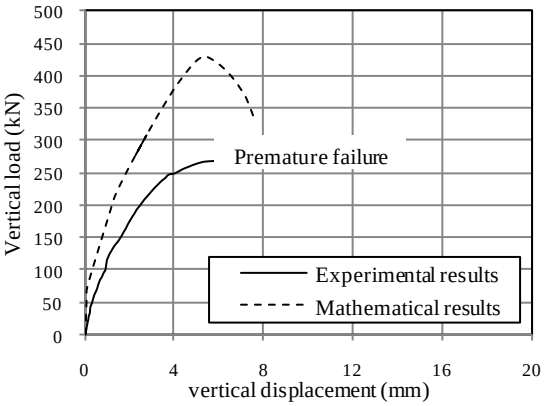

(e) Specimen EW22

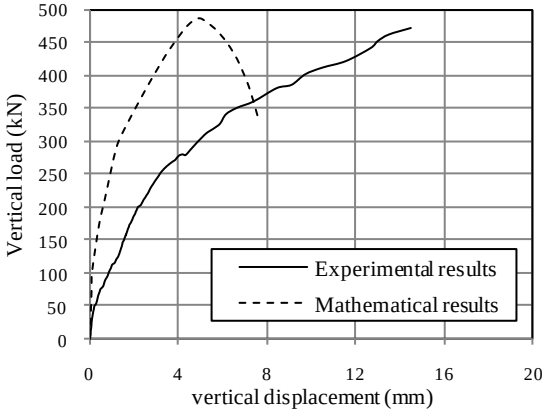

(f) Specimen EW23

Figure 7.14 Load-displacement behaviour of tested wall specimens as obtained experimentally and predicted using the proposed method

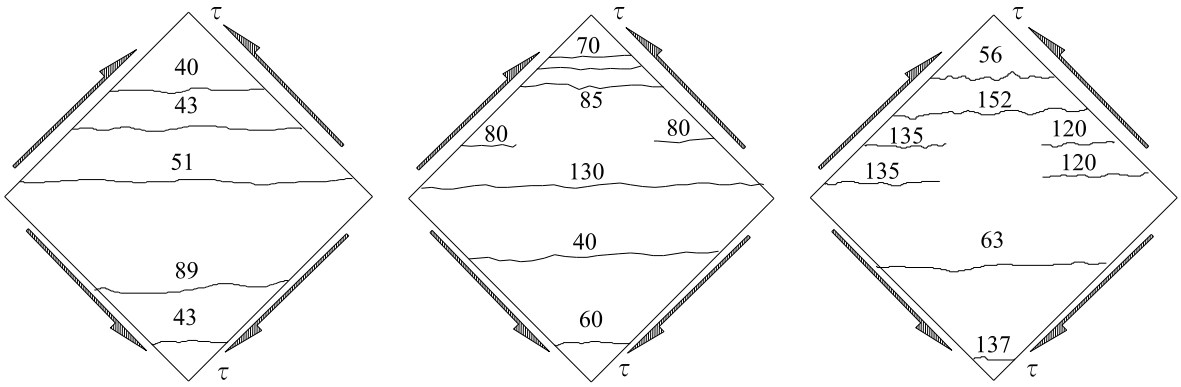

(a) Conventional unit P1 (b) Composite unit P2 (c) Composite unit P3

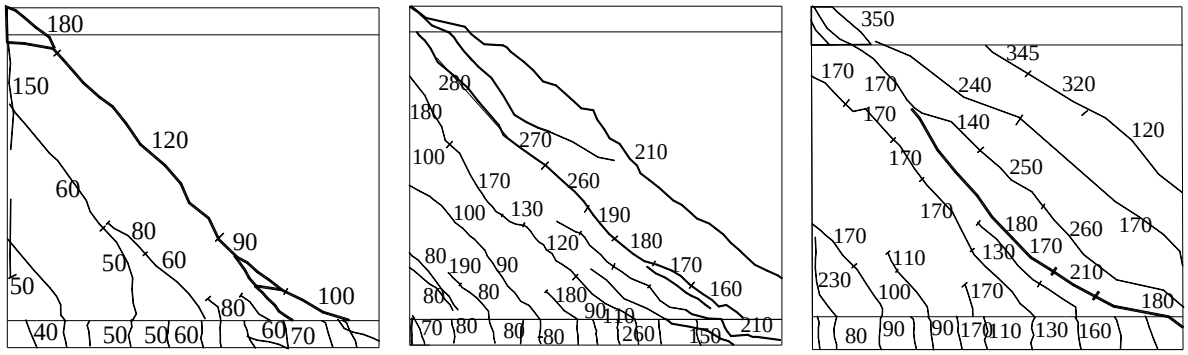

(d) Conventional wall EW1 (e) Composite wall EW12 (f) Composite wall EW13

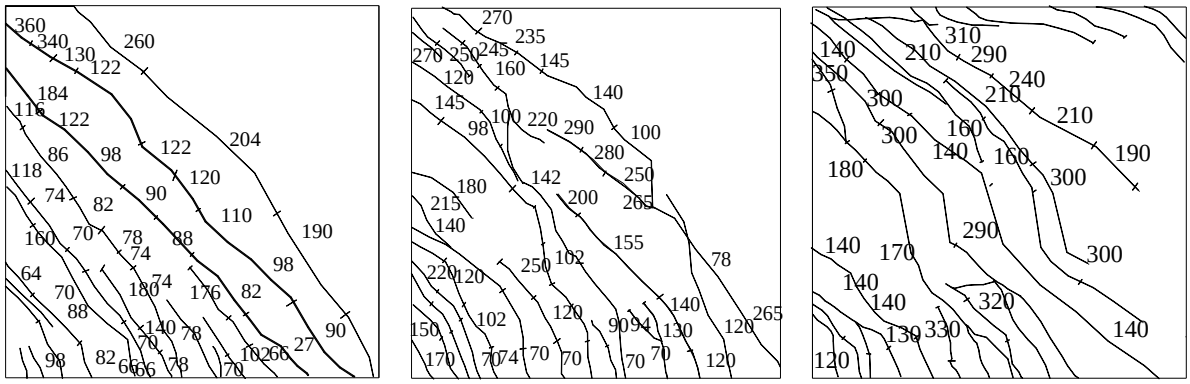

(g) Conventional wall EW21 (h) Composite wall EW22 (i) Composite wall EW23

Figure 7.15 Experimental crack patterns at failure

As a further assessment of the proposed cracking angle equations, their predictions of the values of α were calculated for all wall specimens tested under lateral loading and the values were compared to the experimental ones.

A comparison of the directions of the main cracks according to experimental results and the new cracking angle is shown in Figure 7.16. It can be seen that the new proposed cracking angle matched with acceptable accuracy the experimental cracking map.

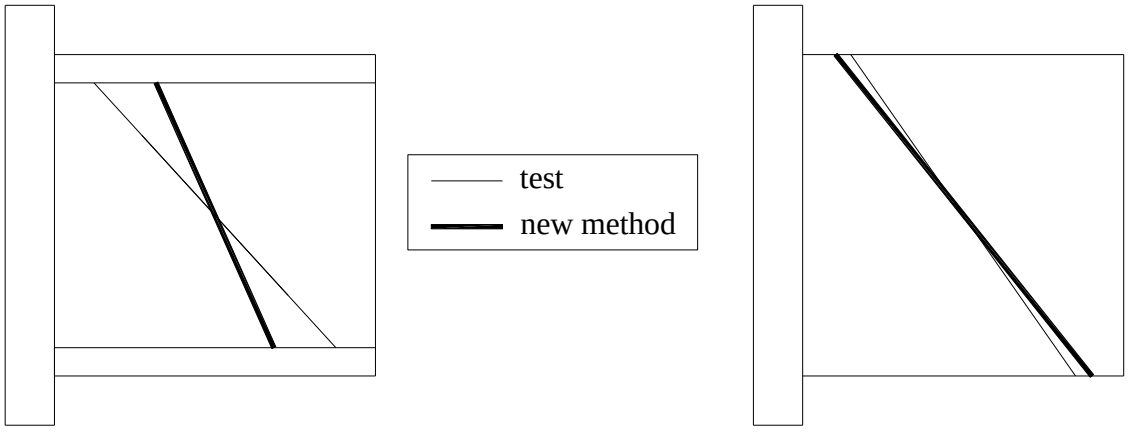

(a) First group (b) Second group

Figure 7.16 Comparison between the cracking angles for each group as found experimentally and predicted using the new method

Chapter 8 Summary, conclusions and future work

8.1 Introduction

This chapter outlines the highlights and main conclusions of the research. Future lines of research are also suggested.

8.2 Summary of research

The behaviour of conventionally-reinforced concrete structural walls was reviewed briefly. Because of the inadequacy of these walls in earthquake load design, various alternative designs were proposed in the past. Some were accepted in the construction industry namely; diagonally reinforced concrete walls, steel plate walls, steel plate composite walls and steel-concrete-steel composite walls, while others were not implemented in applications including double skin-profiled composite walls and perforated steel plate composite concrete walls. All designs were shown to improve the performance of structural walls but suffered from various limitations. Overall, composite alternatives appeared to provide robust systems with high strength, extended ductility and adequate energy dissipation. However, concerns remained related to plate buckling at relatively low shear stresses and overall high cost. Based on the comparison between various alternatives, a design of an encased-plate composite structural wall system was introduced. The proposed system consisted of a reinforced concrete wall with a steel plate embedded inside it. The longitudinal reinforcement bars maintained a strong connection between the two components; a feature that provided stiffening against plate buckling and improved the composite action within the concrete wall.

The behaviour of encased-plate composite walls under pure in-plane shear was investigated in an experimental study involving a number of wall units. A special rig was designed and fabricated to apply pure shear stresses to the wall units. Tests were

carried out first on the individual components of composite wall before considering composite walls. Ten small-scale units were designed and tested, two of which were unstiffened steel plates, one was conventionally-reinforced, and seven were encased-plate composite. Tests on composite units were intended to cover the behaviour up to failure, taking into consideration the effect of plate thickness, concrete strength, reinforcement content and wall thickness. A common failure mechanism suggested that the failure of composite walls was associated with extensive concrete damage, yielding of rebars and formation of diagonal tension field in the encased-plate. The failure mechanism highlighted also the potential importance of the interaction between the encased-plate and the surrounding concrete and the lateral support against plate buckling as provided by the concrete and the rebars. It also became clear that if the concrete cover to the plate was not enough, it would be unable to prevent plate buckling, leading to cover peeling and overall premature failure. Among the parameters considered in this part of the study, only the concrete cover to the plate and the plate thickness had a considerable effect on the behaviour of composite walls under pure in-plane shear.

In the framework of the preliminary investigations to study the behaviour of encased-plate composite walls under monotonically increased lateral loads, tests were carried out on seven specimens. The specimens represented the critical storey element of a structural wall system in a multi-storey building with a scale of approximately 1:5. Depending on the results obtained from investigating the behaviour of encased-plate composite walls under pure in-plane shear, the main parameter included in this study was the plate thickness. The specimens were designed to fail in either shear or flexural mode. The test results revealed that the use of encased-plate had no effect on the failure mode of composite walls. However, encased-plate composite walls exhibited less shear

distortion, had greater neutral axis depth and showed significant increases in secant stiffness and ductility compared to conventionally-reinforced walls.

The test programme used a full-field deformation measurement system based on digital photogrammetry and particle image velocimetry (PIV). An examination of conventional measuring methods has established the potential of using this approach. The output of the technique compared well with the results obtained from conventional measuring instruments. The proposed deformation measurement system provided detailed deformation data, and could be used to plot displacement and strain contours on the whole specimen surface. The availability of inexpensive, off-the-shelf, digital cameras and photogrammetry software systems made the technique more feasible and affordable for broad and diverse experimental testing applications.

A finite element model that simulates the behaviour of encased-plate composite walls was developed. The element types, the mesh density and the concrete model's plastic damage parameters were obtained from initial sensitivity studies. The reliability of the model was demonstrated through three case studies involving isolated walls, coupled walls and encased-plate composite beams, respectively, in addition to the experimental results obtained in this study. Close match between the numerical and experimental results was observed particularly in the load-displacement behaviour, the ultimate capacity, the crack pattern and the strain development in the rebars and the encased-plates. Following successful validation, the model was used to conduct a parametric study to assess the effect of variables which were thought to have a considerable influence on the behaviour of encased-plate composite structural walls. A number of hypothetical conventional and encased-plate walls with larger capacities and dimensions than those tested experimentally were analysed using the proposed numerical model.

The parametric study comprised 57 hypothetical walls with different combinations of wall geometry, plate size and reinforcement layout, and comparisons of behaviour concentrated on the load-displacement behaviour, initial stiffness, cracking pattern and ultimate load. The finite element model provided better understanding of the behaviour, and the analysis results showed that walls' aspect ratio, thickness of encased- plate, axial loading and central panel's longitudinal reinforcement were the main parameters affecting the behaviour of encased-plate composite walls. The central panel's transverse reinforcement (stirrups) and the concrete strength appeared to have little effect on the behaviour.

An analysis method to predict the shear strength and behaviour of conventionally-reinforced structural walls under both monotonic and cyclic loading was developed. The method was based on the softened truss model and utilised a newly proposed cracking angle of the concrete strut. The cracking angle was estimated using a regression analysis involving the reported shear capacity values of 100 experimental structural walls. The analysis paid particular attention to the geometric wall properties, reinforcement ratios, internal stresses and concrete strength. The proposed method was used to predict the shear capacity and deformation behaviour of the test walls, both pre- and post-cracking, and the results compared well with the experimental data. The proposed strut cracking angle also matched well the cracking patterns obtained experimentally. Having validated the proposed analysis method, a mathematical model was developed to predict not only the ultimate shear strength, but also the deformation behaviour of encased-plate structural walls throughout their post-cracking loading history. When compared with experimental results, the mathematical results were found to yield realistic predictions of shear strength and behaviour of encased-plate composite structural walls.

In the light of the experimental observations and numerical modelling, it can be concluded that encased-plate composite structural wall system presented an attractive structural option in lateral load resisting wall applications especially when high shear stresses were expected.

8.3 Conclusions

Based on the research conducted within this project, the following conclusions could be drawn:

- The shear strength and ductility of conventionally-reinforced walls can significantly be improved by embedding a steel plate centrally within the cross-section. The greater shear strength of this structural system is attributed mainly to the composite action between the steel plate and the concrete.
- The behaviour of an encased-plate composite wall under pure in-plane shear is different from that of its individual components due to the interaction between the encased-plate and the concrete. While the initial stiffness of the composite wall is higher than that of the individual components, no improvement is expected in ultimate load carrying capacity.
- The encased-plate provids a substantial contribution to the section flexural stiffness, and hence reducing walls' lateral deformation at all loading stages. As would be expected, increasing the plate thickness causes significant increases in the initial stiffness and ultimate capacity of composite walls.
- Concrete strength has little effect on the behaviour of encased-plate composite walls under pure in-plane shear, but it has a considerable influence on the initiation of cracks.

- Concrete cover to the plate appears to play a vital role governing the behaviour of composite walls under in-plane shear. Sufficient cover is required to prevent buckling of thin plates, and hence maintain both the plate and the concrete without significant damage under high load levels.
- Encased-plates appear to have no effect on the mode of failure of composite walls. However, encased-plate composite walls exhibit less shear distortion and show higher stiffness and ductility compared to conventionally-reinforced walls. The extension and shortening of the boundary wall elements reduce substantially with the addition of encased-plates due to the increase in the walls' in-plane axial stiffness.
- The initial stiffness and ultimate load capacity of encased-plate composite walls are significantly reduced with higher walls' aspect ratios.
- The encased-plate's contribution in increasing the walls' load carrying capacity is more pronounced in short walls than in squat and cantilever walls.
- Axial loads have a considerable effect in decreasing the ductility of encased-plate composite walls, but lead to a considerable improvement in the load carrying capacity.
- The central panel's reinforcement has a little effect on the initial stiffness of composite walls. Although longitudinal reinforcement clearly decreases the post-cracking ductility and increases the load carrying capacity, transverse reinforcement has a negligible effect on the load carrying capacity of encased-plate composite walls. This trend suggests that there is no rationale behind providing more than the minimum transverse reinforcement in the design of composite walls, which is needed to provide lateral support against buckling of the encased-plate, and to reduce concrete shrinkage.

- Increasing the longitudinal reinforcement in the boundary elements has an effect on increasing the initial wall stiffness, and it clearly increases the load carrying capacity of composite walls.
- The full-field deformation measurement system based on digital photogrammetry and particle image velocimetry (PIV) offers diverse unique advantages over conventional measuring techniques.
- The softened truss model with the newly proposed cracking angle can predict the shear capacity of conventionally-reinforced structural walls more accurately than the fixed angle solution and the ACI (2008) method. The close match of the method's shear strength predictions to experimental results is promising and indicates the success of the proposed method.
- The value of the strut cracking angle proposed in this study can be used to predict the load-deformation behaviour of structural walls subjected to either combined axial and lateral loads or only lateral loads. It is also suitable for walls subjected to either monotonic or cyclic loads.
- The softened truss model can also predict the shear strength and deformation behaviour of encased-plate composite walls. The close match of the method's results to experimental behaviour is indicative of the effectiveness of the proposed analysis method.

8.4 Recommendations for future research

The author believes that the work described in the current research provides a platform for the basic understanding of the behaviour of encased-plate composite walls under both pure in-plane shear and lateral loads. A number of interesting questions still remain unanswered, new topics of research have been opened for investigation and several propositions require validation. The suggested lines of research are as follows:

- Since the behaviour of structural walls under cyclic loading is different from that under monotonic loading, investigating the behaviour of the composite wall system under cyclic loading should be useful.
- Experimental testing is still required to investigate the performance of composite walls under combinations of lateral and axial loading. Axial loading may initiate plate buckling early and lead to premature failure of the composite wall.
- Typical small-scale and full-size wall models should be subjected to earthquake motions by using a shaking table facility driven by real earthquake records. The study results can be used to understand the behaviour of the composite system under actual seismic conditions.
- A detailed feasibility study is needed to assess the practical problems associated with this type of construction. The study should include the buildability of the composite system and the use of pre-cast composite walls.
- Further research is required to perform a cost comparison between composite and traditional wall systems, while considering the various factors that can affect the overall construction cost.
- Experimental testing on composite walls utilising plates with special surface roughness or shear studs to improve bond between the steel plate and the concrete is needed.
- Investigating the behaviour of encased-plate composite coupled walls with one or two bands of openings would be useful to extend current research into coupled walls.
- Further validation of the proposed analysis method is required. Thus, additional tests of walls with different geometry, loading conditions and concrete strength are of immediate importance.

References

- Abdel-Sayed, G., Bakht, B., and Jaeger, L. G. (1994). Soil-Steel Bridges: Design and Construction, McGraw-Hill Inc., New York.
- Abdullah, M. S. (1993). "Reinforced concrete beams with steel plates for shear," PhD Thesis, University of Dundee, Dundee, UK.
- Adrian, R. J. (1991). "Particle-Imaging Techniques for Experimental Fluid Mechanics." Annual Review of Fluid Mechanics., 23(1), 261-304.
- Adrian, R. J. (2005). "Twenty years of particle image velocimetry." Experiments in Fluids, 39(2), 159-169.
- Ahmed, W. and Bransby, M. (2009). "Interaction of Shallow Foundations with Reverse Faults." Journal of Geotechnical and Geoenvironmental Engineering, ASCE, 135(7), 914-924.
- American Concrete Institute (ACI). (2008). "Building Code Requirements for Structural Concrete." (ACI 318-08) and Commentary (ACI 318R-08), Farmington Hills, Michigan, USA.
- Astaneh-Asl, A. (2001) "Seismic Behavior and Design of Steel Shear Walls " SEOANC Seminar, Structural Engineers Assoc. of Northern California, San Francisco.
- ASTM A370-06. (2006). "Standard Test Methods and Definitions for Mechanical Testing of Steel Products."
- Baglin, P. S. (1998). "Plate reinforcement for shear : the analysis, design and detailing of plate reinforced concrete beams," PhD thesis, University of Dundee, Dundee, UK.
- Bales, F. B. (1985). "Close-range photogrammetry for bridge measurement." Transportation Research Record, 950, 39-44.

- Bales, F. B., and Hilton, M. H. (1985). "Application of Close-Range Terrestrial Photogrammetry to Bridge Structures." Virginia Highway and Transportation Research Counci.

- Barda, F., Hanson, J. M., and Corley, W. G. (1977). "Shear strength of low-rise walls with boundary elements." Reinforced Concrete Structures in Seismic Zones, Publication SP-53, American Concrete institute, Detroit, 149-202.

- Basler, K. (1961). "Strength of Plate Girders in Shear." Journal of the Structural Division. ASCE, 87,No. ST7, 151-180.

- Bisby, L., Take, W. A., and Caspary, A. (2007). "Quantifying strain variation in FRP confined concrete using digital image correlation: proof-of-concept and initial results." Asia-Pacific Conference on FRP in Structures (APFIS 2007).

- British Standards Institution. (1986). "BS1881-125." Testing concrete. Methods for mixing and sampling fresh concrete in the laboratory, London, BSI.

- British Standards Institution. (2002). "BS EN 12390-3:2002." Testing hardened concrete. Compressive strength of test specimens, London, BSI.

- British Standards Institution. (2005). "BS EN 1993-1-1:2005." Eurocode 3: Design of steel structures - Part 1-1: General rules and rules for buildings, London, BSI.

- British Standards Institution. (2008). "BS EN 1992-1-1:2004." Eurocode 2: Design of concrete structures- Part 1-1: General rules and rules for buildings., London, BSI.

- Caccese, V., Elgaaly, M., and Chen, B. (1993). "Experimental Study of Thin Steel-Plate Shear Walls Under Cyclic Load." Journal of Structural Engineering, ASCE, 119(2), 573-587.

- Cardenas, A. E., Russell, H. G., and Corley, W. G. (1980). "Strength of Low-rise Structural Walls, Reinforced Concrete Structures Subjected to Wind and Earthquake Forces." Reinforced concrete structures subjected to wind and earthquakes forces, Publication SP-63, ACI, Detroit, 221-241.

- Collins, M. P. (1973). "Torque-twist characteristics of reinforced concrete beams." Inelasticity and Non-Linearity in Structural Concrete, study No.8, University of Waterloo Press, 211-231.

- Cooper, M. A. R., and Robson, S. (1990). "High precision photogrammetric monitoring of the deformation of a steel bridge." The Photogrammetric Record, 13(76), 505-510.

- Dabbagh, H. (2005). "Strength and ductility of high-strength concrete shear walls under reversed cyclic loading," PhD thesis, The University of New South Wales, Sydney, Australia.

- Dallas, R. W. A. (1996). "Architectural and archaeological photogrammetry." Close Range Photogrammetry and Machine Vision, 283-301.

- Driver, R. G., Kulak, G. L., Kennedy, D. J. L., and Elwi, A. E. (1998). "Cyclic Test of Four-Story Steel Plate Shear Wall." Journal of Structural Engineering, ASCE, 124(2), 112-120.

- Erkmen, B. and Schultz, A. E. (2007). "Self-centering behaviour of unbonded precast concrete shear walls." Earthquake Resistant Engineering Structures VI 93: 185-194.

- Farvashany, F. E., Foster, F. J. and Rangan, B. V. (2008). "Strength and Deformation of High-Strength Concrete Shearwalls." ACI structural journal, 105(1): 21-29.

- Fintel, M. (1991). "Shearwalls - an answer for seismic resistance?" Concrete International, 13(7), 48-53.

- Fintel, M. (1995). "Performance of buildings with shear walls in earthquakes of the last thirty years." PCI Journal, 40(3), 62-80.

- Forno, C., Brown, S., Hunt, R. A., Kearney, A. M., and Oldfield, S. (1991). "Measurement of deformation of a bridge by Moire photography and photogrammetry." Strain, 27(3), 83-87.

- Fraser, C. S. (2000). Industrial measurement applications, in: Close Range Photogrammetry and Machine Vision, Whittles Publishing, Roseleigh House, Latheronwheel, Caithness, KW5 6DW, Scotland, UK.

- Gallocher, S. C. (1993). "The Behaviour of Composite Wall With Profiled Steel Sheeting," PhD thesis, The University of Strathclyde, Glasgow, UK.

- Gulec, C. K., Whittaker, A. S. and Stojadinovic, B. (2008). "Shear Strength of Squat Rectangular Reinforced Concrete Walls." ACI Structural Journal. 105(4): 488-497.

- Gulec, C. K., Whittaker, A. S. and Stojadinovic, B. (2009). "Peak shear strength of squat reinforced concrete walls with boundary barbells or flanges." ACI structural journal. 106(3): 368-377.

- Gupta, A. (1996). "Behaviour of High Strength Concrete Structural Walls," PhD Thesis, Curtin University of Technology, Perth, Western Australia.

- Gupta, A., and Rangan, B. V. (1998). "High-Strength Concrete (HSC) Structural Walls." ACI structural journal. 95(2), 194-205.

- Harries, K. A., Mitchell, D., Cook, W. D., and Redwood, R. G. (1993). "Seismic response of steel beams coupling concrete walls." Journal of Structural Engineering, ASCE, 119(12), 3611-3629.

- Hegger, J., Sherif, A., and Gortz, S. (2004). "Investigation of Pre- and Postcracking Shear Behavior of Prestressed Concrete Beams Using Innovative Measuring Techniques." ACI Structural Journal, 101(2), 183-192.

- Hibbitt, Karlsson, and Sorensen. (2008). ". Abaqus: Standard Users Manual." Detroit, MI.

- Hirosawa, M. (1975). "Past experimental results on reinforced concrete shear walls and analysis on them." Kenchiku Kenkyu Shiryo, No. 6, Building Research Institute, Ministry of Construction, Tokyo, 277 (in Japanese).

- Hossain, K. M., and Wright, H. D. (2004a). "Experimental and theoretical behaviour of composite walling under in-plane shear." Journal of Constructional Steel Research, 60(1), 59-83.

- Hossain, K. M. A., and Wright, H. D. (2004b). "Performance of double skin-profiled composite shear walls - Experiments and design equations." Canadian Journal of Civil Engineering, 31(2), 204-217.

- Hossain, K., and Wright, H. (1995). "Composite walling with special reference to the stabilization of building frames." Proceedings of the Nordic Steel Construction Conference, Swedish Institute of Steel Construction, Stockholm, Malmo, Sweden, 531–538.

- Hsu, T. T. C. (1993). Unified theory of reinforced concrete, CRC Press, New directions in civil engineering, Boca Raton, Fla.; London.

- Hsu, T. T. C., and Mo, Y. L. (1985). "Softening of concrete in low-rise shearwalls." ACI Journal, 82(6), 883-889.

- Hwang, S. J., Fang, W. H., Lee, H. J., and Yu, H. W. (2001). "Analytical model for predicting shear strength of squat walls." Journal of Structural Engineering, ASCE, 127(1), 43-50.

- Iliya, R., and Bertero, V. (1980). "Effect of amount and arrangement of wall-panel reinforcement on hysteretic behavior of reinforced concrete walls." Report No. UCB/EERC-80/04. California: University of California Berkeley. Earthquake Engineering Research Center (EERC).

- Irwin, A. W. (1984). "Design of shear wall buildings." Construction industry and research institute association, CIRIA 102.

- Jauregui, D. V., White, K. R., Woodward, C. B., and Leitch, K. R. (2003). "Noncontact photogrammetric measurement of vertical bridge deflection." Journal of Bridge Engineeering, 8(4), 212-222.

- Jiang, R., Jregui, D. V., and White, K. R. (2008). "Close-range photogrammetry applications in bridge measurement: Literature review." Measurement, 41(8), 823-834.

- Johnson, G. W. (2001). "Digital close-range photogrammetry - A portable measurement tool for public works." Presented at the Coordinate Measurement Systems Committee 2001 Conference, Albuquerque, NM, 13–17.
- Kabeyasawa, T., and Hiraishi, H. (1993). "Test and analyses of high-strength reinforced concrete shear walls in Japan." ACI SP, 176(13), 281-310.
- Kassem, W. and Elsheikh, A. (2010). "Estimation of Shear Strength of Structural Shear Walls." Journal of Structural Engineering, ASCE, In Press (doi:10.1061/(ASCE)ST.1943-541X.0000218).
- Khaloo, A. (2002). "Compressive Behavior of Concrete Confined with High-Stiffness Perforated Steel Plates." Asian Journal of Civil Engineering, 3(3), 57-74.
- Khaloo, A., and Shokoufi, M. N. (2002). "Behaviour of concrete shear walls reinforced with perforated steel plates." Proceedings of the international seminar,university of Dundee, Dundee, UK, 147-155.
- Kim, B. G. (1989). "Development of a photogrammetric system for monitoring structural deformations of the sturgeon bay bridge." Development of a Photogrammetric System for Monitoring Structural Deformations of the Sturgeon Bay Bridge.
- Kong, F. K. (2003). Reinforced Concrete Deep Beams, Taylor & Francis Books, Inc.
- Kuhn, P., Peterson, J. P., and Levin, L. R. (1952). "A summary of diagonal tension Part I : methods of analysis." National Advisiory Committee for Aeronautics, Technical Note 2662
- Lam, W. Y. (2006). "Plate-reinforced Composite Coupling Beams – Experimental and Numerical Studies " PhD thesis, The University of Hong Kong, Hong Kong.
- Lam, W. Y., Su, R. K. L., and Pam, H. J. (2001). "Embedded steel composite coupling beams-a new proposal." Proceedings of the International Conference on Construction; 93–104.

- Lam, W. Y., Su, R. K. L., and Pam, H. J. (2002). "The performance and design of embedded steel composite coupling beams." Proceeding of Structural Engineers World Congress, 365-373.

- Lam, W. Y., Su, R. K. L., and Pam, H. J. (2003). "Strength and ductility of embedded steel composite coupling beams." Advances in Structural Engineering, 6(1), 23-35.

- Lam, W. Y., Su, R. K. L., and Pam, H. J. (2004a) "The effects of shear connectors on plate-reinforced composite coupling beams." 2nd International Conference of Structural Engineering, Mechanics and Computation, Cape Town, South Africa.

- Lam, W. Y., Su, R. K. L., and Pam, H. J. (2004b). "Seismic performance of plate reinforced composite coupling beams." Proceedings of 13th World Congress on Earthquake Engineering, Vancouver, B.C., Canada.

- Lam, W. Y., Su, R. K. L., and Pam, H. J. (2005). "Experimental study on embedded steel plate composite coupling beams." Journal of Structural Engineering, ASCE, 131(8), 1294-1302.

- Lampert, P., and Thurlimann, B. (1968). "Torsionsversuche an Stahlbetonbalken (Torsion tests of reinforced concrete beams), Bericht Nr. 6506–2; (1969) Torsion-Biege-Versuche an Stahlbetonbalken (Torsion-bending tests on reinforced concrete beams), Bericht Nr. 6506–3, Institut fur Baustatik, ETH, Zurich, (in German)."

- Lee, H. J., and Kuchma, D. A. (2007). "Seismic overstrength of shear walls in parking structures with flexible diaphragms." Journal of Earthquake Engineering, 11(1), 86-109.

- Lee, H. J., Kuchma, D. A., Baker, W., and Novak, L. C. (2008). "Design and Analysis of Heavily Loaded Reinforced Concrete Link Beams for Burj Dubai." ACI Structural Journal, 105(4), 451-459.

- Lee, J., and Fenves, G. L. (1998). "Plastic-damage model for cyclic loading of concrete structures." Journal of Engineering Mechanics, ASCE, 124(8), 892-900.

- Lefas, I. (1988). "Behaviour of reinforced concrete structural walls and its implication for ultimate limit state design," PhD thesis, University of London, London, UK.

- Lefas, L. D., Kotsovos, M. D., and Ambraseys, N. N. (1990). "Behaviour of reinforced concrete structural walls: strength, deformation characteristics, and failure mechanism." ACI structural journal, 87(1), 23-31.

- Lubliner, J., Oliver, J., Oller, S., and Onate, E. (1989). "A plastic-damage model for concrete." International Journal of Solids and structures, 25(3), 299-326.

- Maier, J., and Thurliamann, B. (1985). "Bruchversuche an Satahlbetonscheiben." Institut fur Baustatik und Konstruktion ETH, Zurich, (in Germany), 130.

- Mansour, M. Y., Dicleli, M., and Lee, J. Y. (2004). "Nonlinear analysis of R/C low-rise shear walls." Advances in Structural Engineering, 7(4), 345-361.

- Marsono, A. K. (2000). "Reinforced concrete shear walls with regular and staggered openings," PhD thesis, University of Dundee, Dundee, UK.

- Mau, S. T., and Hsu, T. C. (1987). "Shear Behaviour of reinforced Concrete Framed Wall Panels with Vertical Loads." ACI Structural Journal, 84(3), 228-234.

- Megson, T. H. G. (1977). Aircraft structures for engineering students, London Edward Arnold.

- Megson, T. H. G. (1996). Structural and stress analysis, Arnold, London.

- Mimura, H., and Akiyama, H. (1977). "Load-Deflection Relationship of Earthquake-Resistant Steel Shear Walls With a Developed Diagonal Tension Field." ransactions, Architectural Institute of Japan, 260, 109-114.

- Mo, Y. L. (1993). "Dynamic tests on reinforced concrete shear walls." National Science Council Project. Report No. 81-0410-E006-521, Taiwan (in Chines).
- Murty, C. V. R. (2004). "Why are buildings with shear walls preferred in seismic regions?" Learning Earthquake Design and Construction, Building Materials and Technology Promotion Council, New Delhi, India, New Delhi, India.
- Nielsen, M. P. (1984). Limit analysis and concrete plasticity, Englewood Cliffs, N.J. Prentice-Hall.
- Oesterle, R. G., Aristizabal-Ochoa, J. D., Shiu, K. N., and Corley, W. G. (1984). "Web crushing of reinforced concrete structural walls." ACI Journal, 81(3), 231-241.
- Pappa, R. S., Giersch, L. R., and Quagliaroli, J. M. (2001). "Photogrammetry of a 5m inflatable space antenna with consumer-grade digital cameras." Experimental Techniques, 25(4), 21-29.
- Paulay, T. (1980). "Earthquake-resisting shear walls-New Zealand Design trends." ACI Journal, 144-152.
- Paulay, T., and Binney, J. R. (1974). "Diagonally reinforced coupling beams of shear walls." ACI Special Publication, SP-42, 579–598.
- Paulay, T., and Priestley, M. J. N. (1992). Seismic design of reinforced concrete and masonry buildings, Wiley, New York, USA.
- Paulay, T., Priestley, M. J. N., and Synge, A. J. (1982). "Ductility in earthquake resisting squat shearwalls." ACI Journal, 79, 257-269.
- Penelis, G. G., and Kappos, A. J. (1997). Earthquake Resistant Concrete Structures, E & FN Spon, London, UK.
- Raongjant, w. (2007). "Seismic Behaviour of Lightweight Reinforced concrete Shear Walls," Ph D thesis, Rajamangala University of Technology Thanyaburi, Thailand.

- Redzuan, R. (2004). "Experimental evaluation and analytical modeling of shear bond in composites slabs," Virginia Polytechnic Institute and State University

- Ritter, W. (1899). "Die Bauweise Hennebique (Construction Techniques of Hennebique)." Schweizerische Bauzeitung, Zürich, 33(7), 59-61

- Sabouri-Ghomi, S. (1989). "Quasi Static and Dynamic Hysteretic Behaviour Of Unstiffened Steel Plate Shear Walls " PhD thesis, University of Wales, College of Cardiff. , Cardiff, UK.

- Sainsbury, R. N., and Shipp, S. J. I. (1983). "National westminster tower: some aspects of construction." Institution of Civil Engineers Proceedings, pt. 1, Design construction, 74, 435-471.

- Salonikios, N. T., Kaos, A. J., Tegos, I. A., and Penelis, G. G. (1999). "Cyclic Load Behaviour of Low-Slenderness Reinforced Concrete Walls: Design Basis and Test Results." ACI Structural Journal, 96(4), 649-660.

- Salonikios, T. N., Kappos, A. J., Tegos, I. A., and Penelis, G. G. (2000). "Cyclic load behavior of low-slenderness reinforced concrete walls: Failure modes, strength and deformation analysis, and design implications." ACI Structural Journal., 97(1), 132-141.

- Seilie, I. F., and Hooper, J. D. (2005). "Steel plate shear walls: Practical design and construction." Modern steel construction, 45(4), 37-43.

- Shaingchin, S., Lukkunaprasit, P., and Wood, S. L. (2007). "Influence of diagonal web reinforcement on cyclic behavior of structural walls." Engineering structures, 29(4), 498-510.

- Su, R. K. L., Lam, W. Y., and Pam, H. J. (2009). "Experimental study of plate-reinforced composite deep coupling beams." The Structural Design of Tall and Special Buildings, 18(3), 235-257.

- Subedi, N. K. (1989). "Reinforced concrete beams with plate reinforcement for shear." Proceedings of Institute of Civil Engineering. 1, Design construction, 87, 377-399.

- Subedi, N. K., and Baglin, P. S. (1999). "Plate reinforced concrete beams: experimental work." Engineering Structures, 21(3), 232-254.

- Subedi, N. K., and Coyle, N. R. (2002). "Improving the strength of fully composite steel-concrete-steel beam elements by increased surface roughness-An experimental study." Engineering Structures, 24(10), 1349-1355.

- Takahashi, Y., Takemoto, Y., Takeda, T., and Takagi, M. (1973). "Experimental Study on Thin Steel Shear Walls and Particular Bracings Under Alternative Horizontal Load." Preliminary Report, IABSE Symposium on Resistance and Ultimate Deformability of Structures Acted on by Well-defined Repeated Loads, Lisbon, Portugal, pp. 185–191.

- Teng, J. G., Chen, J. F., and Lee, Y. C. (1999). "Concrete-filled steel tubes as coupling beams for RC shear walls." Proceedings of the 2nd International Conference on Advaces in Steel Structures, 391-399.

- Teychenné, D. C., Franklin, R. E., Erntroy, H. C., and Marsh, B. K. (1998). Design of normal concrete mixes, Building Research Establishment, CRC.

- Thorburn, l. J., Kulak, G. l., and Montgomery, C. J. (1983). "Analysis of Steel Plate Shear Walls ", Department Of Civil Engineering, The University Of Alberta, Edmonton, Alberta, Canada.

- Timler, P. A., and Kulak, G. L. (1983). "Experimental Study Of Steel Plate Shear Walls ", Department of Civil Engineering, The University of Alberta, Edmonton, Alberta, Canada.

- Tromposch, E. W., and Kulak, G. L. (1987). "Cyclic and Static Behaviour of Thin Panel Steel Plate Shear Walls." Structural Engineering Report No. 145, Department of Civil Engineering, University of Alberta, Edmonton, Canada.

- Tsuda, K., Nakayama, T., Eto, H., Akiyama, K., Shimizu, A., Tanouchi, K., and Aoyama, H. (2001)"Experimental Study on Steel Plate Reinforced Concrete Shear Walls with Joint Bars." Transaction, SMiRT 16, Washington DC, 1-8.

- Vecchio, F., and Collins, M. P. (1981). "Stress-strain characteristics of reinforced concrete in pure shear." IABSE Colloquium Delft 1981: Advanced

Mechanics of Reinforced Concrete, Final Report (International Association for Bridge and Structural Engineering). 34, 211-225.

- Vecchio, F., and Collins, M. P. (1986). "The Modified-Field Compression Theory for Reinforced Concrete Elements Subjected to Shear." ACI Journal, 83(2), 219-231.

- Vermeer, P. A., and de Borst, R. (1984). Non-Associated Plasticity for Soils, Concrete and Rock, Delft: Heron.

- Wagner, H. (1931). "Flat Sheet Metal Girders with Very Thin Webs, Part I – General Theories and Assumptions." Technical Memo No. 604, National Advisory Committee for Aeronautics, Washington, D.C, USA.

- Warner, R. F., Rangan, B. V. and HAll, A. S. (1989). Reinforced concrete. Melbourne, Longman Cheshire Pty. Ltd.

- White, D. J., and Take , W. A. (2002). "GeoPIV: Particle Image Velocimetry (PIV) software for use in geotechnical testing." Cambridge University, Engineering Department -Technical Report D-SOILS-TR322.

- White, D. J., Take, W. A., and Bolton, M. D. (2003). "Soil deformation measurement using particle image velocimetry (PIV) and photogrammetry." Geotechnique, 53(7), 619-631.

- White, D., Randolph, M., and Thompson, B. (2005). "An image-based deformation measurement system for the geotechnical centrifuge." Intemational Journal of Physical Modelling in Geotechnics, 5, 1-12.

- Whiteman, T., Lichti, D., and Chandler, I. (2002). "Measurement of deflections in concrete beams by close-range digital photogrammetry." Symposium on Geospatial Theory, Processing and Applications, 2002 - isprs.org.

- Woodhouse, N. G., Robson, S., and Eyre, J. R. (1999). "Vision metrology and three dimensional visualization in structural testing and monitoring." Photogrammetric Record, 16(94), 625-641.

- Wright, H., Evans, R., and Gallocher, S. (1992). "Composite walling." Composite Construction in Steel and Concrete II, Publication by ASCE, , Atlanta, GA, USA, 783-797.

- Wright, H., Hossain, A., and Gallocher, S. (1994). "Composite walls as shear elements in tall structures." Publication by ASCE, Atlanta, GA, USA, 140-145.

- Yu, H. W., and Hwang, S. J. (2005). "Evaluation of softened truss model for strength prediction of reinforced concrete squat walls." Journal of Engineering Mechanics, ASCE, 131(8), 839-846.

- Zhang, L.-X. B., and Hsu, T. T. C. (1998). "Behavior and Analysis of 100 MPa Concrete Membrane Elements." Journal of Structural Engineering, ASCE, 124(1), 24-34.

- Zhao, Q., and Astaneh-Asl, A. (2002). Cyclic behavior of traditional and an innovative composite shear wall, Rep. No. UCB-Steel-01/2002,Dept. of Civil and Environmental Engineering, Univ. of California, Berkeley, Calif, USA.

- Zhao, Q., and Astaneh-Asl, A. (2004). "Cyclic Behavior of Traditional and Innovative Composite Shear Walls." Journal of Structural Engineering, ASCE, 130(2), 271-284.

- Zhao, Q., and Astaneh-Asl, A. (2007). "Seismic Behavior of Composite Shear Wall Systems and Application of Smart Structures Technology." International Journal of Steel Structures, KSSC, 7, 69-75.